Quantum-Based Modelling and Simulation of Materials Used In Small-Scaled Plasmonic Devices

BY

LATEEF ADESOLA AKINYEMI

A thesis submitted for the degree of
Doctor of Philosophy
in the Department of Electrical Engineering,
Faculty of Engineering and the Built Environment, University of Cape Town
AUGUST 2020

Supervisor: Emeritus Professor Alireza Baghai-Wadji

Declaration

I hereby declare that: (1) the above thesis is my own unaided work, both in conception and execution, and that apart from the normal guidance of my supervisor, I have received no assistance apart from that stated below; (2) except as stated below, neither the substance nor any part of the thesis, has been submitted in the past, or is being, or is to be submitted for a degree in the University, or any other University.

I am now presenting the thesis for examination for the Degree of PhD in Electrical Engineering. I also grant the University free license to reproduce the above thesis in whole or in part, for the purpose of research.

LATEEF ADESOLA AKINYEMI — 30 July 2020 — Signed by candidate

Name — Date

Dedication

This thesis report is dedicated to ALMIGHTY ALLAH, Late Prince L.O Akinyemi, Late Princess S.A Akinyemi (Mrs), Late Alimat Shadiat Akinyemi, Chief (Prince) Saliu Adekunle Akinyemi (Father S), Professor (Prince) Kabir'Olusegun Akinyemi, Prince S. Adedeji Akinyemi, Mr and Mrs Johnson Ikuseedun, Mrs Yemisi Ige Adesola-Akinyemi, Prince Ameen Adeyemisola Abisoye Akinyemi, friends, well-wishers and my lecturers that have made an indelible positive impact during my course of study and in general.

Acknowledgements

The search of knowledge from the mathematical point of view of nature, for me, is one of the highest beauteous tasks in the complexness of humanity and its highest primal form, best-known as physics as a subject, one of the followers of sterling adoption and effect on south-western body, at the least dates back the Galileo era. This allows the acknowledgements in principle to the entire mankind for having completed to the end of this research work, would be just a humble ostentatiousness and puffiness, from the small glint of homo, chap of the odyssey in this special vehicle known as planet Earth as the only home of man is constantly bathed in a steady rain of knowledge and technology demands. Nevertheless, the other people, whom we usually address as relations, nuclear and extended families or colleagues have got one or two stories of life to tell, in this boundless world inside us in this life, in this odyssey termed beingness. To those people, who are in some other form, they are to whom only I express my wholehearted, genuine, true and honest thanks for being the designers of each one of the alphabets, equations, notations, letters, results and symbols in this modest, honourable, and downright reading of this wide macrocosm.

Firstly, I would like to express profoundly my gratitude to Almighty God and my late parents Princess S.A Akinyemi and Prince L.O Akinyemi alongside my late sister (Princess

Shadiyyah Akinyemi) and late cousin Nurudeen Akinyemi all of the "blessed memory" the supporters of my beingness with their counselling, pieces of advice during their lifetime and for showing me that state of being myself in every situation, not only in academic pursuit, is the instrument to keep the skyline thus far, however, with the capability of visualizing it always near. I give thanks to Almighty God for them, to S.A Akinyemi and L.O Akinyemi for being my biological parents, who unconditionally accepted my selection of having them as family, alongside my siblings: Chief (Prince) Saliu Adekunle Akinyemi (The first Baale of Olufoworesetie), Professor (Prince) Kabir' Olusegun Akinyemi, and Prince Safiriyy Adedeji Akinyemi ("Ijebu Worldwide") and my cousins, in particular, Ibrahim Mufutau, Kayode Ibrahim and nieces and nephews. For their love and unconditioned devotedness, I thank you most sincerely and kindly. On the other hand, I want to thank boundlessly and immeasurably my supervisor as well as adviser Emeritus Professor Alireza Baghai-Wadji. I could recall thousands of moments that I was not adapted at all and indifferent to some technical details, and your response was a father's every moment, patiently and painstakingly - lot of love in a serene condition that for many grounds and many thanks for giving so much to me in terms of critical thinking, scientific rigour and mathematical gifts. Therefore, you are a building block and central to this process of my programme at the University of Cape Town. To my closest friends, who with their love and regardless limitless errors they have supported me, they deserve this lustrous sky that always pleases us in boundless tasks, long and numberless tales of life, engineering and science seeking an improved path, more equitably globe. Thank you for letting this path something honest, a journey worth embarking. To Olufemi Joshua Okunbanjo and his family, Wasiu Shina Majule and his family, Festus Oluwaseun Ojeyemi

and his family, Jide Muftau Usman and his family, Olujide Olulonye and his family, Olufemi David Adebogun, Kamolideen Abiodun Salisu and his family especially Aminat Abiola Salisu (Nee Mustapha) and a host of others which I cannot mention because of paucity of time and space. I simply say thank you very much and hope to see you for the rest of my life since you have been outstanding when I have been minute in inadequate and calamitous times. In addition to friends, I have also been fortunate extremely to work closely with remarkable and extraordinary people in Communication Research Group (CRG) at the University of Cape Town namely Oladejo Sunday Oladayo and his family who doubles to be a coding expert and support during the CFDM and DFT coding stages, Ekwe Stephen Obono and his family who also doubles as the graphics designer for this thesis, Michael Tarerefa,Ajibare Adedotun Temitope, Paul Orim and host of others. To my micro research group (Computational Electronics), the likes of Wassim Lorgat, Mahmood Akbari, Yeatzer and Bruce Mkhaliphi, I say a big thank you to you all. I thank Mr and Engr. (Mrs) Comfort Oluwaseyi Folorunso (Brosco and Sisco(PhD)) and members of the Folorunso's family kindly for their support, fasting and prayers during and after the programme. Also special thanks goes to the Head of Communications Research Group (CRG) in person of Mr Neco Ventura for his unflinching support and mentorship and members of the CRG, members of academic and non-academic Staff, Department of Electrical Engineering, Faculty of Engineering and the Built Environment, University of Cape Town, Western Cape, South Africa. To my good and humble friend Akanbi Bamidele Abiodun (Phier 025) with his Abaniseloluwa family, I say thank you very much for your support during and after the programme with the gift of the customised jersey (Ajo se wa konibaje In Sha Allah from

the Apanisile family eyan Letua034). Additionally, my appreciation also goes to my senior colleagues, lecturers and supervisors (undergraduate at LASU) in no particular order: Engr. N.T Makanjuola and members of his family; Engr. O.O Shoewu (PhD) and members of his family; Engr. A. A Ajasa and members of his family; Mr A.O Ogunlewe and members of his family ; Mary Abosede Adedoyin (PhD(Mrs)) and host of others in the Department of Electronic and Computer Engineering, Faculty of Engineering, Lagos State University, Epe Campus, Lagos, Nigeria. Furthermore, the financial supports of the following bodies are equally acknowledged and appreciated highly: Tertiary Education Trust Fund(TETFUND, Nigeria), Postgraduate Funding Office for International and Refugee Students (UCT, South Africa), TELKOM for SATNAC Conference, UCT Council Bail-Out Fund (UCT, South Africa), FOOTHOLD and many more. With such a large group of people I have met, I think this Acknowledgements section will be incomplete without mentioning of some very talented and gifted Postdoctoral researchers. In particular, I would like to acknowledge: Ramoni Olakunle Adeogun (PhD) who always encourages and offers assistance at all times via proofreading of my manuscripts, Razieh Morad (PhD) who also increases my knowledge in quantum mechanics. Thanks also to Enoruwa Obayiuwana (PhD) for proofreading and encouragement to test the water by submitting the thesis and Joseph Folorunso Orimolade (PhD) who doubles as a father figure at all times and the proofreading of the thesis as well. Worthy of note is all members of Cape Town Duah group and JK MSA UCT most especially Associate Professor Abdur-Rahim Adebisi Giwa (PhD) [The Imam Agba of Cape Town, Chemistry Dept, LAUTECH, Nigeria], Ismail Babatunde Adefeso (PhD: The Emeritus Amir), Afolabi Abdul-Wasiu (Amir), Khadijah Tolulope Dauda (PhD (Mrs)) and

members of their families for their financial, spiritual and motivational supports during the programme, I say a big Jazzakhahllah Khairan. In addition, the following friends are equally acknowledged and appreciated in no particular order: Ajayi Nurudeen Abimbola (PhD)(My all-time HOC from B.Sc to PhD level), Gbolahan Ridwan Aiyetoro (PhD), Abdulakeem Adedipe (Akay), Abdulazeez Adeyemi Anjorin (PhD), Mario Zapata Herrera (PhD), Cesar Martinez Flores (PhD) and many more. Of course, this thesis would not be feasible and practicable without the unflinching, unwavering, unshakable and unconditional support of my family. Words cannot express how grateful I am to my caring wife, who at all times sacrificed so much so that I could finish my degree. I also thank gratefully and graciously Prince Ameen Adeyemisola Abisoye Adeboye Akanbi Fortune (by his mother) Ayomide (by his Grandma) Abiodun Folami (by his Grandpa) Akinyemi (Carbon copy of this author - this is my son to whom I am well-pleased and grateful to the creator). It is also important to acknowledge the following: Ifedayo Ojuetimi, Omolola Mosumola Faloye, Oluwadare Adeyemo, the Ikuseeduns, the Akinyemis, the Ekwes, the Oladejos for the respective role played in this odyssey of my programme.

Contents

Abstract

The study of Plasmonics has been evolutionary and fascinating over the last few decades. This area of research has attracted extensive interest predominantly as a result of the possibility to direct and confine light at the nano-scale level using metallic materials as fundamental building blocks. This provides an explanation to the interaction of light and nano-sized metallic devices. The optical properties of nano-structured systems depend on the collective resonance of conducting electrons which are determined by the geometrical features as well the polarization characteristics of the incident light and frequency. For large systems with size in the order of tens of the size of nano-scale materials, the response has been extensively studied and is now well understood. The response of these large systems can be described using classical Maxwell's equations with reasonable accuracy. On the other hand, the application of this classical solution to Plasmonic-based nano-particles is severely limited by quantum phenomena such as tunnelling and non-local screening. These quantum effects can neither be described nor explained by the classical method. There is, therefore, the need to understand how the theory of quantum method can be utilized to describe the properties of nano-materials. This forms the main focus of this thesis.

Firstly, the extension of existing classical models to Plasmonic materials is examined. It is ascertained that most of these models are designed for usage only in the high-frequency region. Furthermore, the use of Plasmonic devices including Metal-Insulator-Metal (MIM) and Insulator-Metal-Insulator (IMI) configuration are explored. An algorithm to determine and generate imaginary wave-vector numerically is proposed. The dissipation of electromagnetic fields, dielectric function, electric field, and magnetic field are computed for various values of complex wave-vector. Additionally, a one-dimensional quantum-based frequency-dependent dielectric function for small-scale devices is investigated. A Rigorous analysis and approximation are carried out on a 1-D model and a nano-wire geometry. The effect of transition band and investigation of optical materials of nano-wire for 1-D, 2-D, and 3-D are included in the analysis. The Eigen-pairs of the underlying canonical and associated perturbed quantum systems are computed and utilized for this study. Galerkin's method has been employed to discretize the boundary-value of interest. The introduction of the Sinc function throughout the analysis ensures the robustness and soundness of the computation. The analytical and numerical results demonstrate that the real- and imaginary parts of the dielectric function are even and odd function, respectively, as expected.

More so, the cubical, cuboid and spherical geometries of metallic nano-particles are employed to examine the effects on the material. These effects of size-dependent damping constant on the metallic nano-particles and not forgetting the optical properties of the material such as dielectric function, refractive index and absorption coefficient which are considered worthy of investigation in this thesis. Hence, in this thesis, a customized, flexible, and computational software package for efficient assessment of small-scaled Plasmonic

devices has been developed in 1-D and 2-D for regular geometry using the Standard Finite Difference Method (SFDM) and Conservative Finite Difference Method (CFDM). This study has been motivated, predominantly, by the tremendous interest in the examination of these geometrical structures. The package enables us to solve the desired homogeneous Dirichlet boundary-value problem. Then, the developed program is applied to solve the time-independent Schrödinger equation for the modelling and simulation of the physical properties of metallic nano-particles. Furthermore, the results obtained from SFDM and CFDM are compared. Finally, the concept of density functional theory (DFT) alongside the Kohn-Sham equation boundary-value problem with Dirichlet condition has been employed and demonstrated in this thesis to be a good candidate in solving and computing optical properties such as frequency-dependent dielectric function in small scale metallic nanoparticle of interest. Additionally, neither CFDM nor DFT schemes have been applied to determine optical properties of metallic nanoparticles in the literature, making it the first time such schemes will be used to compute optical properties.

List of Abbreviations

1-D	One-Dimensional
2-D	Two-Dimensional
3-D	Three-Dimensional
A.D	Anno Domino
BO	Born-Oppenheimer
BVP	Boundary Value Problem
CGSM	Conjugate Gradient System Method
CFDM	Conservative Finite Difference Method
DC	Direct Current
DFT	Density Functional Theory
DMD	Dielectric-Metal-Dielectric
DoF	Degree of Freedom
DOS	Dipole Oscillator Strength
DOSS	Density of States
DR	Dispersion Relation
FEG	Free Electron Gas
FEM	Finite Element Method
GGA	Generalized Gradient Approximate
GS	Ground State
HEG	Homogenous Electron Gas
HF	Hartree-Fork
HK	Hohenberg-Kohn
IBT	Interband Transition
IMI	Insulator-Metal-Insulator
KS	Kohn-Sham
LDA	Local-density Approximation
LHS	Left Hand Side
LRPA	Lindhard Random Phase Approximation
LSALP	Linearly Shifted Associated Legendre Polynomials
MATLAB	Matrix Laboratory
MDM	Metal-Dielectric-Metal
MG	Maxwell Garnett
MIM	Metal-Insulator-Metal
MIMIM	Metal-Insulator-Metal-Insulator-Metal
MTICMC	Micro-Targeted Infrared Cancer Medical Care
PDE	Partial Differential Equation
QAFDDF	Quantum Adjusted Frequency-Dependent Dielectric Function
QCM	Quantum Corrected Model
QED	Quantum Electrodynamics
R	Radius

RHS	Right Hand Side
RPA	Random Phase Approximation
SFDM	Standard Finite Difference Method
SP	Symmetric Property
SPPS	Surface Plasmon Polaritons
TE	Transverse Electric
TEMEELS	Transmission Electron Microscope Electron Energy Loss Spectroscopy
TM	Transverse Magnetic
TRK	Thomas-Reiche-Kuhn

List of Tables

List of Figures

Chapter 1

Introduction

1.1 Background and Motivation

In the last few decades, the sphere of nanotechnology has rapidly grown from fantasy into purely technology and science [1]. Nevertheless, in its early stage, nanotechnology puts together the subjects such as chemistry, biology and physics in addition to mathematics, computer, engineering and information technology. This gives wealthy and robust reasons for brand spanking new studies, and the developing capability and capacity to achieve one of technological know-how's best pursuits; to comprehend and imitate organic structures. During the last 1.5 billions years and more, world has maximized systems and structures of such stunning difficulty that current studies is most effective beginning to free up their techniques and secrets. The achievement originates from the nano-size particles in which the existences of everyone are made from. These particles carrying out straightforward functions, however, do now not constitute a residing entity. But, while mixed, the comments

and feedbacks among particles or molecules as it were permits the structure in form of system to respond to external excitations and in the long run, replicate the nature of existence. Richard Phillips Feymann became one of the early pioneers to realize the abilities unfolded if one is capable of manipulating and controlling nano-size structures [2] , and considering the impact in which the solid state physics has achieved outstandingly. It is now feasible and realistic to correctly construct devices of thousands of nano-sizes region; but, the primary challenges and limitations of such gadgets or devices are in their nature of structures. This gives rise to ever-developing problems to make sure that each element is connected to the entire device. The controlling and harvesting of self-organised organic structures ought to offer approach to construct and design three-dimensional (3-D) systems and therefore allow, among different matters, minute and quicker computer systems. Presently, this is within the space of technology fantasy as there are so many demanding situations dealing with this aim. These days, be it technology or science, is able to manipulate or comprehend the system behaviour of atomistic structures in addition to gadgets with sizes and dimensions more than approximately a micron. The area among these regions is more challenging to study or examine.

A primary motive for these challenges is that a great deal of technological know-how which is based on optically detection in which the gadgets under investigation are required. Regrettably, light can hardiest provide data in form of information on systems bigger than its wavelength. Hence, visible light has values of wavelength in the range of 400 nm and 900 nm and therefore , devices smaller than this cannot be investigated. A further challenge is

that of the issue of coupling light to nano-sized systems is extremely weak. This leads to another challenge in the underlying comprehension of nanometre particles.

Prior to the 19^{th} century, engineers and scientists thought that traditional physics was created in Newton's surmises of mechanics and Maxwell's concept of electromagnetism made the required description and interpretations of the innate universe [3]. However, this conviction began to decompose or break following the findings of modern arms of physics. Therefore, the laws of thermodynamics and electrodynamics resulted into absurdity. They were once used to radiating system based on Planck's theory in which the radiating energy should be quantified. Hence, Albert Einstein revealed that the electromagnetic theories and mechanics need to be altered. He, therefore, depicted these ideas in his theory of relativity. Further issues and challenges happened when particle or atom is being modelled by employing the theories and laws of electromagnetism and mechanism [1],[4–8]. Sometimes in 1905, Albert Einstein accurately surmised that the developments in the field and energy for the quantum matter take place in leaps which are plural of $\hbar\omega$ where $\hbar$ is defined as the reduced Planck's constant and ω is the frequency of the field [9]. By 1913, when Neils Bohr penned a radical essay regarding the hydrogen atom [10]. The advancement of theory of quantum mechanics occurred rapidly within years 1925 till 1929 immediately the field theory, quantum electrodynamics (QED), the Paul A Dirac equation and Schrödinger equation were carried out in large size [11]. The theories and laws which were true and correct for fine-scale systems are not appropriate for nanometre systems. It is worth mentioning that the theories and laws of Newton in physics remain exact to forecast large system performance yet when it approaches quantum mechanics challenges and it confronts the uncommon behaviour of such

a structure, moreover, quantum mechanics theory turns out to be more suitable in relation to quick particles or further ultra thin materials. Hence, classical and semi-classical basics cannot explain quantum phenomena that occur succinctly.

Quantum mechanics is based on the theory of structure which had been presented to describe, correct, and predict the behaviour of a huge range of material schemes. This can be explained from the fundamental viewpoint till atoms, nuclei and radiating system to particles and solid [11]. It is therefore important that one should wonder at scientists and physicists such as Erwin Rudolf Josef Alexander Schrödinger and Werner Karl Heisenberg who pioneered and developed the systems needed for quantum computations. It is then obvious that these scientists cum theorists were tough-minded realists, motivated to extend the novel scheme as a result of lack of classical physics to shed more light or perhaps describe nature at the electronic and atomic scales. Hence, the need is critical for practical engineers and physicists to enhance their expertise in quantum ideas and methods [12]. In this thesis, one of the primary focus of the study will be to model the quantum based phenomena regarding frequency dependent dielectric function for small scale Plasmonic devices in a fathomable form. The goal of this study is to address these quantum based problems by providing solutions. The first stage of the investigation is the transformation of quantum-based problems into mathematical forms which can be solved using software packages such as MATHEMATICA, Python, MATLAB, etc. The effort here is to evolve a modern approach for formulating quantum-based problems into more fathomable equivalents. The thesis also aims to investigate more effective and efficient approaches for solving the plethora of unresolved quantum-based problems.

Furthermore, other aim of this study is to carry out main review, modelling and simulation of problems involving some geometrical structures such as cubical, cuboid and spherical under boundary conditions. In order to advance this aim, it demands knowledge and application of theories such as basis functions and its implement to resolve the Schrödinger equation so as to acquire the eigenpairs (eigenvalues and eigenfunctions). We use these eigenpairs to determine the frequency-dependent dielectric function via the matrix elements and oscillator strength of the particle. The primary focus of the study relies on one- and two-dimensional geometrical structures.

As a first step, the basics of quantum mechanics as employed to geometrically based structures must be obtained. By assuming a one- or two-dimensional geometry with potentials and employing the necessary theories and theorems, the essential boundary-value problem must be solved to acquire the needed eigenpairs of a supposed particle propagating in the structure with potential. Therefore, a scheme will be applied for the algebraic process that comes after the formulation of the governing equations in form of partial or ordinary which has been utilized. Furthermore, another aim of this study is to identify the optical properties of a perturbed potential cage in one dimension. This tells us that there is a potential cage and afterwards disturbs with the applied electromagnetic field. Therefore, the physical properties such as dielectric function of an assumed single electron wave function within this disturbed cage system will be computed.

The limitation of present fine-scale techniques encourages and spurs researchers, scientists and engineers to foresee the growth of the nano-sized devices. By carrying out study in this sphere of research, quantum mechanics principles is the best essential part of theoretical

physics with immense uses in realistic and pragmatic physics which prevents inadequacies of classical physics at electronic and atomic regions. In order to justify the use of quantum mechanics to solve the real problem, it is appropriate to state the meaning of quantum explicitly. By quantum, it means how much in Latin language context, alludes to distinct units that in the theory of quantum mechanics allocates to energy of particle (atom) in steady or balanced state.The finding of the fact that waves can be presumed as a tiny packet of energy which is referred to as quanta resulted into the beginning of quantum mechanics.

The fundamental concept that resulted into the finding of quantum mechanics was the research of light which is in form of electromagnetic wave. This begins a description for spectra of light radiated by various type of particles. Initially, it was giving reason for electrons inhabiting in its orbit, which cannot be described by classical means. Furthermore, in 1900, Max Karl Ernst Ludwig Planck discovered that the energy of waves is discrete in nature called quanta. Albert Einstein employed this ground-breaking discovery to demonstrate that electromagnetic waves such as light comprise fundamental atom referred to as photon [13], [14]. This entity called photon has distinct energy level which instantly relies on the frequency of the wave.

The pioneer of the contemporary theory is the early twenty five years of theory of quantum mechanics [15]. The early quarter of the 20th century was referred to as a golden period for advance or development in quantum mechanics. Engineers and scientists comprising Louis Victor Pierre Raymond de Broglie, Niels Henrik David Bohr, Erwin Rudolf Josef Alexander Schrödinger , Werner Karl Heisenberg, Paul Adrien Maurice Dirac, Max Karl Ernst Ludwig Planck, Albert Einstein and other notable people had outstanding

contributions in determining and fostering quantum mechanics [15], [16]. The establishment of quantum mechanics offers us with an idea that emerges to be in total conformity to our experimental understanding of all relativistic phenomena [17].

Furthermore, quantum mechanics is a better basic idea than Newtonian classical based mechanics. Hence, it does explain the phenomena which are in tiny or minute scale region and classical mechanics approaches cannot be used to provide explanation for the noticed phenomena. For example, from Newtonian standpoint, a particle in an atomistic environment must move towards centre nucleus and collapses into it. On the contrary to classical viewpoint, electron is seen to be moving in a circular region around the nucleus. Additionally, in quantum mechanics theory, by formulating the nature of the system at any period is determined by a complex-valued wave function. Hence, from the mathematical standpoint, fact of the matter is that the likelihood of determining of an electron at a specific period and zone close to the nucleus can be derived is contrary to classical approach that could not compute the forecast of conjugated parameters such as position and momentum concurrently. In reality, electron is constantly taken onto consideration to be found around in the range with hidden but precise location. Hence, the inadequacy to precisely determine a particle position is stated in the principle of Heisenberg's uncertainty.

Broadly speaking, quantum mechanics can illuminate four kinds of phenomena in which classical form cannot define. These are wave particle duality, uncertainty principle, physical quantities discretization and quantum entanglement. Major part of our modern technology operates on a scale which has important quantum effect. For example, transistor, laser, microscope and electron are greatly affected by quantum consequences. Hence, transistors

are known to be semiconductor-based microelectronic devices in which the investigation resulted to their development through the diodes [18]. Authors, scientists and researches are shifting towards the control of quantum states. The attempt led to the progress of a safe broadcasting of data in form of information by the concept of quantum cryptography. The final aim is the building of quantum-based computer systems so that it can function rapidly quicker than the present ones in computational functions. Additionally, quantum teleportation is one of the the topics of current interest which allows transmission of quantum states across random distances [19–29]. It then depicts the significance of conceptual idea of energy levels, electron wave functions, band gaps, likelihood density of electrons, localization of electrons and other parameters in a connected state. For instance, the idea of electron wave function tells us that it is a final result in terms of solution for its Schrödinger equation and a function which includes all the pieces of information regarding the system.

In standard or traditional mechanics (also known as classical mechanics), the transfer of a particle of specific mass m has been made possible if it experiences energy more than the potential step and equally reflection appears for energy that is much less than the potential step. The traditional particle having a velocity possessing energy more than the potential step changes as it moves from one step to another. Nevertheless, in quantum mechanics, the case is different, and the electron with energy more than the potential step may not necessarily be transmitted. While, in the case of quantum mechanics, the wavelike nature of the electron ensures that it senses the presence of variations in potential. Hence, electron can also permeate the potential. Potential functions imposed in a quantum potential-cage (well) does perturb the entire system and thereby induces the system to be in another eigenstate.

Moreover, computation of the perturbed eigenpair becomes an inevitability, for discovering other parameters such as specific energy state. Consequently, problems in relation to one- and two- dimensional quantum potential-cage requires to be studied.

Contemporary technology allows to link specific quantum particles in different confines much longer time. Controlling and management of nano-system involves a tweaking command of quantum-caged shape and subsurface in turn requires crucial impact on blocking or allowing different channel phenomenon. For all these kinds of instances, a reasonably realistic utilization of classical quantum mechanical formality depicts an appropriate influence. Many essays on different views of the infinite potential well [30–36] have illuminated novel knowledge in the domain of harmonizing the canonical quantization case for the Hamiltonian operator with Neumann or Dirichlet Boundary Conditions.

Furthermore, an infinite potential-well problem is the most fundamental of all instances in which to investigate the phenomenon of discrete energy levels in confined states and is regarded in the literature as of the "smoking guns" of theory of wave mechanics. The Schrödinger equation possesses closed-form solutions for such a simple potential function. Although infinite potential cage ascribes many of profound technological value for the intuitions it permits and hence is of extreme physical significance. On the basis of boundary conditions, there is a possibility to utilize its solution in explaining remarkably vital systems. By employing its actual valued solution, the quantum wells or cages also known as heterostructure junction which comprises layers of different semiconductor materials in which these materials have unequal energy band gaps [37]. Conversely, a quantum cage is a potential-cage that envelops particles which were initially free to travel in three dimensions ,

to two dimensions, while confining them to fill a planar area [38]. The aforementioned facts and considerations in conjunction with the importance of the theoretical discoveries and possible recommendation of a standardised method for a powerful computing investigation of disturbed systems had stimulated, impelled, provoked, justified and encouraged me and had an effect on my embarking on this study.

Moment and time we understand the significance of ideas for quantum mechanics by providing an invaluable intuition to create and have a full grasp of nano-scale systems. The certainties that valuable devices can be created and constructed based on specific particles or molecules have been previously illustrated by past investigator.

1.2 Objective of the Study

The important purpose of this study is to investigate the theoretic and mathematical calculations of on one- and two- dimensional (1-D and 2-D) conventional and perturbed quantum-based potential-cage problems of small-scale plasmonic devices. We aim to formulate a method that offers powerful, flexible and customized computation of disturbed eigenvalues and eigenfunctions, thereby removing the complexity and complication associated with the conventional calculation. The problem is modelled as a boundary value problem in this regard, it is a perturbed quantum potential-cage. Hence, perturbations are occasioned by adding potential function $V(x)$ in a single particle box function. Consecutively, the corresponding perturbed (modified) eigenpairs are calculated.

Our approach consists of a single particle subjected to boundary value conditions. To resolve such a perturbed system, we have represented the problem in a canonical form. This

canonical form is just the infinite potential-cage. Simply put, we start with the infinite quantum potential-cage scenario due to the accessibility of the equivalent complete set of eigenfunction in closed-form.

We then utilize the closed form solutions to solve the formulated problems regarding dielectric function and operators emanating from a particular commonly allowed set. Therefore, we start with the original 1-D and cubical quantum potential-caged system of a cubical geometry with potential function $V(x)$ clearly defined. If the potential is infinite, the particle has zero probability to be there. This means that we assume that $V(x)$ is zero when the particle or a single electron is in the structure and infinite when it is outside. The eigenpairs are obtained. These eigenpairs are then used to determine the frequency dependent dielectric function via the application of matrix elements and oscillator strength of the electron when the particle has transited from one state (initial) to another state (final) with the aid of perturbation.

Consequently, the eigenpairs of the initial problem are obtained. In this study, we focus on the cubical, cuboid and spherical geometries of a single electron confined in the structure with the imposition of boundary conditions. As has been mentioned in this study the presented scheme can directly be expanded to tackle more complex geometries.

1.3 Problem Statement

Due to non-comprehensive numerical technique for modelling and simulation of plasmonic device applications and particularly small-scale devices as a result of scaling of semiconductor devices from macro to micro up to nano region, there is an urgent need for exploration

and investigation of different models applicable in this field of study. In this work, efforts will be geared towards addressing this lacuna by applying a novel numerical technique, the Conservative Finite Difference Method to the modelling and simulation of frequency-dependent dielectric function in plasmonic and small- scale device applications for the next generation.

1.4 Methodology

This research comprises analytical derivations, ab initio modelling as well as computer simulations. The approaches adopted in this study include analytical and theoretical formulations, Standard Finite Difference Method and Conservative Finite Difference Method (CFDM) for the simulation of devices. The merit of using a conservative numerical scheme such as CFDM is that it preserves the original properties of differential operator involved after discretization. Computer simulations using MATLAB and other software tools will be presented in evaluating the developed models.

1.5 Scope of the Study

The main focus of this research is to develop a model for frequency-dependent dielectric function for plasmonic devices in the 21st-century applications. The scope of this work covers small-scale devices, metallic materials and optoelectronic devices for next-generation applications. The evaluations of the proposed models are implemented in MATLAB and Mathematica simulation packages. While this work can be carried out in known simulation

environments such as C_{++}, Python, or any available high-level computing platform, such evaluation is considered as future work.

1.6 Research Questions

The current computational algorithms developed so far for small-scale devices such as Plasmonic device, Metal-Dielectric-Metal (MDM) have not considered a numerical scheme that can be used to simulate the models for metals and dielectrics at small- scale range. This calls for further investigation on the modelling and implementation for these devices to perform effectively with reduced computational complexity. This research aims to provide answers to the following open research questions:

- How can the mathematical models for material functions in small-scale devices such as plasmonic device be derived? Appropriate modelling is necessary for the development of materials and also for evaluation of the properties of these materials under different operating conditions.

- How can the derived higher-order correction material functions be incorporated and used to simulate and model the plasmonic devices effectively?

- If applied, how do the new models, techniques and devices perform compared to existing ones?

1.7 Contribution of the Study

The fact-finding of this study which is well documented in this thesis has generated as well as added novel knowledge in the area of nanotechnology and materials in small scales for plasmonic devices. Furthermore, the new ideas are already chronicled and detailed in the author's publication(s) evaluated at the end of this section under paper publications. Figure 1.1 underlines the major contributions of the quantum-based frequency-dependent dielectric function for small-scale Plasmonic devices in this research. The comprehensive structure of the thesis title puts forward in this thesis can be worded as follows:

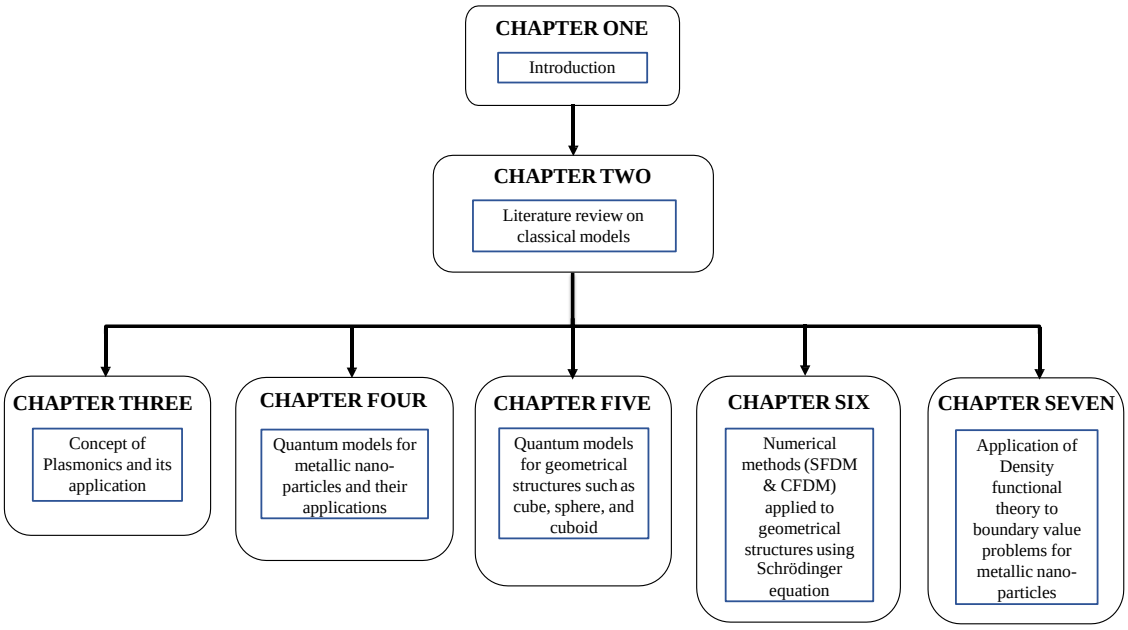

Figure 1.1: Full Structure of the study contribution.

The main contributions of this study are summed up and encapsulated as follows:

- Firstly, a thorough and in-depth review of some common models for small-scale metallic devices for nanotechnology and plasmonics is presented. The literature provides general information for study and investigation in device modelling and implementation for both the classical and quantum-based devices for plasmonic, photonic and small-scale applications. The output of the fact-finding review leads to the discourse on some of the open research challenges that need to be resolved and addressed properly to complement and enhance the performance of the metallic materials in the next generation device's applications.

- A rigorous quantum model for spherical metallic nano-structure is developed and simulated with data from the literature to test the applicability of the models.

- The concept of DFT along with Kohn-Sham equation boundary value problem subject to homogeneous or inhomogeneous Dirichlet conditions have been applied to compute frequency-dependent dielectric functions.

The following is the list of publications that has been published from this thesis.

[C.1] Lateef Adesola Akinyemi and Alireza Baghai-Wadji, "Quantum physics-based modelling of frequency-dependent dielectric function for small-scale devices in optical communications," *2017 IEEE Global Wireless Summit* (GWS), 15-18 Oct., 2017 Cape Town, South Africa, pp. 78-82.

[J.1] Lateef Adesola Akinyemi and Alireza Baghai-Wadji,"The Effects of Damping Constant of Electron and Size on Quantum-based Frequency-dependent Dielectric Function of Small Metallic Plasmonic Devices," 'Under Review'

[J.2] Lateef Adesola Akinyemi and Alireza Baghai-Wadji,"Comparative Analysis of Numerical Solutions to Boundary-Value Problem for Geometrical Structures," 'To be submitted '

1.8 Summary of the Chapter

This study primarily resolves some of the above-mentioned technical issues in systems and devices and its application to Plasmonic devices. The research presented in this thesis is structured and arranged into six chapters as shown in Fig. 1.2. To report the detailed and comprehensive information of this study, the organization of this thesis is as follows : In this section of Chapter one, we give general information regarding the background and the motivating components on why taking up this study is worthwhile. It also centres on the aims and goals (objectives) of our study and presents information about the methodology adopted or employed towards achieving the goal(s) of results of this specific research. In Chapter two , related works and other relevant underlying techniques for the understanding of the classical systems and models are thoroughly and comprehensively reviewed and presented. Chapter three discusses the rudimentary concept of quantum mechanics-based models for small-scale plasmonic devices. Chapter three examines the application of metallic-insulator-metallic (MIM). In this section (Chapter three also), we consider three and five

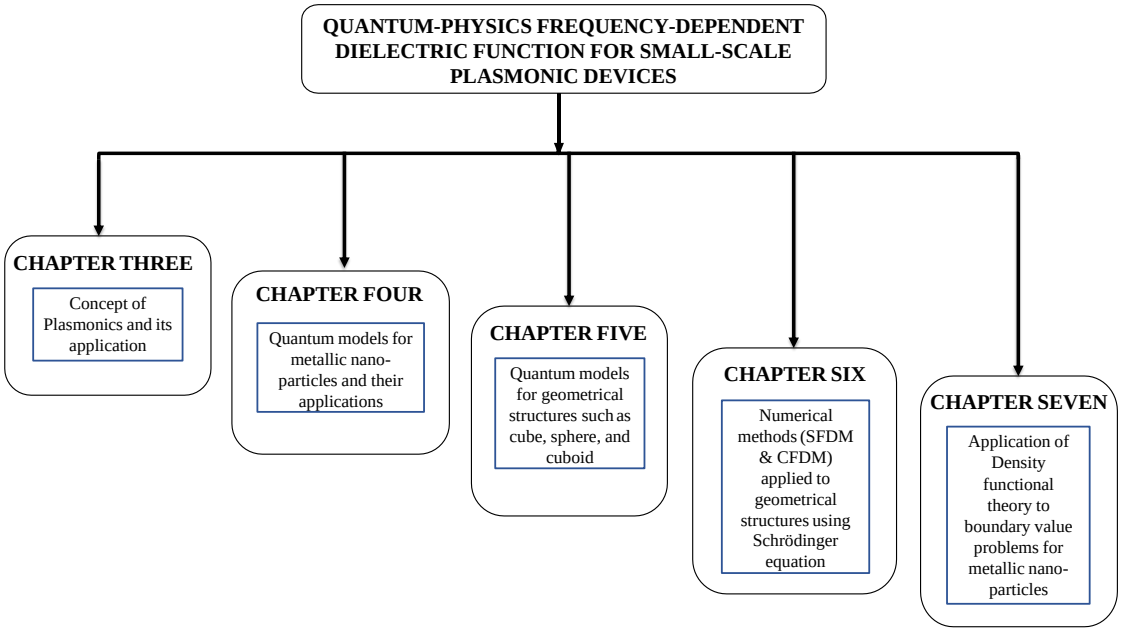

Figure 1.2: The organization of the thesis.

layers of metal-insulator-metal (MIM) and metal-insulator-metal-insulator-metal (MIMIM) structures, respectively, in which the propagation distance and other parameters such as electric field are examined. We consider both the transverse electric (TE) and transverse magnetic (TM) modes with results presented. Additionally, in Chapter four, we theoretically and rigorously deal with one, two and three dimensional structure cases based on concise formulation and method. The introduction of sinc-function at some point throughout the mathematical formulation guarantees the usefulness and robustness of the calculation. Hence, the analysis and numerical evaluation of 1-D and 2-D results show that the real- and imaginary parts of the frequency-dependent dielectric function are even and odd functions accordingly or mutatis mutandis. In Chapter five, here, we apply this model (quantum

type) to cubical, cuboid and spherical nano particles structures. We obtain the frequency-dependent dielectric function for only cubical and spherical structures while assuming a single electron and subject to boundary conditions. By applying this model to cubical, cuboid and spherical nano-particle structure, we obtain the frequency -dependent dielectric function for small- scale plasmonic devices. The metallic materials used in this study are gold, silver and copper because of their widespread applications in plasmonics and optical communications. Chapter six introduces the concept of Standard Finite Difference Method (SFDM) and Conservative Finite Difference Method (CFDM) to solve the boundary value problem for small-scale plasmonic devices. A customized and flexible software program (codes) for implementing SFDM and CFDM has been developed for 1-D and 2-D cases with and without punctured geometry These two schemes are employed for 1-D and 2-D cases with and without punctured geometry. The package enables us to solve the desired homogeneous Dirichlet boundary value problem. Then, the developed program is applied to solve time-independent Schrödinger equation for the modelling and simulation of physical properties of metallic nano-particles. Furthermore, the numerical results obtained from SFDM and CFDM are presented and compared. It is worth mentioning that, to the best of author's knowledge, no such scheme has been found in the literature or developed to solve this particular problem using these schemes to investigate the optical properties such as frequency-dependent dielectric function. In Chapter seven, the concept of density function theory has been employed and demonstrated to solve and compute optical properties such as frequency-dependent dielectric function via Kohn-Sham boundary value problem using

conjugate gradient scheme (CGS). Chapter eight concludes this study with recommendations and future work highlighted.

Chapter 2

Literature Review

In this chapter, we shall thoroughly review related works on various models used for metallic device for plasmonic applications. Before then, we need to motivate why these classical models for metallic materials are the suitable candidates for modelling plasmonic devices. Plasmonics is speedily a changing sub-area of Nanophotonics that is responsible for the interaction of electromagnetic field (light) and plasmon surface which are referred to simply as the collection of oscillation of charges which takes place at the interface between the conducting (metallic) and insulator (dielectric) materials [39]. A class of resonating devices are designed and manufactured from metallic nano-structures which has the capability to restrict condensed optical energy to small domains of area, considerably less than a wavelength of optical light in free space. Furthermore, numerous extraordinary impacts can be accomplished and obtained alongside waveguides designed with metallic materials namely guiding of light at optical frequencies with a minute, X-ray-similar wavelength, or perhaps with a negative optical index. The potential uses of plasmonics are in abundance

in any area which might have the benefit of increased management of photons; from single-molecule bio-detection to beam-steering. Similar technologies such as micro-targeted infrared cancer (MTICM) medical care and "cloaks of invisibility" have been done [40].

The work in [40] focused on the development of applications for optical communications, opto-electronics and so on. In this sub-field, plasmonics satisfies the requirements for optical interlinks that are sufficiently small to exist with nano-electronic circuits. State-of-the-art technologies comprise tiny low-power working devices like all-optical based modulators or electro-optic based type. Inert plasmonic-based devices [41], or simply called "light-conducting antennas," are being employed to reinforce the efficiency of detecting devices (detectors) and emitters , and to reap daylight for photovoltaic systems [42].

The steady communication between diminutive metallic particles and light has been used for several decades, better known in the field of establishing very colourful tinted glass window panels by heat-treating metallic materials such as salts in contrary lucid glass. The great Roman artists also designed and manufactured outstanding dichromatic glass artefacts, despite only single piece lasts safe, the famous cup of Lycurgus dates back in the 4th century Anno Domino (A.D) [43].

2.1 Classical Models and its Application

In this section, various classical models used in the modelling of small scale plasmonic devices will be described and their simulation results will be presented. In this section, the optical constants and dielectric-based frequency response will be discussed. The reaction of a frequency dependent material to incident light is usually stated as the complex dielectric

function written as $\epsilon = \epsilon' + i\epsilon''$ or as complex refractive index expressed as $\mathrm{n}^* = n + ik$. In spite of the fact that these variables or parameters are usually referenced to be optical constants, they are not firm or fixed parameters and certainly, the different and several phenomena of the interaction of light and matter (material) emerge from their operational dependence on wavelength (frequency or energy).

Whereas (ϵ', ϵ'') are a better suitable form for linking to the Maxwell's equations, the refractive index components (n, k) are best related directly to the physical observation of the attenuation of waves and velocity of the system. Hence, the two entities or equations are interchangeably equivalent and related to one another, and to the dielectric function or permittivity denoted as ϵ [44]. Upon simplification , the real and imaginary parts of permittivity and refractive index, respectively, can be put in compact form as

$$\epsilon_r' = \frac{\epsilon'}{\epsilon_0} = n^2 - k^2 \tag{2.1}$$

$$\epsilon_r'' = \frac{\epsilon''}{\epsilon_0} = 2nk \tag{2.2}$$

$$n = \sqrt{\frac{\sqrt{\epsilon_r'^2 + \epsilon_r''^2} + \epsilon_r'}{2}} \tag{2.3}$$

$$k = \sqrt{\frac{\sqrt{\epsilon_r'^2 + \epsilon_r''^2} - \epsilon_r'}{2}} \tag{2.4}$$

where ϵ_0 is the permittivity of free space, and the assumption here is that the material is not magnetic in nature such that permeability of free space denoted as $\mu_o = \mu$.In the following when there is no danger of ambiguity ,the subscript r will be omitted for

notational simplicity. For linearly frequency-dependent materials, the optical constants are usually linked to phenomenological material termed susceptibility denoted as χ. Thus, the relationship that connects the dielectric function and susceptibility of any material is given as [45]:

$$\epsilon = 1 + \chi \tag{2.5}$$

From Maxwell's equation, the constitutive relation that connects the polarization of material ($\mathbf{P}$) and susceptibility with the application of electric field ($\mathbf{E}$) can be expressed as

$$\mathbf{P} = \epsilon_0 \chi \mathbf{E} \tag{2.6}$$

where it is assumed that the medium is free space and the dielectric constant can be estimated by observing the optical power reflection and transmission from samples, or possibly best generally, by gauging the change in a polarization beam state based on reflection.

Sometimes, the optical properties of several materials are nearly independent of frequency at a minimum over a given area of interest in the range. For instance, for a lucid dielectric material, namely glass or silicon oxide (ϵ_{SiO_2}) usually approximated to be 2.5 across the visible region [46]. Additional feebly dispersive materials can frequently be handled efficiently with a constant dielectric which is done however only through a small spectral range. The difference between feebly and non-dispersive materials is rather arbitrary and relies solely on the frequency capacity of the user's study; for instance, vacuum is a non-dispersive material. The next section will briefly give the genesis of the classical models used in the modelling of small-scale devices for plasmonics.

2.1.1 Genesis of the Classical Models for Device Application

The optical features of material (also referred to as matter in this context) can be viewed and understood with regards to classical models as physical models of the diminutive structure. The permittivity of any material models can be applied to obtain the refractive index and absorption coefficient constants for dielectrics, metals and insulators at a distinct wavelength or frequency that can be used to describe the dielectric-metal, metal-metal, dielectric-dielectric interface signal interaction. In this section, the following existing models will be discussed and their respective dielectric functions and refractive indices computed. Also, the models will be compared in order to examine the impact of some of the underlying assumptions and the approaches employed to produce the models for reliable and accurate results. It must be noted that all subsequent models are existing modifications of the Drude model with varying degree of complexity involved. In the area of plasmonics (light-matter interaction), there are several models available, namely Drude (D) [47], Free-electron gas (EFG) [48] , Lorentz [49] , Lorentz-Drude (LD) [50], Sellmeier [51], [47], Brendel-Bormann (B-B) [50–54], Multi-Oscillator (M-O) [47].

The computation of the dielectric function for each model typically comprise the following steps:

1. Write out the governing equation of motion in differential form.

2. Apply Fourier transform to step (1) above.

3. Compute the displacement of the electron from equilibrium state.

4. Obtain the dipole moment for each electron in the atom of the material.

5. Obtain the polarization of the material (Number of electrons per volume).

6. Compute the Dielectric constant or permittivity of the material.

In this study, with no loss of generality that a charge carrier simply regarded as electron in a material is treated as damped harmonic system oscillator subject to the driving forces in terms of applied electromagnetic fields (specifically electric field). The electron (e) is characterized by its mass denoted as m which is displaced from its equilibrium position x via the applied electric field denoted as **E**. It is also assumed that the forces on this electron particle can be cast as a linear spring force denoted as $\mathbf{F} = \beta x$, with a velocity dependent damping expressed as $\mathbf{F} = \alpha \dot{x}$ and not forgetting the driving force generated by the local electric field of the incident light $e\mathbf{E}$. Hence, the equation of the motion for all the forces can be cast as

$$m\ddot{x} + \alpha\dot{x} + \beta x = e\mathbf{E}. \tag{2.7}$$

By normalizing (2.7) with the mass of electron and introducing of $\omega_0^2 = \frac{\beta}{m}$ and $\gamma = \frac{\alpha}{m}$, then (2.7) simplifies to

$$\ddot{x} + \gamma\dot{x} + \omega_0^2 x = \frac{e\mathbf{E}}{m}. \tag{2.8}$$

It is assumed that a time-harmonic $e^{-i\omega t}$ solution to equation (2.8) is applied via Fourier transform and the solution via substitution of ($\dot{x} \leftrightarrow -i\omega x$ and $\ddot{x} \leftrightarrow -\omega^2 x$):

$$x = \frac{\frac{e\mathbf{E}}{m}}{\omega_0^2 - \omega^2 - i\gamma\omega} \tag{2.9}$$

Based on the response for a single particle oscillator in (2.9), the optical characteristics of a metallic material comprising a group of oscillators are derived in the sequel. Denoting the dipole moment of each oscillator as $p = ex$; the polarization P of an ensemble of N oscillators per volume is $\mathsf{P} = \frac{\mathbf{N}p}{V}$. Thus, equation (2.9) can be cast as

$$\mathsf{P} = \frac{\omega_p^2}{\omega_0^2 - \omega^2 - i\gamma\omega}\epsilon_0\mathsf{E}, \tag{2.10}$$

where ω_p denotes the plasma frequency of the electron expressed as function of electron density as:

$$\omega_p^2 = \frac{\frac{\mathbf{N}}{V}e^2}{m\epsilon_0} \tag{2.11}$$

Without any loss of generality, the frequency-dependent dielectric function can be put in the following form depending on the model that is available for use by substituting it into equation (2.5):

$$\epsilon(\omega) = 1 + \frac{\omega_p^2}{\omega_0^2 - \omega^2 - i\gamma\omega} \tag{2.12}$$

The imaginary part of the dielectric function only contributes to dielectric loss . The imaginary part of dielectric function signifies the dielectric loss in medium and is tagged as the lossy component. In order to measure its magnitude, one can calculate the loss tangent.

2.1.2 Drude Model for Metallic Material

The Drude model applied kinetic theory (valid for neutral dilute classical gas of non-interacting "molecules" or "atoms") to metals. As modified scenario of time-dependent region approaches, the metal-dielectric frequency description is aimed at [55], [56], [51], [47], [50], [48], [57], [58] going through the conventional *ab initio* calculations. The Drude model is applied to compute the dispersion features of metals only with the following assumptions [55], [56]:

1. Between collisions, electrons move in a straight line in the absence of any electromagnetic field. Effect of electron-electron interaction is ignored (independent electron approximation -reasonably valid). However, the effect of the electron-ion interaction is not taken into account.

2. Electrons achieve thermal equilibrium by collisions with lattice. They emerge after collision at a random direction with speed appropriate to the temperature of the region where collision happens; the hotter the region, the higher the speed of the emerging electrons.

3. The electrons are in state of equilibrium when no external field is applied.

4. The mass of the atom (nucleus) is substantially larger than the mass of electron. Therefore, the nucleus of the atom is considered immobile and the mass of electron is used for the analysis of the spring-like system.

5. Damping is introduced as a result of collisions that occur within the lattice which makes the electrons to scatter; thereby, generating heat. It should be noted that the Drude model is a special case of Lorentzian where the resonance frequency is zero.

The expression for this model is given as

$$\epsilon(\omega) = 1 - \frac{f_0\omega_p^2}{\omega^2 + i\gamma\omega}. \tag{2.13}$$

In Eq. (2.13), f_0 denotes the oscillator strength taken as unity and the plasma frequency ω_p is identified with the free electron or known as intraband transitions and depends solely on electron density and mass of electron as stated previously. The damping factor γ includes all the scattering interactions that occur in the atom either electron-electron, ionic or electron-phonon. Hence, there is a restricted region of either wavelength or frequency to which this model yields reasonable approximation.

2.1.3 Free Electron Gas Model

When the damping factor γ in the Drude model in (2.13) is zero, then the expression for the dielectric function for a free electron gas [51], [48] becomes:

$$\epsilon(\omega) = 1 - \frac{f_0\omega_p^2}{\omega^2} \tag{2.14}$$

2.1.4 Lorentz Model for Dielectric Function

The Lorentz model describes the motion of an electron bound and connected to a positive ion core in an electric field. Here, it is assumed that the motion of the ion core is negligible

and that a linear restoring force acts on the electron. When bounded electrons or lattice interact with electromagnetic field, they generally oscillate around their equilibrium position. From quantum mechanical point of view, these changes of energy implies that system moves from one energy state to another. Classically, the approximation of oscillation is done by a damped oscillator. A damping force exists because various collision processes (electron-electron interaction, electron-lattice interaction etc.) extract energy through scattering. Assuming a driving force and damping force are included in a system that has a spring-like oscillator. The simplest type of damping here is linearly proportional to the velocity of the electron and the force with a system of a damped harmonic oscillator [51], [47],[49], [50], [59], [58]. Lorentz model adds the natural frequency of the spring to the equation in which the spring oscillates and commonly found in insulators. The dielectric expression for this model is given as:

$$\epsilon(\omega) = 1 + \sum_{j=1}^{k} \frac{f_j \omega_p^2}{\omega_j^2 - \omega^2 - i\gamma_j \omega} \tag{2.15}$$

In (2.15), f_j denotes the j^{th} oscillator strength for this model, the plasma frequency ω_p associated with interband transitions is the number of oscillators with frequency ω_j.

2.1.5 Sellmeier Model

The Sellmeier model is a special case of Lorentzian where the absorption is zero [51], [47]. Therefore, the dielectric expression is given as:

$$\epsilon(\omega) = 1 + \sum_{j=1}^{k} \frac{f_j \omega_p^2}{\omega_j^2 - \omega^2} \tag{2.16}$$

2.1.6 Lorentz-Drude Model

The Lorentz-Drude model is usually applied for the parametric property of the dielectric optical constants of metals [51], [60], [61] [47], [49], [50]. Over the years, it has been proven that the dielectric function can be expressed in complex form having real and imaginary parts denoting the dispersion and absorption coefficients , respectively. The dielectric function is given as:

$$\epsilon(\omega) = \epsilon^{intra}(\omega) + \epsilon^{inter}(\omega) \tag{2.17}$$

This distinguishes clearly the intraband contributed by free electron impacts (Drude model) and the bound electron also known as interband effects or transitions described generally by semi-quantum model of the form of Lorentz model. By combining the two models together, it results in

$$\epsilon(\omega) = 1 - \frac{f_0\omega_p^2}{\omega^2 + i\gamma\omega} + \sum_{j=1}^{k} \frac{f_j\omega_p^2}{\omega_j^2 - \omega^2 - i\gamma_j\omega}. \tag{2.18}$$

2.1.7 Brendel-Bormann Model

In this model, the focus is on the interband part of the Lorentz model of the dielectric function stated in Eq. (2.15) above. The Gaussian function has been established to be better approximation than Lorentzian function in terms of broadening function. If the same weight and full width at half-maximum are the assumptions making for the spectral absorption line function, the Lorentzian broadening expression has extended shapes compared with the Gaussian function. With this background, Brendel-Bormann applied the Gaussian function to the Lorentz function resulting in the convolution of two functions to simplify the Lorentz oscillator. This means that the Lorentz model is replaced by Brendel-Bormann

by a term called polynomial tagged χ_j as stated in Eq. (2.18) which is modified by applying complementary error function approach. It should be noted that the k in (2.19) is the number of Brendel-Bormann oscillators adopted to explain the concept of interband part of the frequency. Hence, an appreciable and non-rigid shape for absorption profile is derived through an analytic function [51], [50], [52], [53], [54], [62], [63], [64]. The mathematical expression for the dielectric function for Brendel-Bormann model can easily be shown to be:

$$\epsilon_{BB}(\omega) = 1 - \frac{f_0\omega_p^2}{\omega^2 + i\gamma\omega} + \sum_{j=1}^{k} \chi_j(\omega), \tag{2.19}$$

where $\chi_j(\omega)$ is the Brendel-Bormann polynomial function expressed mathematically as:

$$\chi_j(\omega) = \frac{1}{\sqrt{2\pi\sigma_j}} \int_{-\infty}^{\infty} d\eta \exp^{[-\frac{(\eta-\omega_j)}{2\sigma_j^2}]} \times \frac{f_j\omega_p^2}{(\eta^2 - \omega^2) - i\gamma_j\omega} \tag{2.20}$$

2.1.8 Multi-oscilator Model

This model is also an extension of the Lorentz model by adding different interband terms in order to elongate the authenticity range of the model which is largely applied among the researchers in the field to compute the frequency- and wavelength-dependent optical features of metals. This model is found on the models of material oscillators [47]. The expression of the resulting dielectric function can be obtained by rationalizing the general expression for Lorentz-Drude model to obtain an expanded version into real and imaginary parts of the function. The summary of different models as briefly discussed is summarized in Table (2.1).

Table 2.1: Adaptive and comparative differences among the dielectric functions of optical materials [51].

S/N	Model	Complexity	Mathematical Expression	Region and Error
1	Drude	Very simple	$\epsilon(\omega) = 1 - \frac{f_0\omega_p^2}{\omega^2+i\gamma\omega}$	IR with high error rate
2	Free Electron Gas	Simple,Inefficient	$\epsilon(\omega) = 1 - \frac{f_0\omega_p^2}{\omega^2}$	IR with HER
3	Lorentz	Simple,inefficient	$\epsilon(\omega) = 1 + \sum_{j=1}^{k} \frac{f_j\omega_p^2}{\omega_j^2-\omega^2-i\gamma_j\omega}$	IR-Visible-NUV
4	Sellmeier	Simple,inefficient	$\epsilon(\omega) = 1 + \sum_{j=1}^{k} \frac{f_j\omega_p^2}{\omega_j^2-\omega^2}$	IR-Visible-NUV with HER
5	Lorentz-Drude	Hard,less efficient	$\epsilon(\omega) = 1 - \frac{f_0\omega_p^2}{\omega^2+i\gamma\omega} + \sum_{j=1}^{k} \frac{f_j\omega_p^2}{\omega_j^2-\omega^2-i\gamma_j\omega}$	IR-Visible-NUV with HER
6	Brendel-Bormann	Accurate,Efficient	$\epsilon_{BB}(\omega) = 1 - \frac{f_0\omega_p^2}{\omega^2+i\gamma\omega} + \sum_{j=1}^{k} \chi_j$	IR-Visible-NUV with NER
7	Multioscillator	Complex,less efficient to B-B	$\epsilon(\omega) = 1 + \sum_{j=1}^{k} \frac{f_j\omega_p^2}{\omega_j^2-\omega^2-i\gamma_j\omega}$	IR-Visible-NUV with LER

2.2 Numerical Results and Discussion

A MATLAB program was used to generate the real and imaginary parts of the complex dielectric function $\epsilon(\omega)$. In Fig. 2.1, the relative permittivity is plotted against the frequency over a range of values. The real part of complex function of the Drude model when frequency is infinity ($\omega = \infty$), the $\Re e(\epsilon(\infty)) = 0$ and the $\Im m(\epsilon(0)) = \infty$. The resonance occurs when $\omega_p = \omega_0$. Also, the $\Re e(\epsilon(\infty)) = 1$ and the $\Im m(\epsilon(0)) = 0$. The evenness of the real part and the oddness of the imaginary part are shown in Fig. 2.1(a) with the real and imaginary parts gradually increasing from the positive to negative, however, as frequency approaches zero, both parts of the dielectric function grow infinitely. Figure 2.1(b) shows the FEG model of dielectric function of material plotted against frequency. Here, the real part is depicted only, growing infinitely as frequency tends to zero. The imaginary part is zero because of the vanishing damping parameter ($\gamma = 0$) in FEG. The graph of complex dielectric function of Lorentz model against frequency is shown in Fig. 2.1(c) below. There is a negative or anomalous dispersion for the real part of dielectric function. However, there is a progressive and sharp increase in the real part of $\epsilon(\omega)$ while on resonance, the imaginary is absorptive (high absorption;) i.e., the loss is high. The loss is very high near resonance. The damping rate determines the width of resonance. The larger the value of γ, the wider the resonance width and vice versa. Far away from resonance, the loss is very low. Figure 2.1(d) is a graph of Sellmeier model for silver material for vanishing damping factor ($\gamma = 0$). This means that the imaginary part is zero while the real part of the complex dielectric function or permittivity of the material is depicted with a striking resemblance of tangential graph. Also, the real part is at infinity as the frequency approaches zero (i.e., $\omega \to 0$).

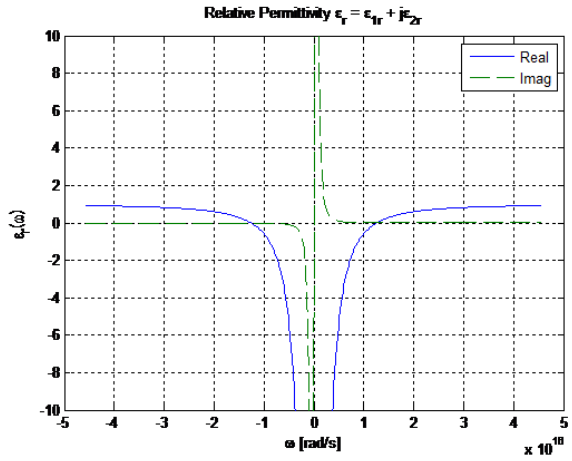

(a) The permittivity versus frequency for Drude model (Ag)

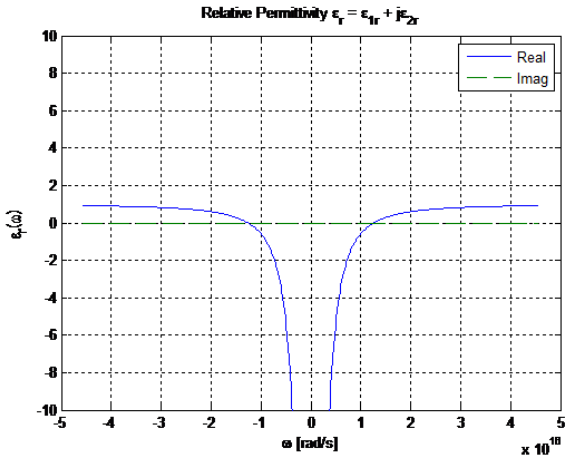

(b) The permittivity versus frequency for Free Electron gas model (Ag)

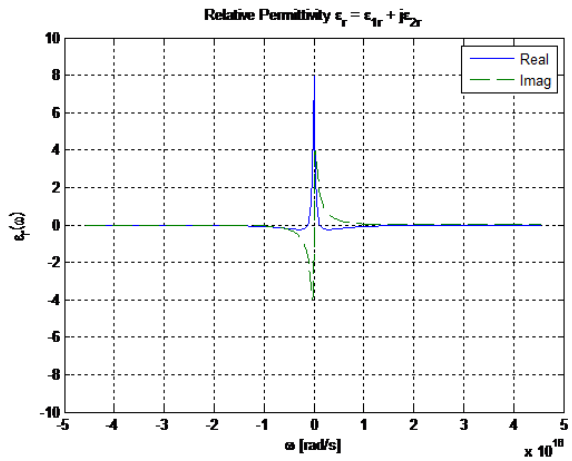

(c) The permittivity versus frequency for Lorentz model (Ag)

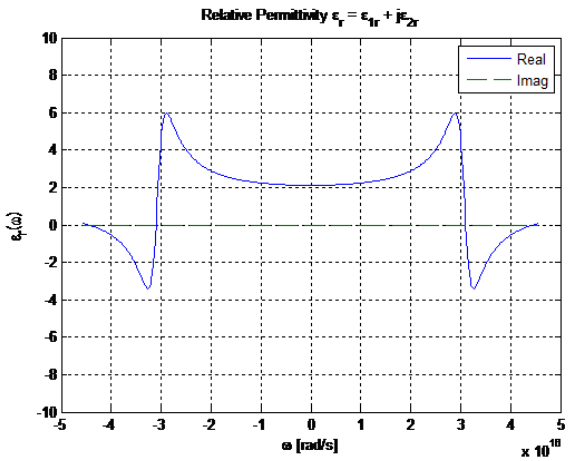

(d) The permittivity versus frequency for Sellmeier model (Ag)

Figure 2.1: The various plots of models (Drude, FEG, Lorentz and Sellmeier) of $\epsilon(\omega)$ against frequency (ω) for silver material (Ag) are displayed in (a)-(d).

The graph of Lorentz-Drude for the complex dielectric function $\epsilon(\omega)$ is shown in Fig. 2.2(a). The permittivity is plotted against frequency (ω) in rad/s. When frequency ω tends to zero i.e. ($\omega \to 0$), both the real and imaginary parts of $\epsilon(\omega)$ grow infinitely or at infinity (∞). Also, the real and imaginary parts of $\epsilon(\omega)$ are even and odd functions with symmetric

and anti-symmetric form as depicted in the graph which agree with the analytical approach. Furthermore, the result of the complex dielectric function of Brendel Model against the frequency is shown in Fig.2.2(b). This is similar to the Lorentz-Drude model in Fig. 2.2(a). However, why studying the polynomial function (the correcting factor) for this model, each oscillator was studied extensively and observed that at $j = 1$ for $\chi(\omega)$ in Eq. (2.20), there was a pathological behaviour or singularity as frequency approaches zero i.e.($\omega \rightarrow 0$). As depicted in Fig. 2.2(b), all the constituents of the correcting factor obey the even and odd functions for real and imaginary parts of $\chi_j(\omega)$. Figure 2.2(c) shows the graph of a Multioscilator model for a complex dielectric function $\epsilon(\omega)$ with the frequency (ω) along the horizontal axis of the graph. From the curve, it can be inferred that the $\Re e(\epsilon(\omega))$ decreases with a negative slope indicating an anomalous dispersion at this stage. Consequently, there is a sharp jump when plasma frequency is equal to resonant frequency or perhaps the point at which the real part crosses the horizontal axis ($\omega_p = \omega_0$). In this case, the $\Im m(\epsilon(\omega))$ part has a gain in the left-hand plane while on the right-hand plane, it is absorption ;.i.e., high loss and in this case, with the real and imaginary parts gradually increasing (normal dispersion for real part with positive slope and absorption for the imaginary part). But as frequency approaches zero, both parts of the dielectric function grow infinitely.

For the Lorentz-Drude model, it was observed that few information was available after extending the range from 5eV to 30eV in [26]. However, a significant information concerning the behaviour of the metallic material used was observed in the case of Brendel Bormann model. With this extension of range from $0.1 - 5$eV to $0.1 - 30$eV, much can be said about the optical property of the material at this point. In this study, the MATLAB modelling

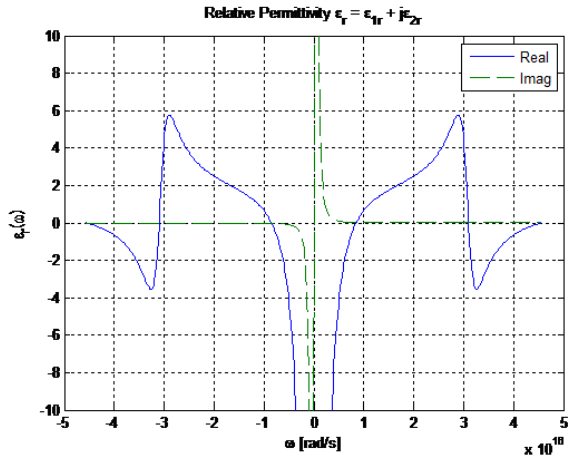

(a) The permittivity versus frequency for Lorentz-Drude model (Ag)

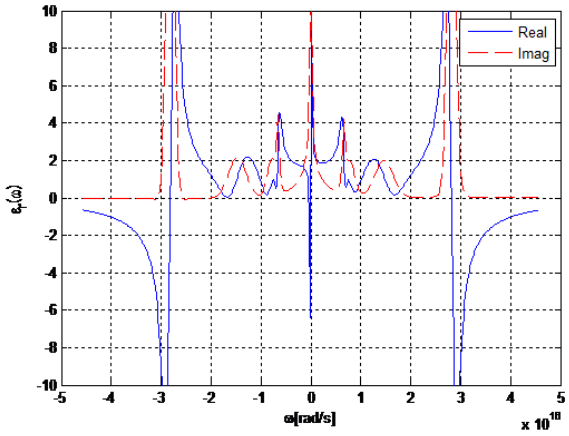

(b) [The permittivity versus frequency for Brendel-Bormann model (Ag)

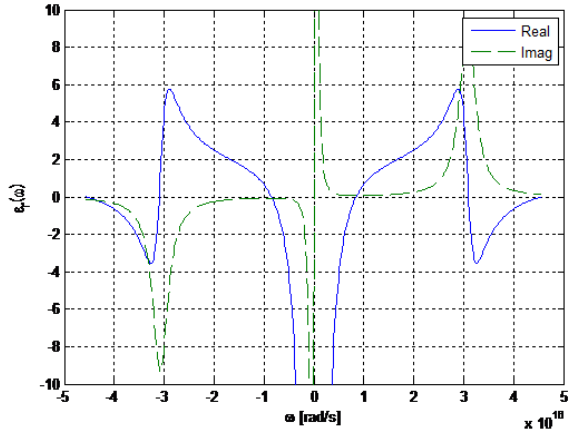

(c) The permittivity versus frequency for Multioscillator model (Ag)

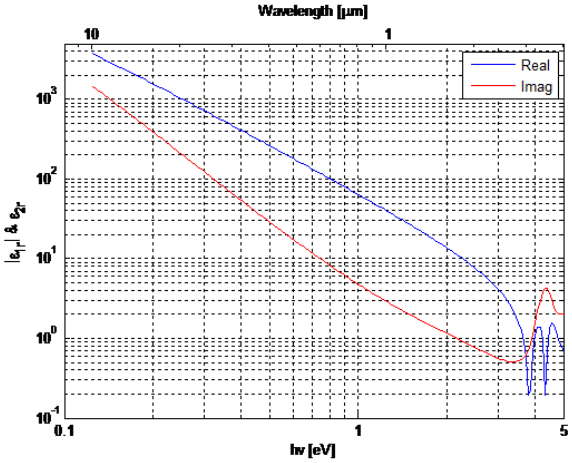

(d) The permittivity versus frequency for LD at 5 eV model (Ag)

Figure 2.2: The plots of various models of $\epsilon(\omega)$ against frequency (ω) for silver material (Ag)

using the data obtained from [26] were used to model, illustrate and discuss a wide range of frequency for the models. The influence of the parameters of the model such as $\omega_0, \omega_p, \epsilon(\infty)$ and γ was also investigated. The pathological behaviour of the Brendel-Bormann model as ω approaches zero was thoroughly investigated. The odd- and evenness of the real and

imaginary parts of each model were studied extensively through the closed-form expression as well as the simulation results. Therefore, the frequency-dependent dielectric function (permittivity) of the material can be used to ascertain when a material will reach its threshold before breaking down or perhaps the limit at which the permittivity of the material can no longer operate further. Hence, this calls for further investigation on how to model a material that can operate as frequency tends to zero or by proposing new models that can accommodate this requirement without showing any sign of pathological behaviour.

2.3 Summary of the Chapter

A far-reaching review of latest and new development in optical communications, plasmonics and its like for the future of device modelling of small-scale plasmonic application has been brought forward in this Chapter. Notably, a comprehensive description of the types of models for the relevant materials has been presented. Furthermore, the technical problems which may occur as a consequence of incorrect use of material types and models for a particular case have been outlined. Also, existing classical models for the device modelling and their applications have been studied to offer further understanding into the modelling of the new scheme as espoused in this dissertation. Furthermore, a concise explanation of some of the existing models regarding the modelling of plasmonic devices alongside their formulation has been put forward.

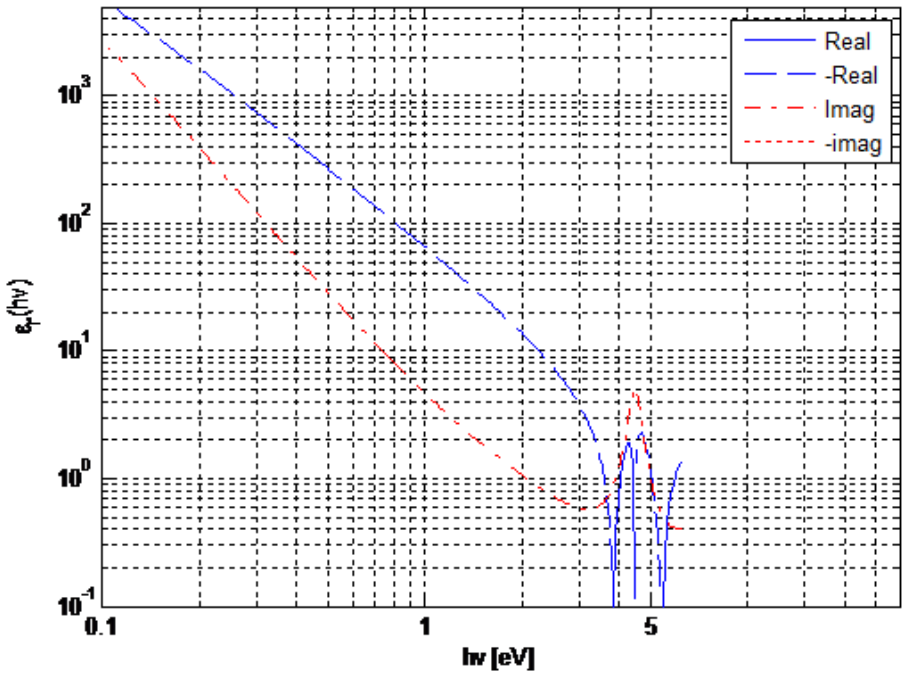

(a) The plot of ϵ vs Energy for LD model from 0.1-30 eV

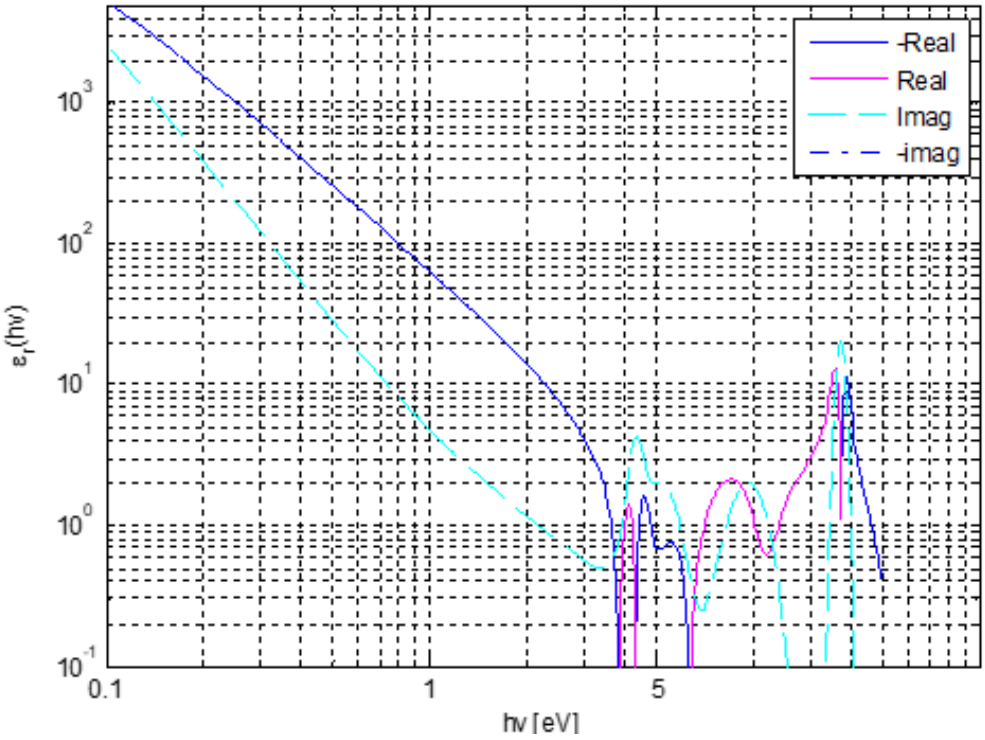

(b) The plot of ϵ vs Energy for BB from 0.1-30 eV model

Figure 2.3: The various plots of models of $\epsilon(\omega)$ against frequency (ω) for silver material (Ag) for LD and BB.

Chapter 3

Plasmonics and its Application

3.1 Introduction

In this chapter, Surface Plasmon Polaritons (SPPs) for planar system (metal-dielectric), three-layer based system (metal-dielectric-metal or dielectric-metal-dielectric), five-layer system analysis and n-layer dimension systems in general for transverse magnetic (TM) and transverse electric (TE) modes are presented. The concept of Plasmonics is defined to be the interaction between metallic material and non-metallic material (dielectric or insulator) when electromagnetic wave or signal is impinged on the surface of the material and one examines the response of the material as a result of this process [65]. In the previous chapter, we have presented the models used for both metallic and dielectric devices [66]. Generally speaking, materials exhibit peculiar characteristics in response to the various parts of incident light spectrum. They have high reflectivity property for frequencies as far as the visible region of the electromagnetic spectrum, hindering light rays from permeating them. Consequently,

metallic materials are generally considered as good conductors at low frequency [67], [39]. However, from the near-infrared frequencies and above, penetration of incident light increases resulting in absorption of light [68]. Additionally, in the ultra-violet frequency region, metal acts as dielectric medium, enabling radio waves to pass through it with varying degrees of signal loss or attenuation. Regarding noble metals, namely silver, copper or gold, strong absorption between bands of electron owing to what is called interband transition or change takes place, and this is the reason they have propensity to be lossy in this region.

3.2 The Surface Plasmon Polaritons (SPPs) for Metal-dielectric Interfaces

In the present section, the requirements for the lifetime or simply put occurrence of surface plasmon polaritons (SPPs) is examined thoroughly. Therefore, the macroscopic Maxwell's set of equations could easily be used to obtain the response of metals as a result of presence of electromagnetic. This scheme usually makes assumption that the minute alterations in the field are estimated on average through distance greater than the fine structure, and hence ignores the ins and outs of the basic interactions between particles which are fully charged in the media [39], [69]. Therefore, the two Maxwell's equations that involve the curl operator can be cast in the form as in Eqs. (3.1 and 3.2) not ignoring the remaining two equations which are pivotal in the decoupling of Maxwell's equations.

$$\nabla \times \mathbf{E} = -\frac{\partial \mathbf{B}}{\partial t} \tag{3.1}$$

$$\nabla \times \mathbf{H} = -\frac{\partial \mathbf{D}}{\partial t} \tag{3.2}$$

$$\nabla \cdot \mathbf{D} = \rho \tag{3.3}$$

$$\nabla \cdot \mathbf{B} = 0. \tag{3.4}$$

Having stated the above set of equations, now by taking the curl of Eq.3.1 and considering $\mathbf{B} = \mu_o \mathbf{H}$ in which the μ_o has been defined to be the free space of magnetic permeability.

$$\nabla \times \nabla \times \mathbf{E} = -\nabla \times \frac{\partial \mathbf{B}}{\partial t} = -\mu_o \frac{\partial (\nabla \times \mathbf{H})}{\partial t} = -\mu_o \frac{\partial^2 \mathbf{D}}{\partial t^2} \tag{3.5}$$

By employing the vector identity of the curl of a curl of a vector $\nabla \times \nabla \times \mathbf{E} \equiv \nabla(\nabla.\mathbf{E}) - \nabla^2 \mathbf{E}$ and considering the divergence of the product of a scalar and a vector $\nabla \cdot (\varepsilon \mathbf{E}) \equiv \mathbf{E} \cdot \nabla \varepsilon + \varepsilon \nabla \cdot \mathbf{E}$. Owing to the absence of charge externally;i.e, $\nabla \cdot \mathbf{D} = 0$ is assumed, then Eq.3.5 can be expressed as

$$\nabla(-\frac{\mathbf{E} \cdot \nabla \varepsilon}{\varepsilon}) - \nabla^2 \mathbf{E} = -\mu_o \varepsilon_r \varepsilon_o \frac{\partial^2 \mathbf{E}}{\partial t^2}. \tag{3.6}$$

Without any loss of generality, it is assumed that the permittivity has no variation with distance of the order of a single incident wavelength along the direction of propagation; i.e, $\nabla \varepsilon = 0$, Eg.3.6 simplifies to the equation termed wave equation [39], [70], [71], [72]:

$$\nabla^2 \mathbf{E} - \frac{\varepsilon_r}{c^2} \frac{\partial^2 \mathbf{E}}{\partial t^2} = 0. \tag{3.7}$$

In this equation, the speed of light in free space is denoted by c and is to equal to $\frac{1}{\sqrt{\mu_o \varepsilon_o}}$. To this end, to obtain a well-confined generating wave solutions at the metal/ dielectric

interface, an electric field in free space with harmonic Time-dependence is adopted in such a way that $\mathbf{E}(\mathbf{r},t) = \mathbf{E}(\mathbf{r})e^{-i\omega t}$ which is then substituted in Eq.(3.7) to give

$$\nabla^2\mathbf{E} + \nu_o^2\varepsilon\mathbf{E} = 0, \tag{3.8}$$

where $\nu_o = \frac{\omega}{c}$ denotes the wave-vector in free space of generating wave. The Fig.(3.1) below depicts a planar configuration of the dielectric-metal interface, in which the electromagnetic wave is passed through it in the x-axis direction, and dielectric function ε changes in a single dimension (i.e., in the direction of z-axis). In the straightforward two-dimensional geometry, the surface at $z = 0$, consisting of a dielectric (in this study, we consider air for simplicity) metal interface, supports the propagating or generating electromagnetic waves.

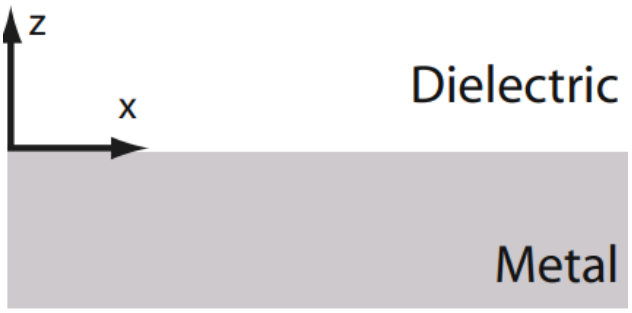

Figure 3.1: Schematic of planar geometry (Dielectric-Metal Interface) in which the electromagnetic wave propagates through in the direction of x-axis [39].

Hence, the expression for the electric field of the electromagnetic wave in x-direction can be expressed as $\mathbf{E(r)} = \mathbf{E}(z)e^{i\beta x}$. Thereby, the convention $\mathbf{r} = (x, y, z)$ has been used along with $\beta = \nu_x$ which represents the complex-valued propagation constant. The electromagnetic wave propagates in the x-direction as depicted in Fig. 3.1, [39]. By substituting the

expression $\mathsf{E}(x, y, z)$ into Eq.(3.8) and simplifying:

$$\frac{\partial^2 \mathbf{E}(z)}{\partial z^2} + (\nu_o^2 \varepsilon - \beta^2)\mathbf{E}(z) = 0 \tag{3.9}$$

It should be noted that the magnetic field **H** can be expressed analogous to (3.9). Equation (3.9) does denote the fundamental equation for directed electromagnetic modes in planar optical wave-guides and can be employed to obtain spatially-based fields profile and dispersion diagram link. Hence, it can be used to individually split the field components into electric field (E-field) **E** and magnetic field (H-field) **H**. This can be achieved by applying the Maxwell's curl equations as in Eq.(3.1) and (3.2), resulting in separate E-field and H-field constituents of E_x, E_y, E_z and H_x, H_y, H_z, respectively. Also, for the plane geometry depicted in Fig.(3.1), the direction of propagation along the x-axis and in the direction of the y-axis, requiring $\frac{\partial}{\partial x}$ and $\frac{\partial}{\partial y}$, respectively, to be $i\beta$ and zero. The process simplifies the set of equations and the resulting equations after further simplification can be split into another two sets of independent equations expressing the type of polarization of the electromagnetic wave available. In the case of transverse magnetic (TM) polarised waves along the the direction of x-axis, the components of field involved such as

$$\frac{\partial^2 \mathbf{E}(z)}{\partial z^2} + (\nu_o^2 \varepsilon - \beta^2)\mathbf{E}(z) = 0 \tag{3.10}$$

are naturally not zero and are closely related by systems of equations:

$$E_x = \frac{-i}{\omega \varepsilon_0 \varepsilon} \frac{\partial H_y}{\partial z} \tag{3.11}$$

$$E_z = \frac{-\beta}{\omega\varepsilon_0\varepsilon} H_y \tag{3.12}$$

And the general expression for the transverse magnetic wave equation can be put in the compact form,

$$\frac{\partial^2 \mathbf{H}(y)}{\partial z^2} + (\nu_o^2\varepsilon - \beta^2)\mathbf{H}(y) = 0. \tag{3.13}$$

Furthermore, identical systems of equations can be realized for the transverse electric wave equation with non-zero H_x, H_z, and E_y components .

Having laid the foundational background of the concept of surface plasmon polaritons and the likes, then to obtain the solutions of SPP electromagnetic wave at the boundary of dielectric-metal, the field solutions in direction of x-axis can be in the domains $z > 0$ and $z < 0$ in the conductive metal and insulator, as shown in Fig. (3.1). By employing Eq. (3.13) ,

$$\left.\begin{aligned} H_y(z) &= B_2 e^{i\beta x} e^{-\nu_2 z} \\ E_x(z) &= iB_2 \frac{1}{\omega\varepsilon_o\varepsilon_2} \nu_2 e^{i\beta x} e^{-\nu_2 z} \\ E_z(z) &= -B_2 \frac{\beta}{\omega\varepsilon_o\varepsilon_2} e^{i\beta x} e^{-\nu_2 z} \end{aligned}\right\} \qquad z > 0 \tag{3.14}$$

and for the other half in the region of $z < 0$ can be given compactly as :

$$\left.\begin{aligned} H_y(z) &= B_1 e^{i\beta x} e^{\nu_1 z} \\ E_x(z) &= iB_1 \frac{1}{\omega\varepsilon_o\varepsilon_1} \nu_1 e^{i\beta x} e^{\nu_1 z} \\ E_z(z) &= -B_1 \frac{\beta}{\omega\varepsilon_o\varepsilon_1} e^{i\beta x} e^{\nu_1 z} \end{aligned}\right\} \qquad z < 0 \tag{3.15}$$

In this present chapter, let $\nu_j \equiv \nu_{z,j}(j = 1, 2)$ which has been defined and stated to be wave-vector constituent orthogonal to the dielectric-metal boundary and B_1 and B_2 are the coefficients representing the E-field and H-field, respectively. In Eqs. (3.14) for $E_z(z)$ and $E_z(z)$ in (3.15) indicate that the E-field constituents of a transverse magnetic mode which are restricted at the interface between metal and dielectric (assuming ν_1 and ν_2), and decay in the direction of perpendicular to the z-axis direction. Hence, it is sufficient to define the term 'skin depth' as the reciprocal of wave-vector expressed as $\tilde{z}{=}|\nu_z|^{-1}$ and specifies the decay length of the electric and magnetic fields orthogonal to the boundary surface which measures the confinement of the wave. Therefore, at the boundary when $z = 0$, $H_y(z)$ and $E_x(z)$ are constant; i.e., continuous thereby leading to the condition where $B_1{=}B_2$ and the relationship between the wave-vectors ν_1 and ν_1 alongside their corresponding dielectrics ϵ_1 and ϵ_2, respectively can be put in compact form upon simplification as:

$$\frac{\nu_2}{\nu_1} = \frac{\epsilon_2}{\epsilon_1} \tag{3.16}$$

It is worth noting that the sign form adopted in explaining Eqs. (3.14) and (3.15), that the constraint of the electromagnetic wave at the boundary must be $\Re e(\varepsilon_1) < 0$, which leads to a highest E-field intensity at the face. Consequently, there exists a surface wave simply in superstructures of relevant materials with the reverse signs of the real term of their dielectric functions.

Therefore, the H-field component denotes as H_y fulfils the requirement of wave equation in Eq. (3.13) which gives:

$$\begin{aligned} \nu_1^2 &= \beta^2 - \nu_0^2 \varepsilon_1 \\ \nu_2^2 &= \beta^2 - \nu_0^2 \varepsilon_2 \end{aligned} \tag{3.17}$$

By combining Eqs. (3.16) and (3.17), the dispersion relation can be obtained for the surface plasmon polaritons at the dielectric-metal boundary as depicted in Fig.(3.1) as:

$$\nu_{SPP} = \nu_0 \sqrt{\frac{\varepsilon_1 \varepsilon_2}{\varepsilon_1 + \varepsilon_2}} \tag{3.18}$$

The ν_{SPP} in this equation represents the component part of the wave-vector of the surface plasmon polaritons in the direction of propagation. Similarly, the TE polarized wave progresses by fulfilling the conditions of continuity at the boundary for E-field component E_y and H-field component H_x resulting in the following criterion after substitution and simplification:

$$B_1(\nu_1 + \nu_2) = 0 \tag{3.19}$$

In the present case, the electromagnetic wave confinement at the boundary demands that $\Re e(\nu_1) > 0$ and $\Re e(\nu_2) > 0$, and can be obtained provided that $B_1 = 0$. This condition results into this case where $B_1 = B_2 = 0$,that is practical and feasible. Consequently, it is established that no surface waves or modes occur for transverse electric (TE) polarized wave, notwithstanding just the transverse magnetic (TM) polarized wave exists, as established in [39].

3.3 Concept of Dispersion Relationship at Metal-dielectric Boundary Interfaces

In this section, the phrasal word dispersion relation has been defined in the literature to mean change in the refractive index of material with respect to the incident light's frequency. With this definition, the stage has been set to now relate the mathematical formalism associated with the dispersion relation of a material. From Eq. (3.18), we have established a Drude model-like for dielectric function for an non-damped free oscillation of electron with the assumption that it is lossless material; i.e., metal. Figure (3.2) depicts a diagrammatic dispersion of surface plasmon polaritons at the boundary of a metallic material while ignoring the damping factor in (2.13) characterised by a dielectric function as expressed in Eq.(3.18) with the medium being air with $\epsilon_1 = 1$ and silica (a group of IV metal oxide $\epsilon_2 = 2.25$) has been used for the results in this thesis for the case of other medium (dielectric);i.e., air-silica interface [39]. The two straight lines emanating from origin indicate the lines of light for surface plasmon polariton in the absence of excitation. However, the two curves far right depict the curves of air and silica as a result of excitation which has taken place. Consequently, it can be viewed from the representation that owing to the wave-vectors' mismatch which has taken place between the surface plasmon polaritons (SPPs) and the light line flexes, it is required specially a technique called phase matching to do the excitation of SPPs at the interface. This technique can achieve its objective by changing the metals' surface, for instance, by adding imperfections into the system configuration.

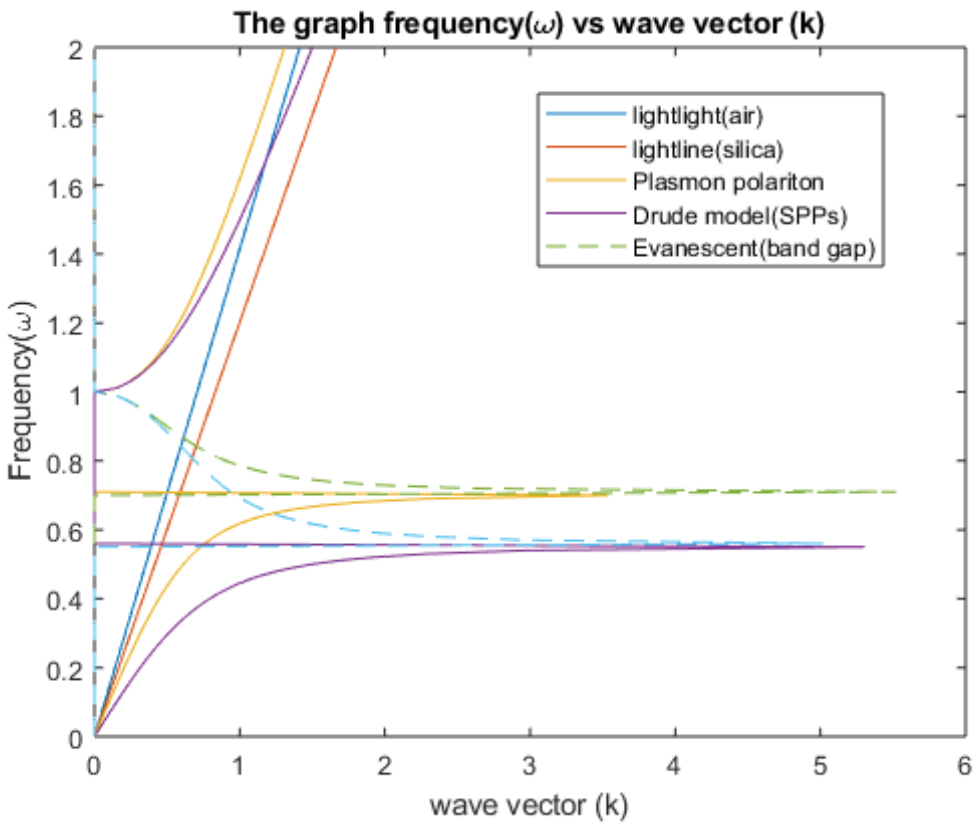

Figure 3.2: Dispersion relation of SPPs at the interface between a Drude metal with negligible collision frequency and air (grey curves) and silica (green curves).

Furthermore, as for the half-way infrared and smaller frequencies (or minute wave-vectors), the propagation of SPPs constant is more closely to the wave-vectors of the appropriate light lines and the electromagnetic waves expand across numerous wavelength bands into the permittivity range. In third mode, the SPPs function as what is called Zenneck waves as they are the same and propensity to propagate analogous to the dielectric-metal or metal-dielectric boundary interface. Additionally, in the case of large wave-vectors, the SPPs' frequency advances to the surface of the plasmon frequency denoted as ω_{SP} expressed as this in compact form $\omega_{SP} = \omega_p/\sqrt{1+\varepsilon_2}$, and the restricting limit of inconsiderable damping

constant (i.e. $\Im m(\varepsilon_1 = 0)$). This propagation constant of SPPs tends to infinity which leads to what is known as group velocity which also tends to zero. Hence, a set of frequencies in this region possesses the characteristics of electrostatic property and is referred to as surface plasmon.

Besides, in Fig.(3.2), it is assumed that a perfect lossless metallic material should have the dispersion relation outlined in Eq. (2.14) termed free electron gas (FEG) model previously stated. Although it can be said that real metallic materials like copper, silver, or gold are affected by the influence of interband transition which results into a rise in damping effect and thereby increasing the absorption level of the electromagnetic waves by the metallic surface. Because of the complex nature of dielectric function ε of real metals, the surface plasmon polariton generating constant is complex as well and hence any propagation through the interface between metal-dielectric is dampened with degree of reduction on the basis of types of metallic materials employed in the design. Thus, the propagation length for the SPP is expressed compactly as $L = (2\Im m(\beta))^{-1}$.

3.4 Concept of Multi-layer Based Plasmonic Devices

In the present section, a three-layered system, a five-based system and generalization of the metal-dielectric interface system will be discussed with results of each of the first two cases for transverse electric (TE) mode and transverse magnetic (TM) mode being presented at the end of the section.

3.4.1 The Case of Three-layered System at Metal-dielectric Interface

In this present section, the solutions of Maxwell's equations for electromagnetic radiation confined in a three-layer based system consisting of dielectric-metal-dielectric (DMD) or insulator-metal-insulator (IMI) system as depicted in Fig. (3.3) are examined. The metallic material is sandwiched between the pair of insulator or dielectric coating layers [73], [74]. The

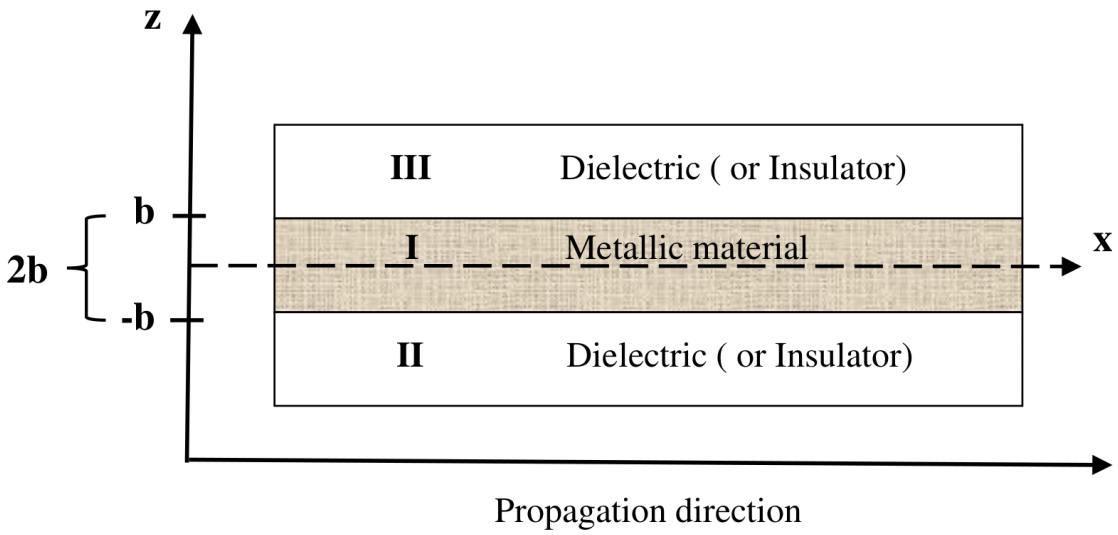

Figure 3.3: Diagramatic geometry of a three-layered (DMD or IMI) system consisting of fine metallic layer(I) interspersed between two unbounded semi-space (dielectric or insulator films) II and III.

starting case will be the transverse magnetic polarised wave propagating in the direction of x-axis and restricted to the metallic material-dielectric or insulator boundary surface. Hence, by employing the established wave Eq. (3.6), the magnetic and electric field constituents or components as the case may be for the mode in the upper domain $z > b$ can be cast in this

form compactly as after further simplification:

$$\left.\begin{aligned} H_y(z) &= Ce^{i\beta x}e^{-\nu_3 z} \\ E_x(z) &= iC\frac{1}{\omega\varepsilon_o\varepsilon_3}\nu_3 e^{i\beta x}e^{-\nu_3 z} \\ E_z(z) &= -iC\frac{\beta}{\omega\varepsilon_o\varepsilon_3}e^{i\beta x}e^{-\nu_3 z} \end{aligned}\right\} \qquad z > b \tag{3.20}$$

and for the lower $z < -b$ can be given compactly :

$$\left.\begin{aligned} H_y(z) &= De^{i\beta x}e^{\nu_2 z} \\ E_x(z) &= -iD\frac{1}{\omega\varepsilon_o\varepsilon_2}\nu_2 e^{i\beta x}e^{\nu_2 z} \\ E_z(z) &= -B\frac{\beta}{\omega\varepsilon_o\varepsilon_2}e^{i\beta x}e^{\nu_2 z} \end{aligned}\right\} \qquad z < -b \tag{3.21}$$

Furthermore, in the range $-b < z < b$, it can be inferred that the two functions exponentially based field components of the transverse magnetic form do exist, because the metallic material film is of definite size, and the governing equations that describe this case can be expressed as:

$$\left.\begin{aligned} H_y(z) &= Ee^{i\beta x}e^{\nu_1 z} + Fe^{i\beta x}e^{-\nu_1 z} \\ E_x(z) &= -iE\frac{1}{\omega\varepsilon_o\epsilon_1}\nu_1 e^{i\beta x}e^{\nu_1 z} + iF\frac{1}{\omega\varepsilon_o\varepsilon_1}\nu_1 e^{i\beta x}e^{-\nu_1 z} \\ E_z(z) &= E\frac{\beta}{\omega\varepsilon_o\epsilon_1}e^{i\beta x}e^{\nu_1 z} + F\frac{\beta}{\omega\varepsilon_o\varepsilon_1}e^{i\beta x}e^{-\nu_1 z} \end{aligned}\right\} \qquad -b < z < b \tag{3.22}$$

Given that the dielectric constants in the domains **II** and **III** are identical; i.e., $\nu_2 = \nu_3$ and $\varepsilon_2 = \varepsilon_3$, therefore, the continuity of E and H at the boundaries of the three-based layers

geometry results into a system of four system equations coupling C, D, E, and F which are unknown coefficients to be determined :

$$Ce^{-\nu_1 b} - Ee^{\nu_1 b} = Fe^{-\nu_1 b} \tag{3.23}$$

$$\frac{C}{\epsilon_2}\nu_2 e^{-\nu_2 b} + \frac{E}{\epsilon_1}\nu_1 e^{-\nu_1 b} = \frac{F}{\epsilon_1}\nu_1 e^{-\nu_1 b} \tag{3.24}$$

$$De^{-\nu_2 b} - Ee^{-\nu_1 b} = Fe^{\nu_1 b} \tag{3.25}$$

$$-\frac{D}{\epsilon_2}\nu_2 e^{-\nu_2 b} + \frac{E}{\epsilon_1}\nu_1 e^{-\nu_1 b} = \frac{F}{\epsilon_1}\nu_1 e^{\nu_1 b} \tag{3.26}$$

As was mentioned in the preceding section, the magnetic field component of $\mathbf{H}(H_y)$ transverse part which fulfils the condition of wave equation in the three domains, yields:

$$\nu_j = \beta^2 - \nu_0^2 \varepsilon_j \tag{3.27}$$

where ν_j with $j = 1, 2, 3$ denotes the wave-vectors in the three-layered geometry as shown in Fig.(3.3) . The above set of equations can be solved compactly in two ways: Firstly, by making an assumption that coefficient F has an initial value of one i.e. $F = 1$ thereby leading to a reduction into the following 3×3 matrix of the form:

$$\begin{bmatrix} e^{-\nu_2 b} & 0 & -e^{\nu_1 b} \\ \frac{\nu_2}{\epsilon_2} e^{-\nu_2 b} & 0 & \frac{\nu_1}{\epsilon_1} e^{-\nu_1 b} \\ 0 & e^{-\nu_2 b} & -e^{\nu_1 b} \end{bmatrix} \begin{bmatrix} C \\ D \\ E \end{bmatrix} = \begin{bmatrix} e^{-\nu_1 b} \\ \frac{\nu_1}{\epsilon_1} e^{-\nu_1 b} \\ e^{\nu_1 b} \end{bmatrix} \tag{3.28}$$

Here, we have used Q^T to be a matrix of the form $[C, D, E]$ which is the representation of a column-vector being transposed to row-vector and P^T to be $[e^{-\nu_1 b}, \frac{\nu_1}{\epsilon_1} e^{-\nu_1 b}, e^{\nu_1 b}]$, respectively. Note that the Q^T and P^T are column-vectors transposed into row-vectors, respectively. The solvability condition for (3.28) requires the determinant of the 3×3 matrix at the L.H.S to be zero. This leads to the dispersion relation:

$$e^{-4\nu_1 b} = \frac{(\frac{\nu_1}{\varepsilon_1} + \frac{\nu_2}{\varepsilon_2})^2}{(\frac{\nu_1}{\varepsilon_1} - \frac{\nu_2}{\varepsilon_2})^2} \tag{3.29}$$

An alternative approach to obtain the Eq. 3.29 is by solving this set of of linear equations which then lead into a more compact form expressed as this with no loss of generality ($\varepsilon_2 \neq \varepsilon_3, \nu_2 \neq \nu_3$):

$$e^{-4\nu_1 b} = \frac{\frac{\nu_1}{\varepsilon_1} + \frac{\nu_2 \nu_1}{\varepsilon_2 \varepsilon_1} + \frac{\nu_3}{\varepsilon_3}}{\frac{\nu_1}{\varepsilon_1} - \frac{\nu_2 \nu_1}{\varepsilon_2 \varepsilon_1} - \frac{\nu_3}{\varepsilon_3}} \tag{3.30}$$

By making the assumption that $\nu_2 = \nu_3$ and $\varepsilon_2 = \varepsilon_3$, then Eq. (3.30) becomes Eq. (3.29). The dispersion relation can then be split into the following equations:

$$\left.\begin{aligned} \tanh(\nu_1 b) &= \frac{-\nu_2 \varepsilon_1}{\nu_1 \varepsilon_2} \\ \tanh(\nu_2 b) &= \frac{-\nu_1 \varepsilon_2}{\nu_2 \varepsilon_1} \end{aligned}\right\} \qquad (\varepsilon_2 = \varepsilon_3, \nu_2 = \nu_3) \tag{3.31}$$

The pair of equations in Eq. (3.31) denotes the DR explaining the restricted electromagnetic modes under the DMD or IMI geometrical structure as depicted in Fig. (3.3). The first of the pair of equations above describes imparity or (odd) modes as $E_x(z)$ exhibits odd whereas $H_y(z)$ and $E_z(z)$ show the characteristics of even functions. In the same vein, the other part of Eq. (3.31) explains even modes which $E_x(z)$ obeys, while $H_y(z)$ and $E_z(z)$ conform with the odd function features as reported in [39]. With a view of analysing the performance of E-field and H-field at DMD at the boundary, a DR for electromagnetic waves in an arbitrary homogeneous isotropic multi-layered-film system is examined for TM polarization (i.e., surface plasmons and some wave-guide modes) . Here, only one mode is solved for, which depends on an initial guess selected by the user. To achieve this, a simple algorithm is written as follows:

1. Initialize different material properties such as thickness, number of materials, wavelength and so on.

2. Generate imaginary wave-vector plot for first wavelength.

3. Start the initial guess of wave-vector by selecting a point on the plot of wave-vector.

4. Solve dispersion relation numerically.

5. Compute the required fields such as electric, magnetic, propagation length and other relevant parameters.

6. Plot the necessary graphs as required for surface wave TM

Algorithm:1 To determine and generate Imaginary wave-vector numerically

Initialization: $d,\ c,\ m,\ \lambda$
Preallocate: r_x = zeros (length(λ), 1)
Preallocate: r_o = zeros (length(λ), 1)
Preallocate: r_{photon} = zeros (length(λ), m)
    for a = 1:length (λ) **do**
        $r_o(a) = \frac{2\cdot\pi}{\lambda(a)}$
        $\omega = r_o(a)\cdot$ c
        $\epsilon = N^2(a)$
        $\epsilon = \sqrt{(a)}$

            for b=1:m **do**
                if real $(N^2(a,b)) > 0$ **do**
                    $r_{\mathsf{photon}} = r_o(a) \cdot N(a,b)$
                else
                    $r_{\mathsf{photon}}(a,b) = \infty$
                end
            end
                if a=1 **do**

                    $r_x(guess) = r_{xin}$
                else
                $r_x(guess) = r_x a - 1$
                end
                if flag=1 && a=1 **do**

                    $bar = waitbar$
                end
                $r_x(a) = r_x$
                $r_x(a) = r_x(solved) + \mathrm{i} r_x(solved)$
                $waitbar(\frac{a}{length(\lambda)})$
            for b=1:m **do**
                    $r_j(a,b) = \sqrt{\epsilon(b)\cdot(\frac{\omega}{c})^2 - r_x^2(a)}$
            end
        end

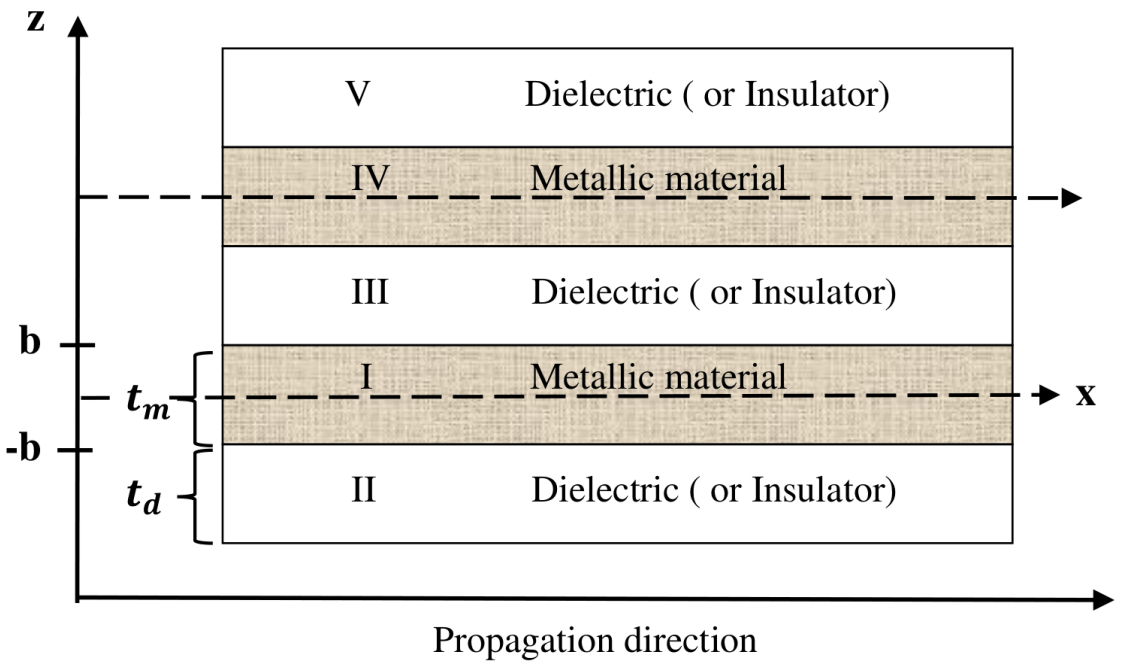

Figure 3.4: Diagramatic geometry of a five-layered (DMDMD or IMIMI) system consisting of fine metallic layers (I, IV) interspersed between two unbounded semi-space (dielectric or insulator films) II, III and V.

Additionally, for the case of five-layered system as shown in Fig. (3.4), the same concept applied for a three-layered system will be used for the surface wave of TE and TM modes. The difference here is that the number of layers has been increased , more complex to analyse and in the final analysis for the convergence of this case, it takes time to converge and requires more computing resources.

For the case of one (DMD) in this thesis, we input ϵ or dielectric constant for the chosen material, gold for instance into the software package as required to calculate other optical parameters. We define three layers and five layers with semi-infinite domains $d = [NaN, \epsilon, NaN]$ and $d = [NaN, \epsilon_1, \epsilon_2, \epsilon_3, NaN]$, respectively. Here, d denotes the thickness of the material in nm and NaN represents a semi-infinite layer. It should be

stated that the number of layers can be increased straightforwardly . The more the layers, the more difficult it becomes to achieve convergence, unless a supercomputer is used. A code is written to solve the wave-vector ν numerically. It should be noted that it is safer and computational efficient to arrange the dispersion equation in the form of matrix rather than in the form of Eq. (3.30) because of its complex nature. Hence, different solutions for wave-vector values are obtained. This depends on the initial ν value assigned initially by using mouse in the complex plane of the wave-vector.

3.4.2 Generalization of Dispersion Relation for m-films Multilayer System at Metal-dielectric Interface

To have a full grasp of metal-dielectric or dielectric-metal interface and the optical feature of the surface plasmon polariton, we will attempt to solve the eigen based propagation types of the directed and guided waves also known as dispersion relation. In this present section, we will generalize a finite but large thin-film system. We will customize the m-layers problem by solving the dispersion relation (DR) afterwards. Since we will generalize the system and deal with m thin-film multilayer system, the solution of DR for m generally. Considering the transverse magnetic mode-type in the present section for the boundary waves on not magnetic material. To explain the mode of propagation in a multilayer geometry with no leak experienced, in this thesis, we assume two transverse or short waves in each thin-layer and individual transient waves for the top and the bottom media with the conventional propagation value denoted as ν_x in the direction of the x-axis.

By means of a comparison of the interface conditions of the H-field at all plane boundaries, the following system of $(m+1)$ equations for m thin films having two media on the top and the bottom can be obtained :

$$\begin{aligned}
&\alpha_{t,u} = \alpha_{1,u}e^{-ir_1l_1} + \alpha_{1,d}e^{ir_1l_1} \\
&\alpha_{1,u} + \alpha_{1,d} = \alpha_{2,u}e^{-ir_2l_2} + \alpha_{2,d}e^{ir_2l_2} \\
&\quad\vdots \\
&\alpha_{j,u} + \alpha_{j,d} = \alpha_{j+1,u}e^{-ir_{j+1}l_{j+1}} + \alpha_{j+1,d}e^{ir_{j+1}l_{j+1}} \\
&\quad\vdots \\
&\alpha_{m,u} + \alpha_{m,d} = \alpha_{b,d}
\end{aligned} \tag{3.32}$$

Those equations describe the magnetic field (H-field). The coefficients α match with the TM type. Conversely, for the case of E-field mode, we obtain the following set of $(m+1)$ equations as:

$$\begin{aligned}
&-\frac{r_t}{\epsilon_t}\alpha_{t,u} = -\frac{r_1}{\epsilon_1}\alpha_{1,u}e^{-ir_1l_1} - \frac{r_1}{\epsilon_1}\alpha_{1,d}e^{-ir_1l_1} \\
&-\frac{r_1}{\epsilon_1}\alpha_{t,u} - \frac{r_1}{\epsilon_1}\alpha_{1,d} = -\frac{r_2}{\epsilon_2}\alpha_{2,u}e^{-ir_2l_2} - \frac{r_2}{\epsilon_2}\alpha_{2,d}e^{-ir_2l_2} \\
&\quad\vdots \\
&-\frac{r_j}{\epsilon_j}\alpha_{j,u} - \frac{r_j}{\epsilon_j}\alpha_{j,d} = -\frac{r_{j+1}}{\epsilon_{j+1}}\alpha_{j+1,u}e^{-ir_{j+1}l_{j+1}} - \frac{r_{j+1}}{\epsilon_{j+1}}\alpha_{j+1,d}e^{-ir_{j+1}l_{j+1}} \\
&\quad\vdots \\
&-\frac{r_m}{\epsilon_m}\alpha_{m,u} + \frac{r_m}{\epsilon_m}\alpha_{m,d} = -\frac{r_b}{\epsilon_b}\alpha_{b,d}
\end{aligned} \quad . \tag{3.33}$$

In Eqs.3.32 and 3.33, the following notation has been employed: $t = top$, $d = down$, $b = bottom$, l=the thickness, and r_x=propagation constant. l_j represents the thickness of the jth layer, r_x denotes the orthogonal component of the complex-valued wave-vector in the jth layer. The $\alpha_{j,u}$ and $\alpha_{j,d}$ stand for the respective coefficients of the field for the pair waves in each of the thin-films. In the top and bottom semi-infinite media, there is merely one mode that decays to zero at the far-field. The orthogonal component of the wave-vector r_j for the jth layer satisfies the conservation of momentum expressed: $(m_j r_0)^2 = r_x^2 + r_j^2$. Here, r_0 denotes wave-number in free space vacuum and m_j is referred to as the index of refraction.

The Eqs. (3.32) and (3.33) can be cast in the matrix form using $(2m+2) \times (2m+2)$ matrix $\mathbf{F}$, and the coefficients represented by α's in a $(2m+2)$ vector $\mathbf{Y}$ as follows:

$$\boldsymbol{W} = \begin{bmatrix} -1 & e^{-ir_1 l_1} & e^{-ir_1 l_1} & 0 & \cdots & 0 \\ 0 & \ddots & \ddots & \ddots & \ddots & 0 \\ 0 & 0 & 0 & \ddots & -1 & 1 \\ \frac{r_t}{\epsilon_t} & \frac{-r_1}{\epsilon_1} e^{-ir_1 l_1} & \frac{r_1}{\epsilon_1} e^{ir_1 l_1} & 0 & \cdots & 0 \\ 0 & \ddots & \ddots & \ddots & \ddots & 0 \\ 0 & 0 & 0 & \cdots & \frac{-r_m}{\epsilon_m} & \frac{-r_b}{\epsilon_b}, \end{bmatrix} \tag{3.34}$$

and

$$\boldsymbol{Y} = \begin{bmatrix} \alpha_{t,u} \\ \alpha_{1,u} \\ \alpha_{1,d} \\ \vdots \\ \alpha_{b,d}. \end{bmatrix} \tag{3.35}$$

Introducing the $(2m + 2)$ null column vector zero:

$$\boldsymbol{WY} = 0. \tag{3.36}$$

Hence, the determinant of $\mathbf{W}$ equals zero; i.e., $\det\{\mathbf{W}\} = 0$ provided Eq. (3.36) fulfils the condition of non-zero vector $\mathbf{Y}$. This is the dispersion relation for this system. In order to solve for the permissible mode in the system, the complex-valued r_x must be determined algorithmically and numerically.

On the other hand, consider the transverse mode for dispersion relation for a multilayer thin-films which can be solved similar way to the transverse magnetic mode as explained earlier.

The dispersion relation for the m thin film structure must be solved numerically. The formulation depends on the complicated nature of coefficients β (i.e., the coefficient of E-field) rather than that of the magnetic field, which leads to the distinct formula of the interface conditions. Furthermore, almost the same notations are employed here for the TE mode in the same manner for TM except the following changes: β denotes the coefficients of E-field

whereas α stands for the coefficient of H-field previously. l_j represents the thickness of the jth layer, N_j or ϵ_j is the index of refraction or dielectric function, respectively, r_j is the wave-vector of the jth layer, $\beta_{j,u}$ and $\beta_{j,d}$ represent the complex coefficients of the E-field for the pair of waves in each thin film, and the wave-vector r_j for the jth thin layer can be expressed as the condition for the conservation of momentum: $(N_j r_0)^2 = r_x^2 + r_j^2$. By combining (i.e., coupling or matching) the condition at the boundary of the E-field at the plane interface (all) comparison of the interface conditions of the H-field at all the plane boundaries, the following system of equations for m thin films having two media on the top and bottom can be obtained satisfying the interface conditions for the **E**- and **H**-fields:

$$\begin{aligned}
&\beta_{t,u} = \beta_{1,u} e^{-ir_1 l_1} + \beta_{1,d} e^{ir_1 l_1} \\
&\beta_{1,u} + \beta_{1,d} = \beta_{2,u} e^{-ir_2 l_2} + \beta_{2,d} e^{ir_2 l_2} \\
&\qquad \vdots \\
&\beta_{j,u} + \beta_{j,d} = \beta_{j+1,u} e^{-ir_{j+1} l_{j+1}} + \beta_{j+1,d} e^{ir_{j+1} l_{j+1}} \\
&\qquad \vdots \\
&\beta_{m,u} + \beta_{m,d} = \beta_{b,d}
\end{aligned} \tag{3.37}$$

The above equation is for electric field (E-field). The coefficient β matches with the TE type. Conversely, for the case of H-field mode, we obtain a set of equations as expressed as:

$$\begin{aligned}
&- N_t\beta_{t,u} = -N_1\beta_{1,u}e^{-ir_1l_1} + N_1\beta_{1,d}e^{ir_1l_1} \\
&- N_1\beta_{1,u} + N_1\beta_{1,d} = -N_2\beta_{2,u}e^{-ir_2l_2} + N_2\beta_{2,d}e^{ir_2l_2} \\
&\quad\vdots \\
&- N_j\beta_{j,u} + N_j\beta_{j,d} = -N_{j+1}\beta_{j+1,u}e^{-ir_{j+1}l_{j+1}} + N_{j+1}\beta_{j+1,d}e^{ir_{j+1}l_{j+1}} \\
&\quad\vdots \\
&- N_m\beta_{m,u} + N_m\beta_{m,d} = N_b\beta_{b,d}
\end{aligned} \tag{3.38}$$

The above equations can be cast compactly using $(2m+2) \times (2m+2)$ matrix $\mathbf{Z}$ and the coefficient represented by β's in a $(2m+2)$ vector $\mathbf{Y}$ are obtained in the following way:

$$\boldsymbol{Z} = \begin{bmatrix}
-1 & e^{-ir_1l_1} & e^{-ir_1l_1} & 0 & \cdots & 0 \\
0 & \ddots & \ddots & \ddots & \ddots & 0 \\
0 & 0 & 0 & \ddots & -1 & 1 \\
N_t & -N_1e^{-ir_1l_1} & N_1e^{ir_1l_1} & 0 & \cdots & 0 \\
0 & \ddots & \ddots & \ddots & \ddots & 0 \\
0 & 0 & 0 & \cdots & -N_m & N_b
\end{bmatrix} \tag{3.39}$$

And vector equation is given as :

$$\boldsymbol{Y} = \begin{bmatrix} \beta_{t,u} \\ \beta_{1,u} \\ \beta_{1,d} \\ \vdots \\ \beta_{b,d} \end{bmatrix} \tag{3.40}$$

Using the $(2m + 0)$ column null vector 0,

$$\boldsymbol{ZY} = 0. \tag{3.41}$$

The determinant of the matrix $\mathbf{Z}$ equals zero; i.e., $\det\{\mathbf{Z}\} = 0$ provided that the Eq. (3.36) fulfils a condition of non-zero vector denoted by $\mathbf{Y}$. This is the dispersion relation for this system. In order to solve for the permissible mode of the system, the complex-valued r_x must be determined.

3.5 Numerical Results and Discussion

Results of numerical computations using implementation of the expression for refractive index and dielectric constant will be presented in the sequel. The refractive index or dielectric function used for the metallic (i.e. gold) was computed from a single dielectric layer on the glass. The gold metallic material is sandwiched between the water and the glass. The calculation of the index of refraction of the dielectric material was experimentally obtained via fitting. The data were obtained from [75]. The computed refractive index or dielectric

function relies on the wavelength with greater value for shorter wavelength. Figure 3.6(a) shows the the dissipation curve for the problem at hand in which the propagation length is plotted against the wavelength in vacuum. It is observed that it is not parabolic considering the generated wave-vector and range of wavelength used. In Fig. 3.6(b), the r_{photon} and r_0 of the propagation constants are plotted as indicated with black colour while the real part of r_x and r_o are graphed in Fig.3.6(b). This shows a linear graph and it is a dispersion relation for the angular frequency against wave-vector. This is a demonstration of the nature of dispersion relation. Figure 3.6(b) shows the dispersion curve in the first zone which is defined as the original form in reciprocal space. It repeats at regular intervals in space, $\frac{2\pi}{\lambda(a)}$ where wavelength depends on a. It should be noted that the relationship is not always linear when the real-part of wave-vector (r_x) is plotted and this case will be shown in the following section. The linearity of the mode wavelength nm against vacuum wavelength (nm) is demonstrated in Figs. 3.6(a and b). It is observed that as the mode wavelength increases, the real-part of the photon wave-vector increases as well as the real-part of the complex wave-vector which has been numerically computed. Furthermore, the magnetic field component is shown in Fig. 3.6(c) in which the real-part of H is plotted against the position. The minimum and maximum real components of magnetic field are shown as well. In addition, quivering characteristics of E-field along the x and z axes are shown with dashed line in the same Fig. 3.6(c). In Fig. 3.6(c), the plot of position against field strength is shown for the magnetic field (H-field). There is an observation in which the curve rises to zero or unity in a resemblance of square root function and linearly increases to approximate 10 nm and increases quadratically as depicted in Fig. 3.6(c). The curve in red indicates the

quivering characteristics in the thin layer in consideration. The E-field (vector plot) as well as E-field (intensity plot) is shown in Fig. 3.6(d). This is for a single case of computed wave-vector. These curves change as the values of wave-vector differ based on the initial guesses or conditions. The propagation length can be determined by calculating the reciprocal of the decay constant. Figure d shows the propagation lengths of the plasmon field in the geometry. The longer propagation length can be achieved when the width of the material is reduced while keeping a large plasmon mode.

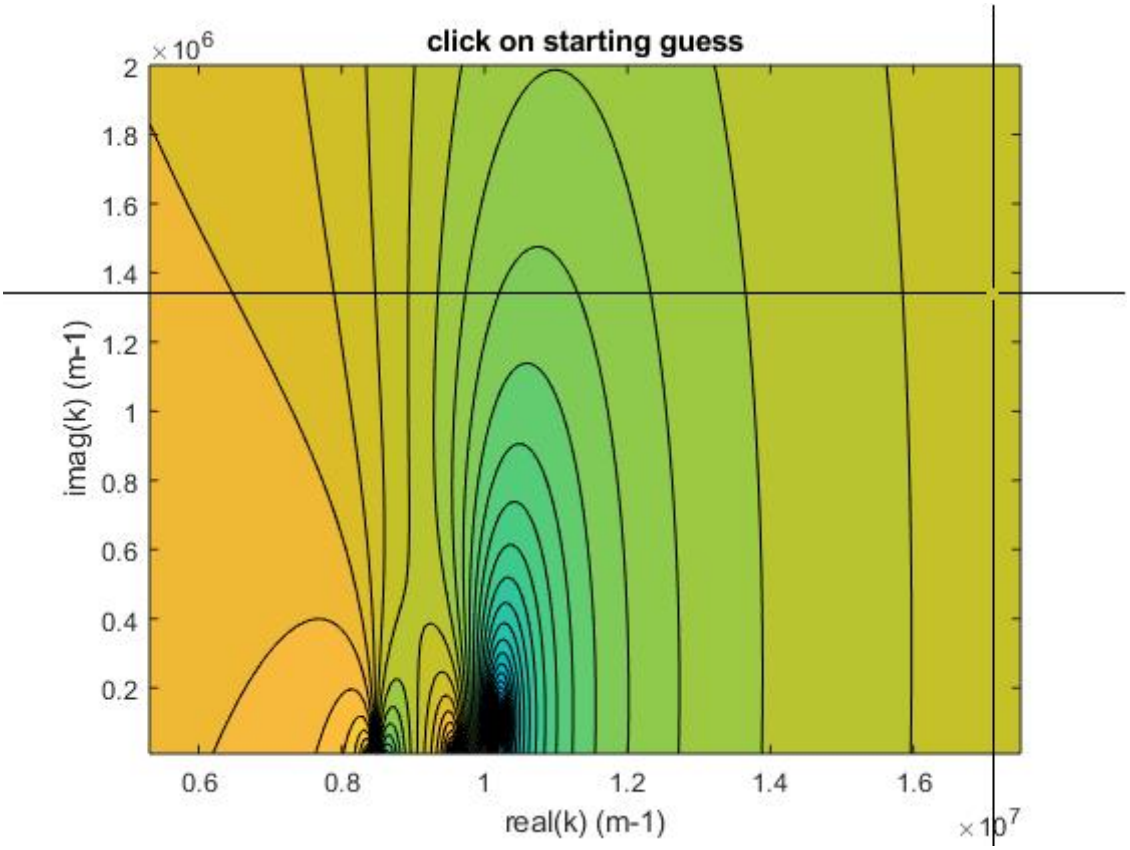

Figure 3.5: Numerical computation for wave-vector using initial guessing at r=16671502.02 +i88323.61.

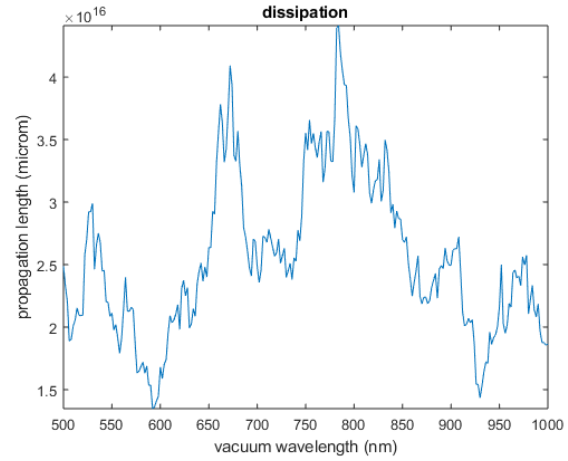

(a) Dissipation

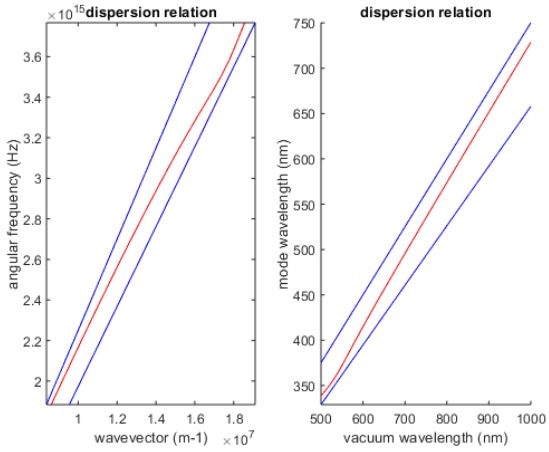

(b) Dispersion relation

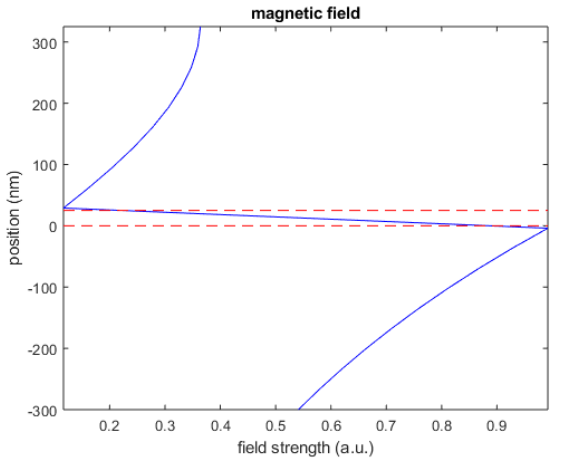

(c) Magnetic Field

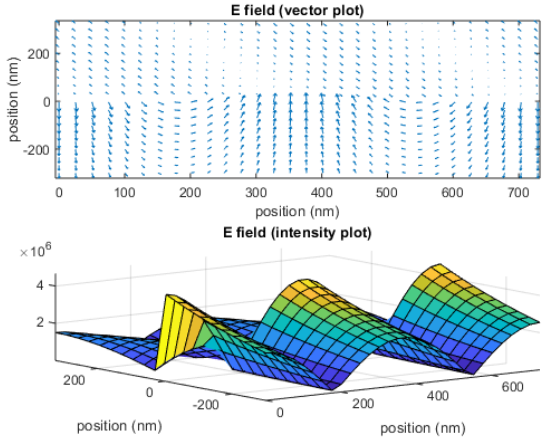

(d) E-field

Figure 3.6: Various values of fields and propagation length for r=16671502.02 + i88323.61 at λ=500:1000 nm .

Figure 3.7(a) shows the dissipation curve for the problem at hand in which the propagation length is plotted against the wavelength in vacuum. It is observed that it is parabolic in nature as observed in Fig. 3.6(a) in the sense that as the wavelength increases, the propagation length increases as well. In Fig. 3.7(b), the r_{photon} and r_0 of the propagation constants are plotted as indicated with black colour while the real-part of r_x and r_o are

graphed in Fig. 3.7(b). This shows a linear graph and it is a dispersion relation for the angular frequency against wave-vector. This is a demonstration of the nature of dispersion relation. Figure 3.7(b) shows the dispersion curve in the first zone which is defined as the original form in reciprocal space. It repeats at regular intervals in space, $2\pi/\lambda(a)$ where wavelength depends on a. Note that the relationship between real-part of the wave-vector (r_x) and spacial length is not always linear. This will be illustrated in subsequent results. The linearity of the mode wavelength nm against vacuum wavelength (nm) is demonstrated in Figs. 3.7(a and b). It is observed that as the mode wavelength increases, the real-part of the photon wave-vector increases as well as the real-part of the complex wave-vector which has been numerically computed. Furthermore, the magnetic field component is shown in Fig. 3.7(c) in which the real-part of H is plotted against the position. The minimum and maximum real components of magnetic field are shown as well. In addition, quivering characteristics of E-field along the x and z axes are shown with dashed line in the same Fig. 3.7(c). In Fig. 3.7(c) , the plot of position against field strength is shown for the magnetic field (H-field). It is also observed in Fig. 3.7(c) that the curve exhibits properties of a square root function and afterwards, it linearly increases to approximate 10 nm and increases quadratically as depicted in Fig. 3.7(c). The other curve in red indicates the quivering characteristics in the thin layer in consideration. The E-field (vector plot) as well as E-field (intensity plot) is shown in Fig. 3.7(d). This is for a single case of computed wave-vector. These curves change as the values of wave-vector differ based on the initial guess. The propagation length can be determined by calculating the reciprocal of the decay constant. Figure (3.7a) shows the propagation lengths of the plasmon field in the geometry. The longer propagation length

can be achieved when the width of the material is reduced while keeping a large plasmon mode.

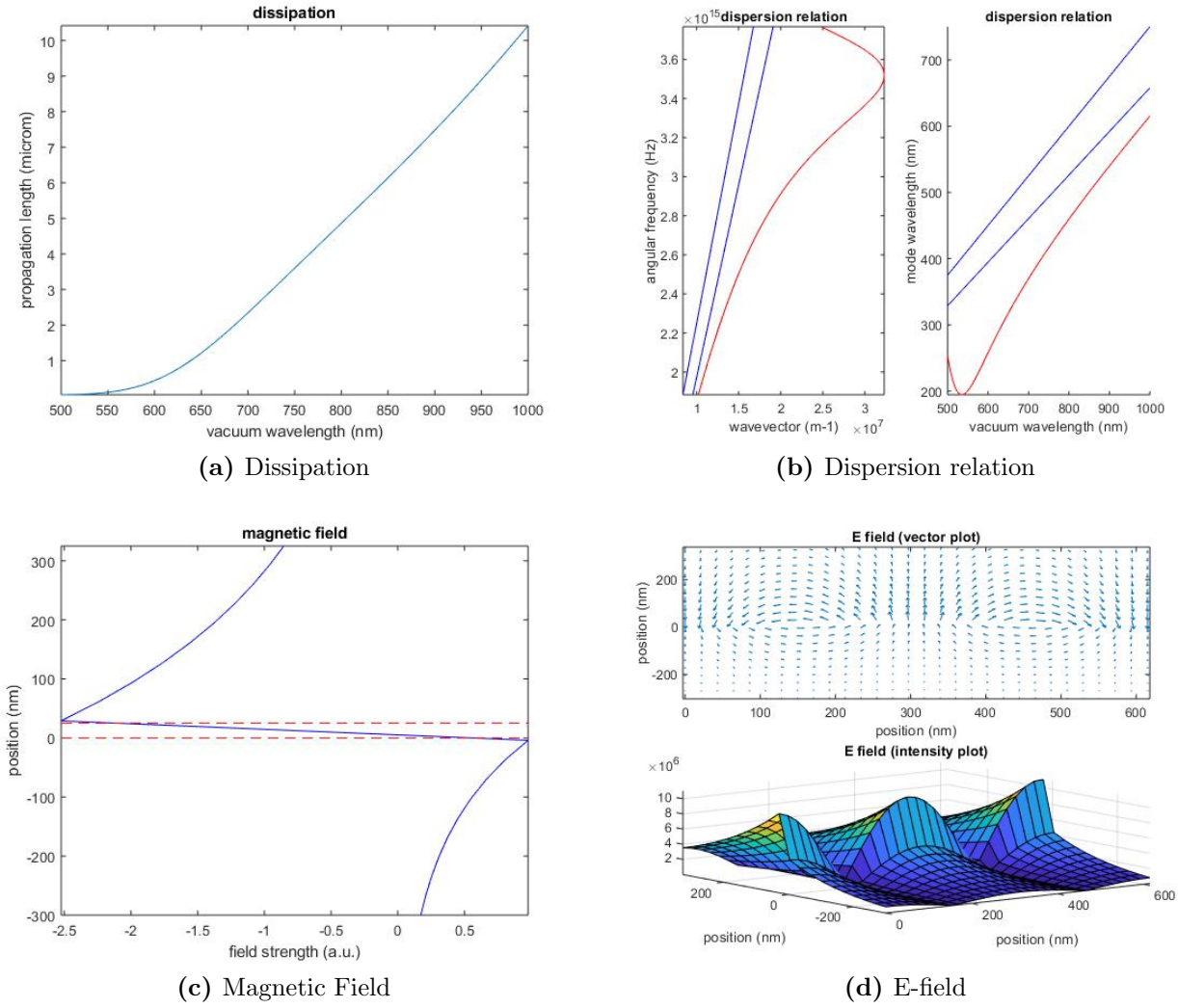

(a) Dissipation

(b) Dispersion relation

(c) Magnetic Field

(d) E-field

Figure 3.7: Various values of fields and propagation length for r=9144808.46 + i53513.11 at λ=500:1000 nm .

Figure 3.8(a) shows the dissipation curve for the problem at hand in which the propagation length is plotted against the wavelength in vacuum. It is observed that it is a not parabolic due to generated wave-vector and range of wavelength used as shown in

Fig. 3.6(a). In Fig. 3.8(a), the r_{photon} and r_0 of the propagation constants are plotted as indicated with black colour while the real-part of r_x and r_o are graphed in Fig. 3.6(a). This shows a linear graph and it is a dispersion relation for the angular frequency against wave-vector. This is a demonstration of the nature of dispersion relation. Figure 3.8(b) shows the dispersion curve in the first zone which is defined as the original form in reciprocal space. It repeats at regular intervals in space, $2\pi/\lambda(a)$ where length of wavelength depends on a. It should be noted that it is not always linear when the real-part of wave-vector (r_x) is plotted and this case will be shown in the following section. The linearity of the mode wavelength nm against vacuum wavelength (nm) is demonstrated in Figs. 3.8(a and b). It is observed that as the mode wavelength increases, the real-part of the photon wave-vector increases as well as the real-part of the complex wave-vector which has been numerically computed. Furthermore, the magnetic field component is shown in Fig. 3.6(c) in which the real part of **H** is plotted against the position. The minimum and maximum real components of magnetic field are shown as well. In addition, quivering characteristics of E-field along the x and z axes are shown with dashed line in Fig. 3.8(c). In Fig. 3.8(c) , the plot of position against field strength is shown for the magnetic field (H-field). There is an observation in which the curve rises to zero or unity in a resemblance of square root function and linearly increases to approximate 10 nm and increases quadratically as depicted in Fig. 3.8(c). The other curve in red indicates the quivering characteristics in the thin layer in consideration. The E-field (vector plot) as well as E-field (intensity plot) is shown in Fig. 3.8(d). This is for a single case of computed wave-vector. These curves change as the values of wave-vector differ based on the initial guess. The propagation length can be determined by calculating the reciprocal

of the decay constant. Figure (3.8d) shows the propagation lengths of the plasmon field in the geometry. The longer propagation length can be achieved when the width of the material is reduced while keeping a large plasmon mode.

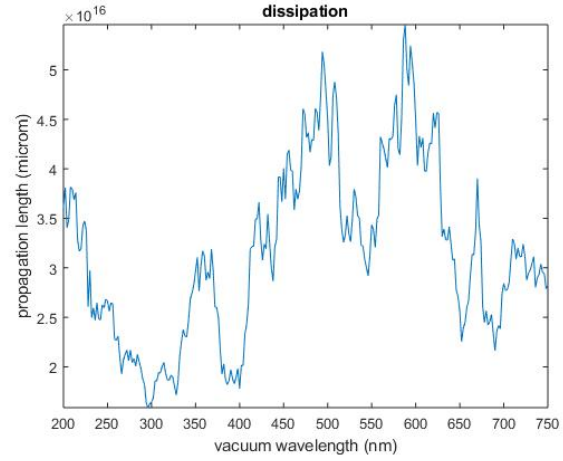

(a) Dissipation

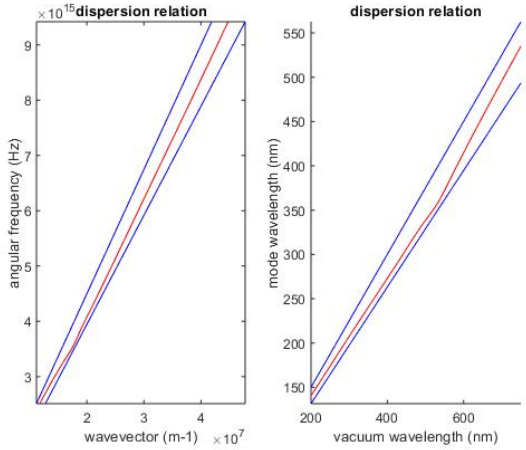

(b) Dispersion relation

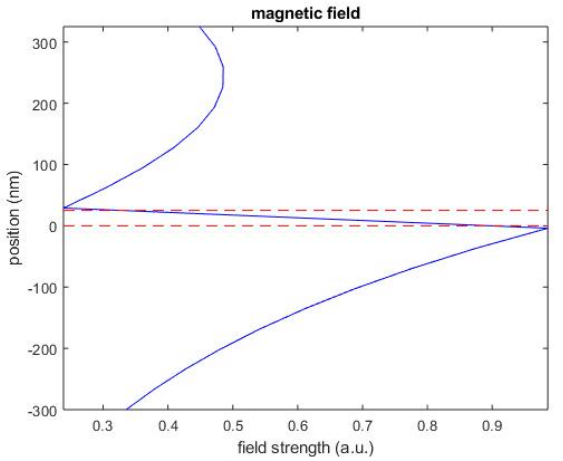

(c) Magnetic Field

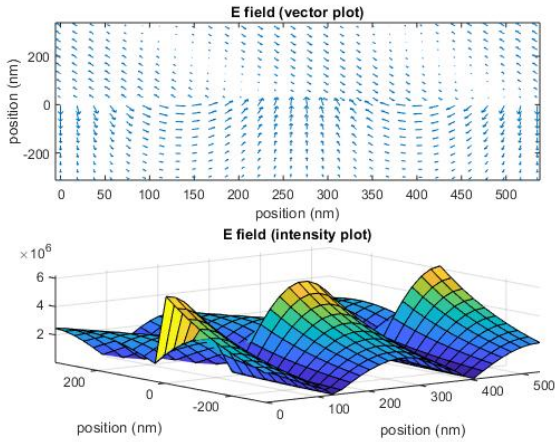

(d) E-field

Figure 3.8: Various values of fields and propagation length for r=8246098.79 + i117332.36 at λ=500:750 nm.

In Fig. 3.9(a), the r_{photon} and r_0 of the propagation constants are plotted as indicated with black colour while the real part of r_x and r_o are graphed in Fig. 3.9(a). This does not

show a linear graph and it is a dispersion relation for the angular frequency against wave-vector. This is a demonstration of the nature of dispersion relation based on the wavelength used and generated wave-vector as shown in the caption of the figure. Figure 3.9(b) shows the dispersion curve in the first zone which is defined as the original form in reciprocal space. It repeats at regular intervals in space, $2\pi/\lambda(a)$ where the length of wavelength depends on a. It should be noted that it is not always linear when the real-part of wave-vector (r_x) is plotted and this case will be shown in the following section. The linearity of the mode wavelength nm against vacuum wavelength (nm) is demonstrated in Fig. 3.9(b). It is observed that as the mode wavelength increases, the real-part of the photon wave-vector increases as well as the real-part of the complex wave-vector which has been numerically computed. Furthermore, the magnetic field component is shown in Fig. 3.9(c) in which the real-part of **H** is plotted against the position. The minimum and maximum real components of magnetic field are shown as well. In addition, quivering characteristics of E-field along the x and z axes are shown with dashed line in the same Fig. 3.9(c). In Fig. 3.9(c) , the plot of position against field strength is shown for the magnetic field (H-field). There is an observation in which the curve rises to zero or unity in a resemblance of square root function and linearly increases to approximate 10 nm and increases quadratically as depicted in Fig. 3.9(c). The other curve in red indicates the quivering characteristics in the thin layer in consideration. The E-field (vector plot) as well as E-field (intensity plot) is shown in Fig. 3.9(d). This is for a single case of computed wave-vector. These curves change as the values of wave-vector differ based on the initial guess. The propagation length can be determined by calculating the reciprocal of the decay constant. Figure (3.9d) shows the propagation

lengths of the plasmon field in the geometry. The longer propagation length can be achieved when the width of the material is reduced while keeping a huge plasmon mode.

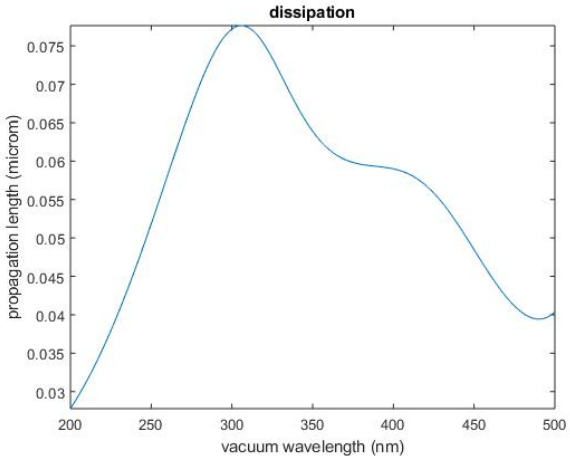

(a) Dissipation

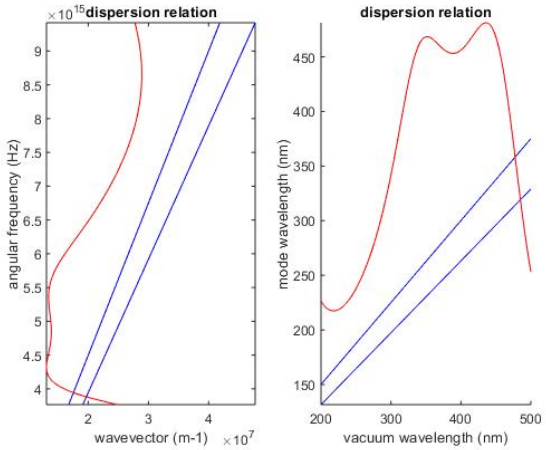

(b) Dispersion relation

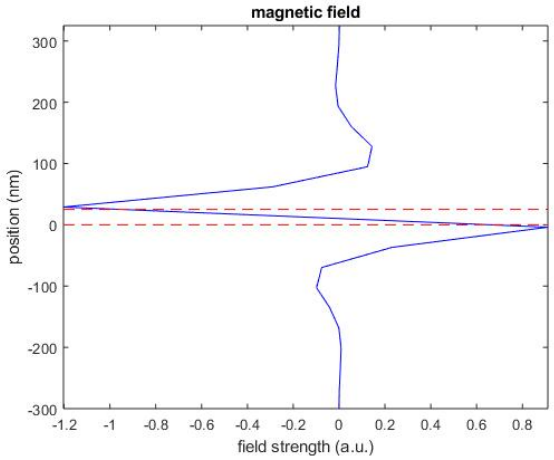

(c) Magnetic Field

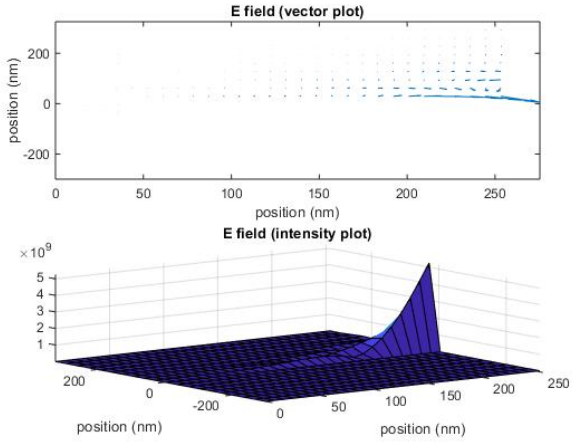

(d) E-field

Figure 3.9: Various values of fields and propagation length for r=10745635.08+i1068819.24 at λ=200:500 nm.

3.6 Summary of the Chapter

The concept of plasmonics and its application has been discussed and explored in this Chapter. The application of this includes the MIM and IMI for three, five, and multi-layered system. The implementation of these cases has been assessed based on the propagation length, H-field, E-field and dispersion relation of the material used. The simulation results show that the wave-vector can be used to compute various parameters as depicted in the chapter. Although it requires a careful and well-thought-out scheme for the wave-vector to be calculated by clicking a point within the displayed region as an initial guess using the cursor of the mouse as a way of customizing the program. Consecutively, the dispersion relation, propagation length and other relevant metrics such as fields can be computed with the convergence rate depending on the initial point guess.

Chapter 4

Quantum Models for Metallic Nano-particles and its Application

4.1 Introduction

In this section, quantum models will be examined and applied to solve various nano-particle geometries such as a cube, sphere, and cuboid. The investigation of metallic nano-particles is very important and has drawn great interest due to its capability to improve the field of optical communication on the nanometre region, which ensures the materials fascinating for different uses in wide areas of scientific discipline. The control of metallic material characteristics in the nano-sized domain depends on capability and skill to handle the size in order to broaden the uses in various fields of study [76]. Some of the most common metals used in this field of study are silver, gold, aluminium, and copper. Out of these metals, silver and gold materials are dominant. For example, silver metallic nano-particle have remarkably

essential uses in the area of engineering, biomedical engineering, and science. To describe the dielectric function of metallic nano-particles, the quantum computation is carried out on the impacts owing to bound electrons. That is a consideration that must be taken into account when computing the contributions of dielectric function as a result of inter-band transitions with the existence of the direct current (DC) magnetic field. To do this, the concept of the perturbation theory of the density matrix needs to be studied and applied.

Furthermore, in [77], the frequency-dependent dielectric function of a domed- shaped shell with quantum-size impacts was carried out. In this work, a rigorous, systematic and analytical basis of the quantum role and impact using linearly-shifted associated Legendre polynomials (LSALP) approach as employed in the work. This approach is used to construct an orthonormal eigenbasis approximation for a single electron Hamiltonian for a spherical shell. Besides, the methodical and analytical findings offer an exact, quantifiable modification to the frequency-dependent dielectric-function of metallic shells with the diametre smaller than 10 nm. The drawbacks of the technique are that the issues of breaking of symmetry and coupling of two core-shells remain unresolved. In addition, in [78], who worked on the linking of both classical and quantum plasmonics using the quantum modified model since the conventional electrodynamics is unable to explain the coupling over the nanometre intervals or openings of the particle. This Quantum Corrected Model (QCM) incorporates the quantum-mechanical impacts throughout the conventional electrodynamic environment. Hence, the scheme was able to model the junction among the adjacent nano-particles through the use of the response of dielectric function. The QCM contains tunnelling of electron and tunneling resistivity at the interval in large and complex structures. However, some

of the demerits of the QCM approach are that it fails to show categorically if it can be applied for both regular and irregular structures and the exhaustive quantum simulations are still not practicable and realistic for large systems. Also, in [79], the study was based on plasmonic resonances of specific metallic nano-particles by applying a scheme known as aberration corrected transmission electron microscope imaging alongside monochromated scanning Transmission Electron Microscope Electron Energy-loss Spectroscopy (TEMEELS). This approach permits direct similarity between a particle's structure and the plasmon resonance. Hence, when the diametre of the nano-particles reduces from 20 nm to 2 nm, the plasmon resonance changes to greater energy by a factor of 0.5 eV which is a considerable variation from the conventional results. The advantage of this is that it is an experimental-based approach rather than a theoretical scheme. Besides, the plasmonic resonance and quantum electrodynamics of metallic nano-systems carried out in [80] were based coherent motion of its conduction electron as a result of application of incident light to the structure.

Also, the Quantum Electrodynamics (QED) was proposed similar to [81] but using a theoretical approach. This theory was used to explain the interaction between the virtual field and fluctuating electrons. In the end, the closed-form theory results replicate very well the experimental data. Additionally, [82] worked on the impacts of quantum size in metallic nano-particles and tiny films. In this thesis, an expanded and modified scheme called Random Phase Approximation (RPA) was used to compute the dielectric function infinite region of minute wave-vectors. This idea was employed to a straightforward free-electron model for diminutive metallic particles. One of the drawbacks of this study is that there is no result to show for the quantum formalism. Also, the effects of interband between the valence and

conduction bands were not considered. In the work of [83], the quantum size impacts on the optical characteristics of minute metallic nano-particles were studied. In this study, an RPA approach was used alongside with number-conserving relaxation time approximation. The results obtained showed that the far-infrared absorption coefficient diverges when the critical size of the particle approaches. The multiple quantum effects for small particles were not investigated due to the local field that may not be taken as purely transverse.

In [84], the effect of magneto-optical based response of metallic nano-particle groups was studied. In the work, the interaction between the light-energized dipoles of nano-particles was investigated using dipole approximation. Thereby, it was assumed that the total interacts with the direct current (DC) of the magnetic field and linearly biased light fulfilled by the azimuthal polarization. Hence, the results showed that the Faraday rotational effect and ellipticity of Faraday are sinusoidal-shaped function. Consequently, close to the surface plasmon frequency, both the Faraday ellipticity and Faraday rotation increase. However, the study fails to explore the effect of the size dispersion of magneto-optical property influences the overall behaviour of the particle. Also, the magneto-optical response of trimmers, fractal clusters, tetrameters is yet to be investigated. In [85], the effect of Faraday rotation in a disordered medium was probed. The coherent-potential approximation was employed, which is based on retarded and advanced Green's functions. The results showed that the disorder enhanced the transversal time by an additional factor in comparison with a free light propagation time. One of the drawbacks of this study is that the lack of numerical implementation for this rigorous and theoretical formulation. Besides, in [86], the study relied on a two-dimensional dipolar matching in monolayers of gold and silver nano-particles on a

substrate of dielectric. This study applied both the conventional Drude model for the effects of intraband and Lindhard Random Phase Approximation (LRPA) for the role of interband band to the overall dielectric-function of metallic particles. The Pines and Noziere theory was used to compute the damping factor of the particle and Maxwell-Garnett (MG) model was used for the case of isolated nano-particles in suspension. Therefore, the red shifted spectra observed in this study was due to dipolar effects of the metallic nano-particles. Accordingly, in [87], the impacts of interband transitions regarding the Faraday rotation in metallic nano-particles was the centre of the investigation. This study was based on a quantum model for the description of frequency-dependent dielectric function in the presence of a direct current magnetic field. Besides, the study also focused on the effects in dielectric function as a result of interband changes which are vital in the ultraviolet and blue region for rare metals employed in plasmonic applications. The results obtained showed that the DC magnetic field effect is a change in the optical frequency resulting in interband transition (IBT) by a factor $\pm\mu B/\hbar$. However, some of the limitations of this study are: non-detailed computation of anisotropic parameters of the gold particles, approximation of density matrix for the perturbed state, and the numerical implementation of a three-dimensional (3D) model are yet to be investigated.

4.2 Quantum Model of Dielectric Function Using Perturbation Technique

In this present section, the computation of quantum effects resulting from bound electron is studied. The quantum effect is characterized via computation of the contribution of frequency-dependent dielectric function due to the occurrence of inter-band changes in response to direct current magnetic field.

Consider a single-electron Hamiltonian given as :

$$\hat{\mathbf{H}} = \frac{1}{2m_0}[\hat{p} - e\hat{\mathbf{A}}(\hat{r}, t)]^2 + e\hat{\phi}(\hat{r}, t) + \hat{U}(\hat{r}) \tag{4.1}$$

where $\hat{\mathbf{A}}$, e, and $\hat{\phi}$, denote vector potential of the EM field, charge, and scalar potential of electromagnetic field, respectively, and $\hat{U}$ represents the periodic potential of the lattice. Hence, the standard momentum operator for the electrons is expressed as $\hat{p} = -i\hbar\vec{\nabla}$. The kinetic momentum operator for the physical momentum can be put in this form [87]:

$$\vec{\pi} = \hat{p} - e\hat{\mathbf{A}} \tag{4.2}$$

It is worth noting that when the operator is squared, in Eq.(4.1) defines the energy. Furthermore, assume that the scalar potential $\hat{\phi}$ to be zero, which defines the condition for Coulomb gauge. The vector potential $\hat{\mathbf{A}}$ consists of a term for direct current magnetic field, $\hat{A}_0$ and a second term for the alternating current optical field $\hat{A}_1$. Additionally, the optical field serves as a standard unquantified field which fluctuates as $e^{-i\omega t}$. The imperturbable

by optical field, the electron bands, emanate from the solution of a Hamiltonian with the kinetic energy, the DC magnetic field, and lattice periodic potential can be cast compactly as:

$$\hat{\mathbf{H}}_0 = \frac{1}{2m_0}[\hat{p} - e\hat{\mathbf{A}}_0]^2 + \hat{U}(\hat{r}) \tag{4.3}$$

The conditions can be stated that: for weak DC magnetic field, the term that has a quadratic form in $\hat{\mathbf{A}}_0$ can be ignored and the impact of the cross-term involving $\hat{p}$ stands for the orbital Zeeman splitting which simplifies to:

$$\hat{\mathbf{H}}_0 = \frac{1}{2m_0}[\hat{p}]^2 + \hat{U}(\hat{r}) - \vec{\mu} \cdot \mathbf{B} \tag{4.4}$$

To compute the frequency-dependent dielectric function $\epsilon(\omega)$ using a quantum mechanical approach, the averages of polarization are statistically essential. This can be achieved by characterizing a quantum operator locally termed $\hat{\rho}_e(r)$ known as density operator for a single-electron charge density.

4.2.1 The Density Operator

The computation of the perturbed density matrix denoted as $\hat{\rho}_1$ using quantum Liouville equation:

$$\frac{\partial \hat{\rho}}{\partial t} = \frac{1}{i\hbar}[\hat{\mathbf{H}}, \hat{\rho}], \tag{4.5}$$

where $\hat{\mathbf{H}} = \hat{\mathbf{H}}_0 + \hat{\mathbf{H}}_1$; More so, $\hat{\mathbf{H}}_1 = -\frac{e\hat{\mathbf{A}}_1}{m_0}(\hat{p} - e\hat{A}_0)$; $\hat{\rho} = \hat{\rho}_0 + \hat{\rho}_1$ and assuming the following: $[\hat{\mathbf{H}}_0, \hat{\rho}_0]$ and ignoring the small nonlinear term denoted as $[\hat{\mathbf{H}}_1, \hat{\rho}_1] \approx 0$.Therefore,

the motion of the particles can be described by this equation for the perturbation as:

$$\frac{\partial \hat{\rho}_1}{\partial t} \approx \frac{1}{i\hbar}\{[\hat{H}_0, \hat{\rho}_1] + [\hat{H}_1, \hat{\rho}_0]\} \tag{4.6}$$

Assuming the expansion of $\hat{H}_1$ and $\hat{\rho}_1$ in unperturbed states in a linear combination form as:

$$\left.\begin{aligned} \hat{H}_1 &= \sum_i \sum_f |f\rangle\langle f|\hat{H}_1|i\rangle\langle i| \\ \hat{\rho}_1 &= \sum_i \sum_f C_{f,i}|f\rangle\langle i| \end{aligned}\right\} \tag{4.7}$$

Following the estimation of the commutator with the assumption that the $e^{-i\omega t}$ time-dependence for $\hat{\rho}_1$ with $C_{f,i} = |f\rangle\langle i|$ is determined and the transition in the density operator can be computed not forgetting that the only matrix components $C_{f,i} = |f\rangle\langle i|$ of $\hat{\rho}_1$ in the basis states of unperturbed Hamiltonian $\hat{H}_0$, then $\hat{\rho}_1$ assumes the following compact form,

$$\hat{\rho}_1 = \sum_i \sum_f \frac{(w_i - w_f)|f\rangle\langle f|\hat{H}_1|i\rangle\langle i|}{\hbar(\omega + i\gamma) + E_i - E_f}. \tag{4.8}$$

4.2.2 Computation of Thermal and Volume Averages

The dipole moment is defined as $\hat{d}(r) = e\hat{r}|r\rangle\langle r|$ and statistically averaged as $d(r) = Tr[\hat{\rho}\hat{d}(r)]$. Hence, the one-electron charge density is denoted as $\hat{\rho}_e(r)$, the one-electron current density represented as $\hat{j}_e(r)$ and the electron velocity is given as $\hat{v} = \hat{\pi}/m_0 = (\hat{p} - e\hat{A})/m_0$. Then, the statistically mean values of these operators can be determined from the trace using

density operator as:

$$\left.\begin{aligned} \rho_e(r) = \langle \hat{\rho}_e(r) \rangle = Tr(\hat{\rho}\hat{\rho}_e(r)) \\ j_e(r) = \langle \hat{j_e}(r) \rangle = Tr\hat{\rho}\hat{j}_e(r) \\ \rho = \frac{N}{V} Tr(\hat{\rho}e) \\ \hat{P} = ne\hat{r} \\ \mathbf{P} = Tr(\hat{\rho}ne\hat{r}) \end{aligned}\right\} \tag{4.9}$$

4.2.3 The Computation of Averaged Electric Polarization and Susceptibility

The disturbance fluctuates at frequency ω and therefore, the response of the electric polarization oscillates at similar rate employing only the shift $\hat{\rho}_1$ in density matrix can be obtained as:

$$\left.\begin{aligned} P = Tr[\hat{\rho}_1 \hat{P}] = ne \sum_i \sum_f \langle f|\hat{\rho}_1|i\rangle\langle i|\hat{r}|f\rangle \\ P = \frac{ne^2\hbar}{\omega + i\gamma} \sum_i \sum_f \frac{(w_i - w_f)\langle i|\hat{v}|f\rangle\langle f|E\cdot\hat{v}|i\rangle}{\left[\hbar(\omega+i\gamma) + E_i - E_f\right]\left(E_i - E_f\right)} \end{aligned}\right\} \tag{4.10}$$

The change in frequencies between the final and initial states is $\hbar\omega_{if} = E_i - E_f$. The frequency-dependent susceptibility constituents can be expressed as:

$$\chi_{ab}(\omega) = \frac{ne^2}{\hbar\varepsilon_0\left(\omega + i\gamma\right)} \sum_i \sum_f \frac{\left(w_i - w_f\right)\langle i|\hat{v}_a|f\rangle\langle f|E\cdot\hat{v}_b|i\rangle}{\omega_{if}(\omega + i\gamma + \omega_{if})} \tag{4.11}$$

Finally, the frequency-dependent dielectric function via the use of perturbation theory can be cast compactly as:

$$\epsilon(\omega) = 1 + \chi_{ab}(\omega) \tag{4.12}$$

4.2.4 The Application of Theoretical Band Models

To apply this result, it is necessary to employ energy levels suitable for the bands in hand as shown in Fig. 4.1. Hence, the discussion will be limited to a parabolical model containing two bands in which the bands are separated by the energy gap E_g. The masses for occupied (lower) and upper (unoccupied) bands are effective in nature; i.e., effective masses, respectively. Every band is influenced by the Zeeman change in one direction. Hence, it is possible to gauge and measure energies from the top of the lower band [88], [89]. Therefore, the respective energies for initial state (occupied band) denoted by E_i and the energies for the final state of the electron denoted by E_f for which they can be equated as $E_i = E_h$ and $E_f = E_e$, where E_h and E_e are energies for holes and electrons, respectively. For this reason, the initial and final energies can be put in this form:

$$\left.\begin{aligned} E_i = E_h &= -\frac{\hbar^2 k_i^2}{2m_h^*} - \frac{1}{2} m_i \hbar \omega_B \\ E_f = E_e &= E_g - \frac{\hbar^2 k_f^2}{2m_e^*} - \frac{1}{2} m_f \hbar \omega_B \end{aligned}\right\} \tag{4.13}$$

where k_i, k_f, m_i, m_e^*, m_h^*, and m_f represent initial wave-vector, final wave-vector, azimuthal quantum number of particle in initial state, azimuthal quantum number of particle in final state, effective mass of the electron, and effective mass of the holes, respectively. The Zeeman

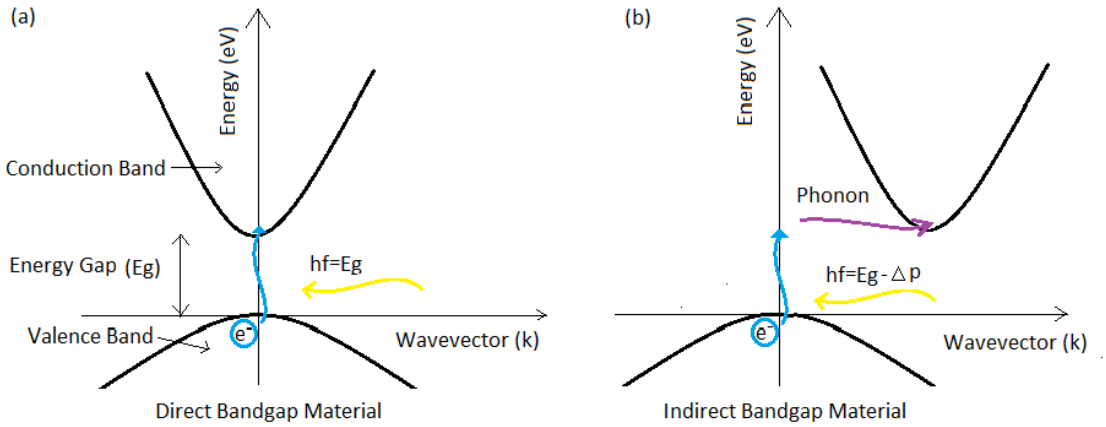

Figure 4.1: A parabolic two-band model for direct and indirect bandgaps alongside two separated bands with energy gap E_g [87] .

changes are applicable to positively charged particle. The orbital angular quantum numbers for initial and final states m_i and m_f, mutatis mutandis. They are constrained by the azimuthal quantum numbers for every band, ℓ_i and ℓ_f, appropriately. **Assumption**: The vertical shifts that preserve linear impulse (momentum) denoted as $\hbar k$ and an inconsiderable light quantum momentum. This means that just momentum-conserving based transitions between the two chosen bands for particular wave-vector k are examined. Hence, the transition frequencies can be cast in this way compactly as:

$$\omega_{if} = \omega_g - s^2 + \frac{1}{2}\Delta m \omega_B \tag{4.14}$$

where $\frac{1}{m^*} = \frac{1}{m_e^*} + \frac{1}{m_h^*}$, ω_g, s, and Δm represent gap frequency, scaled wave-vector, and orbital angular momentum quantum number, accordingly and are represented as [87]:

$$\left.\begin{aligned} \omega_g &\equiv \frac{E_g}{\hbar} \\ s &\equiv \sqrt{\frac{\hbar}{2m*}} \\ \Delta m &\equiv m_f - m_i \end{aligned}\right\} \tag{4.15}$$

4.2.5 A One-dimensional Model Based on Theory

Let the frequency-dependent inter-band susceptibility be represented as:

$$\chi_v(\omega) = WY_v(\omega) \tag{4.16}$$

where W includes all the invariable (constant) normalized factors, and the inter-band transition integral denoted as $Y_v(\omega)$ comprises all temperature dependence and frequency represented as:

$$\left.\begin{aligned} W &= \frac{8Vne^2|M|^2\hbar\pi}{3m_0^2\varepsilon_0(2\pi)^3}\left(\frac{2m*}{\hbar}\right)^{\frac{3}{2}} \\ Y_v(\omega) &= \frac{1}{\omega + i\gamma}\sum_{m_i,m_f}\int_0^{s_F} dss^2\frac{(w_i - w_f)}{\omega_{if}} \times \left\{\frac{\delta_{mf} = m_i + v}{\omega + i\gamma + \omega_{if}} + \frac{\delta_{mf} = m_i - v}{\omega + i\gamma - \omega_{if}}\right\} \end{aligned}\right\} \tag{4.17}$$

Furthermore, by transforming the integral equation above from s domain to η domain with effect of magnetic field denoted by B, further simplification gives:

$$Y_v(\omega) = \frac{\omega_{2v}}{\omega + i\gamma} \sum_{m_f} \int_{\omega_g}^{\eta_F} d\eta \frac{\eta g_{mf}(\eta)(\eta - \omega_g)^{\frac{1}{2}}}{(\eta^2 - \frac{\omega_B^2}{4})(\eta^2 - \omega_v^2)} \tag{4.18}$$

The symbols in this equation are:

$$\left.\begin{aligned} \omega_v \equiv \omega + i\gamma + \zeta_v = \omega + i\gamma + \frac{v\omega_B}{2} \\ \omega_{2v} \equiv \omega + i\gamma + \zeta_{2v} = \omega + i\gamma + v\omega_B \\ g_{mf}(\eta) \approx 1 - F\left(E_f - E_i\right) = 1 - F\left(\eta, m_f\right) = w_i - w_f \\ E_f \approx \hbar\left(\omega_g - s^2 + \frac{m_f\omega_B}{2}\right) = \hbar(\eta - \frac{m_f\omega_B}{2}) \\ \eta = \omega_g + s^2 \\ \omega_F \equiv \omega_F + \frac{v\omega_B}{2} \end{aligned}\right\} \tag{4.19}$$

Substituting (4.19) into (4.18 and simplifying,

$$Y_v(\omega) = \frac{\omega_{2v}}{\omega + i\gamma} \sum_{m_f} \int_{\omega_g}^{\eta_F} d\eta \frac{(\eta^2 + \gamma^2 - \omega_F^2)\eta \cdot g_{mf}(\eta - \omega_g)^{\frac{1}{2}}}{(\eta^2 + \gamma^2 - \omega_F^2)^2 + 4\gamma^2\omega_F^2}. \tag{4.20}$$

4.2.6 A One-dimensional Band Based on an Approximation Scheme

The approximation made for the (4.10) is highlighted as follows. It is assumed without no loss of generality that w_1=0, w_f=0 while letting the upper integration limit to approach

infinity;i.e., $s_F \to \infty$. Hence, Eq. (4.10) in terms of frequency after computation becomes:

$$Y_v(\omega) = \frac{\pi g_m}{2(\omega + i\gamma)^2}\left\{ i\sqrt{\omega_v - \omega_g} - \sqrt{\omega_v + \omega_g} + \sqrt{\omega_g - \zeta_v} + \sqrt{\omega_g + \zeta_v} \right\} \tag{4.21}$$

In other words, expressing it in terms of energy (eV), then it gives:

$$Y_v(E) = \frac{\pi g_m \hbar^{\frac{3}{2}}}{2(E + iE_\gamma)^2}\left\{ i\sqrt{E_v - E_g} - \sqrt{E_v + E_g} + \sqrt{E_g - E_B} + \sqrt{E_g + E_B} \right\} \tag{4.22}$$

Finally, by the use of **Artangent** function which produces almost exact results as theory is employed as a means of approximation technique. This closed-form expression gives:

$$Y_v(E) = \frac{\pi g_m \hbar^{\frac{3}{2}}}{2(E + iE_\gamma)^2}\left\{ i\sqrt{\sqrt{(E - E_g)^2 + E_\gamma^2}\left(\cos 0.5 \arctan \frac{E_\gamma}{E - E_g} + i \sin 0.5 \arctan \frac{E_\gamma}{E - E_g}\right)} \right.$$
$$\left. + \sqrt{\sqrt{(E + E_g)^2 + E_\gamma^2}\left(\cos 0.5 \arctan \frac{E_\gamma}{E - E_g} + i \sin 0.5 \arctan \frac{E_\gamma}{E - E_g}\right)} + 2\sqrt{E_g} \right\} \tag{4.23}$$

4.3 Numerical Simulations and Discussion

This is the interband transition (IBT) contribution to the susceptibility from the 1D band model. In this model, both the real and imaginary parts remain positive for all frequencies ranging from 200 nm to 1000 nm as shown in Figs. 4.2 (a) and 4.2(b). This is the interband transition (IBT) contribution on the permittivity from the 1-D band model. In this model, both the real and imaginary parts remain positive for all frequencies ranging from 200 nm to 1000 nm as shown in Figs. 4.2 (c) and 4.2 (d). This is the interband transition (IBT) role on

the Susceptibility from the 1D band model. In this model, both the real and imaginary parts remain positive for all energies ranging from 1.2407 to 6.2035 eV as permittivity increases as depicted in Figs. 4.3(a) and 4.3(b). This is the interband transition (IBT) effect on the permittivity from the 1-D band model. In this model, both the real and imaginary parts remain positive for all energies ranging from 1.2407 to 6.2035 eV as permittivity increases as depicted in Figs. 4.3(c) and 4.3(d). The IBT contribution to the permittivity for the 1-D band model as functions of photon energy in eV. The solid curves apply the full theory in Eq.(14), including the Fermi occupation factors for room temperature (300K). The dashed curves show the result of assuming an unoccupied upper band, obtaining permittivity from Eq. (4.11) which are shown in Figs.4.4(a) and 4.4 (b). It is assumed in the simulations that $omega_B$ and E_B are zero for tractable solution, simplicity and its complexity. The interband electronic transitions are known to have a considerable effect on dielectric properties of metals especially silver and gold. Although it is common to consider only a simple Drude model for a quasi-free electron, it is inadequate to describe the absorption in metallic particles. However, for the optical effects such as absorption or Faraday rotation, it is obvious that a correct description of dielectric function for bulk material or macroscopic sample wholly determines the outcome. If the absorption cannot be obtained through fitting, then it is very difficult to see how the Drude model could explain the effects very well. Hence, to do this, the inclusion of the interband transition for the bound electrons based on Quantum formulation. The computation carried out here is specifically for nanoparticles in the presence of DC magnetic field B. The shift in energy states used here is a Zeeman shift due to the DC magnetic field for electrons in bands of specified angular momentum. The details of the interband

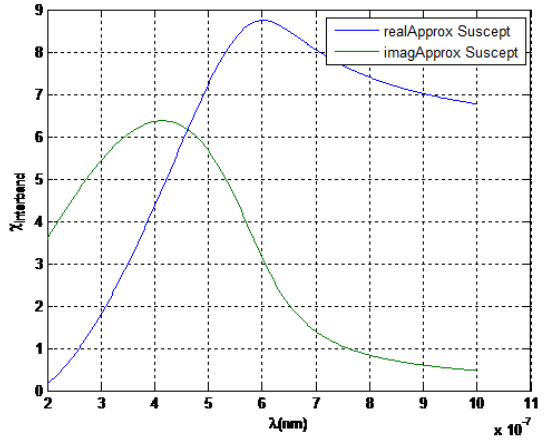

(a) The graph of frequency-dependent (approximation) susceptibility against wavelength (nm)

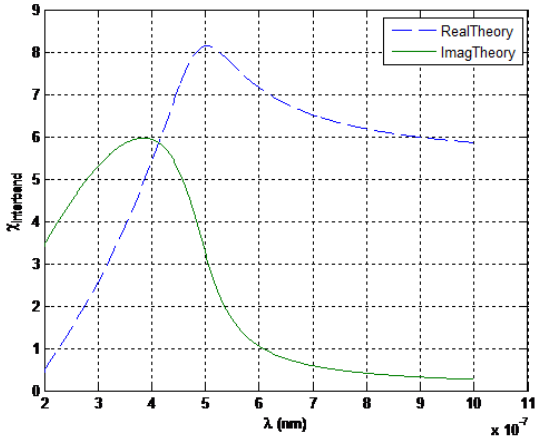

(b) The graph of frequency-dependent (theory) susceptibility against wavelength (nm)

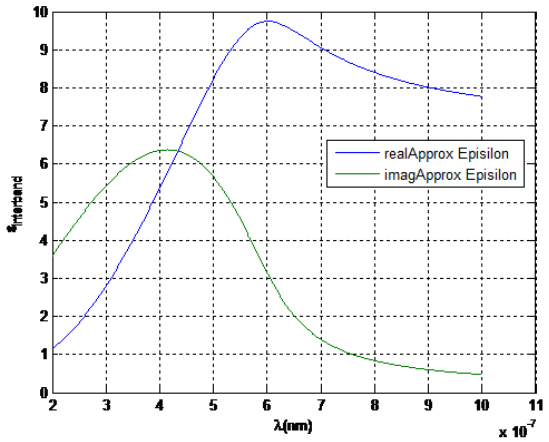

(c) The graph of frequency-dependent (approximation) dielectric function against wavelength (nm)

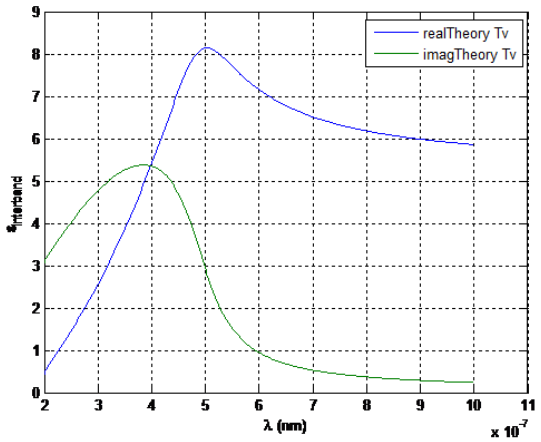

(d) [The graph of frequency-dependent (theory) dielectric function against wavelength (nm)

Figure 4.2: Plots of material parameters versus wavelength in nm

transitions (IBT) integral for the 1-D band model for the effects such as absorption were derived and shown graphically. The numerical calculation that was carried out which led to the value of amplitude factor Q and other dielectric parameters used for the simulation in which the real and imaginary parts remain positive for wavelength greater than 200 nm.

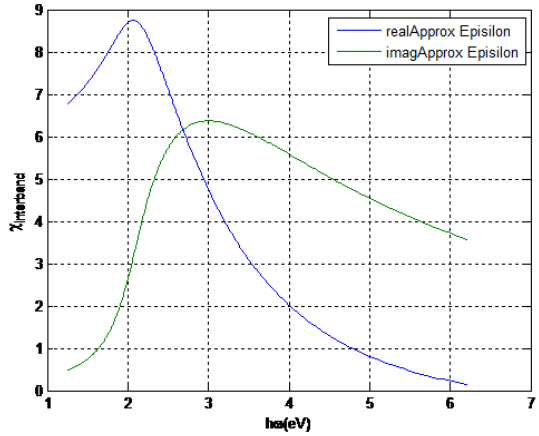

(a) The graph of frequency-dependent (approximation) susceptibility against energy (eV)

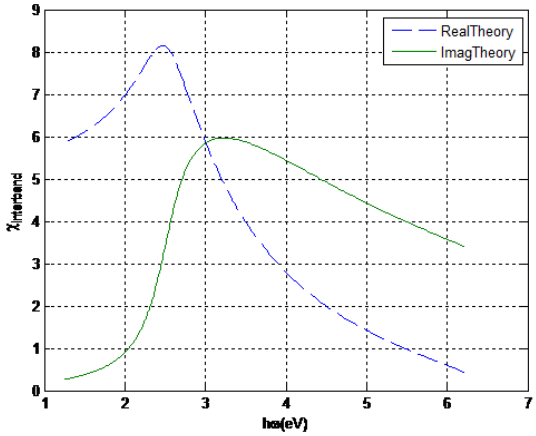

(b) The graph of frequency-dependent (theory) susceptibility against energy (eV)

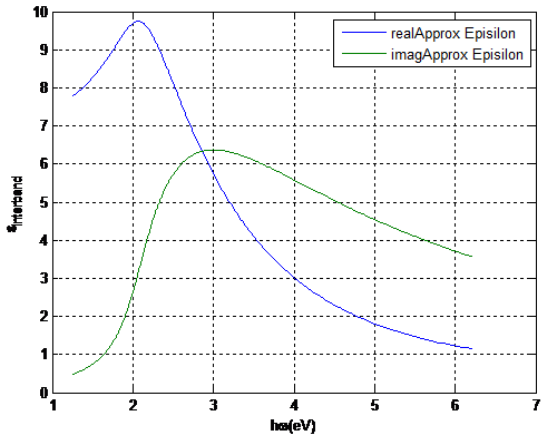

(c) The graph of frequency-dependent (approximation) dielectric function against energy (eV)

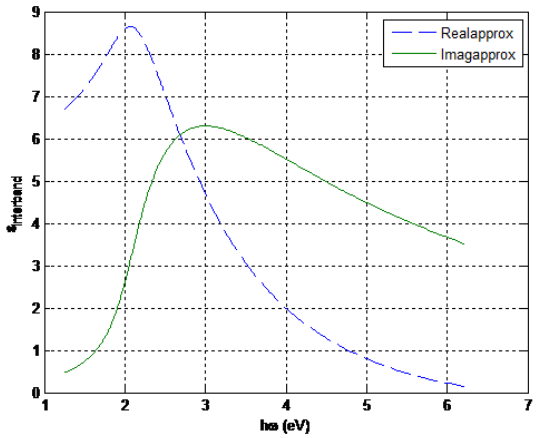

(d) The graph of frequency-dependent (theory) dielectric function against energy(eV)

Figure 4.3: Plots of material parameters versus energy in eV

It is expected to perform well when applied to the Faraday rotation properties of a dilute solution of nanoparticles. These discrepancies may be due to uncertainty in the true value of gold volume fraction. It may also be aggregation and backscattering effects which are not included in the model.

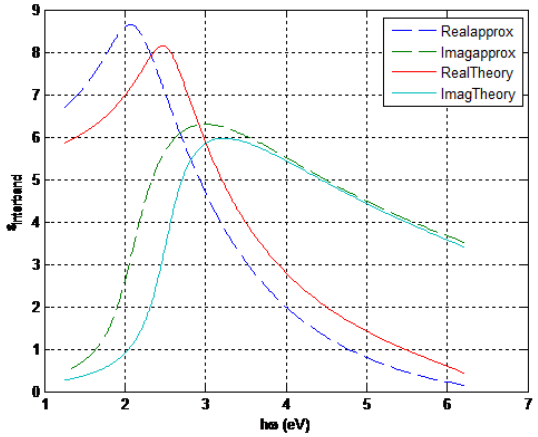

(a) The graph of frequency-dependent dielectric function (theory and approximation). against energy(eV)

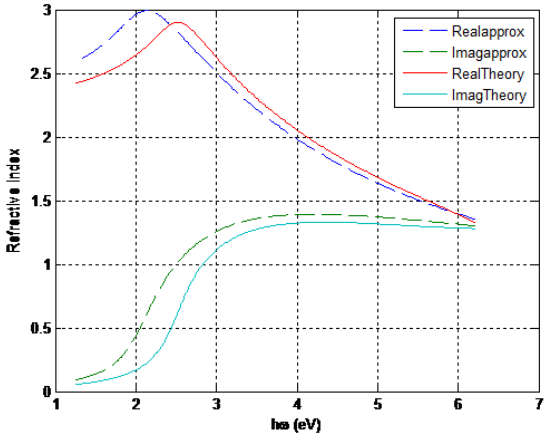

(b) The graph of refractive index for theory and approximation against energy (eV)

Figure 4.4: Graphs of material parameters for real and imaginary parts of both $\epsilon_{interband}$ and refractive index versus energy in (eV).

4.4 Frequency-dependent Dielectric Function for 1-D, 2-D, and 3-D Small-scale Devices in Optical Communication Applications

The characteristics of the system rely not only on its materials features such as permeability, susceptibility, refractive index, the dielectric but also on the shape, size and so forth. Hence, the aim of this present section here is to go one step further and set up a physics-inspired problem-solving approach. This study takes into consideration a 1-D structure of the concept and findings as put forward in [90] following the same procedural steps. Considering a complex boundary-value problem and analysis which will be regarded as the initial or original problem, the proposed scheme requires that construction of an auxiliary problem, which imitates or is similar to the original problem, nevertheless, makes it much easier than the perturbation making the transition of an electron to be possibly feasible and practicable.

This research assumes a single electron model, which adopts a non-interacting electron gas subject to a uniform potential cage depending on the circumstances or case-by-case basis. The straightforwardness of the supposition enables the construction of a computational physics expression for the frequency-dependent dielectric function for a boundary-value problem (BVP) which is the focus in this study. Inspired and spurred by the optical features of a metallic material at the nano-region for the design, device modelling and applications in science and engineering, this research examines the frequency-dependent dielectric function for 1-D, 2-D, and 3-D problems in a closed-form. Finally, 1-D and 2-D numerical results are presented.

4.4.1 The Auxiliary Unperturbed Problem Construction for 1-D Frequency-dependent Dielectric Function

Examine the time-independent Schrödinger equation,

$$H\psi(x) = E\psi(x), \tag{4.24}$$

where $\psi(x)$, H, and E stand for the wave function, the Hamiltonian operator and the Eigenvalues, respectively. The electron will be restricted to the class of the wave functions which vanish at the boundary points $x = 0$ and $x = L$. We set for instance the potential $V(x) = 0$ for $x \in [0, L]$. This means that the potential cage experienced by the electron in the metallic material is zero and outside the metallic wire is infinite. Therefore, the eigenvalues and the corresponding eigenfunctions of (4.24) are strictly positive based on the hermiticity of the Hamiltonian. By substitution, it can be corroborated that the solutions of Eq. (4.24) above are wavefunctions and eigenvalues, respectively [90], [91];

$$\psi_n(x) = \sqrt{\frac{2}{L}} \sin\left(\frac{n\pi x}{L}\right) \Longleftrightarrow E_n = \frac{\hbar^2}{2m_e}\frac{\pi^2 n^2}{L^2} \tag{4.25}$$

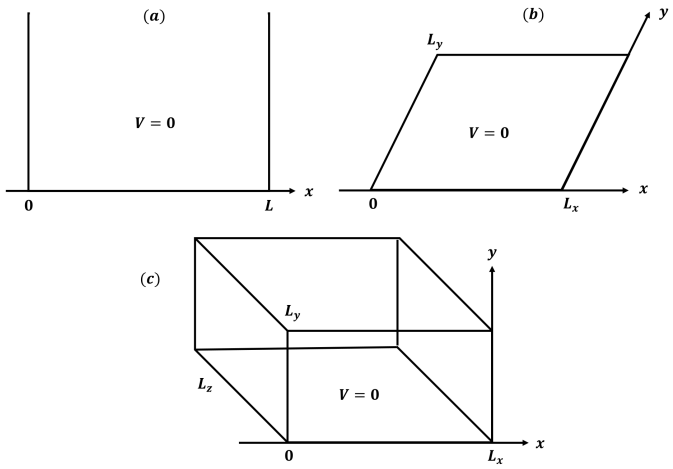

Figure 4.5: The geometry of the problem: (a)1D , 2D and (c) 3D [90]

4.4.2 Quantum Mechanical Description of Dielectric Coefficient for a Perturbed Metallic Material

The closed-form expression for the frequency-dependent dielectric function will be obtained subsequently. It is assumed that an E-field in a metallic wire of dimension L ;i.e., a 1-D scenario as shown in Fig. 4.5(a). Moreover, it is assumed that the E-field is polarized linearly along the positive direction of the x axis direction and as stated in as $E(r,t) = E_x \sin(\omega t)$ [90]. It should be pointed out that the E-field is related to the polarization of any material as:

$$\varepsilon(\omega) = 1 + \frac{P(\omega)}{\epsilon_0 E(r,t)} \tag{4.26}$$

To calculate the polarization and subsequently the dielectric function of the geometry of metallic nano-wire, the quantum mechanical method will be utilized, due to the confinements of the particles in nano region. In the first place, it is furthermore assumed that the system is unperturbed for $t \leq 0$ and its wavefunction is characterized by the time-independent

Schrödinger equation

$$H^0\psi(x) = E_i\psi(x), \tag{4.27}$$

wherein H^0 is the unperturbed Hamiltonian of the system and $\psi_i(x)$ denotes the wavefunction corresponding to the initial state i of the system with the eigenenergy E_i. The $\mathbf{r} \equiv (x, y, z)$ denotes the position vector of a point inside the nano-wire of metallic geometry under consideration. When the E-field is applied at time $t = 0$, the wavefunction depends on time and there is electrons transition from initial state to final state owing to perturbation. The final state of the electrons transition state is denoted by f and the time-dependent wavefunction is given by $\Psi_f(x, t)$ and can be resolved utilizing:

$$i\hbar\frac{\partial\Psi_f(r,t)}{\partial t} = [H^0 + H_1(t)]\Psi_f(r,t) \tag{4.28}$$

where $H_1(t)$ is the perturbed Hamiltonian as a result of E-field , stated as

$$H_1(t) = exE(r,t). \tag{4.29}$$

By substituting (4.28) into (4.29), the solution becomes:

$$\Psi_f(r,t) \;=\; \frac{e\epsilon_x}{2}\sum_i^{\infty}\langle\psi_i(r)|x|\psi_f(r)\rangle\psi_f(r) \times e^{\frac{-iE_f(t)}{\hbar}}\left[\frac{1-e^{i(\omega_{i,f}+\omega)t}}{\omega_{i,f}+\omega} + \frac{1-e^{i(\omega_{i,f}-\omega)t}}{\omega_{i,f}-\omega}\right] \tag{4.30}$$

wherein $\omega_{i,f} = \frac{(E_f - E_i)}{\hbar}$. The induced dipole moment experienced per electron by the electron owing to effect of polarization and perturbation can be calculated as:

$$P_f(\omega) = \langle \psi_f(r,t)| - ex|\psi_f(r,t)\rangle. \tag{4.31}$$

Hence, the total polarization over the entire volume of the wire of length L is

$$P_t(\omega) = \frac{1}{V_d}\sum_{f}^{\infty} P_f(\omega), \tag{4.32}$$

where V_d represents the total volume of the nano-metallic structure. Consequently, the dielectric function for the metallic nano-wire is computed with perturbation $H_1(t)$ for electron transition to take place as indicated. These functions affect the perturbation in the expression. The frequency-dependent dielectric function, expressed as $\epsilon(\omega)$, and is the equation below after factoring all the effects of damping as [92], [93], [77]:

$$\varepsilon(\omega) = 1 + 1 + \frac{2e^2}{\epsilon_0 V_d \hbar}\sum_{i}\sum_{f}\frac{|\langle\psi_i(r)|r|\psi_f(r)\rangle|^2\omega_{i,f}}{\omega_{i,f}^2 - \omega^2 - i\omega\gamma}. \tag{4.33}$$

4.4.2.1 Mathematical Formulation of 1-D Metallic Nano-wire

To obtain the dielectric function, we need to compute dipole matrix elements of the electron states from the initial to the final along the x-axis denoted as $M_{if} = \langle\Psi_f(x)|x|\Psi_i(x)\rangle$ given in (4.33), with the total number of electrons being denoted by N_{elec}, and the frequency difference $\omega_{i,f}$ in 1-D. Given the initial and final states of the electron as:

$$\psi_i^x(x) = \sqrt{\frac{2}{L_x}} \sin\left(\frac{n\pi x}{L_x}\right); \quad \psi_f^x(x) = \sqrt{\frac{2}{L_x}} \sin\left(\frac{(n+\Delta n)\pi x}{L_x}\right) \tag{4.34}$$

$$M_{if}^x = \int_0^{L_x} dx x \left\{ \sqrt{\frac{2}{L_x}} \sin\left(\frac{n\pi x}{L_x}\right) \sqrt{\frac{2}{L_x}} \sin\left(\frac{(n+\Delta n)\pi x}{L_x}\right) \right\}. \tag{4.35}$$

By performing the integration over x in the interval $x = [0, L_x]$, it is easily shown that:

$$M_{if}^x = \frac{L_x}{2} \left\{ \text{sinc}^2 \left[\left(n + \frac{\Delta n}{2} \right) \pi \right] - \text{sinc}^2 \left(\frac{\Delta n \pi}{2} \right) \right\}, \tag{4.36}$$

where $\text{sinc}(\cdot) = \frac{\sin(\cdot)}{(\cdot)}$. The frequency difference $\omega_{i,f}$ is given as

$$\omega_{i,f} = \omega_{n,\Delta n} = \frac{\hbar \pi^2}{2m_e} \left\{ \frac{\Delta n(2n + \Delta n)}{L_x^2} \right\}. \tag{4.37}$$

.

Finally, the total number of electron denoted as N_{elec} and the linear electron density represented as n_{elec} are expressed without loss of generality as:

$$N_{elec} = \frac{2K_F L_x}{\pi}; \quad n_{elec} = \frac{2K_F}{\pi} \tag{4.38}$$

where K_F denotes the radius of the particle in K-space or all filled quantum states correspond to grid-points that are within a distance from the origin at Fermi circle or n_f in n-space is the maximum number of filled electron at Fermi level. To compute the dielectric function, the oscillator strength

$$S_{i,f} = \frac{4m_e \omega_{i,f} |M_{i,f}|^2}{\hbar N_{elec}}, \tag{4.39}$$

Hence, the frequency-dependent dielectric function for problems of arbitrary dimensions can be expressed as,

$$\varepsilon(\omega) = 1 + w_p^2 \sum_i \sum_f \frac{S_{i,f}}{\omega_{i,f}^2 - \omega^2 - i\omega\gamma}. \tag{4.40}$$

Expressing (16) in non-dimensional form,

$$\epsilon(\omega) = 1 + \sum_i \sum_f \frac{S_{i,f}}{(\frac{\omega_{i,f}}{w_p})^2 - (\frac{\omega}{w_p})^2 - i(\frac{\omega}{w_p})(\frac{\gamma}{w_p})}. \tag{4.41}$$

Where w_p is the plasma frequency, m_e is electron mass, γ is the damping constant, $S_{i,f}$ the oscillator strength.

4.4.2.2 Mathematical Formulation of 2-D Metallic Nano-wire

To obtain the dielectric function, we compute matrix elements for the electron transition from the initial state to the final state denoted by $M_{if} = \langle \Psi_f(x,y)|xy|\Psi_i(x,y)\rangle$ given in (4.33), the total number of electrons N_{elec}, and the frequency difference $\omega_{i,f}$ in 2-D. The transitions of electron are assumed to take place in both x-axis and y-axis. The canonical two-dimensional initial-and final sates, respectively, are

$$\psi_i(x,y) = \sqrt{\frac{2}{L_x}} \sin\left(\frac{n\pi x}{L_x}\right) \sqrt{\frac{2}{L_y}} \sin\left(\frac{m\pi x}{L_y}\right), \tag{4.42}$$

$$\psi_f(x,y) = \sqrt{\frac{2}{L_x}} \sin\left(\frac{(n+\Delta n)\pi x}{L_x}\right) \sqrt{\frac{2}{L_y}} \sin\left(\frac{(m+\Delta m)\pi y}{L_y}\right). \tag{4.43}$$

$$M_{if}^{x} = \int_{0}^{L_x} dx x \sqrt{\frac{2}{L_x}} \sin\left(\frac{n\pi x}{L_x}\right) \sqrt{\frac{2}{L_x}} \sin\left(\frac{(n+\Delta n)\pi x}{L_x}\right) \tag{4.44}$$

$$M_{if}^{y} = \int_{0}^{L_y} dy y \sqrt{\frac{2}{L_y}} \sin\left(\frac{m\pi y}{L_y}\right) \sqrt{\frac{2}{L_y}} \sin\left(\frac{(m+\Delta m)\pi y}{L_y}\right) \tag{4.45}$$

By performing the integration over the range specified, then it can easily be shown that $M_{if} = M_{if}^{x} M_{if}^{y}$ for the product gives

$$M_{if} = \frac{L_x L_y}{4} \left\{ \text{sinc}^2\left((n+\frac{\Delta n}{2})\pi\right) - \text{sinc}^2\left(\frac{\Delta n\pi}{2}\right) \times ... \text{sinc}^2\left((m+\frac{\Delta m}{2})\pi\right) - \text{sinc}^2\left(\frac{\Delta m\pi}{2}\right) \right\} \tag{4.46}$$

where $\text{sinc}(.) = \frac{\sin(.)}{(.)}$ and $sinc(0) = 1$. The frequency difference term $\omega_{i,f}$ is given as

$$\omega_{i,f} = \omega_{n,\Delta n,m,\Delta m} = \frac{\hbar\pi^2}{2m_e} \left\{ \frac{\Delta n(2n+\Delta n)}{L_x^2} + \frac{\delta m(2m+\Delta m)}{L_y^2} \right\} \tag{4.47}$$

The total number of electron N_{elec} and the 2-D electron density n_{elec} are [16],

$$N_{elec} = \frac{L_x L_y K_F^2}{2\pi}; \quad n_{elec} = \frac{K_F^2}{2\pi}, \tag{4.48}$$

where K_F denotes the radius of the particle in K-space or all filled quantum states correspond to grid-points that are within a distance from the origin at Fermi circle or n_f in n-space is the maximum number of filled electron at Fermi level.

4.4.2.3 Mathematical Formulation of 3-D Metallic Nano-wire

To obtain the dielectric function, we need to compute the matrix element for the transition of electrons from the initial state $\Psi_i(x,y,z)$ to the final state $\Psi_f(x,y,z)$ denoted as $M_{if} = \langle\Psi_f(x,y,z)|x,y,z|\Psi_f(x,y,z)\rangle$ given in Eq. (4.33), the total number of electrons N_{elec}, and the frequency difference $\omega_{i,f}$ in 3-D. In 3-D analysis, the matrix elements occurring along the z-axis are considered in addition to previously derived ones along x- and y-axis. The x-axis and y-axis components have been considered earlier in the 2-D analysis.

$$\psi_i(x,y,z) = \sqrt{\frac{2}{L_x}}\sin\left(\frac{n\pi x}{L_x}\right)\sqrt{\frac{2}{L_y}}\sin\left(\frac{m\pi y}{L_y}\right)\sqrt{\frac{2}{L_z}}\sin\left(\frac{l\pi z}{L_z}\right) \tag{4.49}$$

$$\psi_f(x,y,z) = \sqrt{\frac{2}{L_x}}\sin\left(\frac{(n+\Delta n)\pi x}{L_x}\right)\sqrt{\frac{2}{L_y}}\sin\left(\frac{(m+\Delta m)\pi y}{L_y}\right)\sqrt{\frac{2}{L_z}}\sin\left(\frac{(l+\Delta l)\pi z}{L_z}\right) \tag{4.50}$$

$$M_{if}^x = \int_0^{L_x} dx x\sqrt{\frac{2}{L_x}}\sin\left(\frac{n\pi x}{L_x}\right)\sqrt{\frac{2}{L_x}}\sin\left(\frac{(n+\Delta n)\pi x}{L_x}\right) \tag{4.51}$$

$$M_{if}^y = \int_0^{L_y} dy y\sqrt{\frac{2}{L_y}}\sin\left(\frac{n\pi y}{L_y}\right)\sqrt{\frac{2}{L_y}}\sin\left(\frac{(m+\Delta m)\pi y}{L_y}\right) \tag{4.52}$$

$$M_{if}^z = \int_0^{L_z} dz z\sqrt{\frac{2}{L_z}}\sin\left(\frac{l\pi z}{L_z}\right)\sqrt{\frac{2}{L_z}}\sin\left(\frac{(l+\Delta l)\pi z}{L_z}\right) \tag{4.53}$$

By performing the integrations in closed-form, then expression M_{if} for the 3-D is obtained,

$$M_{if}^{xyz} =$$
$$\frac{L_x L_y L_z}{8}\left\{\text{sinc}^2\left[\left(n+\frac{\Delta n}{2}\right)\pi\right]-\text{sinc}^2\left(\frac{\Delta n\pi}{2}\right)\times\text{sinc}^2\left[\left(m+\frac{\Delta m}{2}\right)\pi\right]-\text{sinc}^2\left(\frac{\Delta m\pi}{2}\right)\right.$$
$$\left.+\times\text{sinc}^2\left[\left(l+\frac{\Delta l}{2}\right)\pi\right]-\text{sinc}^2\left(\frac{\Delta l\pi}{2}\right)\right\}. \quad (4.54)$$

The frequency difference $\omega_{i,f}$ is

$$\omega_{i,f}=\omega_{n,\Delta n;m,\Delta m;l,\Delta l}=\frac{\hbar\pi^2}{2m_e}\left\{\frac{\Delta n(2n+\Delta n)}{L_x^2}+\frac{\Delta m(2m+\Delta m)}{L_y^2}+\frac{\Delta l(2l+\Delta l)}{L_z^2}\right\} \quad (4.55)$$

The total number of electrons N_{elec} and the volume electron density n_{elec} [94],

$$N_{elec}=\frac{L_x L_y L_z K_F^3}{3\pi^2};\quad n_{elec}=\frac{K_F^3}{3\pi^2}, \quad (4.56)$$

where K_F denotes the radius of the particle in K-space or all filled quantum states correspond to grid-points that are within a distance from the origin at Fermi circle or n_f in n-space is the maximum number of filled electron at Fermi level. To compute the dielectric function, the oscillator strength is given as

$$S_{i,f}=\frac{4m_e\omega_{i,f}|M_{i,f}|^2}{\hbar N_{elec}}. \quad (4.57)$$

Hence, the frequency-dependent dielectric function for problems in arbitrary dimension can be computed as

$$\varepsilon(\omega) = 1 + w_p^2 \sum_i \sum_f \frac{S_{i,f}}{\omega_{i,f}^2 - \omega^2 - i\omega\gamma}. \tag{4.58}$$

Writing in non-dimensional form,

$$\varepsilon(\omega) = 1 + \sum_i \sum_f \frac{S_{i,f}}{(\frac{\omega_{i,f}}{w_p})^2 - (\frac{\omega}{w_p})^2 - i(\frac{\omega}{w_p})(\frac{\gamma}{w_p})} \tag{4.59}$$

where ω_p is the plasma frequency, m_e is electron mass, γ is the damping constant, $S_{i,f}$ oscillator strength.

4.5 Numerical Results and Discussion

In this section, the following parameters are used for the simulation of the frequency-dependent dielectric function for metallic nano-wire for silver (Ag). The length of the wire is 50×10^{-9} metres. The real- and imaginary parts of the frequency-dependent dielectric function against wavelength is computed. The following parameters are used for silver in the simulations: $v_f = 1.39 \times 10^6 ms^{-1}$- this is referred to as Fermi velocity , $\omega_p = 1.36 \times 10^{16} rads^{-1}$ for plasma frequency, $\gamma_{bulk} = 0.016$ for the damping constant in eV.

We choose silver as the metallic material due to the availability of reliable data for the material. The behaviour of the dielectric function for the real part is an even function while the corresponding imaginary part of the dielectric function is an odd function as explicated in Figs. $(4.6 - 4.8)$. The imaginary part of the dielectric function exhibits negative and positive

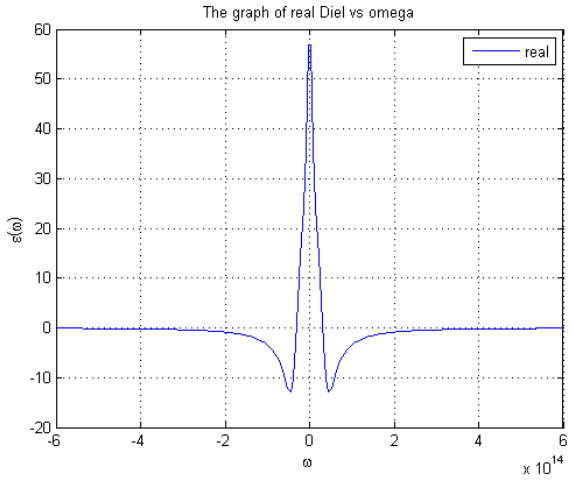

Figure 4.6: The graph of the real part of the dielectric function vs frequency for 1-D

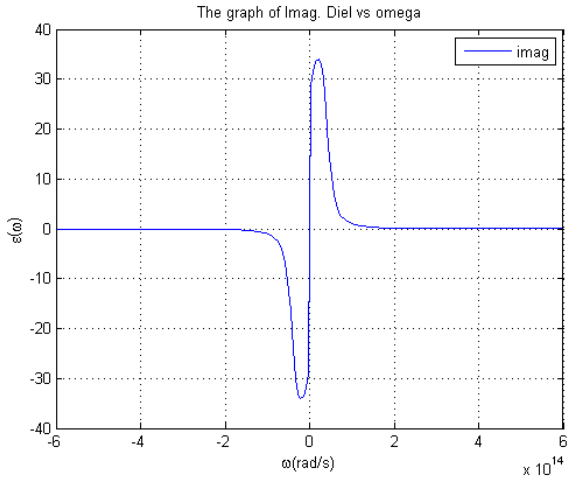

Figure 4.7: The graph of the imaginary parts of the dielectric function vs frequency for 1-D

slopes in certain regions . This (the dielectric function) decays to zero as the frequency tends to plus or minus infinity as shown in Fig. 4.7.

Perhaps, at a point close to operating frequency , the operating frequency ω is greater than the frequency difference $\omega_{i,f}$ giving rise to dips or side lobes for the real part of the the frequency-dependent dielectric function of metallic nano wire. This suggests that different behaviour at different frequency window (low, near and high frequency regions) in

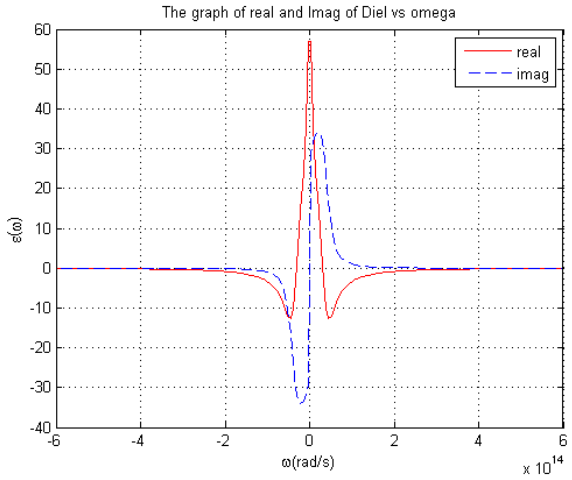

Figure 4.8: The graph of the real and imaginary parts of the dielectric function vs frequency for 1-D

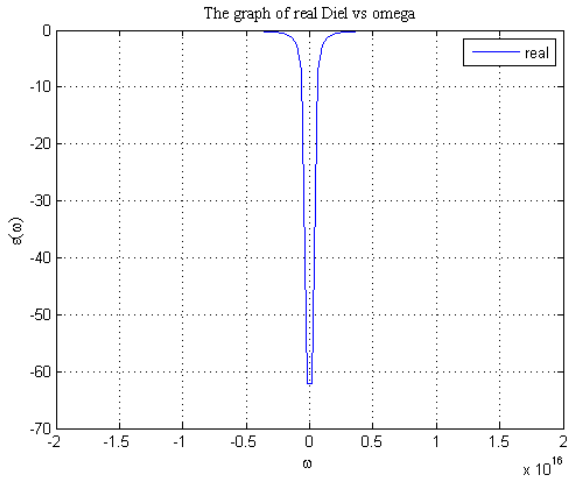

Figure 4.9: The graph of the real part of the dielectric function vs frequency for 2-D

the dielectric function of metallic function as shown in the Fig. 4.6 exists. The graph of the real- and the imaginary parts of the 1D metallic nanowire is shown in Fig. 4.8.

Owing to a change of sign in operating frequency ω and the frequency difference $\omega_{i,f}$, there is a negative shape of the real-part giving rise to dips. Furthermore , due to comparison of frequency at various regions, the real- and the imaginary parts intersect. For $\omega_{i,f} > \omega$, the real-part of $\varepsilon(\omega)$ is positive while for $\omega_{i,f} < \omega$, $\varepsilon(\omega)$ is negative and assumes dips or side

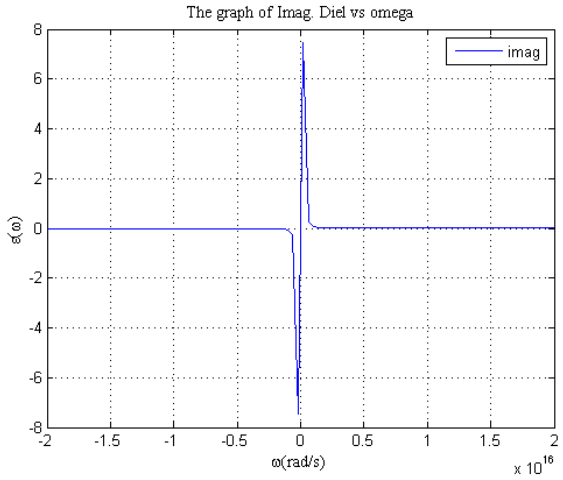

Figure 4.10: The graph of imaginary part of the dielectric function vs frequency for 2-D

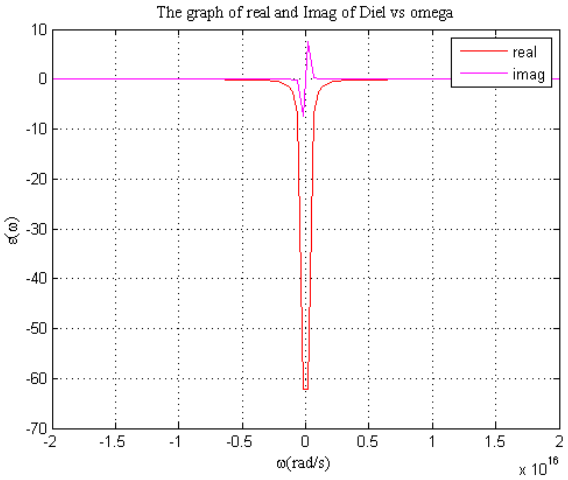

Figure 4.11: The graph of real and imag. parts of dielectric function vs omega for 2-D

lobes as shown in Fig. 4. The Figs. $(4.9 - 4.11)$ depict the real-part, the imaginary part and the dielectric function against operating frequency ω for the 2-D metallic nano wire. There is no dip in the real-part of the dielectric function for the 2-D as observed in 1-D. If multiple resonances exist and are close each other, the overall response will be superposition of the individual resonance which may cause such dips meaning that the electric field (E) and electric displacement field (D) will be 180 out of phase.

4.6 Summary of the Chapter

In this section, we have obtained the quantized energy levels and corresponding eigenfunctions of a free electron inside a metallic structure. We utilized them to derive expressions for the dielectric function of metallic material in 1-, 2-, and 3-D dimensions. However, the numerical result of 3-D metallic nano-wire frequency-dependent dielectric function is not included in this thesis. The Physics-inspired quantum mechanical frequency-dependent dielectric function in this thesis is based on the characteristics of non-interacting electron gas confined within a small and thin metallic structure. Our results provide an intuition on how the quantum phenomena introduce the geometrical parameters into the frequency-dependent dielectric function of a thin metallic geometry changes the eigenfunctions and eigenvalues. The study of these small-scale problems exhibiting quantum phenomena for different shapes is exceptionally crucial for real-world engineering applications such as lasers, quantum computers, quantum communication systems, and transistors, etc. Hence, metallic materials with their distinctive optical properties can offer novel opportunities in the design of the relevant devices and miniaturized electronic and photonic devices for the challenging applications in the 21st century.

Chapter 5

Application of Quantum Models to Geometrical Nanostructures

5.1 Introduction

The advances in the area of nano-optics and surface plasmon resonance have been tremendous in recent years. The metallically-based spherical geometry of tiny and microscopic sizes have drawn attention from scientists and investigators alike. This is owing to their optical, anisotropic and huge viability and plausibility characteristics for instance confinement of optical light, focusing of light, enhancement of fields, field localization in the vicinity of the edges and an increase in absorption with extended wavelength as compared with spherical-structure systems. Hence, these properties and features of the system are expected and envisaged to possess the capability and prospective applications in different areas of engineering namely nano-antennas, transistor, quantum computers, lasers, and quantum

telecommunications system [95–100]. The geometries that will be studied thoroughly in this work are metallic-based cube, cuboid, and spherical nano-particles. The metallic properties of these geometries devolve not only on their material properties but also on shape, size, and so forth. Furthermore, it has been established in the literature that when shapes and sizes of geometrical structures are large, the geometric material features have no basis to depend on one another. But, assuming that the dimensions of the geometrical structure are significantly less than the material mean free path particle (electron), then innate material characteristics such as permittivity, susceptibility, and refractive index will rely on the geometric properties due to effects of confinements of electrons. With additional reduction in the sizes of geometrical structure till they are of electron's wavelength, specific quantum phenomena will be revealed. Conventionally, these effects cannot be construed and expounded except the theory of quantum mechanics is employed. The extended random phase approximation was utilized for the quantum size effects in thin films and metallic particles in [81],[95],[96]. It is used only for a single free electron model for tiny particles and therefore, the electronic polarizability of the metallic film was obtained via closed-form approach for the optical characteristics in the plasma resonance region. The inhomogeneous quantum dots of the excitons were examined in a robust confinement domain [97]. These semiconductor particles have an internal structure, with an interior core that functions as a repulsive potential for the electrons utilizing a macro-scale model for the interpretation of the permittivity inconsistency at the boundary points. Furthermore, in [98], the effects of the plasmon line shape of metallic nano-shells were investigated in the region of 100 nm to 250 nm in size for non-homogenous broadening owing to the shell size and core spreading.

Additionally, the scattering effect by a dimer (also known as two spherical nano-particles) was examined using a system-based approach model. This scheme employs the translation features alongside the quasi-static approximation for spherical harmonics to capture the features of the two spherical nanoparticles completely. The change in size effects on the light optical performance of extremely-diminutive metallic particles was explored. In the range exceeding nano-metric scale, the response of the nano-particles as a result of optical light deeply relies on the size changes due to changes in the allowable electronic transitions [100]. Besides, in [77], the frequency-dependent dielectric function of spherical shells with quantum effects as a function of size was investigated; however, the coupling of two or more spherical-based nanoparticles was not considered. Thus, other optical properties are taken into consideration [101–103] in which the effect of nonlinearity and linearity of optical properties was dealt with. Within the frame of closed-form wavefunctions and arithmetical discretized energy levels, the subject of linear and nonlinear absorption coefficients of spherical shells was hypothetically examined. In [104] and [105], the oscillation effect of Aharonov-Bohm for magneto-light properties in semiconductor particles for nonhomogeneous one and the qualitative measurement of single-electron wells for the measurement and determination of nano-particles shape using Wuff principle were investigated, respectively.

5.2 Frequency-dependent Dielectric Function for Cubic Structure

In this section, the cubical geometry will be the subject of discourse and how to compute and study the effects of size-dependent damping constant on the overall of frequency-dependent dielectric function and the absorption. Firstly, in [106], it was highlighted that the continued electronic band in the conduction form of a metallic material should split up into distinct and discernible individual states when the sizes of the metallic material turn out to be very small. Furthermore, in [107], the formulation of this problem of electronic conduction bands was investigated quantitatively and ever since, extensive efforts have been made to examine the effects of quantum size. Such impacts have been undoubtedly observed in fine conductive thin-films [108]. In recent times, the absorption range for the far-infrared of metallic particles has been demonstrated to contain a system that may, in addition, turn out to have or exhibit a quantum size effect [109].

Although several remarkably meticulous measurements of electron loss and visible absorption on tiny particles in the spectral range of the surface plasmon resonance have exhibited no direct or immediate effect of quantum size. The most far-reaching impact noted on the size reduction of the metallic particle up to $10\mathring{A}$ was the widening of the surface plasmon resonance top. This widening can be characterized numerically by a reduction of particle mean free path length owing to scattering away the particle on the surface [110–117] . In practice, this macroscopical description appears to suit the data most importantly than the linear response by the quantum mechanical concepts [81], [118], [119].

Therefore, it is the objective of this study to give additional information in terms of a quantum mechanical formulation. By adding the size effect to the damping constant and the suitability of the formulation in the nano region, striking results are obtained which give significant intuition and understanding into, in particular, surface plasmon absorption and frequency-dependent dielectric function for the cubical geometry.

5.2.1 Quantum Mechanical Approach for a Single Electron Gas in a Cubical Nano-particle

In Chapter four, the subject of classical models has been explained in detail. Here, we will build on the existing model to apply it to the cubical geometry. Further effects of size can be obtained by modifications in the frequency-dependent dielectric function of the metallic material itself. Considering the structure of the Drude model dispersion relation,

$$\varepsilon(\omega) = \varepsilon_\infty - \frac{\omega_p^2}{\omega^2 - i\gamma\omega}, \tag{5.1}$$

The desired modifications can be implemented. For metallic particles in which their size is lower than $100\mathring{A}$, scattering of the particles away from the surface of the particle allows the contribution to the overall damping constant be modelled as,

$$\gamma = \gamma_{bulk} + \frac{v_F}{L}. \tag{5.2}$$

Here, γ, v_F, and L denote the damping constant which is the inverse of the lifetime of the particle, Fermi velocity of the particle, and the length of the particle that depends on the particle's size, respectively.

Having stated this, the most basic quantum mechanical model that can be utilized to characterize the problem at hand is that of loose and mobile electrons in a cubical finite square well with limitless sides [90], [81]. Therefore, for the single-electron wave functions of this type are put in a compact form

$$\psi_{n,m,l}(x,y,z) = \sqrt{\frac{2}{L_x}}\sin\left(\frac{n\pi x}{L_x}\right)\sqrt{\frac{2}{L_y}}\sin\left(\frac{m\pi y}{L_y}\right) \times \sqrt{\frac{2}{L_z}}\sin\left(\frac{l\pi z}{L_z}\right). \tag{5.3}$$

For a cubical geometry, let $L(= L_x = L_y = L_z)$ denote the length of one edge of the potential well and quantum numbers n, m, and l are positive integers. Thus,

$$\psi_{n,m,l}(x,y,z) = \sqrt{\frac{8}{L^3}}\sin\left(\frac{n\pi x}{L}\right)\sin\left(\frac{m\pi y}{L}\right)\sin\left(\frac{l\pi z}{L}\right). \tag{5.4}$$

Hence, for each wavefunctions, the associated energy levels are succinctly put as:

$$E_{n,m,l} = E_0(n^2 + m^2 + l^2) \tag{5.5}$$

with $E_0 = \pi^2\hbar^2/(2mL^2)$ being energy that depends only on the edge length of the cubical geometry. Therefore, the frequency-dependent dielectric function of a single metallic particle

for the model at hand can be expressed as:

$$\varepsilon(\omega) = \varepsilon_\infty + \frac{\omega_p^2}{N} \sum_i \sum_f \frac{s_{if}(F_i - F_f)}{\omega_{if}^2 - \omega^2 - i\omega\gamma_{if}} \tag{5.6}$$

in which ε_∞ has been associated with the contribution from interband, N represents the number of electrons confined to the cubical box and ω_p denotes the plasmon frequency. The frequency ω_p being a function of electronic density n_e, the charge e, and the effective mass $m*$ is expressed as $\omega_p^2 = 4\pi n_e e^2/m*$. Additionally, F_i , F_f and γ_{if} [120] represent the Fermi-Dirac distributions for the initial and final electron states, and the damping constant for the electron dipole transition from the initial state i to the final state f, respectively. The usual definition for oscillator strength for the particle transition from one state to another is

$$s_{if} = \frac{2m\omega_{if}}{\hbar} |\langle f|z|i\rangle|^2. \tag{5.7}$$

The change in the transition frequencies from the initial state to final state for which the polarization is assumed to be along the z-axis can be expressed as:

$$\omega_{if} = \frac{E_f - E_i}{\hbar} = \frac{E_0}{\hbar}\left[(n_f^2 + m_f^2 + l_f^2) - (n_i^2 + m_i^2 + l_i^2)\right] \; = \frac{E_0}{\hbar}\Delta l(2l + \Delta l) \tag{5.8}$$

where the following assumptions have been made: that $n_f = n_i$, $m_f = n_i$, $l_i = l$ and $l_f = l + \Delta l = l_i + \Delta l$. By considering transitions of electron only in the z -axis direction, the oscillator strength can be cast in this form.

$$s_{if} = \frac{2mE_0\Delta l(2l+\Delta l)}{\hbar}|\langle f|z|i\rangle|^2. \tag{5.9}$$

Assume the initial- and final states wavefunctions of the electron to be, respectively:

$$\left.\begin{aligned}\psi_{n_i,m_i,l_i}(x,y,z) &= \sqrt{\frac{8}{L^3}}\sin\left(\frac{n_i\pi x}{L}\right)\sin\left(\frac{m_i\pi y}{L}\right)\sin\left(\frac{l_i\pi z}{L}\right)\\ \psi_{n_f,m_f,l_f}(x,y,z) &= \sqrt{\frac{8}{L^3}}\sin\left(\frac{n_f\pi x}{L}\right)\sin\left(\frac{m_f\pi y}{L}\right)\sin\left(\frac{l_f\pi z}{L}\right)\end{aligned}\right\} \tag{5.10}$$

The following expression is used to evaluate the matrix element and oscillator strength of the particle:

$$\langle f|z|i\rangle = \int_0^L dx \underbrace{\sin\left(\frac{n_i\pi x}{L}\right)\sin\left(\frac{n_f\pi x}{L}\right)}_{\Gamma_a(x)}\int_0^L dy\underbrace{\sin\left(\frac{m_i\pi y}{L}\right)\sin\left(\frac{m_f\pi y}{L}\right)}_{\Gamma_b(y)} \times\int_0^L dzz\underbrace{\sin\left(\frac{l_i\pi z}{L}\right)\sin\left(\frac{l_f\pi z}{L}\right)}_{\Gamma_c(z)} \tag{5.11}$$

The following trigonometric relationships can be used:

$$\left.\begin{aligned}\sin(\alpha)\sin(\beta) &= -\frac{1}{2}\cos(\alpha+\beta)+\frac{1}{2}\cos(\alpha-\beta)\\ \int_0^L dzz\cos(\theta z) &= L^2\,\mathrm{sinc}(\theta L)-\frac{L^2}{2}\,\mathrm{sinc}^2(\frac{\theta L}{2})\end{aligned}\right\} \tag{5.12}$$

By substituting Eqs. (5.9) and (5.11) into (5.10), with individual integral being carried out, then, Eq.(5.10) becomes:

$$\langle f|z|i\rangle = L\delta_{m_i,m_f}\delta_{n_i,n_f}\left\{\delta_{l_i,l_f}+\frac{1}{2}\,\mathrm{sinc}^2\left[\frac{\pi(l_i+l_f)}{2}\right]-\frac{1}{2}\,\mathrm{sinc}^2\left[\frac{\pi(l_i-l_f)}{2}\right]\right\} \tag{5.13}$$

Table 5.1: Case I: $l_i \neq l_f$

l_i	l_f	$l_i - l_f$	$l_i + l_f$	M	N
$\Theta^{l_i=1}$	$\Theta^{l_f=3}$	$E^{l_i-l_f=-2}$	$E^{l_i+l_f=4}$	0	0
$\Theta^{l_i=1}$	$E^{l_f=2}$	$\Theta^{l_i-L_f=-1}$	$\Theta^{l_i+l_f=3}$	1	1
$E^{l_i=2}$	$\Theta^{l_f=3}$	$\Theta^{l_i-l_f=-1}$	$\Theta^{l_i+l_f=5}$	1	1
$E^{l_i=2}$	$E^{l_f=4}$	$E^{l_i-l_f=-2}$	$E^{l_i+l_f=6}$	0	0

Table 5.2: Case II: $l_i = l_f$

l_i	l_f	$l_i - l_f$	$l_i + l_f$	M	N
$\Theta^{l_i=1}$	$\Theta^{l_f=1}$	$\Theta^{l_i-l_f=0}$	$E^{l_i+l_f=2}$	1	0
$E^{l_i=2}$	$E^{l_f=2}$	$\Theta^{l_i-l_f=0}$	$E^{l_i+l_f=4}$	1	0

Here, $|i\rangle$ and $|f\rangle$ are real-valued parameters describing the initial and final states of the electron. Furthermore, m_i, m_f, n_i, n_f, l_i and $l_f \in \mathbb{N}$ and $(m_i{+}m_f)$, $(n_i{+}n_f)$, $(l_i{+}l_f) \in \mathbb{N} \neq 0$. Note also that the Tables 5.1 ans 5.2 depict the two different cases for the validity of Eq. (5.12):

$$\left.\begin{aligned} \operatorname{sinc}[\pi(l_i + l_f)] = 0 \\ \operatorname{sinc}[\pi(m_i + m_f)] = 0 \\ \operatorname{sinc}[\pi(n_i + n_f)] = 0 \\ \operatorname{sinc}^2[\pi(l_i + l_f)] = 0 \\ \operatorname{sinc}^2[\pi(l_i + l_f)] = 0 \\ \operatorname{sinc}^2[\pi(m_i + m_f)] = 0 \\ \operatorname{sinc}^2[\pi(n_i + n_f)] = 0 \end{aligned}\right\} \quad , \tag{5.14}$$

where $M = \sin^2\left[\frac{\pi(l_i-l_f)}{2}\right] / \left[\frac{\pi(l_i-l_f)}{2}\right]$, $N = \sin^2\left[\frac{\pi(l_i+l_f)}{2}\right] / \left[\frac{\pi(l_i+l_f)}{2}\right]$, E stands for even number, and Θ signifies odd number.

In general, it is assumed and verified that when $l_i \neq l_f$ and at least one of the l_i, l_f must be odd number before it can be valid. Therefore, if $l_i \neq l_f$ and one of $l's$ is odd number, using $l_i = l$, $l_f = l + \Delta l$, $l_i + l_f = 2l + \Delta l$ and $l_i - l_f = -\Delta l$, then Eq.(5.12) reduces to:

$$\langle f|z|i\rangle = -\frac{8L}{\pi^2}\delta_{m_i,m_f}\delta_{n_i,n_f}\left[\frac{l(l+\Delta l)}{\Delta^2 l(2l+\Delta l)^2}\right] \tag{5.15}$$

By taking the square of the matrix element of the electron denoted as $\langle f|z|i\rangle$ leads to:

$$|\langle f|z|i\rangle|^2 = \frac{64L^2}{\pi^4}\delta_{m_i,m_f}\delta_{n_i,n_f}\left[\frac{l^2(l+\Delta l)^2}{\Delta^4 l(2l+\Delta l)^4}\right]. \tag{5.16}$$

Thus, by substituting Eqs. (5.8) and (5.15) into (5.7), the oscillator strength can be expressed as:

$$s_{i,f} = \frac{64}{\pi^2}\delta_{m_i,m_f}\delta_{n_i,n_f}\left[\frac{l^2(l+\Delta l)^2}{\Delta^3 l(2l+\Delta l)^3}\right] \tag{5.17}$$

The following assumptions are made to simplify the problem at hand:

1. The initial states $|i\rangle$ should correspond to a state within the surface of Fermi while final $|f\rangle$ states fall outside the Fermi surface at zero temperature ($T = 0°\mathrm{K}$)

2. Due to the symmetry of the cubical geometry, the horizontal transition along z-axis should be taken into account.

3. The quantum number along the z-axis direction changes by odd numbers; i.e., $\Delta l = 1, 3, 5, 7, 9, ...$

4. The major part of to the overall frequency-dependent dielectric function allowable or acceptable transition relies on the initial and final values of l only.

5. The difference in Fermi-Dirac statistical functions for initial- and final states of the elctrons is assumed to be at zero temperature (fully occupied at valence band and empty at conduction band $F_i - F_f = 0$).

The degeneracy factor including the spin effect is considered in this formulation. Also, it is assumed that the geometry is plane; i.e., 2-D allows us to use the area of a circle and not sphere in 3-D and to compute the degeneracy factor,

$$D_F = \frac{\pi(l_f^2 - l_i^2)}{2} = \frac{\pi(l + \Delta l)^2 - \pi l^2}{2} = \frac{\pi}{2}(2l + \Delta l)\Delta l. \tag{5.18}$$

By equating the volume of a cubical geometry and the volume of the nano-particle to establish the relationship between the cube edge length and the radius of the nano-particle, it gives:

$$R = L\sqrt[3]{\frac{3}{4\pi}} \quad , \tag{5.19}$$

where R is the radius of the nano-metallic particle, L denotes the length of the box, N represents the number of occupied (valence) electrons in each cubical geometry not forgetting $N = l_F^3$, n_e is the electrons density, l_F is the point of intersection of the l-axis on the Fermi sphere. Consequently, the oscillator strength as a function of l and Δl only can be cast

compactly by multiplying Eq. (5.16) by Eq. (5.7) as:

$$S_{l,\Delta l} = \frac{32}{\pi l_F^3} \frac{l^2(l+\Delta l)^2}{\Delta^2 l(2l+\Delta l)^2} \tag{5.20}$$

Finally, Eq. (5.6) can be expressed as:

$$\varepsilon(\omega) = \varepsilon_\infty + \omega_p^2 \sum_{\Delta l=1}^{1,3,5,\ldots} \sum_{l=1}^{l_F} \frac{S_{l,\Delta l}}{\omega_{l,\Delta l}^2 - \omega^2 - i\omega\gamma_{l,\Delta l}} \tag{5.21}$$

The frequency-dependent absorption coefficient can be computed by substituting Eq. (5.20) into the average frequency-dependent dielectric function as obtained in [96], [121–123] to give:

$$\varepsilon^{Ave}(\omega) = \varepsilon_m \frac{\varepsilon(\omega)(1+2f) + 2\varepsilon_m(1-f)}{\varepsilon(\omega)(1-f) + \varepsilon_m(2+f)} \tag{5.22}$$

$$\kappa(\omega) = \frac{\omega \varepsilon_{Im}^{Ave}}{c\varepsilon_m^{\frac{1}{2}}} \tag{5.23}$$

Hence, f, ε_m, c and ε_{Im}^{Ave} denote the fractional volume of the nanoparticles, dielectric medium ε_m, speed of light, and average frequency-dependent dielectric function, respectively.

5.3 Numerical Simulation Results and Discussion of Various Structures

This section presents the numerical simulation results of cubed, cuboid and spherical nanostructures.

5.3.1 Numerical Computation Results for Cubic Particles

In this study, we have computed the real- and imaginary parts of the frequency-dependent dielectric function $\epsilon_1(\omega)$ and $\epsilon_2(\omega)$, respectively, as depicted in Figs. 5.1 and 5.2, using equation (20). A silver-cube metallic nanoparticle has been assumed which is one of the good candidates for the design of small scaled plasmonic devices which has 4096 electrons. In Fig. 5.1, we do not include the effect of damping constant contribution for the size of the particle. In Fig. 5.2, we incorporate the size-dependence of the damping constant effect.

For the transition considered in this work,the following parameters are used for the simulation results: $\gamma = 0.016eV$, $\omega_p/\omega_F = 1.59$, $\epsilon_\infty = 4.0$, $\Delta l = 1$, 3 , f =0.01 and 5, $L = 40 \times 10^{-10}$m and $E_F = 5.5eV$. Hence, the plasma vibration resonance of Ag appears in a zone of great dispersion owing to effect of interband transitions. These transitions must be accounted for by value of ϵ_∞.

Using Eq. (5.20), the real- and imaginary parts of the frequency-dependent dielectric function in terms of the energy of the light incident energy for the nano-particle with $L = 1$ to 10 nm. The relationship between the volume of the cubical geometry and the volume of the nano-particle enables us to establish a relationship between the length L of the box (cube) and the radius (R) of the nano-particle, $R = L\sqrt[3]{\frac{3}{4\pi}}$ as expressed in Eq.(5.8) compared with the Drude model. It is observed that the frequency-dependent dielectric function predicted by the quantum mechanical model differs remarkably with the results obtained by classical means in the region of this study. The major discrepancy observed is that both the real and imaginary parts of $\varepsilon(\omega)$ demonstrate a non-monotonic response based on the quantum

mechanical model, against the flat or monotonous behaviour by employing conventional Drude model. Nevertheless, as the length of the box attains the maximum of 10 nm or higher values as the case may be, the accord with the classical approach is excellent.

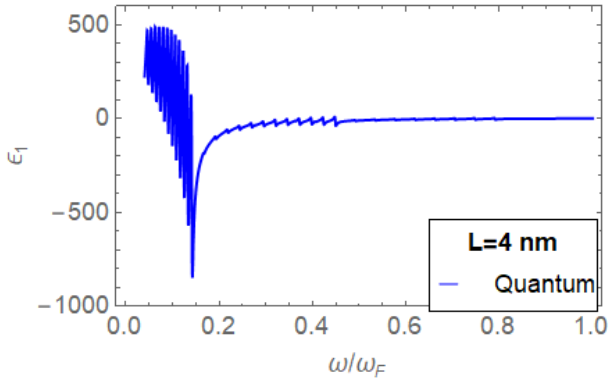

(a) The graph of real-part of frequency-dependent dielectric function ($\varepsilon(\omega)$)

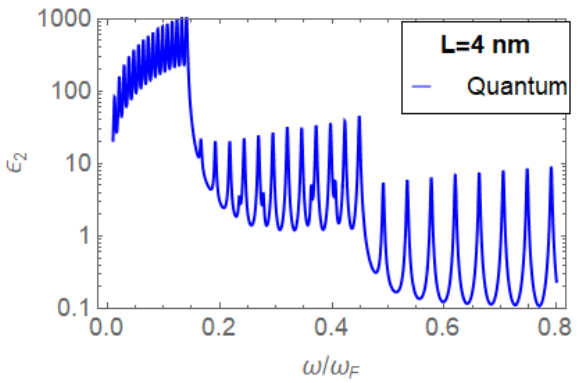

(b) The graph of imaginary part of frequency-dependent dielectric function ($\varepsilon(\omega)$)

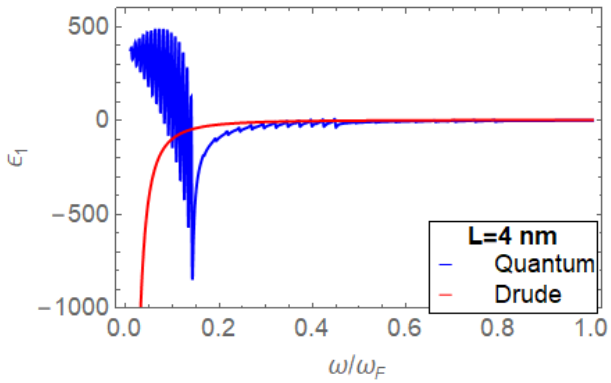

(c) The graph of Drude and quantum models of real parts ($\varepsilon(\omega)$) with constant γ

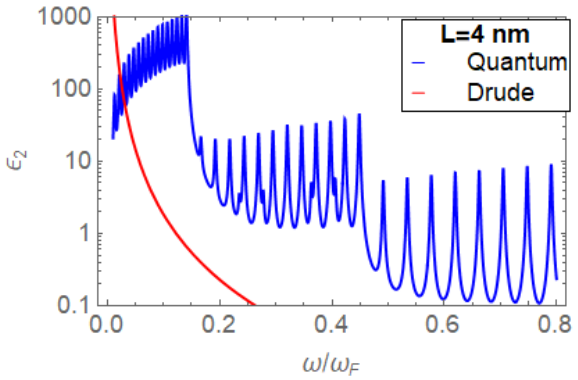

(d) The graph of Drude and quantum models of imaginary parts ($\varepsilon(\omega)$) with constant γ

Figure 5.1: Various plots of dielectric function versus ω/ω_F with constant γ

In our study, we incorporate experimentally-fitted expression to determine this value rather than using the parameter used in [96]. It should be noted and stated clearly that the structure in the spectra of $\epsilon_1(\omega)$ and $\epsilon_2(\omega)$ matches with transitions form states with

various quantum numbers l, the steps show the high frequency boundary for transitions with a particular Δl.

The significance of $\Delta l = 3, 5$ and the algorithmic consequences thereof will be essentially observed for the size of particles in the range of 1 nm to 10 nm. The procedures are the quantitative of cube-shaped geometry of particles and alterations in the other geometries such as spheres, cuboid and so on. The graph of absorption is depicted in Fig. 111. The absorptivity appearing in the range between 0.32 and 0.83 of the energy at Fermi level comprises significant micro-structure which, if observed empirically, would provide conclusive evidence of quantum-size impacts. Furthermore, there are similar steps previously considered for real-and imaginary parts of $\varepsilon(\omega)$. The steps are specific features of cube-shaped or cubic particles and in a way affected the geometry for a cuboid, and so on. The absorption coefficient at the first step ($\Delta l = 3$) below the primary absorption around 0.6 E_F is about two orders of length less than the main plasma apex itself. The second step ($\Delta l = 1$) for the absorption is extremely weak to be visible in the figure and about two orders less than the first ($\Delta l = 2$).

In Figs. 5.1(a-d),the calculated Drude model with damping constant, real- and imaginary parts of the the dielectric function without the damping constant for a size of 40nm are depicted, respectively. Figures.5.2(b-c) depict the computed real- and imaginary parts of the quantum adjusted frequency-dependent dielectric function (QAFDDF) of silver cubical nanopartiles for various widths or sizes spanning from 1nm to 10nm. It is observed from the real- and imaginary parts of the corrected quantum frequency-dependent dielectric function converge to those of bulk model of Drude as the size is decreased. Moreover, it is found

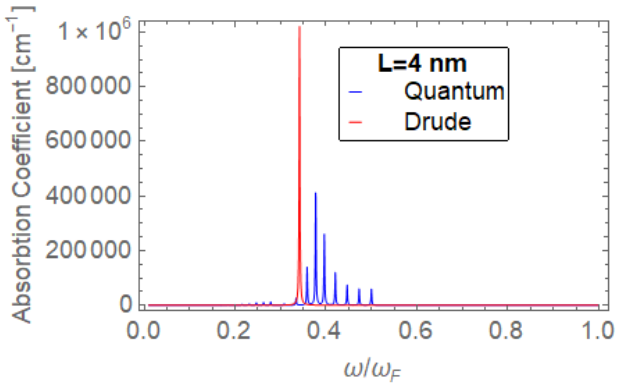

(a) The graph of frequency-dependent absorption coefficient with constant γ

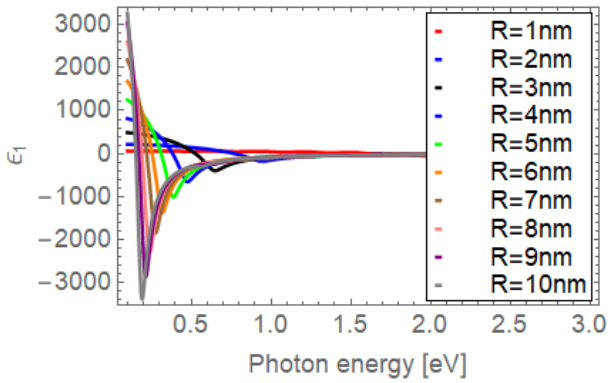

(b) The graph of real part of frequency-dependent dielectric function $\varepsilon(\omega)$ with varying size dependent γ

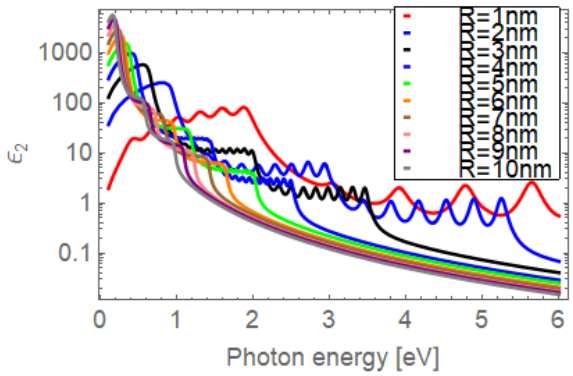

(c) The graph of imaginary part of frequency-dependent dielectric function ($\varepsilon(\omega)$) with varying size dependent γ

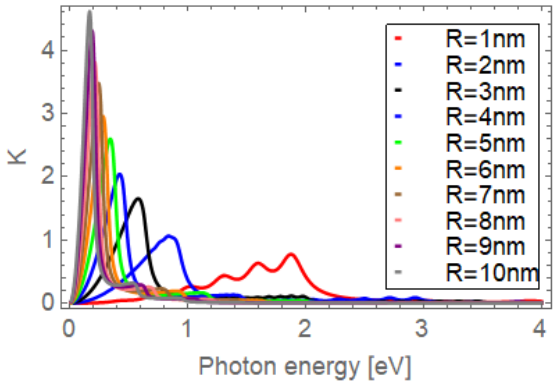

(d) The graph of frequency-dependent absorption coefficient with varying size dependent γ

Figure 5.2: Various plots of dielectric function and absorption coefficient versus photon energy in eV with constant and varying size dependent γ

that the QAFDDF deviates significantly from the bulk model(increased) at long wavelength region while they join into the latter at short wavelength region indicating importance as for which to examine the effects due to the quantum phenomenon for the design of small-scale plasmonic devices. Furthermore, the Figs. 5.2(a) and (d) show the graphs of the frequency dependent absorption coefficient without and with damping constant for a respective photon energy, respectively. In addition, we observe that the dielectric function predicted by

quantum-based model differs remarkably and markedly from the classical-based results in the range of study. The principal disparity is that both the $\Re e\left\{\varepsilon(\omega)\right\}$ and $\Im m\left\{\varepsilon(\omega)\right\}$ show the same behaviour based on quantum model against the unvaried response using classical Drude model. Although as the length attains the limit of 10nm or 16nm, the agreement with the classical based description is excellent.

5.4 Frequency-dependent Dielectric Function for Cuboid Particles

In this section, a similar geometry named cuboid to the cube studied in the previous section is considered. The cuboid has slightly different geometry due to the unequal sides. The wavefunction for a single particle in a cuboid can be expressed as:

$$\psi_{n,m,l}(x,y,z) = \sqrt{\frac{2}{L_x}}\sin\left(\frac{n\pi x}{L_x}\right)\sqrt{\frac{2}{L_y}}\sin\left(\frac{m\pi y}{L_y}\right) \times \sqrt{\frac{2}{L_z}}\sin\left(\frac{l\pi z}{L_z}\right) \tag{5.24}$$

For a general cuboid, let $L \neq L_x \neq L_y \neq L_z$ denote the lengths of the edges of the potential well and n, m, and l be positive quantum integers. Thus,

$$\psi_{n,m,l}(x,y,z) = \sqrt{\frac{8}{L_x L_y L_z}}\sin\left(\frac{n\pi x}{L_x}\right)\sin\left(\frac{m\pi y}{L_y}\right)\sin\left(\frac{l\pi z}{L_y}\right). \tag{5.25}$$

Consequently, the eigenenergy corresponding to $\psi_{n,m,l}(x,y,z)$ becomes,

$$E_{n,m,l} = E_0 \left[n^2 + \left(\frac{mL_x}{L_y} \right)^2 + \left(\frac{mL_x}{L_z} \right)^2 \right] \tag{5.26}$$

with $E_0 = \pi^2\hbar^2/2mL_x^2$ being energy that depends only on the length of the arbitrary selected side of the cuboid. Furthermore, it is assumed that the direction of polarization is along x-axis. The change in the transition frequencies from the initial state to final state for which the polarization in this work is taken to be along z-axis can be expressed as:

$$\omega_{n,\Delta n;m,\Delta m;l,\Delta l} = \frac{E_f - E_i}{\hbar} = \frac{\hbar^2\pi^2}{2m} \left[\frac{(2n+\Delta n)\Delta n}{L_x^2} + \frac{(2m+\Delta m)\Delta m}{L_y^2} + \frac{(2l+\Delta l)\Delta l}{L_z^2} \right] \tag{5.27}$$

where the following assumptions have been made: that $n_f \neq n_i$, $m_f = m_i$, $l_i = l_f$ and $n_f = l + \Delta n = n_i + \Delta n$. By considering transitions of electron only in the z -axis direction, the oscillator strength can be cast in this form. The number of particles, the matrix elements, and the degeneracy factor are expressed, respectively, in compact form as:

$$\left.\begin{aligned} N &= \frac{\pi L_y L_z}{3L_x^2} n_F^3 \\ \langle f|x|i\rangle &= \frac{4L_x}{\pi^2}\delta_{\Delta m,0}\delta_{\Delta l,0} \left\{ \frac{n(n+\Delta n)[(-1)^{\Delta n}-1]}{\Delta^2 n(2n+\Delta n)^2} \right\} \\ D_F &= \frac{\pi(n_f^2 - n_i^2)}{2} \frac{L_y L_z}{L_x^2} = \frac{\pi L_y L_z}{4L_x^2}(2n+\Delta n)\Delta n \end{aligned}\right\} \tag{5.28}$$

With further algebraic manipulations, the oscillator strength along the x-axis direction can be expressed as:

$$S_{n,\Delta n} = \frac{6L_y^2[-2\sin(\frac{\Delta n}{2})]}{\pi L_x^2 n_F^3} \frac{n^2(n+\Delta n)^2}{\Delta n(2n+\Delta n)} \tag{5.29}$$

The directions y and z can be treated analogously, by adequately choosing the lengths (L_x, L_y, L_z) and the indices (m, n, l). Hence, by substituting Eq.(5.28) into Eq. (5.6), the frequency-dependent dielectric function for the cuboid can be computed. The next subsection is devoted to the discussion of the numerical results.

5.4.1 Results and Discussion for Cuboid Particles

In this section, the results of cuboid geometry will be presented and discussed. Figures 5.3(a-d) represent the plots of the Drude and Quantum models for the real-and imaginary parts, respectively. It can be observed that the real-and imaginary parts of the Drude model at $R = 4$ nm show a rising and exponential decay and converge as it tends to zero as clearly depicted in Figs. 5.3 (a and b). The same observation cannot be said of the Quantum model which shows a dip around 0.10 on the ω/ω_F axis for the imaginary part and for the real part the two dips occur around 0.15 and 0.32. This is the effect of the confinement on the optical response.

Furthermore, Figs. 5.4(a-c) show the results of the real-, imaginary parts and absorption coefficient plotted in the same graph for the sake of comparison. It can be inferred that the real-part of the quantum model shows a dip as a result of the values quantum numbers; i.e, $l = 1, 3, 5$ and this cannot be observed in the case of Drude model. Hence, this can be adduced to the effect of confinement on the optical response of the quantum model.

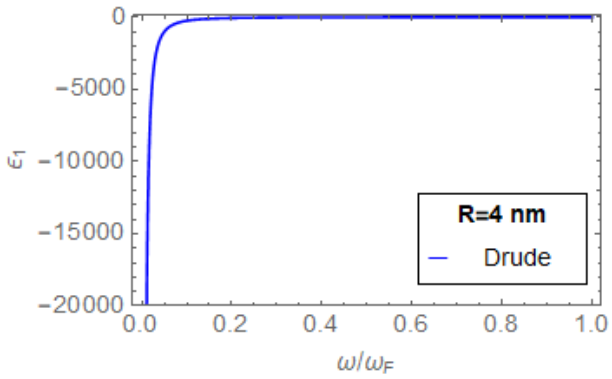

(a) The graph of real part of Drude model vs ω/ω_F

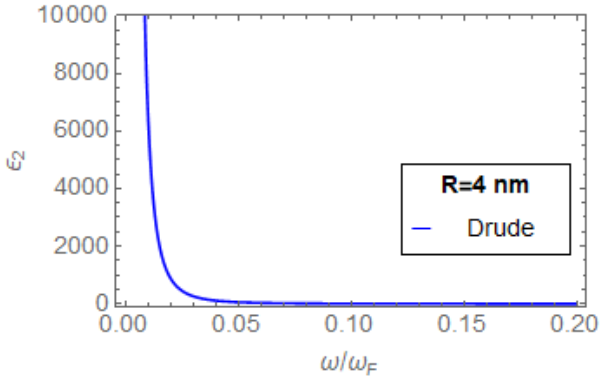

(b) The graph of imaginary part of Drude model vs ω/ω_F

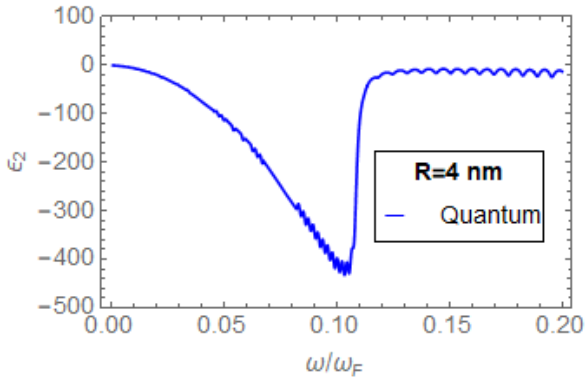

(c) The graph of imaginary part of quantum model vs ω/ω_F

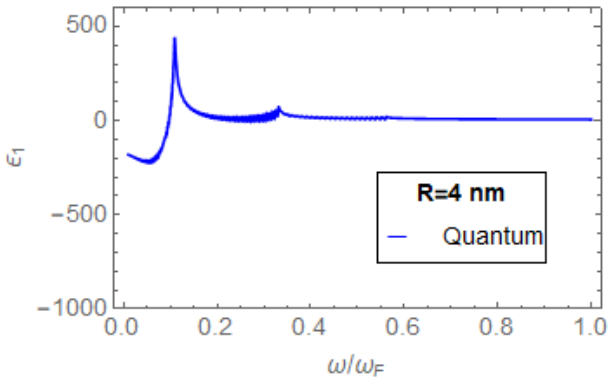

(d) The graph of real-part of quantum model vs ω/ω_F

Figure 5.3: Plots of the real- and imaginary parts for Drude and quantum models of the dielectric function vs ω/ω_F

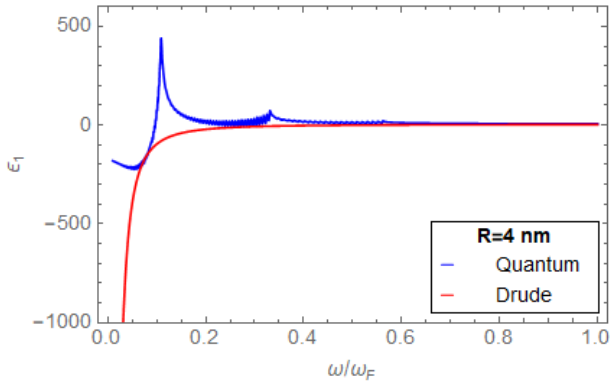

(a) The graph of real part of Drude and quantum models vs ω/ω_F

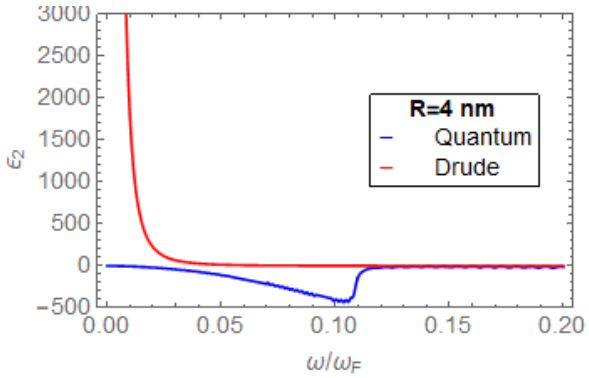

(b) The graph of imaginary part of Drude and quantum models vs ω/ω_F

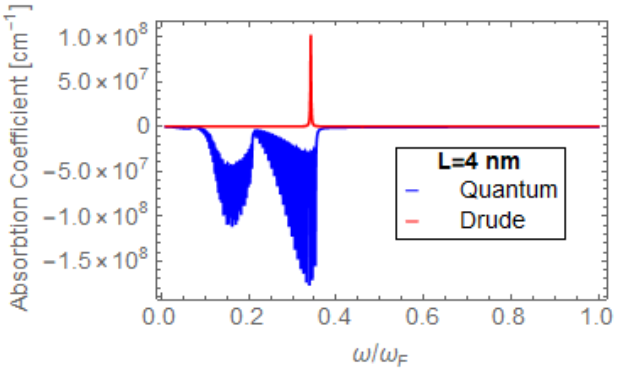

(c) The graph of absorption of Drude and quantum models vs ω/ω_F

Figure 5.4: Plots of the real and imaginary parts for Drude and quantum models dielectric function with absorption vs ω/ω_F

Moreover, Figs.5.5(a-c) display the results of the real-, imaginary parts and absorption coefficient for the various sizes of the nano-particles ranging from 1 nm to 6 nm. There is a blue-shift as the particle's size reduces and a consecutive oscillation occurs for the various sizes of nano-particle.

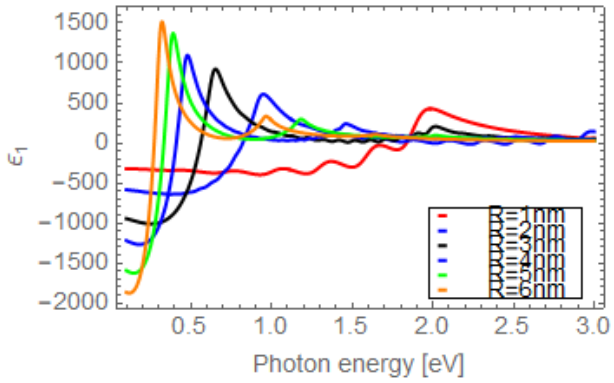

(a) The graph of real-part of quantum model vs energy (eV)

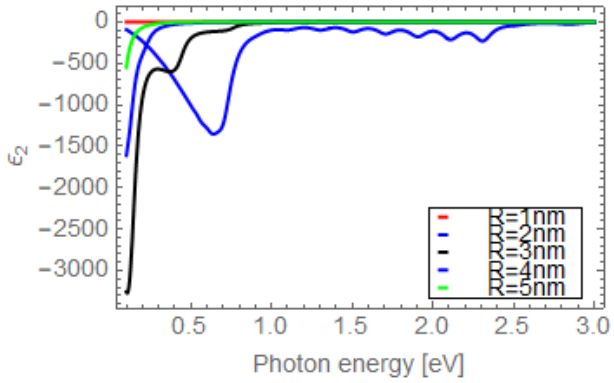

(b) The graph of imaginary part quantum model vs energy (eV)

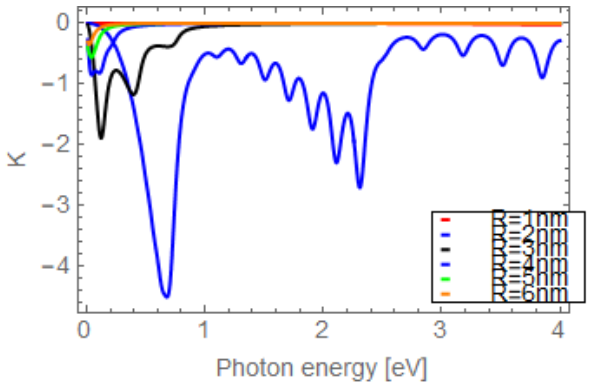

(c) The graph of absorption coefficient vs energy (eV)

Figure 5.5: Plots of the real and imaginary parts for Drude and quantum models dielectric function with absorption vs ω/ω_F

5.5 Frequency-dependent Dielectric Function for Spherical Nano-particles

In the present section, the analysis of the significance of an explanation of electronic changes in minute nanoparticles via the frequency optical response to tiny shifts of size in devices in sub-nanometres region. We provide the computations of the optical response of such systems by employing the rigorous eigenvalues and their corresponding wavefunctions for nanospherical particles with diametres exceeding 10 nm, to achieve the frequency-dependent dielectric function under various conditions of confinement. The major objective is to utilize the resulting frequency-dependent dielectric function to compute the spectral absorption of a single electron restricted in a spherical geometry in two instances: i) an infinite spherically-based restriction and ii) a finite spherically-based constraint, in which, the parameter of the depth of the wells is computed after the adjustment of the number of atoms that consisted of every sphere, thus, the dipole matrix elements and the energies provide a more precise or exact information of the response via optical means. Furthermore, the widely-used numerical scheme Finite Element Method (FEM) could be employed to compute the frequency-dependent dielectric function by solving the Maxwell's equations to determine the electric field enhancement in systems involving general geometries. However, in this study, our focus is on the dielectric function and absorption coefficient of small spherical particles.

5.5.1 Motivation

The phrase "localization of surface plasmons" or "localized surface plasmon polaritons" in the domain of nano-particles is a matter of thorough examination due to strong scattering and absorption properties they induce in sub-wavelength systems. These characteristics depend on the size,material type, shape, refractive index or shape of the circumferential material [124]. Every parameter is worthy of being investigated for adequate description of the behaviour of optical response in the nano-region. Most computations carried out usually employ model proposed by Mie [125]. Mie's method results in sound agreement with the experimental data involving nano-particles up till maximum size of 10 nm by utilizing the optical constant parameters provided by Johnson and Christy [75]. In the case of small particles, this scheme realizes inadequate agreement, and more particularly, when it comes to sizes of particles in the region of 1 nm to 10 nm, the surface plasmons become increasingly crucial in comparison with the volume of response thereby significantly affecting the collection of modes of localized particles at the surface domain. On the contrary, the quantum effects are substantially significant because of the particles which might be able to overflow the particle through limited confinement, and fascinating quantum phenomena emerge for the structures in sub-nanometres range.

This section centres on the description of optical response, using quantum physics for describing spherical nano-particles with radii considerably, less than 10 nm. To this end, we outline the steps involved in the calculations of the frequency-dependent dielectric function of the spherical particles by assuming that a single electron is confined to the field as, with discrete eigenenergies. A meticulous computation is carried out as regards to the

energies of the electron and the corresponding eigen wavefunctions for both finite-and infinite restraint instances, depending on the size of the particle. In both cases, we utilize the closed-form eigenfunctions to acquire the frequency-dependent dielectric function to compute more reliably the optical response of the system considered. We examine the results obtained for the frequency-dependent dielectric function in terms of the absorption coefficient and refractive index allowing a comparison with experimental results as obtained in [79].

5.5.2 Quantum Description of Dielectric Function for Spherical Geometry: Accurate Scheme

As it has been repeatedly mentioned in the literature, when the size of device (nano-particle) is below 10 nm , the continous electronic band of a nano-particle splits into noticeable distinct energy levels (states). Such impacts have been noticed in various experiments conducted using metallic nano-particles, [79], [96] showing a marked distinction between the results obtained in quantum region (size of particle being in the range of 10 nm) and that of 10 nm to 100 nm. As its primary estimation to characterize the optical response of a single electron gas in a metallic nano-particle, [96] depicted a straightforward quantum model where the mobile single electron gas is restricted to an infinite cubical potential cage as discussed in the previous section Eq.(5.6). The frequency-dependent dielectric function of an electron in metallic nano-particle, subject to the effect of electromagnetic wave, with direction of polarization being in z-axis, and, the frequency ω,

$$\varepsilon(\omega) = \varepsilon_\infty + \frac{\omega_p^2}{N} \sum_i \sum_f \frac{s_{if}(F_i - F_f)}{\omega_{if}^2 - \omega^2 - i\omega\gamma_{if}}, \tag{5.30}$$

with the terms ε_∞, s_{if}, ω_{if} and γ_{if} as defined earlier. Consider an infinite spherical potential cage in the Schrödinger equation describing a single electron. Solving the Schrödinger boundary conditions, results in the electron wavefunctions as obtained in [126–129],

$$\psi_{n,l,m}(r,\theta,\phi) = \frac{1}{|j_{l+1}(\alpha_{nl})|}\sqrt{\frac{2}{R^3}} j_l\left(\frac{\alpha_{nl} r}{R} Y_l^m(\theta,\phi)\right), \tag{5.31}$$

where j_l denotes the spherical Bessel functions, Y_l^m represents the conventional spherical harmonics, α_{nl} stands for the n^{th} zero-crossing of j_l, and R stands for the radius of the spherical nano-particle. Hence, the discrete eigen-energies E_{nl} of the problem at hand , associated with the $l^{\text{th}}$of the spherical Bessel function are,

$$E_{nl} = \frac{\hbar^2 \alpha_{nl}^2}{2mR^2}. \tag{5.32}$$

The matrix entries of the single-electron, assuming the direction of polarization to be along the z-axis, together with $z = r\cos\theta$ are,

$$|f\langle|z|i\rangle| = \int_0^{2\pi}\int_0^{\pi}\int_0^{R} dr d\theta d\phi r^3 \sin\theta\cos\theta \psi_{n_f,l_f,m_f}(r,\theta,\phi)\psi_{n_i,l_i,m_i}(r,\theta,\phi). \tag{5.33}$$

Upon further simplification, expansion, and algebraic manipulations, Eq.(5.32) splits into an angular integral component (aic), which is a function of the quantum numbers (l, m), and the radial integral component (ric), which depends on the R, and the quantum numbers (n, l). More specifically,

$$\left.\begin{aligned} I^{aic}_{l,m} &= \sqrt{\frac{(l_i+m_i+1)(l_i-m_i+1)}{(2l_i+1)(2l_i+3)}}\delta_{\Delta l,+1} + \sqrt{\frac{(l_i+m_i)(l_i-m_i)}{(2l_i+1)(2l_i-1)}}\delta_{\Delta l,-1} \\ I^{ric}_{n,l} &= \frac{1}{|j_{l_f+1}(\alpha_{n_f l_f})|}\frac{1}{|j_{l_i+1}(\alpha_{n_i l_i})|}\frac{2}{R^3}\int_0^R drr^3 j_{l_f}\left(\frac{\alpha_{n_f l_f} r}{R}\right) j_{l_i}\left(\frac{\alpha_{n_i l_i} r}{R}\right) \end{aligned}\right\} \quad . \tag{5.34}$$

Using the results in Eq. (5.33), Eq. (5.32) gives,

$$|f\langle|z|i\rangle| = I^{aic}_{l,m} \times I^{ric}_{n,l}. \tag{5.35}$$

The expression at the right-hand-side differs from zero, provided $\Delta l = l_f - l_i = \pm 1$. This selection criterion results as the principle that must be in order to for the current algorithm to be valid. Hence, the oscillator strength for the single electron in a spherical cage can be cast as

$$s_{if} = \frac{2m\omega_{if}}{\hbar}|f\langle|z|i\rangle|^2. \tag{5.36}$$

5.5.3 Quantum Description of the Dielectric function for Spherical Particles: An Approximate Scheme

An alternative approach for obtaining the wavefunctions and their corresponding eigenenergies as is the approximative scheme put forward in [79]. The resulting eigenenergy values are,

$$E_{nl} = \frac{\hbar^2\pi^2}{8MR^2}(2n+l+2)^2 = \frac{\hbar^2}{2MR^2}\left[\pi(n+\frac{l}{2}+1)\right]^2. \tag{5.37}$$

For the approximate wave-functions, we utilize the asymptotic expression for the spherical Bessel function, as described, e.g., in [126], [127],

$$j_l \approx \frac{1}{x}\cos\left[x - \frac{\pi}{2}(l+1)\right]. \tag{5.38}$$

this expression its validity for the range $x \gg \frac{l^2}{2}+l$ only. In addition, the frequency-dependent absorption can be computed using this expression [130],

$$\sigma(\omega) = \frac{9f\omega\varepsilon_m^{\frac{3}{2}}\Im m\left\{\varepsilon(\omega)\right\}}{c(\Re e\left\{\varepsilon(\omega)\right\}+2\varepsilon_m)^2+(\Im m\left\{\varepsilon(\omega)\right\})^2} \tag{5.39}$$

where the parameters and notations have been defined earlier in the text.

5.5.4 Numerical Results for Spherical Geometry

For eigenvalues, both equations, (5.31) and (5.36), result in contrary and divergent values for metallic nano-particles, for e.g., R=1nm. It can be said that there is an excellent agreement only for $l = 0$ and considerable over-valuation for the case when $l > 0$ based on the experimental computations. We, therefore, solve the Schrödinger equation numerically computing the eigenenergies for each metallic nano-particle. To obtain the frequency-dependent dielectric function, the oscillator strength of the particle is needed for the permissible transitions employing the eigenfunctions of the infinite confinement, which are required to achieve the frequency-dependent dielectric function as expressed in Eq. (5.35).

Worth mentioning that the chosen transitions for this study are between the valence band (occupied states) below the Fermi level and the unoccupied states above the Fermi level, and

the transitions between the unoccupied state only above the Fermi level and occupied ones below the Fermi level, in the broad range of(0 to $6eV$), by obeying the principle of selection golden rule, which states $\Delta l = \pm 1$. This scheme enables us to have full access to the information on the permissible transitions of the electrons in the system. Having stated the framework for the validity of the algorithm, we next embark on computing the frequency-dependent dielectric function using Eq. (5.29), and present the real-, imaginary parts of the dielectric function, the refractive index, and the absorption for the finite and infinite cases, respectively, for a range of particle size extending from 1 nm to 3 nm as shown in Figs. 5.6 to 5.8.

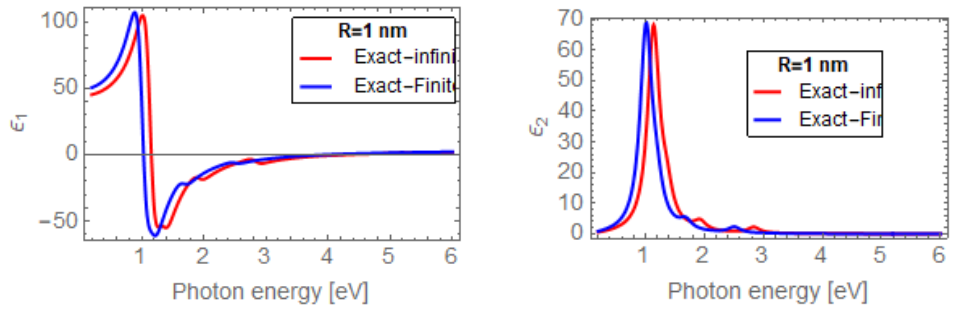

(a) The graph of the real-part of the dielectric function vs energy eV

(b) The graph of imaginary-part of the dielectric function vs energy (eV)

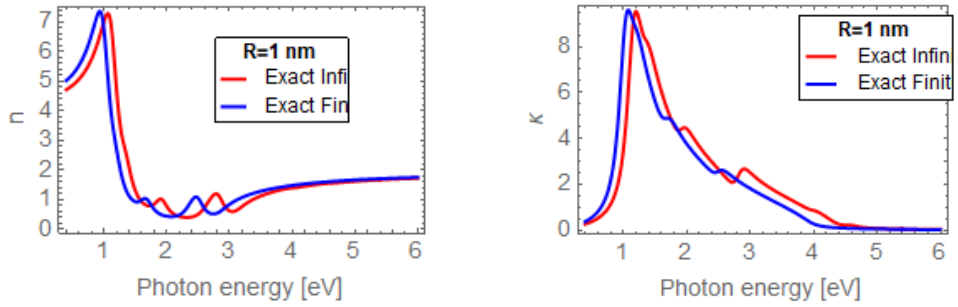

(c) The graph of the real-part of the refractive index vs energy (eV)

(d) The graph of imaginary-part of the refractive index (extinction) vs energy (eV)

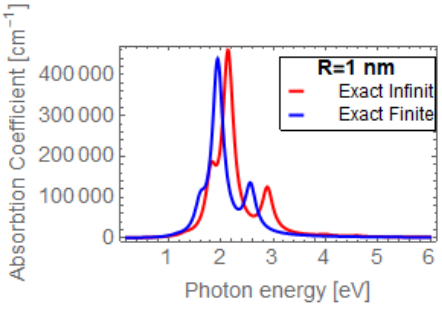

(e) The graph of the absorption coefficient of vs energy (eV)

Figure 5.6: Plots of dielectric function and absorption coefficient versus photon energy in eV with the radius of the particle R=1nm

The continued red lines, equivalent to the exact scheme (infinite), depict, apart from the main summits, feasible transitions with lower intensity. While the blue lines for the exact (finite) solution decrease greatly with the number of transitions in the area of focus, as an impact of the oscillator strength. On the contrary, the position of the energy of the primary peaks is constantly followed by a blue-shifting characteristic regarding the exact scheme for each size of the particle. The objective here is to investigate the mode and pattern of the heights of energy in the imaginary part of the frequency-dependent dielectric function depending on the size of the particle as a form of comparison of the two schemes namely the exact finite and exact infinite. It is observed that the finite scheme forecasts a monotonous blue-shifting as the size of the particle reduces up to a value of $2eV$ at R=1 nm; however, the infinite one depicts the highest value of 1 eV for the same blue-shift. Moreover, it is observed that both of them exhibit consecutive oscillations for the radii.

For the case of absorption, it is observed that the exact infinite and exact finite both exhibit almost the same features when the size of the particle is R=1nm, but different forms for R=2 nm and R= 3 nm, as depicted in Fig. 5.7 and Fig. 5.8, respectively.

Succinctly, at R=1nm, the real-and imaginary parts of the frequency-dependent dielectric function for the exact (infinite) and exact (finite) are almost in agreement based on their respective curves. A similar degree of agreement can be observed for refractive index, extinction coefficient and absorption coefficient, as depicted in Figs. $5.6(a-e)$.

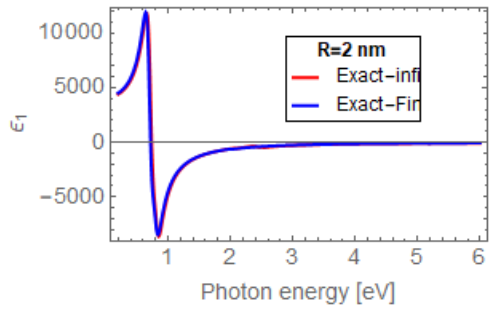

(a) The graph of real-part of dielectric function vs energy (eV)

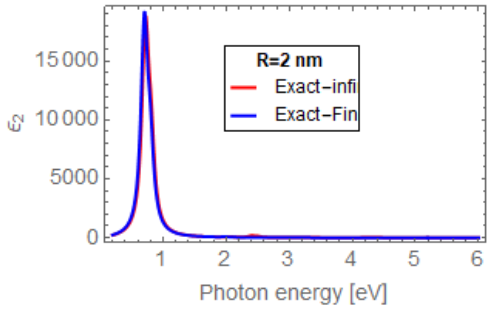

(b) The graph of imaginary part of dielectric function vs energy (eV)

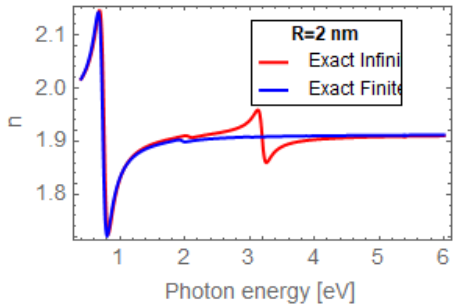

(c) The graph of real-part of refractive index vs energy (eV)

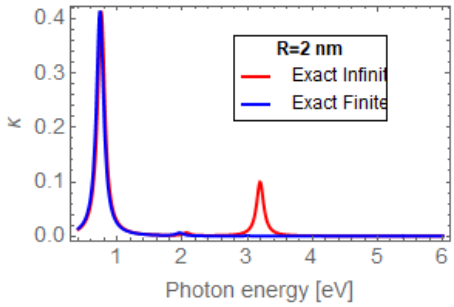

(d) The graph of imaginary part of refractive index (extinction) vs energy (eV)

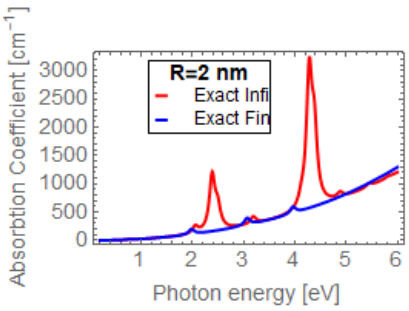

(e) The graph of the absorption coefficient of vs energy (eV)

Figure 5.7: Plots of the dielectric function and absorption coefficient versus photon energy in (eV) with particle radius being R=2nm

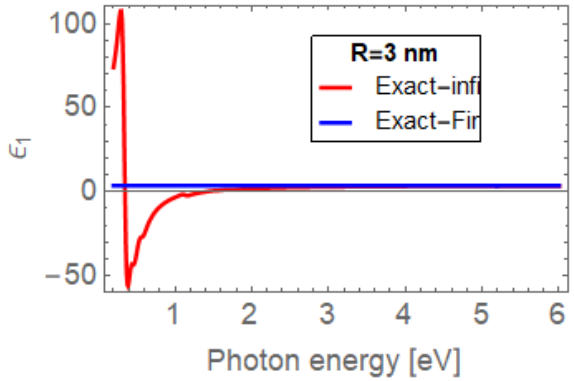

(a) The graph of real-part of dielectric function vs energy (eV)

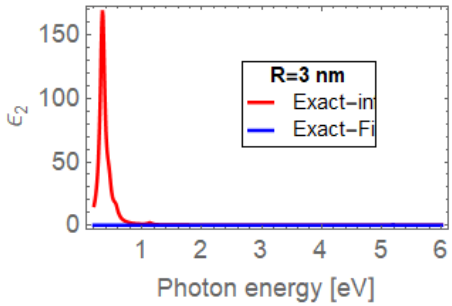

(b) The graph of imaginary part of dielectric function vs energy (eV)

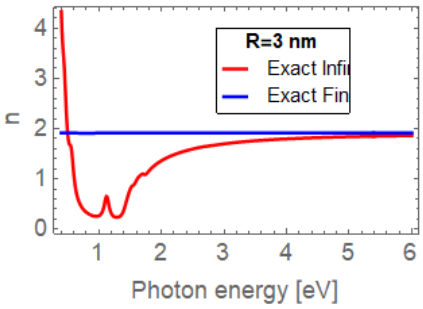

(c) The graph of real-part of refractive index vs energy (eV)

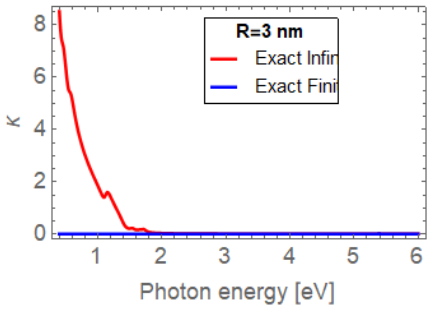

(d) The graph of imaginary part of refractive index (extinction) vs energy (eV)

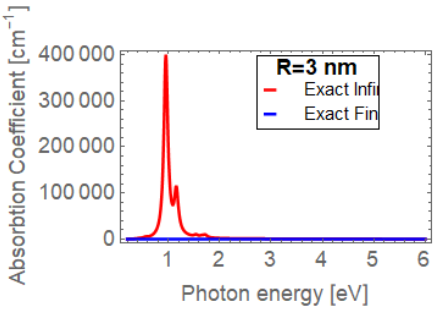

(e) The graph of absorption coefficient of vs energy (eV)

Figure 5.8: Plots of the dielectric function and absorption coefficient versus photon energy in (eV) with size of particle being $R = 3$nm

Furthermore, as the size of the spherical nano-particle increases from $R = 1$nm to 2nm, the exact (finite) and exact (infinite) overlap each other as an indication that both the real-and imaginary parts of the dielectric function, refractive index (extinction coefficient) are in excellent agreement, except in the case of the absorption coefficient which differs markedly, as shown in Fig. 5.7(e). There are two obvious dips exhibited by the exact (infinite) scheme while that of exact (infinite) one grows quadratically. Additionally, in Figs. 5.8$(a-e)$, the real-and imaginary parts of the dielectric function, the refractive index and absorption coefficient, computed for $R = 3$nm, do not agree which may be due to the increase in size of the particle and also the effect of confinement on the optical response of the material. Figures 5.7 and 5.8 show the real-and imaginary parts of the frequency-dependent dielectric function for spherical metallic nano-particle of different sizes computed within the two examined schemes. This can be commended on how the exact finite scheme as a result of greater oscillatory nature of the estimated eigenfunctions, leads to the increase in the number of peaks in the refractive index and absorption coefficient for R=2nm and R=3nm, respectively. Moreover, numerical errors emanated from the exact finite (asymptotic) are observed to be slightly larger than those stemming from the exact infinite scheme of the confinement potential. Therefore, the projections and speculations of this study are situated below the area of measurement error, which can be rectified via the ε_∞ value.

5.6 Summary of the Chapter

The application of quantum model to geometrical nano-particles has been established and presented for cubical, cuboid, and spherical particles. Hence, their optical characteristics

and relevant features such as the absorption coefficient, and dielectric function have been investigated, examined and assessed for particles with shrinking dimensions results obtained for the particle types considered in this Chapter. This study can be useful in the design and modelling of novel nano-electronic devices by determining their respective operating frequency, when subjected to external fields.

Chapter 6

Numerical Solutions to Boundary Value Problem for General Geometrical Structures

In this chapter, the concepts of numerical methods such as the standard finite difference and the conservative finite difference will be discussed and their application to the boundary value problem involving Schrödinger equation for geometrical structure.

6.1 Introduction

Numerical simulation of quantum mechanical based particles remains an open-ended process, and simulations involving more than a pair of particles is still too cumbersome if not impossible. One of the fundamental issues in this procedure is to compute the initial states

for the simulation. To this end, the solutions of the time-dependent Schrödinger equation,

$$H\Psi(r,t) = i\hbar\frac{\partial}{\partial t}\Psi(r,t), \tag{6.1}$$

must be obtained. Here, $\Psi(r,t)$, $\hbar$, H, and i denote the time-dependent eigenfunction, reduced planck constant, Hamiltonian operator, and the imaginary unit, respectively. Solutions to the time-independent Schrödinger equation are expressed as,

$$H\psi(\mathbf{r}) = E\psi(\mathbf{r}) \tag{6.2}$$

where ψ, E, and $\mathbf{r}$ represent the time-independent eigenfunction, the energy, and the position vector comprising all the coordinates in such a manner that $\mathbf{r} = (\mathbf{x_1}, \mathbf{x_2}, \cdots)$. The time-independent eigenfunctions are known as stationary states, and they offer original states for time evolution in numerical or mathematical testing.

6.2 Standard Finite Difference Scheme

In this study, the Standard Finite Difference Method (SFDM) or commonly referred to as the Finite Difference Method (FDM) will be employed to solve an eigenvalue-based problem involving Schrödinger equation. This scheme is considered as the oldest relative to other numerical techniques but still applicable for obtaining numerical solution of partial differential equations (PDEs) [131], [132]. Hence, it is notably suited for the solutions of real-life models of various device problems. Therefore, among all the numerical techniques

[133], [134] currently available for solutions of various nano-particle eigenvalue problems of different structures, the SFDM is probably the easiest and at the same time general one. Nowadays, in spite of the availability of software packages for numerical computations of solving boundary value problem, the SFDM can still be regarded as a numerical method having distinct merits. The merits associated with SFDM are due to its straightforward approach and minimum requirement on hardware.

6.2.1 Fundamentals of SFDM as Applied to Eigenvalue Problems

The eigenvalue problems are very crucial in science and engineering fields. In this work, for illustrative purposes, attempt will be made to use SFDM in solving Schrödinger equation for 1-D problems and subsequently, considering the hydrogen atom as a further example. Generally speaking, an eigenvalue problem is usually cast in matrix form and reads:

$$\mathbf{A}\psi_i = \lambda_i \psi_i \tag{6.3}$$

Given a matrix $\mathbf{A} \in \mathbb{R}^{N\times N}$, to compute the set of the eigenvectors $\{\psi_i | i = 1, ..., N\}$ and the corresponding eigenvalues are expressed in this form $\{\lambda_i | i = 1, ..., N\}$. In theory, for a vector $\mathbf{w}$, the linear combination operation (i.e., matrix-vector multiplication $\mathbb{A}\mathbf{w}$ can be considered and expressed in terms of rotated and stretched copies of $\mathbf{w}$. The eigenfunctions (eigenvectors), ψ_i, are unique vectors for which $\mathbb{A}\psi_i$ is proportional to ψ_i. The time-independent type of the Schrödinger equation, for an electron with mass m moving in the

potential $V(x)$ (i.e., in one spatial direction) can be expressed as:

$$\left[-\frac{\hbar^2}{2m}\frac{d^2}{dx^2}+V(x)\right]\psi(x)=E\psi(x) \tag{6.4}$$

Here, some boundary conditions such as $\psi(\mp\infty)\rightarrow 0$ should be imposed. This equation can be solved for $\psi(x)$ and the energy E. The left-hand side of (6.4) denotes an ordinary differential (linear) operator acting on the eigenfunction $\psi(x)$ and if this equation can be satisfied by meeting the boundary conditions, the impact of the operator is to ensure that $\psi(x)$ is scaled by the E. This process leads to continuous wavefunction $\psi(x)$ and the corresponding eigenvalue E. To change from a continuous to discrete form, there is a need to utilize SFDM to replace the linear differential operators with the finite difference method approximations. This will ensure that the eigenvalue problem that is continuous provided by the Schrödinger's equation will be expressed in discretized matrix form without any loss of generality.

Furthermore, by introducing a grid system defined as $x_j = j\Delta x$ with Δx being a fixed incremental length along the x-axis, and the dummy index $j = 0, 1, 2, ..., J+1$. This means that the left-hand side of the grid (boundary) is at $x = 0$ corresponding to $j = 0$ and the right-hand side of the boundary is at x_f in which $j = J+1$ with $\Delta x = x_f/(J+1)$. Therefore, by letting the wave-function $\psi_j \equiv \psi(x_j)$ and recollecting the usual derivative approximation [135] and hence the Schrödinger's equation of the second-order can be projected onto the

grid-based system and expressed as:

$$-\frac{\hbar^2}{2m}\left[\frac{\psi_{j+1}-2\psi_j+\psi_{j-1}}{\Delta x^2}\right]+V(x_j)\psi_j \approx E\psi_j \tag{6.5}$$

for $j = 2 \rightarrow J-1$. Here, the assumption is that at the boundary points 0 and x_f, the eigenstate vanishes. The simulation domain is the one-dimensional interval $[0, x_f]$. Thus, for the dummy variable $j = 1$ and $j = J$, the discrete boundary equations read:

$$\left.\begin{aligned} -\frac{\hbar^2}{2m}\frac{\psi_2-2\psi_1}{\Delta x^2}+V(x_1)\psi_1 \approx E\psi_1 \\ -\frac{\hbar^2}{2m}\frac{-2\psi_J+\psi_{J-1}}{\Delta x^2}+V(x_J)\psi_J \approx E\psi_J \end{aligned}\right\} \tag{6.6}$$

Again, the approximation scheme as highlighted in (6.3) can be cast in matrix-vector compact form. Assuming $\bar{\psi_j}$ is an approximate on for ψ_j which is the aim and expressing the vectorized form as:

$$\bar{\psi} \doteq \begin{bmatrix} \bar{\psi_1} \\ \bar{\psi_2} \\ \bar{\psi_3} \\ \vdots \\ \bar{\psi_j} \end{bmatrix} \tag{6.7}$$

Defining $q \equiv \hbar^2/(2m\Delta x^2)$ the governing and the two boundary equations can be expressed as:

$$\mathbf{H}\bar{\psi} = \bar{E}\bar{\psi} \tag{6.8}$$

with **H** being,

$$\boldsymbol{H} \doteq \begin{bmatrix} -2q+V(x_1) & q & 0 & \cdots & 0 \\ q & -2q+V(x_2) & q & 0 & \cdots \\ 0 & q & -2q+V(x_3) & q & 0 \\ 0 & 0 & \ddots & \ddots & \ddots \\ \cdots & 0 & 0 & q & -2q+V(x_J) \end{bmatrix} \tag{6.9}$$

the matrix in (6.8) is a tridiagonal matrix, and can be achieved relatively straightforward by utilizing the eigenfunctions as previously stated. The Eqs. (6.8) and (6.9) will be employed in order to compute the eigenenergies and the corresponding eigenvectors for a particle confined to a box to demonstrate the application of this scheme. In addition, the solution of the hydrogen problem will be tackled.

6.2.2 Application of SFDM to Hydrogen Atom

Consider a particle of mass m under the action of central potential $V(r)$; i.e., the potential depends on the distance r from the fixed centre. The Schrödinger equation assumes the form:

$$\left[-\frac{\hbar^2}{2m}\nabla^2 + V(r)\right]\psi(\boldsymbol{r}) = E\psi(\boldsymbol{r}) \tag{6.10}$$

In spherical coordinates [127], the Hamiltonian is

$$\hat{H} = -\frac{\hbar^2}{2m}\frac{1}{r^2}\frac{\partial}{\partial r}\left(r^2\frac{\partial}{\partial r}\right) + \frac{\hat{L}^2}{2mr^2} + V(r), \tag{6.11}$$

where

$$\hat{L^2} = -\hbar^2 \left[\frac{1}{\sin\theta} \frac{\partial}{\partial\theta} \left(\sin\theta \frac{\partial}{\partial\theta} \right) + \frac{1}{\sin^2\theta} \frac{\partial}{\partial\phi} \right]. \tag{6.12}$$

The differential operator $\hat{L^2}$ satisfies: $\hat{L^2} Y_{l,m}(\theta,\phi) = l(l+1)\hbar^2 Y_{l,m}(\theta,\phi)$ and $\hat{L}_z Y_{l,m}(\theta,\phi) = m\hbar Y_{l,m}(\theta,\phi)$. Due to the spherical symmetry of the problem, the energy cannot depend on the operator orientation $\hat{L}$ only but also the azimuthal components. By substituting (6.12) into (6.11),

$$\left.\begin{aligned} \left[-\frac{\hbar^2}{2m} \frac{1}{r^2} \frac{\partial}{\partial r} \left(r^2 \frac{\partial}{\partial r} \right) + \frac{\hat{L}^2}{2mr^2} + V(r) \right] R_{n,l} Y_{l,m}(\theta,\phi) = E R_{n,l}(r) Y_{l,m}(\theta,\phi) \\ \left[-\frac{\hbar^2}{2m} \frac{1}{r^2} \frac{\partial}{\partial r} \left(r^2 \frac{\partial}{\partial r} \right) + \frac{\hbar^2 l(l+1)}{2mr^2} + V(r) \right] R_{n,l} = E R_{n,l}(r) \end{aligned}\right\}. \tag{6.13}$$

Introducing $R(r)$:

$$\left.\begin{aligned} R(r) &= \frac{\psi(r)}{r} \\ \frac{\partial R(r)}{\partial r} = \frac{\partial}{\partial r} \left(\frac{\psi(r)}{r} \right) &= \frac{\partial\psi}{\partial r} \frac{1}{r} - \frac{\psi}{r^2} \\ &= \frac{\partial}{\partial r} \left(r^2 \left[\frac{\partial\psi}{\partial r} \frac{1}{r} - \frac{\psi}{r^2} \right] \right) \end{aligned}\right\} \tag{6.14}$$

Upon simplification, the substitution gives:

$$-\frac{\hbar^2}{2m} \frac{d^2\psi(r)}{dr^2} + \left[\frac{\hbar^2 l(l+1)}{2mr^2} + V(r) - E \right] \psi(r) = 0 \tag{6.15}$$

This equation is the Schrödinger equation in one dimension for a particle under the action of an effective r-dependent potential. The Eq. (6.3) can be combined in the form of Eq.

(6.13) which is a radial form in atomic units i.e. $m_e = 1$, $\hbar = 1$, $q_e = 1$, and where $q_e = \frac{e^2}{4\pi\varepsilon_0}$.

Hence,

$$\left.\begin{aligned} -\frac{\hbar^2}{2m}\frac{d^2\psi(r)}{dr^2} + \left[V_{eff}(r) - E\right]\psi(r) = 0 \\ V_{eff}(r) = \frac{\hbar^2 l(l+1)}{2mr^2} + V(r) \\ -\frac{1}{2}\frac{d^2\psi(r)}{dr^2} + V_{eff}(r)\psi(r) = E\psi(r) \end{aligned}\right\} \tag{6.16}$$

$$-\frac{1}{2}\left[\frac{\psi(r)_{i+1} - 2\psi(r)_i + \psi(r)_{i-1}}{\Delta r^2}\right] + V_{eff,i}\psi(r)_i = E\psi(r)_i \tag{6.17}$$

With index values from $i = 1$ to $i = 4$, Eq. (6.17) becomes :

$$\left.\begin{aligned} -\frac{1}{2}\left[\frac{\psi_2 - 2\psi_1 + \psi_0}{\Delta r^2}\right] + V_{eff,1}\psi_1 = E\psi_1 \\ -\frac{1}{2}\left[\frac{\psi_3 - 2\psi_2 + \psi_1}{\Delta r^2}\right] + V_{eff,2}\psi_2 = E\psi_2 \\ -\frac{1}{2}\left[\frac{\psi_4 - 2\psi_3 + \psi_2}{\Delta r^2}\right] + V_{eff,3}\psi_3 = E\psi_3 \\ -\frac{1}{2}\left[\frac{\psi_5 - 2\psi_4 + \psi_3}{\Delta r^2}\right] + V_{eff,4}\psi_4 = E\psi_4 \end{aligned}\right\} \tag{6.18}$$

Satisfying the boundary conditions, $\psi_0 = \psi(r_0) = \psi_5 = \psi(r_5) = 0$ and rearranging the terms,

$$\left.\begin{aligned} \left(V_{eff,1} + \frac{1}{\Delta r^2}\right)\psi_1 - \frac{1}{2\Delta r^2}\psi_2 = E\psi_1 \\ -\frac{1}{2\Delta r^2}\psi_1 + \left(V_{eff,2} + \frac{1}{\Delta r^2}\right)\psi_2 - \frac{1}{2\Delta r^2}\psi_3 = E\psi_2 \\ -\frac{1}{2\Delta r^2}\psi_2 + \left(V_{eff,3} + \frac{1}{\Delta r^2}\right)\psi_3 - \frac{1}{2\Delta r^2}\psi_4 = E\psi_3 \\ -\frac{1}{2\Delta r^2}\psi_3 + \left(V_{eff,4} + \frac{1}{\Delta r^2}\right)\psi_4 = E\psi_4 \end{aligned}\right\}. \tag{6.19}$$

Arranging the equations (6.19) into matrix form compactly, it gives:

$$\begin{bmatrix} V_{eff,1}+\frac{1}{\Delta r^2} & -\frac{1}{2\Delta r^2} & 0 & 0 \\ -\frac{1}{2\Delta r^2} & V_{eff,2}+\frac{1}{\Delta r^2} & -\frac{1}{2\Delta r^2} & 0 \\ 0 & -\frac{1}{2\Delta r^2} & V_{eff,3}+\frac{1}{\Delta r^2} & -\frac{1}{2\Delta r^2} \\ 0 & 0 & -\frac{1}{2\Delta r^2} & V_{eff,4}+\frac{1}{\Delta r^2} \end{bmatrix} \begin{bmatrix} \psi_1 \\ \psi_2 \\ \psi_3 \\ \psi_4 \end{bmatrix} = E \begin{bmatrix} \psi_1 \\ \psi_2 \\ \psi_3 \\ \psi_4 \end{bmatrix} \tag{6.20}$$

From this trivial instance, a general tridiagonal matrix equation for N grid points can be defined,

$$\mathbf{H}\vec{\psi} = E\vec{\psi}, \tag{6.21}$$

where the entries of the matrix $\mathbf{H}$ are:

$$\left.\begin{aligned} \mathbf{H_{i,i}} &= V_{eff,i} + \frac{1}{\Delta r^2} \\ \mathbf{H_{i,i+1}} &= -\frac{1}{2\Delta r^2} \\ \mathbf{H_{i,i-1}} &= -\frac{1}{2\Delta r^2} \end{aligned}\right\} \tag{6.22}$$

and the Hamiltonian matrix $\mathbf{H}$ is given as:

$$\mathbf{H} = \begin{bmatrix} H_{1,1} & H_{1,2} & 0 & 0 & \cdots & 0 \\ H_{2,1} & H_{2,2} & H_{2,3} & 0 & \cdots & 0 \\ 0 & H_{3,2} & H_{3,3} & H_{3,4} & \cdots & 0 \\ \vdots & \vdots & \vdots & \ddots & \vdots & \vdots \\ 0 & \cdots & 0 & H_{N-1,N-2} & H_{N-1,N-1} & H_{N-1,N} \\ 0 & \cdots & 0 & 0 & H_{N,N-1} & H_{N,N} \end{bmatrix} \tag{6.23}$$

For the application of hydrogen atom that has closed-form solutions in most of the fundamental quantum mechanics and a well-known energy spectrum with wave-functions that permits the comparison of numerical approach. From Eq.(6.13) with $V(r) = -1/r$, the Schrödinger equation for hydrogen atom is obtained and expressed it in matrix form as indicated in Eq.(6.18). To obtain the eigenvalues and eigenfunctions from Eq.(6.19), there is a need to diagonalize it with standard algebraic methods as demonstrated in Eq.(6.18).

The ground state of the hydrogen atom can be found by accounting for the symmetry of the s excited state, e.g., $l = 0$ in (6.13). In order to solve for the ground state, it is assumed that N states for the ground level of the hydrogen atom must be determined. This means that there is a need to have bound and continuum states such as $1s$, $2s$, $3s$, $4s$,$\cdots$, Ns. These states are function of N grid points which for this case will be $N = 2000$. Furthermore, the N states will have N eigenfunctions corresponding to each eigenvalue i.e., where each eigenvalue ($1s$) will have its own eigenfunction (ψ_1). Secondly, the excited state is similar

as before noting that there is a need to specify the angular symmetry l in Eqn. (6.13) for instance $l = 2$ or $l = 3$ as the case may be.

Derivation of dipole oscillator strength of hydrogen atom

For a dipole transition , the density of states of the hydrogen atom can be obtained based on the principle in [136–140] . In principle, a particle of mass m undergoes quantization via the electromagnetic field as discussed in the previous Chapter. For clarity, it is stated here as:

$$\hat{\mathbf{H}} = \frac{1}{2m_e}\left(\hat{\mathbf{p}} - \frac{e}{c}\hat{\mathbf{A}}(\hat{r},t)\right)^2 - e\hat{\psi}(\hat{r},t) + \hat{V}_0(\hat{r}) \tag{6.24}$$

where, it is assumed that the vector potential $\hat{\mathbf{A}}$ is obtained using Maxwell's equations. Thus, Eq. (6.22) is simplified using these relations as follows: $\mathbf{A}\cdot\mathbf{p} - \mathbf{p}\cdot\mathbf{A} = i\hbar\nabla\cdot\mathbf{A}$. Thus, the assumption here is that no presence of source of electrostatic radiation, i.e. $\nabla\cdot\mathbf{A} = 0$ and scalar potential $\psi = 0$. Therefore, Eq.(6.24) becomes:

$$\hat{H} \cong \frac{\hat{p}^2}{2m_e} + \frac{e}{m_e c}\left(\hat{\mathbf{A}}\cdot\hat{\mathbf{p}}\right) + V_0(r) \tag{6.25}$$

The parameters are as defined in (4.1- 4.5). The total Hamiltonian of a charged particle having the electromagnetic field present in the presence of Coulomb gauge condition can be expressed as:

$$\hat{H} = \hat{H}_0 + \hat{V}(t) = -\frac{\hbar^2}{2m_e}\nabla^2 + \hat{V}_0(r) + \frac{e}{m_e c}\left(\hat{\mathbf{A}}\cdot\hat{\mathbf{p}}\right) \tag{6.26}$$

where $\hat{V}(t)$ denotes a perturbation to the unperturbed Hamiltonian $\hat{H}_0$. It is a known fact that the semi-classical scheme of approximation accurately defined the effect of the

external field on the electron (particle) which can either undergo induced emission process or absorption stage [87]. However, it omits the description of the effect of the particles on radiation externally. In this section, the total Hamiltonian consists of time-independent Hamiltonian form $\hat{H}_0$ and time-dependent form $\hat{V}(t)$. From the theory of perturbation, the transition probability of a particle can be obtained, starting with the first-order type and expressing the absorption coefficient in terms of the density matrix of the particle which gives [136]:

$$\left.\begin{aligned} \frac{\partial\sigma}{\partial\Omega} = \frac{\partial W_{fi}^{abs}}{N\partial\Omega} = \frac{e^2}{2\pi\hbar c}\frac{v}{\omega}|\left\langle\psi_f|e^{-ik.r}\epsilon\cdot\mathbf{p}|\psi_{\mathbf{i}}\right\rangle|^2 \\ \frac{\partial\sigma}{\partial\Omega} = -\frac{e^2}{2m\pi\hbar c}\frac{k_f}{\omega}|\left\langle\psi_f|e^{-ik.r}\epsilon\cdot\nabla|\psi_i\right\rangle|^2 \\ \frac{\partial\sigma}{\partial\Omega} = \frac{8\pi^3e^2\nu}{c}|\int d\tau\psi_f x\psi_i|^2 \end{aligned}\right\} \tag{6.27}$$

Here ω, k, v, ψ_i, and ψ_f are the angular frequency, wavenumber of the electromagnetic field radiation, velocity of the electron, wavefunctions for initial-and final states of the electron, respectively. Also, these relations $v = \hbar k/m$, the electron dipole approximation of the form; i.e., $e^{-ikr} \cong 1 + ikr + \cdots$ and $\mathbf{p} = -\mathbf{i}\hbar\nabla$ have been utilized to obtain the matrix entries using linear polarization. In (6.27), the integral $|\int d\tau\psi_f x\psi_i|^2$ denotes the dipole moment of the electron between the initial state and final state, which in turn, is related to the density of states of the hydrogen atom. The parameter x indicates the direction of the polarization of the light photon i.e. along the x-axis direction.

The eigenfunction of the continuous state depends on the frequency and the quantum numbers m and l. Therefore, the integral sign that appears in (6.27) will be estimated for all values of m and l and the outcome will be added. Letting ψ_{n_i,l_i,m_i} and ψ_{n_f,l_f,m_f} denote

the initial-and final eigenstate expressed as [141]:

$$\left.\begin{aligned} \psi_{n_i,l_i,m_i} &= \frac{u_{n_i,l_i(r)}}{r} Y_{l_i,m_i}(\theta,\phi) \\ \psi_{n_f,l_f,m_f} &= \frac{u_{n_f,l_f(r)}}{r} Y_{l_f,m_f}(\theta,\phi) \\ f_{n_f l_f,n_i l_i} &= \frac{2m}{\hbar}\omega_{n_f,n_i} |\left\langle \psi_f | r.\epsilon | \psi_i \right\rangle|^2 \end{aligned}\right\} \tag{6.28}$$

Summing over all the initial states and then averaging over all the final states as described in [141], it gives:

$$\bar{f}_{n_f l_f,n_i l_i} = \frac{1}{2l_i+1} \sum_{m_f=-l_f}^{+l_f} \sum_{m_i=-l_i}^{+l_i} \frac{1}{3} \sum_{i=1}^{3} f_{n_f l_f,n_i l_i} \tag{6.29}$$

$$\bar{f}_{n_f l_f,n_i l_i} = \frac{2m}{3\hbar}\omega_{n_f,n_i} \sum_{m_f=-l_f}^{l_f} \frac{1}{2l_i+1} \underbrace{\sum_{m_i=-l_i}^{l_i} |\left\langle \psi_f | r.\epsilon | \psi_i \right\rangle|^2}_{} \tag{6.30}$$

The Eqs. (6.29) and (6.30) are known as the average dipole oscillator strength of the hydrogen atom. The underbraced summation term will be adjusted to reflect the radial functions for the symmetry of the spherical hydrogen atom. It can be inferred that based on (6.28), the transition probability relies on the particle dipole matrix elements and thus, it is appropriate to express it as simple employing the concept of the spherical symmetry for a single electron. By carrying out the matrix elements process, the Clebsch-Gordan terms will be of this form $|\left\langle l_f, m_f | 1, \nu | l_i, m_i \right\rangle|$ in order to couple the initial quantum numbers to the final ones. It is assumed that for a dipole transition, the rule of selection must be adhered to strictly: for l, the $\Delta l = l_f - l_i = \mp 1$ and for m, the $\Delta m = 0, \pm 1$. Finally, the dipole oscillator strength can

be expressed compactly in atomic units as:

$$\bar{f}_{n_f l_f, n_i l_i} = \frac{2}{3}\left(E_f - E_i\right)\frac{l_>}{2l_i+1}\left(\int_0^\infty \psi_{n_f l_f}(r) r \psi_{n_i l_i}(r) dr\right)^2 \tag{6.31}$$

where $l_>$ is the greater value between l_i and l_f. The indices i and f refer to an initial and final state, where the electronic transition occurs. In addition, the finite difference expression for the density of state can be expressed as:

$$\bar{f}_{n_f l_f, n_i l_i} = \frac{2}{3}\left(E_f - E_i\right)\frac{l_>}{2l_i+1}\left(\sum_{k=1}^{N} \psi_{n_f l_f}(r_k) r_k \psi_{n_i l_i}(r_k)\Delta r\right)^2 \tag{6.32}$$

For this study, different states are used with the following numerical data employed for the simulation and remain constant throughout to enable us to compare the exact solutions with the numerical forms: $N = 2,000$ (the number of points in mesh), $\Delta r = 0.05$ (the spacing), and $L = 20$ (the length of numerical grid for the particle). For example, it is demonstrated in this study using hydrogen atom for the initial state to be $1s^1$ and the final excited state to be $2p^1$. This means that there is a transition from $1s \rightarrow 2p$.

Furthermore, using (6.19) to demonstrate the significance of electronic transitions for the matrix entries when $L = 100$, $N = 2,000$ and $\Delta r = 0.05$, the results obtained numerically are presented in Table (6.1) for eigenvalues, square of matrix elements for various transitions.

In Table (6.2), the results of dipole oscillator strength are presented and compared with a known exact solution in the literature. It is observed that between the transition states from $2p \rightarrow 3s$ and $2s \rightarrow 3p$, the numerical method is close to the exact values obtained and error in percent regarding the difference is computed as well.

Table 6.1: Electronic transitions for $L = 100, N = 2000, \triangle r = 0.05$

$(nl)_i \rightarrow (nl)_f$	**Eigenvalues (u.a.)**	$\lvert\langle\Psi_f\lvert r\rvert\Psi_i\rangle\rvert^2$	$l_>/(2l_i+1)$	$\bar{f}_{n_f l_f, n_i l_i}$
$1s \rightarrow 2p$	$E_{1s} = -0.4997$ $E_{2p} = -0.1249$	1.6672	1	0.4165
$2p \rightarrow 3s$	$E_{2p} = -0.1249$ $E_{3s} = -0.0555$	0.8723	$\frac{1}{3}$	1.3463×10^{-2}
$2s \rightarrow 3p$	$E_{2s} = -0.1249$ $E_{3p} = -0.0555$	9.4256	1	0.4362
$2p \rightarrow 3d$	$E_{2p} = -0.1250$ $E_{3d} = -0.0544$	21.8353	$\frac{1}{3}$	0.6847

Table 6.2: Dipole oscillator strength in comparison with available values

$(nl)_i \rightarrow (nl)_f$	**Exact** $\bar{f}_{n_f l_f, n_i l_i}$	**Finite-differences** $\bar{f}_{n_f l_f, n_i l_i}$	**Error** %
$1s \rightarrow 2p$	0.4162	0.4169	0.14
$2p \rightarrow 3s$	0.01359	0.01346	1.0
$2s \rightarrow 3p$	0.4349	0.4362	0.3
$2p \rightarrow 3d$	0.6958	0.6847	1.6

On a final note, this study further computes the dipole oscillator strength and compares the results with exact results with emphasis on the specificity of transitions that occur between $1s$ to np where n ranges from 2 to 7; i.e., $n = 2, 3, 4, 6, 7$ as summarized in Table 6.3 for numerical data ($L = 100$, $N = 2,000$ and Δr). The Thomas-Reiche-Kuhn (TRK) [140] sum rule is employed for the continuous and discrete values of the exact and the numerical solutions. It is observed that the sum of the two (continuous and discrete) gives one (1)for the exact scheme whereas the numerical scheme almost gives the same result. The error for each transition from $1s$ state to any p state as listed in Table (6.3) is calculated as well.

6.2.3 Application of SFDM to a Particle in a Box Problem

In this section, efforts will be geared towards the application of SFDM to a particle confined in a box or cage to compute the frequency-dependent dielectric function. For instance,

Table 6.3: Dipole oscillator strength comparison for $1s \rightarrow np$ transitions. The numerical data are $L = 100, n = 2,000$ y $\triangle r = 0.05$

$(nl)_i \rightarrow (nl)_f$	**Exact** $\bar{f}_{n_f l_f, n_i l_i}$	**Finite-differences** $\bar{f}_{n_f l_f, n_i l_i}$	**Error** %
$1s \rightarrow 2p$	0.4162	0.4169	0.14
$1s \rightarrow 3p$	7.910×10^{-2}	7.8966×10^{-2}	0.17
$1s \rightarrow 4p$	2.899×10^{-2}	2.9083×10^{-2}	0.32
$1s \rightarrow 5p$	1.394×10^{-2}	1.3814×10^{-2}	0.9
$1s \rightarrow 6p$	7.800×10^{-3}	8.1526×10^{-3}	4.5
$1s \rightarrow 7p$	4.800×10^{-3}	6.8982×10^{-3}	43.7
TRK Discret	0.5650	0.56218	0.5
TRK Continuum	0.4350	0.43733	0.54
TRK Total	**1000**	**0.99951**	

consider a nano-particle in a box of length L by assuming the potential $V(x)$ to be zero. The Schrödinger equation, subject to the boundary conditions $\psi(0) = \psi(L) = 0$:

$$-\frac{\hbar^2}{2m}\frac{d^2}{dx^2}\psi(x) = E\psi(x) \tag{6.33}$$

By letting $x = x_0\bar{x}$, the Eq.(6.31) transforms to a dimensionless form. Also, if the energy E is normalized as $\bar{E} = 2mx_0^2E/\hbar^2$, then, (6.33) gives:

$$-\frac{d^2}{d\bar{x}^2}\psi(\bar{x}) = \bar{E}\psi(\bar{x}) \tag{6.34}$$

the boundary conditions transform from $\psi(0) = \psi(L) = 0$ to $\psi(0) = \psi(L/x_0) = 0$ indicating that $x_0 = L$ and $\psi(x_0\bar{x})$. Since $\psi(x)$ is a function of x_0 and $\bar{x}$. This means that $\psi(x) \rightarrow \psi(x_0\bar{x})$. Therefore, $\psi(x) = \bar{\psi}(\bar{x})$. The final non-dimensional equation to be discretized

becomes:

$$-\frac{d^2\bar{\psi}(\bar{x})}{d\bar{x}^2} = \bar{E}\bar{\psi}(\bar{x}) \tag{6.35}$$

the closed-form solution to (6.35) is,

$$\psi(\bar{x}) = \sqrt{\frac{2}{L}}\sin(\sqrt{\bar{E}}\bar{x}). \tag{6.36}$$

The constant $\sqrt{2/L}$ is obtained as a result of normalization procedure carried out. The $\sqrt{\bar{E}} = n\pi$ and the unnormalized energy becomes $E = \hbar^2 n^2 \pi^2/(2mL^2)$. Here, the objective is to solve this problem numerically, and employ the resulting eigenvalues and eigenfunctions to compute the dielectric function. To the best our knowledge, this is the first time such method will be used to compute the optical property called dielectric function. Thus, to solve this problem numerically, Eq.(6.33) needs to be approximated with SFDM . The dimensionless spatial coordinate $\bar{x}$ runs from $0 \rightarrow 1$. Let $\bar{x_j} = j\Delta\bar{x}$ with $\Delta\bar{x} = 1/(M+1)$ for M being the number of grid points. Assuming $\bar{\psi_j} = \bar{\psi}(\bar{x_j})$ be the discrete unknowns associated with the $\bar{\psi}$ on the spatial grid. Subsequently, by employing the finite difference approximation to the second derivative (6.35), it becomes:

$$-\frac{\bar{\psi}_{j+1} - 2\bar{\psi}_j + \bar{\psi}_{j-1}}{\Delta^2\bar{x}} = \bar{E}\bar{\psi}_j \tag{6.37}$$

letting j to run from 3 to $M-1$. At $j=1$ and $j=M$, homogeneous boundary conditions $\bar{\psi}_0 = 0$ and $\bar{\psi}_{M+1} = 0$ are imposed. Hence,

$$\left.\begin{aligned} -\frac{\bar{\psi}_2 - 2\bar{\psi}_1}{\Delta^2 \bar{x}} &= \bar{E}\bar{\psi}_1 \\ -\frac{\bar{\psi}_3 - 2\bar{\psi}_2 + \bar{\psi}_1}{\Delta^2 \bar{x}} &= \bar{E}\bar{\psi}_2 \\ -\frac{-2\bar{\psi_M} + \bar{\psi}_{M-1}}{\Delta^2 \bar{x}} &= \bar{E}\bar{\psi_M} \end{aligned}\right\} \quad . \tag{6.38}$$

of the discrete values $\bar{\psi}_i$,

$$\left.\begin{aligned} \bar{\psi} &\doteq \begin{bmatrix} \bar{\psi}_1 \\ \bar{\psi}_2 \\ \bar{\psi}_3 \\ \vdots \\ \bar{\psi}_M \end{bmatrix} \\ \mathbb{A}\bar{\psi} &= \bar{E}\bar{\psi} \end{aligned}\right\} \tag{6.39}$$

Consequently, the matrix entries M_{if} for the electronic dipole transitions from initial-state to final-state, the change in frequency ω_{if}, the oscillator strength S_{if} of the nano-particle, and finally the dielectric function $\varepsilon(\bar{\omega})$, can be obtained:

$$\left.\begin{aligned} M_{i,f} &= x_0 \left\langle \bar{\psi}_i(\bar{x}) | \bar{x} | \bar{\psi}_f(\bar{x}) \right\rangle \\ \omega_{if} &= \frac{E_f - E_i}{\hbar} = \frac{\hbar^2}{2mx_0}(\bar{E}_f - \bar{E}_i) \\ S_{if} &= \frac{2m\omega_{if}|M_{if}|^2}{N_e\hbar} \\ \varepsilon(\bar{\omega}) &= 1 + \sum_i \sum_f \frac{S_{if}}{\bar{\omega}_{if} - \bar{\omega}^2 - i\bar{\gamma}\bar{\omega}} \end{aligned}\right\} \tag{6.40}$$

where $\bar{\omega} = \omega/\omega_p$, $\bar{\omega}_{if}$, $\bar{\gamma} = \gamma/\omega_p$ and N_e represent the normalized frequency, normalized change in frequency from the initial- state i to the final-state f, normalized damping constant for the particle and the number of particle, respectively. The numerical results will be presented subsequently. It should be noted that the problem considered here is a 1-D case, however, two- and three dimensional problems can be solved mutatis mutandis.

6.3 Conservative Finite Difference Method: An Eigenvalue Approach

In this section, the concept of the Conservative Finite Difference Method (CFDM) will be discussed and how it can be applied to solve boundary value problems. The concept of CFDM was put forward by Favorskii et. al based on the principle of support-operators [142]. When applying standard numerical schemes for solving boundary value problems, certain properties of the involved differential and/or integral operators might get affected. The conservative techniques ensure that the operators properties remain conserved. For examples, adequate application of CFDM preserves the hermiticity of hermitian operators after being discretized. This ability of designing conservative numerical schemes is outstanding feature, which has not been duly appreciated in computational community, partly due to its comparatively cumbersome implementation. CFDM finds its application in areas such as computational engineering, biomedical engineering and science-based project which offers a system that is easy to execute for a big class of practical challenges in real-life case [135], [142–149].

6.3.1 Discretization of 1-D BVPs Using CFDM

To exemplify the usage of CFDM, consider the 1-D Schrödinger equation with vanishing potential energy term, $V(x)$; i.e.,

$$-\frac{\hbar^2}{2m}\nabla^2\psi(x) = -\frac{\hbar^2}{2m}\frac{d^2}{dx^2}\psi(x) = E\psi(x). \tag{6.41}$$

In order to discretize this ordinary differential equation, the following steps must be taken. To highlight some of the salient features of CFDM, the expression for $\partial/\partial y$ will be provided.

- Construct an expression for the first-order derivative, using trapezoidal rule for the Green's formula for x-axis or y-axis, as the case may be; i.e., $\frac{\partial\psi}{\partial x} = \frac{\oint_c \psi\, \partial y}{A}$, $\frac{\partial\psi}{\partial y} = -\frac{\oint_c \psi\, \partial x}{A}$. Here, A represents the area of the domain of interest.

- Obtaining the second-order derivative, it requires four first-order derivatives or can be expressed in terms of first-order of another variable; i.e., $\partial^2\psi/\partial x^2 = \frac{\partial^2\psi}{\partial x^2} = \partial\phi/\partial x$, where $\frac{\partial\psi}{\partial x} = \phi$.

By applying these steps alongside the concept of CFDM support-operators as canvassed by [143] to discretize Eq.(6.39), it gives:

$$\frac{d^2}{dx^2}\psi(x) \cong \frac{(D_x\psi)_i - (D_x\psi)_{i-1}}{0.5(x_{i+1} - x_i) - 0.5(x_i - x_{i-1})}, \tag{6.42}$$

where $(D_x\psi)_i$ refers to the discrete derivative of ψ with respect to x, and evaluated at the i^{th} grid point (cell-centre). Furthermore, $\cong$ indicates that the expression at the right-hand side is a discrete representation for the differential form at the left-hand side. It is immediate

that the Schrödinger equation corresponding to the interior point i becomes,

$$-\left[\frac{\psi_{i+1}-\psi_i}{x_{i+1}-x_i}-\frac{\psi_i-\psi_{i-1}}{x_i-x_{i-1}}\right]=\frac{2mE\left[(0.5(x_{i+1}-x_{i-1})\right]}{\hbar^2}\psi_i. \tag{6.43}$$

This equation is valid for general non-uniform grids. In this study, a uniform grid has been assumed for simplifying the discussion. letting $a_1 = 1/(x_{i+1} - x_i)$, $a_2 = 1/(x_i - x_{i-1})$ and $\bar{\alpha} = \hbar^2/(2m\Delta x)$, and simplifying,

$$\bar{\alpha}\left[-a_2\psi_{i-1}+(a_1+a_2)\psi_i-a_1\psi_{i+1}\right]=E\psi_i \tag{6.44}$$

with $\bar{E} = E/\bar{\alpha} = \lambda$, and considering the equations associated with all interior points, we obtain the eigenvalue matrix equation,

$$\bar{\mathbf{A}}\psi=\lambda\psi. \tag{6.45}$$

The matrix entries from $\bar{\mathbf{A}}$ are non-dimensional. Next, the schemes SFDM and CFDM are tested in order to ascertain the veracity of the Eqs. (6.37) and (6.43) with internal nodes of the uniform grid system ranging from 5 to 7. In 1-D case, the generating matrices for both schemes agree and give the same results. We are now prompted to investigate the 2-D BVPs using SFDM and CFDM.

6.3.2 Discretization of 2-D BVPs using SFDM and CFDM

Following parallel to those arguments discussed in the case of 1-D BVPs, the 2-D BVPs will be considered next. The idea of discretizing a second-order differential equation using SFDM scheme is straightforwardly done, however, in the case of CFDM it is slightly different in the sense that the starting point is using four nodes as depicted in Fig. (6.1a) to obtain a single cell for the first derivative; i.e., nodes $\rightarrow$ cells formation and using four cells to acquire a single node; i.e., cells $\rightarrow$ nodes for the second-order differential equations as shown in Fig. (6.1b). Figure (6.1c) provides the general overview of the concept of CFDM as applied to 2-D BVPs.

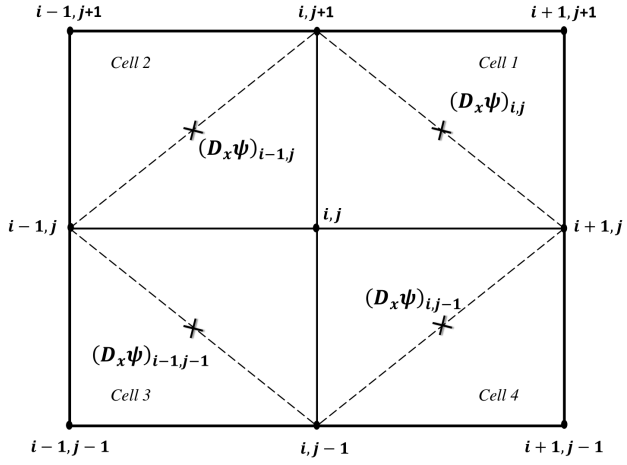

(a) Generation of 1st order difference expressions using four surrounding nodes

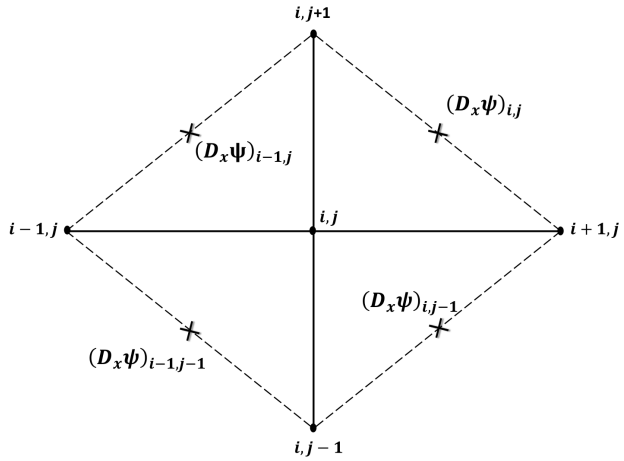

(b) Outcome of generation of 1st order difference expressions leading to 2nd order generation

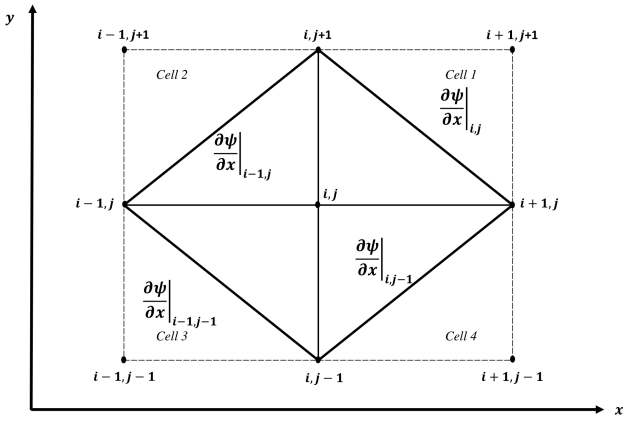

(c) General view of the concept of CFDM for 2-D

Figure 6.1: Schematic stages for the formulation of second-order Schrödinger equation for 2-D using CFDM

The merit of this scheme is that it preserves the original features of the underlying difference operators after the discretization procedure. The two procedures will be demonstrated in the discretization of the second-order differential equation (in the present

case the Schrödinger equation) using CFDM. More specifically,

$$\left.\begin{aligned} -\frac{i\hbar\partial\psi(x,y)}{\partial t} &= -\frac{\hbar^2}{2m}\left[\frac{\partial^2\psi(x,y)}{\partial x^2}+\frac{\partial^2\psi(x,y)}{\partial y^2}\right] \\ \frac{2mE}{\hbar^2}\psi(x,y) &= -\nabla^2\psi(x,y) \\ \tilde{E}\psi(x,y) &= -\nabla^2\psi(x,y) \\ \tilde{A}\psi(x,y) &= \lambda\psi(x,y) \end{aligned}\right\} \quad . \tag{6.46}$$

Here, the normalized energy $\tilde{E}=\lambda$ represents the eigenvalue of the system. Applying CFDM to discretize the differential operator on both sides of Eq. (6.44), it leads to:

$$\tilde{E}\psi_{i,j} = -\left[\frac{-\left\{\frac{y_{i-1,j}-y_{i,j-1}}{2}\tilde{A}x_{i-1,j-1}-\frac{y_{i,j+1}-y_{i+1,j}}{2}\tilde{A}x_{i,j}-\frac{y_{i+1,j}-y_{i,j-1}}{2}\tilde{A}x_{i,j-1}+\frac{y_{i,j+1}-y_{i-1,j}}{2}\tilde{A}x_{i-1,j}\right\}}{Vn_{i,j}}\right]$$
$$-\left[\frac{\left\{\frac{x_{i-1,j}-x_{i,j-1}}{2}\tilde{A}y_{i-1,j-1}-\frac{x_{i,j+1}-x_{i+1,j}}{2}\tilde{A}y_{i,j}-\frac{x_{i+1,j}-x_{i,j-1}}{2}\tilde{A}y_{i,j-1}+\frac{x_{i,j+1}-x_{i-1,j}}{2}\tilde{A}y_{i-1,j}\right\}}{Vn_{i,j}}\right] \tag{6.47}$$

Further simplification results into this:

$$\tilde{E}\psi_{i,j}Vn_{i,j} = \frac{y_{i-1,j}-y_{i,j-1}}{2}\left\{\frac{(\psi_{i,j}-\psi_{i-1,j-1})(y_{i-1,j}-y_{i,j-1})-(\psi_{i-1,j}-\psi_{i,j-1})(y_{i,j}-y_{i-1,j-1})}{2Vc_{i-1,j-1}}\right\}$$
$$-\left(\frac{y_{i,j+1}-y_{i+1,j}}{2}\right)\left\{\frac{(\psi_{i+1,j+1}-\psi_{i,j})(y_{i,j+1}-y_{i+1,j})-(\psi_{i,j+1}-\psi_{i+1,j})(y_{i+1,j+1}-y_{i,j})}{2Vc_{i,j}}\right\}$$
$$-\left(\frac{y_{i+1,j}-y_{i,j-1}}{2}\right)\left\{\frac{(\psi_{i+1,j}-\psi_{i,j-1})(y_{i,j}-y_{i+1,j-1})-(\psi_{i,j}-\psi_{i+1,j-1})(y_{i+1,j}-y_{i,j-1})}{2Vc_{i,j-1}}\right\}$$
$$+\frac{y_{i,j+1}-y_{i-1,j}}{2}\left\{\frac{(\psi_{i,j+1}-\psi_{i-1,j})(y_{i-1,j+1}-y_{i,j})-(\psi_{i-1,j+1}-\psi_{i,j})(y_{i,j+1}-y_{i-1,j})}{2Vc_{i-1,j}}\right\}$$
$$+\frac{x_{i-1,j}-x_{i,j-1}}{2}\left\{\frac{(\psi_{i,j}-\psi_{i-1,j-1})(x_{i-1,j}-x_{i,j-1})-(\psi_{i-1,j}-\psi_{i,j-1})(x_{i,j}-x_{i-1,j-1})}{2Vc_{i-1,j-1}}\right\}$$
$$-\left(\frac{x_{i,j+1}-x_{i+1,j}}{2}\right)\left\{\frac{(\psi_{i+1,j+1}-\psi_{i,j})(x_{i,j+1}-x_{i+1,j})-(\psi_{i,j+1}-\psi_{i+1,j})(x_{i+1,j+1}-x_{i,j})}{2Vc_{i,j}}\right\}$$
$$-\left(\frac{x_{i+1,j}-x_{i,j-1}}{2}\right)\left\{\frac{(\psi_{i+1,j}-\psi_{i,j-1})(x_{i,j}-x_{i+1,j-1})-(\psi_{i,j}-\psi_{i+1,j-1})(x_{i+1,j}-x_{i,j-1})}{2Vc_{i,j-1}}\right\}$$
$$+\frac{x_{i,j+1}-x_{i-1,j}}{2}\left\{\frac{(\psi_{i,j+1}-\psi_{i-1,j})(x_{i-1,j+1}-x_{i,j})-(\psi_{i-1,j+1}-\psi_{i,j})(x_{i,j+1}-x_{i-1,j})}{2Vc_{i-1,j}}\right\} \tag{6.48}$$

Since we are dealing with a 2-D BVP, Vc, Vn represent the arrays for the area cells and nodes or the vectors expressed with nodal area and cell area, respectively. Further manipulations lead to

$$-\alpha_1\psi_{i+1,j+1}+\alpha_2\psi_{i,j}+\alpha_3\psi_{i,j+1}-\alpha_4\psi_{i+1,j}-\alpha_5\psi_{i-1,j}-\alpha_6\psi_{i-1,j+1}-\alpha_7\psi_{i-1,j-1}-\alpha_8\psi_{i+1,j-1}+\alpha_9\psi_{i,j-1} = \tilde{\lambda}\psi_{i,j} \tag{6.49}$$

Details of the derivation are given in the appendix. By letting $\tilde{\lambda} = \tilde{E}Vn$, the resulting eigenvalue equation describing the 2-D BVP using CFDM, can succinctly be expressed as:

$$\mathbf{W}\psi = \lambda\psi \tag{6.50}$$

Conversely, the SFDM for the 2-D case using a five-point computational stencil can be expressed compactly as:

$$4\psi_{i,j} - \psi_{i+1,j} - \psi_{i-1,j} - \psi_{i,j+1} - \psi_{i,j-1} = \bar{\lambda}\psi \tag{6.51}$$

Hereby, it is assumed that the grid is uniform along both axes, with increments $\Delta = \Delta x$ and $\bar{\lambda} = 2\Delta^2 mE/\hbar^2$. We obtain,

$$\mathbf{L}\psi = \bar{\lambda}\psi. \tag{6.52}$$

The results of these schemes are presented in the following section and the numerical results are interpreted appropriately. The algorithmic scheme presented in the form of a flowchart is shown in Fig. (6.2). Figure (6.3) depicts the 2-D grid for the BVP. Dirichlet boundary conditions are imposed for the sake of simplicity. Here, L represents the uniform length of the grid and $V(x, y) = 0$ expresses the vanishing potential inside the simulation domain. The wavefunction on or outside the Dirichlet boundary condition and infinite potential well are taken to be zero. Hence, in achieving the obtained results, the flowchart is followed step-by-step during the implementation of the developed software program.

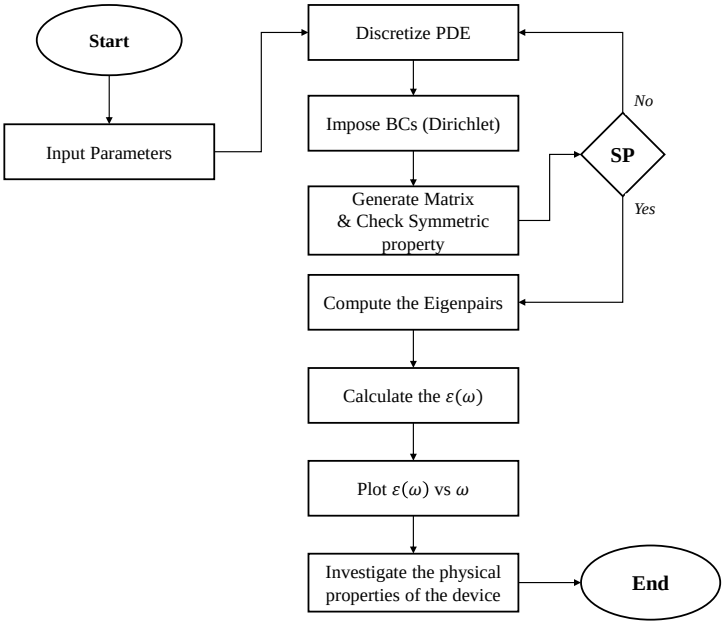

Figure 6.2: The flowchart of the algorithm used for the implemetation of the SFDM and CFDM

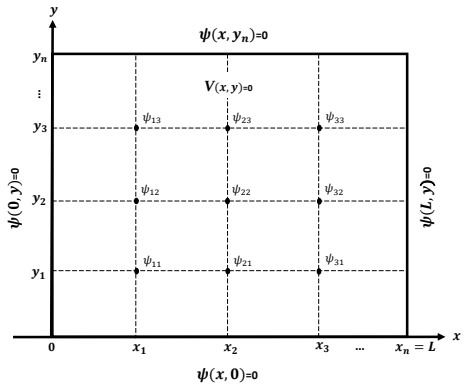

Figure 6.3: The grid used for the implementation of the SFDM and CFDM subject to Dirichlet boundary conditions

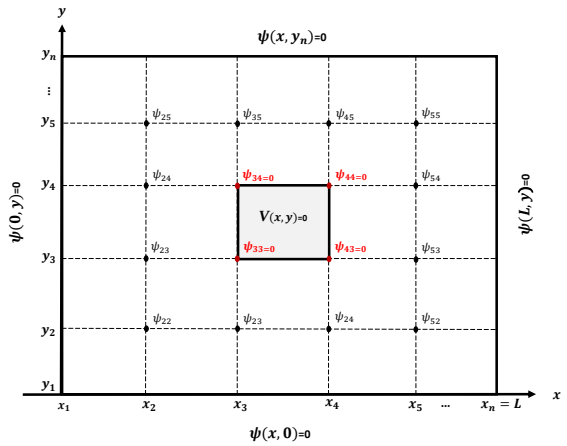

Figure 6.4: The grid used for the implementation of the SFDM and CFDM subject to Dirichlet boundary conditions with punctured scheme

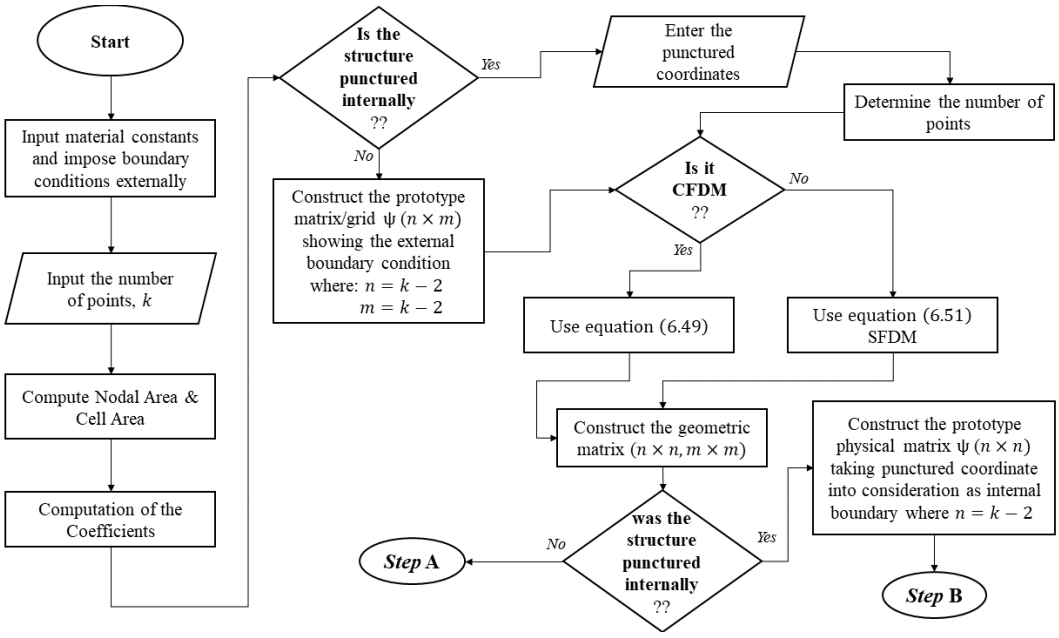

Figure 6.5: The flowchart used for the implementation of the SFDM and CFDM subject to Dirichlet boundary conditions with and without punctured Scheme

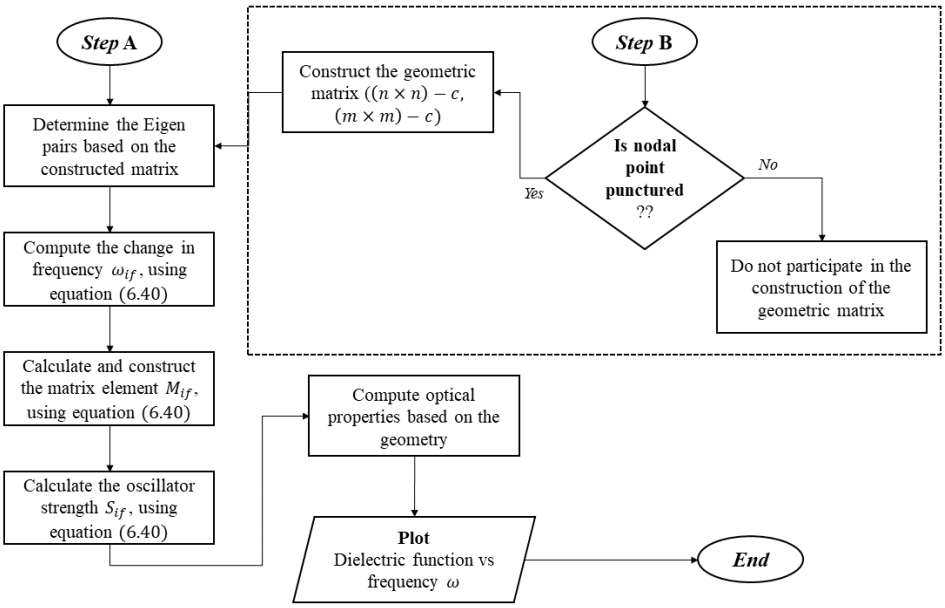

Figure 6.6: The flowchart used for the implementation of the SFDM and CFDM subject to Dirichlet boundary conditions with and without punctured

Figures (6.5) and (6.6) depict the flowchart developed for the implementation of SFDM and CFDM for metallic nanoparticles using the Schrödinger equation. In these figures, the algorithm was designed in a way that it solves the time-independent Schrödinger boundary value problem subject to Dirichlet boundary conditions applied externally and internally for the SFDM and CFDM. The developed code is flexible and robust, allowing the user to have full control over the distribution of the internal boundary points. The algorithm is capable of asking the user how many points to be created internally, apart from the imposed external boundary conditions. It goes further to decide what scheme (SFDM or CFDM) should be employed in the discretization of the partial differential equations (PDEs) of solving the Schrödinger equation. Subsequently, it constructs the system matrix and computes the corresponding eigenpairs. The eigenpairs are used to compute the optical properties of the metallic particles of interest, with fairly general geometries.

6.4 Numerical Results and Discussion of SFDM and CFDM for Unpunctured and Punctured Geometries

In this section, numerical simulations for unpunctured and punctured geometries using SFDM and CFDM are presented.

6.4.1 Results and Discussion for SFDM and CFDM for 2-D Models for Particles

In the following, the numerical results for both the SFDM and CFDM are presented. The numerical solutions using the SFDM and CFDM, with no internal holes, are depicted in Figs. 6.7 (a and b) . Figures 6.7 (c and d) present results of geometries with internal holes. The results show the real-and imaginary parts of frequency-dependent dielectric function, and refractive index for CFDM with a factor approximately ten times that of SFDM. This reveals the conservative nature of CFDM as against the SFDM after going through the discretization process. The discrete solution is highly oscillating as depicted in Fig. 6.7. The same can be said of a case when the geometry is punctured as shown in Figs 6.7 (c and d). The performance of CFDM is superior to SFDM, as expected owing to its conservative. Furthermore, a numerical comparison has been successfully made between the SFDM and CFDM in this thesis and both schemes were employed with and without an internal puncture. The model employed (Figs. 6.3 and 6.4) consists of a uniform grid along both x- and y-axes

for simplicity. A grid of N-by-N points was applied. This geometry has been chosen to demonstrate the differences between the methods without unreal overstatement; improved differences can easily be achieved by using a more robust scheme. The numerical equations were solved on an ACER computer system with core i7, 20G RAM, 1 Terabyte of Hard drives, 250 GB Solid-state drive (SSD). The computation was nearly the same for the 1D system in terms of setting up the system matrix , apart from the few cases that have to do with the computation of coefficients using both methods. However, the difference is appreciable in the case of 2D, as shown in Figs. (6.7- 6.9). As expected, the higher the number of grid points or equivalently, the smaller the mesh size, the smoother the resulting data (curves).

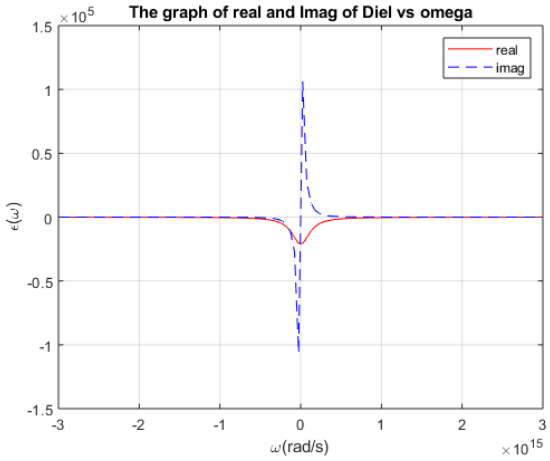

(a) The graph of real-and imaginary parts of the dielectric function vs ω

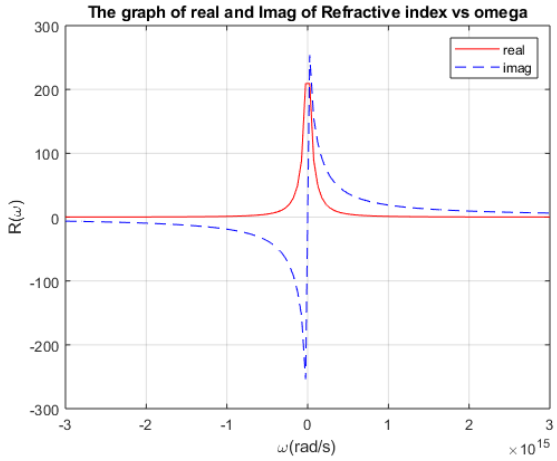

(b) The graph of real-and imaginary parts of the refractive index vs ω

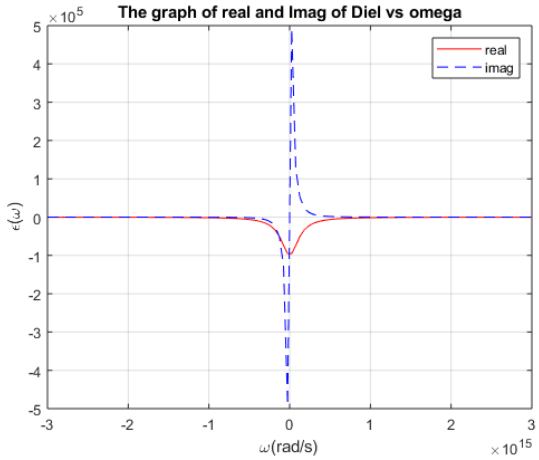

(c) The graph of real-and imaginary parts of the dielectric function (with hole) vs ω

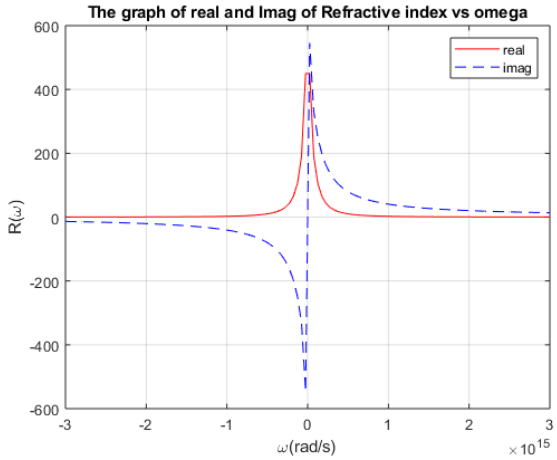

(d) The graph of real-and imaginary parts of the refractive index (with hole) vs ω

Figure 6.7: Plots of real-and imaginary parts for the dielectric function and the refractive index CFDM vs ω

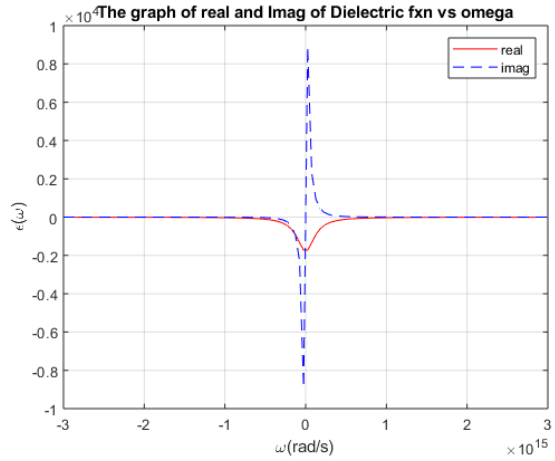

(a) The graph of real-and imaginary parts of the dielectric function vs ω

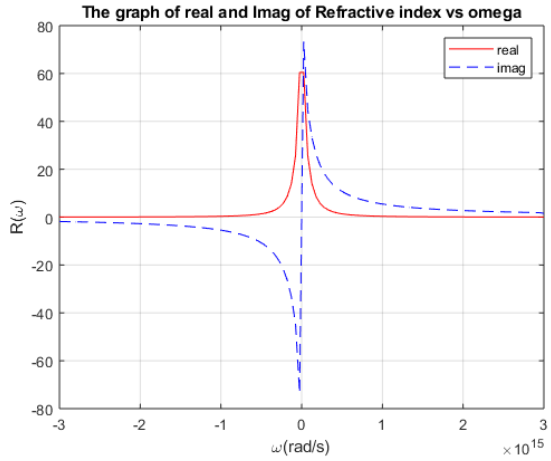

(b) The graph of real-and imaginary parts of the refractive index vs ω

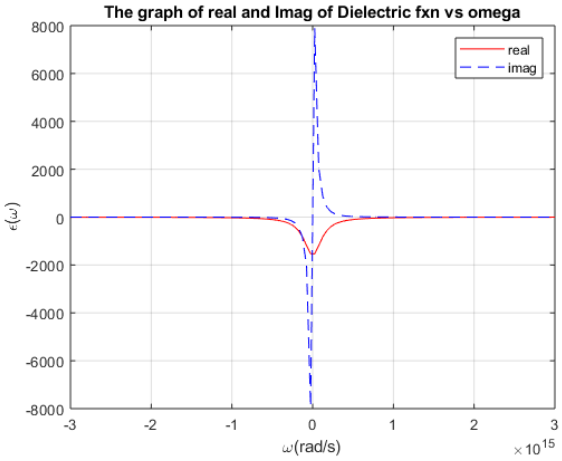

(c) The graph of real-and imaginary parts of the dielectric function (with hole) vs ω

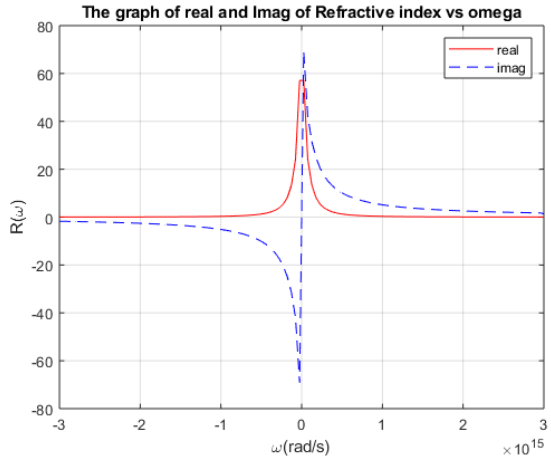

(d) The graph of real-and imaginary parts of the refractive index (with hole) vs ω

Figure 6.8: Plots of real-and imaginary parts for the dielectric function and the refractive index vs ω (SFDM)

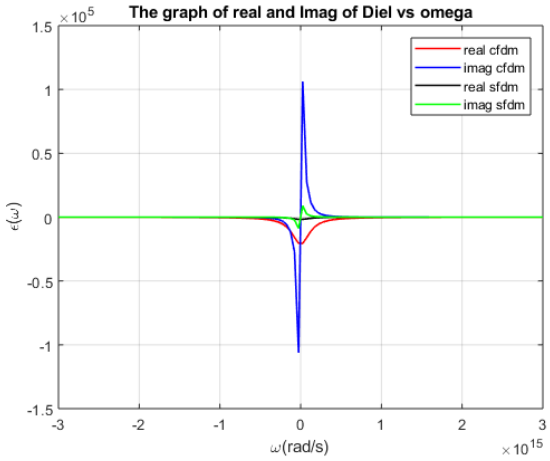

(a) The graph of real-and imaginary parts of the dielectric function vs ω

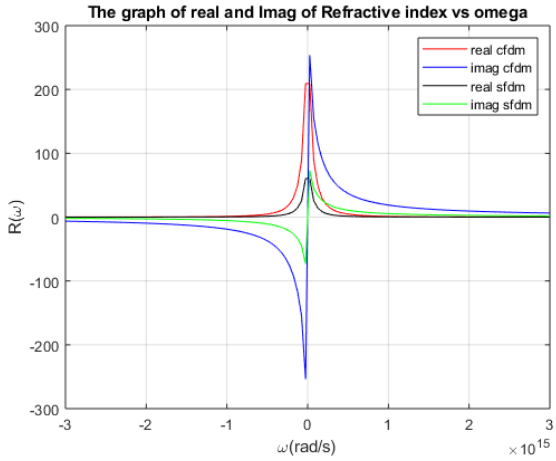

(b) The graph of real-and imaginary parts of the refractive index vs ω

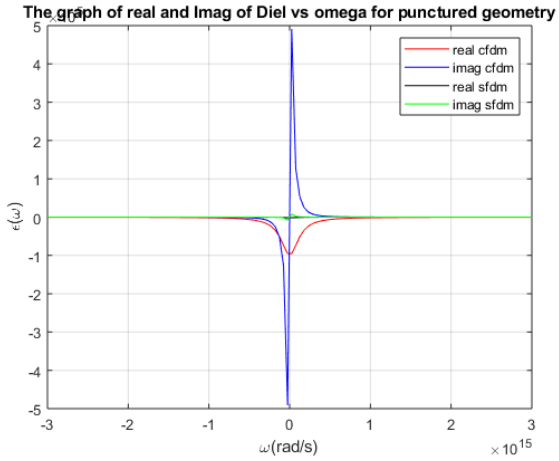

(c) The graph of real-and imaginary parts of the dielectric function (with hole) vs ω

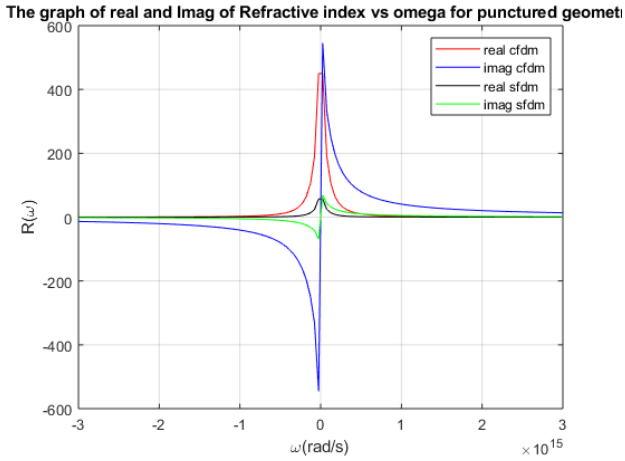

(d) The graph of real-and imaginary parts of the refractive index (with hole) vs ω

Figure 6.9: Numerical comparison between SFDM and CFDM with and without hole of the real-and imaginary parts for the dielectrc function and the refractive index vs ω

6.5 Summary of the Chapter

We have examined the optical properties of metallic nanoparticles of a one- and two-dimensional geometries. To this end, the Schrödinger equation was solved numerically using SFDM and CFDM. The Standard Finite Difference Method was not capable of producing accurate solutions alluding to the loss of some features of the original operator as a result of the discretization. To remedy this shortcoming, and to ensure that salient features of the original differential operator remain unchanged, CFDM was employed. The proposed scheme in this thesis (the successful application of CFDM, as applied to the Schrödinger equation), for the first time promises to have opened up avenues for further research in the field of small-scale plasmonic devices.

Chapter 7

Application of Density Functional Theory to Boundary-Value Problems for Metallic Nano-particles

7.1 Introduction

The current contribution is dedicated to the application of Density Functional Theory (DFT) in plasmonics, photonics and electrical engineering; more specifically in the modelling and simulation of physical properties of metallic nano-particles. The DFT has established itself as a useful computational tool since it can be used either to identify among properties that are left open or corroborate the findings that have been arrived based on the experimental analysis. The computation of a broad range of optical properties by means of DFT permits a strong correlation between experiment and theory, and usually gives rise to crucial limits

regarding the electronic- and geometrical features of the problem being examined. In this study, we firstly present in brief the general theory that forms the foundation of the DFT method. Thereby, the priority is to explain what can be accomplished by implementing DFT and interpreting the numerical results. We focus on relevant optical properties than can be calculated, and highlight DFT's unique computational flexibilities.

In this section, the ground state electronic system is of foundational significance to deducing realistic physical characteristics of the systems considered. Hence, the Schrödinger equation is used to precisely compute the required ground state. The ground state eigenfunction can be computed by minimizing the total energy with respect to all degrees of freedom (DoF) entering the wavefuntion (ψ), subject to the constraints of symmetry of particles and normalization. For an eigenfunction or eigenstate, associated with an eigenstate, the time-independent parameter of the total energy is regarded as the expectation value of the Hamiltonian,

$$E = \frac{\langle \Psi | \hat{H} | \Psi \rangle}{\langle \Psi | \Psi \rangle}. \tag{7.1}$$

The appearance of $\langle \Psi | \Psi \rangle$ in the denominator is for the normalization of the wavefunction. The eigenstates of the Schrödinger time-independent equation are stationary points in nature. Hence, they can be obtained as solutions to the time-independent Schrödinger equation:

$$\hat{H} | \Psi \rangle = E | \Psi \rangle \tag{7.2}$$

Thus, the first stage in computing a ground state system is the consideration of the total Hamiltonian for the system including the electron-electron, nuclei-nuclei, and electron-nuclei

interactions,

$$\hat{H} = KE_e + KE_n + V_{en} + V_{ee} + V_{nn}. \tag{7.3}$$

Explicating the expression at the right-hand side term-by-term:

$$\hat{H} = -\frac{\hbar^2}{2m_e}\sum_i \nabla_i^2 - \frac{\hbar^2}{2M_I}\sum_j \nabla_j^2 - \sum_{i,I}\frac{Z_I e^2}{|r_i - R_I|} + \frac{1}{2}\sum_{i\neq j}\frac{e^2}{|r_i - r_j|} + \frac{1}{2}\sum_{I\neq J}\frac{Z_I Z_J e^2}{|R_I - R_J|} \tag{7.4}$$

The electrons are characterised by using lower- case subindices while the nuclei are denoted by upper-case subindices. The electron mass is denoted by m_e, the nuclei masses and charges, respectively, are denoted by M_I and Z_I; and r_i and R_I are the position vectors specifying the locations of electrons and nuclei, respectively. Equation (7.4) represents the many-body total Hamiltonian comprising Coulombic interactions between the charged particles in the system. H is of paramount significance to further elucidate the building block additive terms at the right-hand side in Eq.(7.4). To simplify the discussion, consider:

$$\hat{H} = \hat{T}_{ee} + \hat{T}_{nn} + \hat{V}_{ext} + \hat{V}_{int} + \hat{V}_{nn} \tag{7.5}$$

where $\hat{T}_{ee}$ and $\hat{T}_{nn}$ are the kinetic energy terms associated with electrons and ions, respectively. Hence, from the electronic perspective, the Coulombian potentials of the nuclei are considered as external to the electrons, and the Coulombian potentials of the electrons interacting with one another are seen to be internal to the system. The Coulombic potential energy of the electron-electron and electron-nucleus interaction, respectively, are denoted

by V_{int} and V_{ext}. The Coulombian nuclei-nuclei interactions are accounted for by the last potential energy term, $\hat{V}_{nn}$.

It is a known fact that the Schrödinger equation with the total Hamiltonian 7.5, and involving more than two interacting bodies, cannot be solved in closed-form. The hydrogen atom is the only archetypical two-body problem in 3-D which can be solved in closed-form. The factorized eigenstates of the H-atom have favourably been utilized in this work. Additionally, using numerical approach, the Hamiltonian gives rise to a system which practically unachievable to provide solution with sound and justified accuracy for all simply insignificant systems. In the next session, the estimation employed to transform this fully interacting, multi-body Schrödinger equation into a flexible and manageable problem are discussed.

7.2 Theoretical Background of Density Functional Theory and Related Studies

To realize the remarkable importance of the Density Functional Theory (DFT) in the twenty-first-century of quantum mechanical modelling and simulation of metallic nano-particles, it is worthwhile to begin with the investigation of the conventional wavefunctions-inspired schemes. The approaches seek to inexact solutions to the known Schrödinger equation, the foundational equation of quantum mechanics that chronicles a rundown any given system involving arbitrarily-shaped metallic nano-particles. The foundation for these methods originates from the research put forward by Hartree and Fock (HF) in the nineteen-century

around 1920s [150]. The HF scheme presumes that the correct Multi-body wavefunctions of the system considered, can be estimated by the use of Slater-determinant of M spin-orbitals. Furthermore, by applying the principle of variational scheme, it is possible to derive a set of M-paired equations for the M-spin orbitals. The numerical solutions of this set of equations lead to the so-called the Hartree-Fork wavefunctions and associated eigenvalues (energies) of the system which are upper-bound estimation of the actual ones.

The principal demerit of the HF scheme is that it explores particles, specifically electrons, as if they were moving around independently from one another. The HF scheme ignores correlation among electrons. On this basis, the effectiveness and straightforwardness of the HF approach is counterbalanced by shoddy implementation for the systems in branches of physics and chemistry, such as bio-inspired inorganic chemistry. Accordingly, HF is now majorly employed purely as an initial step for more rigorous the first principle quantum mechanical schemes, such as paired cluster or configuration interaction concerning HF, for estimating the actual eigenstates. Regrettably, the methods based on the HF scheme normally lead to challenges, when applied to bio-inspired systems.

The DFT seeks to resolve both the inexactness associated with HF and the high demands of computations subsequently following the HF scheme. This objective usually achieved by changing the many-body electron system eigenstate with electronic density as the fundamental entity [151], [152]. The eigenstate of an M electron-system relies on $3M$ variables; i.e., a three spatial parameters for each of the M particles (electrons), the density only depicts on three variables and is, consequently, a much easier problem to cope with. The electron correlation is involved indirectly form from the starting of the process. Present-day

DFT depends on two theorems put forward by Hohenberg and Kohn [153], [154]. The first theorem states that the electronic density uniquely determines the electron wavefunction, and thus all, the derived ground-state features of an electronic system. The second theorem states that the energy (eigenvalue) of electron distribution can be explained as a functional of the electron distribution, and this functional entity is the lowest for the ground-state density. Compactly put, the two theorems can be recast as the ground state densisty uniquely determines the external potential and consequently the wavefunction, energies and further information derived thereof. Hence, the difficulty of solving the many-body Schrödinger equation is avoided and the aim becomes the minimization of a density functional. It should be noted, that while the Hohenberg-Kohn theorems guarantee us that the density functional has become a universal entity; its form is never specified. In theory, the usual implementation of DFT is via the Kohn-Sham scheme. The KS scheme is functionally and practically based on a version of the HF method involving the structure of non-interacting system of particles and resulting in the same density as the starting problem [153].

It should be stated here explicitly that it is computationally straightforward to find solutions for non-interacting systems, since the characterising wavefunctions can be precisely typified as a Slater-determinant of particle orbitals. The nature of the kinetic energy functional of typical system is precisely noted, and solely undetermined parameter is the exchange-correlation functional. Therefore, the principal challenge of DFT is here; The actual functionals for correlation and exchange are yet to be determined, apart from the free-electron gas. Hence, a large number of estimates exist which allow the computation of molecular, electronic, and optical properties at different levels of accuracy.

The foundational, and easiest, approximation is called local-density approximation (LDA). The LDA is the energy that relies solely on the density at the juncture where the functional is analysed [155]. The LDA deduced solution that the density agrees with that of homogeneous electron gas, which has been shown to be an enhancement over Hartree Fock. It is noted that while LDA happens to be a major driving force in the field of solid state physics, however, its successfulness in physics, chemistry, and engineering is at best average owing to its strong propensity for over-binding. The first advancement occurred with the discovery of functionals belonging to the so-called generalized gradient approximation (GGA) which includes a reliance not only on the electron density but also on its gradient. Hence, GGA is capable of describing more suitably the inhomogeneous form of the molecular densities that arise [156–160].

7.3 Summary of Fundamental Theories and Approximations

In this section, the main fundamental theories and approximations for the modelling and simulation of metallic nano-particles are discussed.

7.3.1 Born-Oppenheimer Approximation

By using Born-Oppenheimer (BO) estimation to solve the wavefunction of a single molecule, it is required that the solution of TISE in space is sought. This can be achieved by splitting

the total wavefunction of the system into its electronic- and nuclear constituent terms:

$$\Psi_{tot} = \Psi_e \times \Psi_n \tag{7.6}$$

It is assumed that the ions are big enough to be considered immobile and thus effects related to their motion are negligible. Hence, the total wavefunction describing electrons is solved by assuming the nuclei counterpart to be static. This leads to solving an electronic wavefunction of the TISE:

$$\hat{H}_{ee}(r, R)\Psi_{ee}(r, R) = E_e(R)\Psi_{ee}(r, R) \tag{7.7}$$

where r and R denote the coordinates of the electrons and nuclei, respectively. The Hamiltonian does not involve the kinetic energy associated with nuclei. Therefore, the eigenvalues of the electron energy ($E_e(R)$) rely on the ionic coordinates; R. Once the electronic wavefunction Ψ_{ee} is solved for, it can be employed to generate the potential energy for the Schrödinger equation containing only the nuclei expressed as:

$$\left[T_{nn} + E_{ee}(R)\right] \Psi_{nc} = E\Psi_{nc} \tag{7.8}$$

The energy E at the right-hand side represents the eigenvalues for the whole system. It should be reiterated that, since the nuclei are significantly bigger than electrons, the nuclear coordinates are changed incrementally and the wavefunction for the electrons are fully recalculated for each stage. This is the quintessence of the adiabatic proposition. Therefore, the BO approximate can be viewed as a significant computational accelerator, and generally

provides first-class estimates for obtaining highest degree of function. In the case of strong electron-phonon interactions where the electrons and nuclear positions cannot be separated, the BO approximation is however a powerful first step to providing solutions to these systems through a pertubative method [159].

7.3.2 Concept of Density Functional Theory

The Density Functional Theory (DFT) is pivotal in this study to solve boundary value problems involving metallic nano-particles. Even with efficient approximation techniques such as Born-Oppenheimer approximation and resulting to pseudopotentials, solving the Schrödinger equation with the multi-body Hamiltonian operator in Eq. (7.4), is a daunting undertaking. The Density Functional Theory allows the reformulation of many interacting particles to particles acting inside an effective potential. This effective potential is regarded as the mean-field resulting from other particles in the system.

The overarching idea is that all relevant attributes of the multi-particle system can be deduced from a position-dependent function; i.e., the ground state (GS) density function as $n_{og}(r)$. In other words, by knowing the GS density is tantamount to knowing the GS wavefunction and all other states above GS (excited states). As we gear towards scrutinizing the Kohn-Sham mathematical formulation, there is no need for the Hamiltonian in Eq. (7.4) which operates on a wavefunction in $3M$-dimensional space. Hence, we can make use of autonomous-particle wavefunction and deduce all the features of the system from scalar functions of GS density in three-dimensions. As given by the Born-Oppenheimer approximation, it is instructive to examine the electrons independently from the nuclei. The

nuclei are usually considered as an external potential V_{ext} in which the electrons rest. Hence, the kinetic energy associated with ions and self-interaction potential energy are taken into consideration independently. The Hamiltonian of Eq. (7.4) for the electronic part leads to:

$$\hat{H} = -\frac{\hbar^2}{2m_e}\sum_i \nabla_i^2 - \sum_i V_{ext}(r_i) + \frac{1}{2}\sum_{i\neq j}\frac{e^2}{|r_i - r_j|} \tag{7.9}$$

The 1/2 factor in the 3^{rd} term at the right-hand side ensures that the electron-electron interactions potential are not counted twice. This challenging multi-body problem can generally be split into simpler single-body equations owing to the electronic Coulombian self-interaction or no self-interaction as the case maybe. Thus, the Hohenberg-Kohn propositions give a first insight into a solution to this problem by allocating a unique importance to the GS particle density [156].

7.3.2.1 Hohenberg-Kohn Propositions

It should be stated that DFT is based on two theorems propounded by Hohenberg and Kohn and stated compactly as: *The first theorem states that for any system with interacting particles, the external potential V_{ext} is uniquely determined by up to a constant quantity by the GS electronic particle density.* The second theorem states that *for any external potential V_{ext}, the energy functional can be defined in terms of particles density: $E[n(r)]$.* The particles density which minimizes the aforementioned energy functional is the sought after density associated with GS. Therefore, the proof of the first theorem (by contradiction) can be done in this way by assuming that there are two particles differing by more than a constant with the same GS density [153]. Let the potential 1 and its wavefunction be given

as: $V_{ext}^{(1)} \rightarrow \Psi_0^{(1)} \rightarrow n_0^{(1)}(r)$; $n_0^{(1)}(r) = n_0^{(2)}(r)$ and the potential 2 and its wavefunction be given as: $V_{ext}^{(2)} \rightarrow \Psi_0^{(2)} \rightarrow n_0^{(2)}(r)$. By comparing the expectation value of the wavefunction 1 in Hamiltonian 1 which should be lower than that of wavefunction 2:

$$\langle \Psi_0^{(1)} | H_0^{(1)} | \Psi_0^{(1)} \rangle < \langle \Psi_0^{(2)} | H_0^{(1)} | \Psi_0^{(2)} \rangle \tag{7.10}$$

$$\langle \Psi_0^{(1)} | H_0^{(1)} | \Psi_0^{(1)} \rangle = \langle \Psi_0^{(1)} | T | \Psi_0^{(1)} \rangle + \langle \Psi_0^{(1)} | U | \Psi_0^{(1)} \rangle + \int dr V_{ext}^{(1)}(r) n_0^{(1)}(r) \tag{7.11}$$

$$\langle \Psi_0^{(2)} | H_0^{(1)} | \Psi_0^{(2)} \rangle = \langle \Psi_0^{(2)} | T | \Psi_0^{(2)} \rangle + \langle \Psi_0^{(2)} | U | \Psi_0^{(2)} \rangle + \int dr V_{ext}^{(2)}(r) n_0^{(2)}(r) \tag{7.12}$$

Hence,

$$\langle \Psi_0^{(1)} | T | \Psi_0^{(1)} \rangle + \langle \Psi_0^{(1)} | U | \Psi_0^{(1)} \rangle < \langle \Psi_0^{(2)} | T | \Psi_0^{(2)} \rangle + \langle \Psi_0^{(2)} | U | \Psi_0^{2} \rangle. \tag{7.13}$$

Thus, the expectation value of wavefunction 2 in Hamiltonian 2 should be lower than that of wavefunction 1 as expressed as:

$$\langle \Psi_0^{(1)} | H^{(2)} | \Psi_0^{(1)} \rangle > \langle \Psi_0^{(2)} | H^{(2)} | \Psi_0^{(2)} \rangle \tag{7.14}$$

After some mathematical manipulations,

$$\langle \Psi_0^{(1)} | T | \Psi_0^{(1)} \rangle + \langle \Psi_0^{(1)} | U | \Psi_0^{(1)} \rangle > \langle \Psi_0^{(2)} | T | \Psi_0^{(2)} \rangle + \langle \Psi_0^{(2)} | U | \Psi_0^{(2)} \rangle. \tag{7.15}$$

Therefore, two different potentials cannot lead to identical GS density. This is regarded as absurdity. The GS density uniquely determines the external potential and consequently the wavefunctions, energies, and other derived quantities of interest. The second theorem

depends on the first theorem which states that all features of a system are uniquely determined by the particle density $n(r)$. Hence, the total energy of many-body electronic system is a functional of this density. This can be expressed as:

$$E = E[n(r)] = F[n] + V_{ext} = \int drV_{ext}(r)n(r) + \frac{1}{2}\int drdr'\frac{n(r)n(r')}{|r-r'|} + others \qquad (7.16)$$

In principle, any property of a system can be obtained from the ground state (GS) density can be obtained. One has to determine the M multi-body eigenfunctions and then proceed from this point. Hence, DFT would have a limited value if it were not for the sake of further modification of Kohn-Sham (KS) method which allows one to make useful approximations to the original GS functionals and powerfully account for the underlying physics.

7.3.2.2 Kohn-Sham Theory and Equation

The scheme put forward by Kohn and Sham in 1965 is to bring single electronic orbitals back into play by rewriting the multi-body Hamiltonian of Eq.(7.4) as an independent particle system that produces precisely the same GS density [155], [156]. Essentially, the electrons are imagined to be unrelated except for what is needed to fulfil the Pauli's exclusion principle. An effective potential is then added to estimate the impacts of many-body correlation, however, the problem now becomes one in which the densities interact instead of particle wavefunctions. The vital proof here is that it can be demonstrated that the GS density of the interacting many-body system can be populated from a simpler system of autonomous particles. Thus, all the multi-body interactions are ignored from an effective potential in which the particles (electrons) move.

Consequently, we are concerned with a set of different particle Schrödinger equation that is exactly solvable, in principle. Compactly, it is expressed as:

$$\left(-\frac{\hbar^2}{2m}\nabla^2 + V_{eff}\right)\psi_i = \epsilon_i\psi_i \tag{7.17}$$

where ψ_i denote the autonomous particle orbitals. For a system with M electrons, the GS consists of the M lower-energy orbital. We are then at liberty to derive the density of the system by aggregating the effect of each orbital as expressed as:

$$n(r) = \sum_{i=1}^{M} |\psi_i(r)|^2 \tag{7.18}$$

We now recast the multi-body Hohenberg-Kohn energy functional in the following self-consistent particle compact form:

$$E_{KS}[n] = T_s[n] + \int dr^3 V_{ext}(r)n(r) + E_H[n] + E_{xc}[n] \tag{7.19}$$

Here, $T_s[n]$ is regarded as independent kinetic energy for a single particle and expressed as:

$$T_s[n] = \sum_{i=1}^{M} \langle\psi_i| - \frac{\hbar^2}{2m}\nabla^2|\psi_i\rangle \tag{7.20}$$

In Kohn-Sham method, the functional F is broken down into the following terms:

$$F[n] = \int drn(r)V(r) - \sum_i \int dr\psi_i^*(r)\frac{\nabla^2}{2}\psi_i(r) + \frac{1}{2}\int\int \frac{drdr'n(r)n(r')}{r-r'} + E_{xc}[n] \tag{7.21}$$

The relationship between the density $n(r)$ and the wavefunction $\Psi_i(r)$ is expressed as:

$$n(r) = \sum_i |\Psi_i(r)|^2 \tag{7.22}$$

The HK states that the total energy assumes minimum point with respect to its GS electronic density. This feature equips us with a recipe to calculate the Kohn-Sham wavefunction. The principle of minimum point can be expressed as using functional derivative:

$$\frac{\delta F}{\delta n} = 0 \tag{7.23}$$

$$\frac{\delta F}{\delta \psi_i^*} = \frac{\delta F}{\delta n}\frac{\delta n}{\delta \psi_i^*} = \frac{\delta F}{\delta n}\psi_i \tag{7.24}$$

By unifying the two equations above, the Kohn-Sham orbital should thus satisfy this condition with orthonormal condition expressed as:

$$\frac{\delta F}{\delta \psi_i^*} = 0 \tag{7.25}$$

$$\langle \psi_i | \psi_j \rangle = \delta_{ij} \tag{7.26}$$

This ensures that the density $n(r)$ in (7.22) is accurately minimized to M electrons. Hence, constraint optimization problem, expressed in terms as (7.25) and (7.26), is formally the same as the one in Hartree Fock (HF)formulation, [160]. Next introduce the Lagrange functional

denoted as $\mathcal{L}$ and compactly expressed as:

$$\mathcal{L} = F - \sum_{ij} \lambda_{ij} \left[\langle \psi_i | \psi_j \rangle - \delta_{ij} \right] \tag{7.27}$$

Here, λ_{ij} are the constant Lagrange multipliers. Therein, we search for extreme points for the new functional:

$$\frac{\delta \mathcal{L}}{\delta \psi_i^*} = 0 \rightarrow \frac{\delta F}{\psi_i^*} = \sum_j \lambda_{ij} \psi_j \tag{7.28}$$

The function derivatives $\left(\frac{\delta F}{\psi_i^*}\right)$ can be calculated and evaluated by substituting (7.21) into (7.24) which gives:

$$-\frac{\nabla^2}{2}\psi_i(r) + \frac{\delta}{\delta n}\left[\int dr n(r) V_n(r) + \frac{1}{2}\int\int dr dr' \frac{n(r)n(r')}{|r-r'|} + E_{xc}[n]\right]\psi_i(r) = \sum_j \lambda_{ij}\psi_j(r) \tag{7.29}$$

Employing the definition of functional derivatives, (7.29) can be recast compactly as:

$$\left[-\frac{\nabla^2}{2} + V_n(r) + \int dr' \frac{n(r')}{|r-r'|} + \frac{\delta E_{xc}}{\delta n}\right]\psi_i(r) = \sum_j \lambda_{ij}\psi_j(r) \tag{7.30}$$

In (7.30), the Hartree potential $V_H(r) = \int dr' n(r')/|r-r'|$ and exchange and correlation potential denoted as $V_{xc} = \delta E_{xc}/\delta n$ can be recognised. The matrix entries λ_{ij} of the Lagrange multipliers can be solved using diagonalization process. Hence, after mathematical manipulations and simplifications, the Kohn-Sham (KS) equation which is used in this thesis can be cast as:

$$\left[-\frac{\nabla^2}{2} + V_n(r) + V_H(r) + V_{xc}\right]\psi_i(r) = \epsilon_i \psi_j(r) \tag{7.31}$$

7.3.2.3 Variational Principle and Self-consistent Solution

In order to solve the Kohn-Sham equation, it involves solving the autonomous particle Schrödinger equation (7.17) under the condition that the effective potential V_{eff} and density are agreeable. In theory, this is achieved by numerical method via successfully updating n and V_{eff} to obtain and attain self-consistently as shown in Fig. 7.1. An initial guess for the electron density is made . Subsequently, the V_{eff} is computed by taking into consideration the change of the total energy function with respect to the electron density. This leads to:

$$V_{eff}(r) = V_n(r) + \int dr' \frac{n(r')}{|r - r'|} + \frac{\delta E_{xc}[n]}{\delta n(r)} \tag{7.32}$$

This is an eigenvalue problem. This happens when the majority of the computational

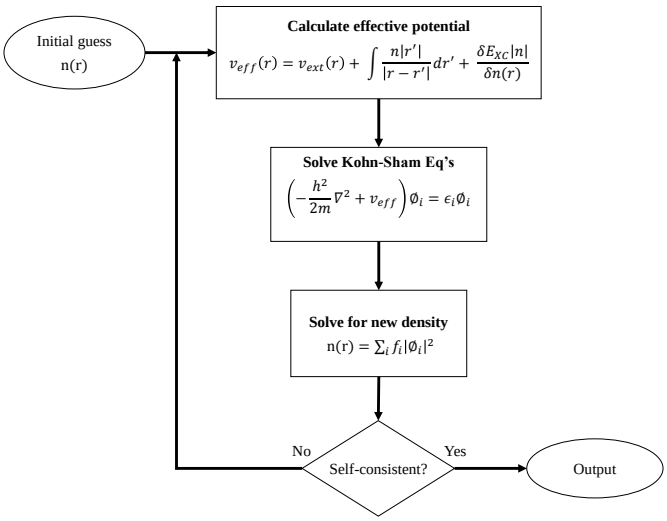

Figure 7.1: The flowcharting steps for the self-consistent scheme employed in solving the Kohn-Sham equation

attempt is exhausted in such a way that so much effort is employed to carry out optimization problem in computational electronics and devices. Eventually, the new particle density

$n(r)$ is computed. Owing to stability issues and challenges, the newly computed density is normally carried out as an average of the old and the new densities for lack of convergence. If it is self-consistent, there exists a solution if not, we recompute V_{eff} for the new density and implement the inner-loop conditions again [156, 157].

7.4 Methods Employed in the Solution of KS

In this section, a mixture of numerical techniques for providing solution to the Kohn-Sham equation are available and can be categorised fundamentally in three different classes namely localized atomic orbitals, atomic sphere schemes, and plane waves and grid system. In this thesis, SFDM is employed for the computations for the discretization of the Laplacian operator emanated from the contribution of kinetic energy. This scheme is capable of creating sharp characteristics that could be challenging to find using other schemes. In this study, methods employed such as conjugate gradient method (CGS), SFDM already discussed in previous chapter and Kronecker products ($\otimes$) to construct 1-D, 2-D, and 3-D functions using SFDM approximation of the Laplacian (Δ) with Dirichlet boundary conditions are briefly discussed [161–164].

The potentials, density and orbitals in Kohn-Sham equations are denoted as distinct points on a grid when using SFDM. Furthermore, the potential energies are diagonal in nature regarding the coordinate representation and more importantly the Laplacian is a sparse matrix operator depending on the approximation employed.

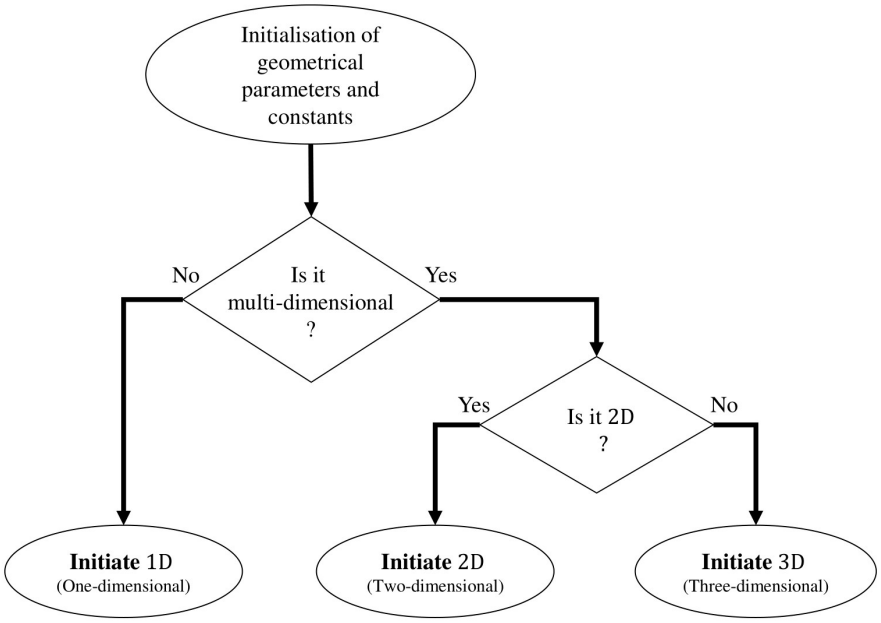

Figure 7.2: The flowcharting steps for the computation of optical properties

For instance, let the Kronecker product scheme in 3-D be denoted by L_{KPS}:

$$L_{KPS} = Dxx \otimes I \otimes I + I \otimes Dyy \otimes I + I \otimes I \otimes Dzz \tag{7.33}$$

Several numerical algorithms are available for calculating the Hartree potential energy (V_H). However, in this thesis, the conjugate gradient scheme is employed because of its fast convergence alongside subspace diagonalization. The Kohn-Sham equations are commonly worked out utilizing sparse matrix eigen-solvers in contrast to other schemes in literature. In this study, a self-consistent scheme as shown in Fig. 7.1 is employed for the representation of DFT computation which involves interacting particles. The first electron density guess is assumed and plugged into Eq. (7.17) and the eigenvalue problem is resolved for a novel set of orbitals. Subsequently, these orbitals are substituted back into Eg.(7.22) in order

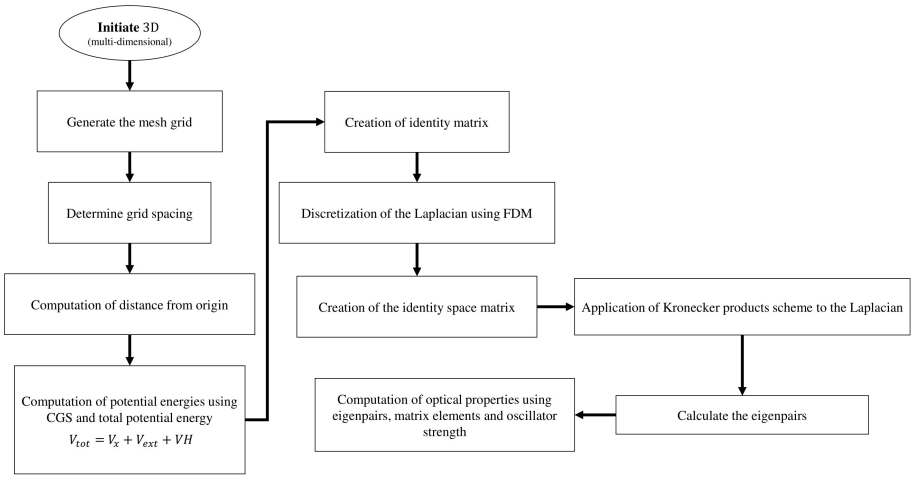

Figure 7.3: The flowcharting steps for the computation of optical properties for 3-D

to generate new density, and the loop iterates or reiterates until convergence measure is attained. Usually, the self-consistent scheme cycle is terminated when the modification in density or the modification in each of the computed eigenvalues becomes less than the set value. However, this does not ensure global convergence as the case may be.

In this study, we introduce local density approximation (LDA), exchange potential, Hartree potential and total energy with self-consistent algorithm to compute the optical properties of interest; i.e, frequency-dependent dielectric function. Firstly, the self-consistent scheme is used to compute the wavefunction. The computed wavefunction is employed to find the electronic density, and subsequently, the density $n(r)$ is employed to compute the Hartree potential energy (V_H) using conjugate gradient scheme. Then, the total energy is calculated alongside the total potential in order to compute eigenpairs. These eigenpairs are then used to compute the frequency-dependent dielectric function of the chosen metallic nano-particles via matrix entries and oscillator strength. Figures 2 and 3 show the steps involved in calculating the frequency-dependent dielectric function by using KS equation. The external

potential has a closed-form expression as $V_{ext} = -N/R$ where N in this case represents the number of electron for instance hydrogen atom; i.e, $N = 1$ and R is the distance of electron from the centre. The $V_H(r) = -4\pi n(r) = -4\pi(2|\psi|^2)$ and $V_x(r) = \left(3/\pi\right)^{\frac{1}{3}} n^{\frac{1}{3}}(r)$ are used, respectively as Hartree potential and exchange potential.

7.5 Results and Discussion for Density Functional Theory

In the following section, the numerical results of this computation concerning the KS using DFT are presented and discussed. The numerical solutions are obtained via simulations using the CGS for the computation of Hartree potential and Kronecker product scheme for the Laplacian with a uniform grid system of equally-spaced gridpoint. The SFDM operator employed to approximate the Laplacian can significantly reduce the accuracy of the computation. It is observed that the CGS converges fast at iteration 53 to a solution with relative residual of 4×10^{-16}. The results show the real-and imaginary parts of frequency-dependent dielectric function and refractive index, respectively. A lattice of N-by-N points was applied.

In this section, the following parameters are used for the simulation of the frequency-dependent dielectric function and refractive index for metallic nano-wire for silver (Ag). The length of the wire is 50×10^{-9} metres. We compute the real-and imaginary parts of the frequency-dependent dielectric function against the wavelength for a configuration of a metallic nano-wire. The following parameters for silver (Ag) are used for our simulations:

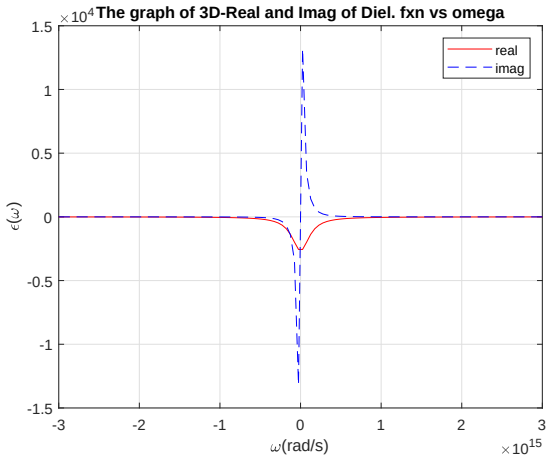

(a) The graph of real-and imaginary parts of the dielectric function vs ω

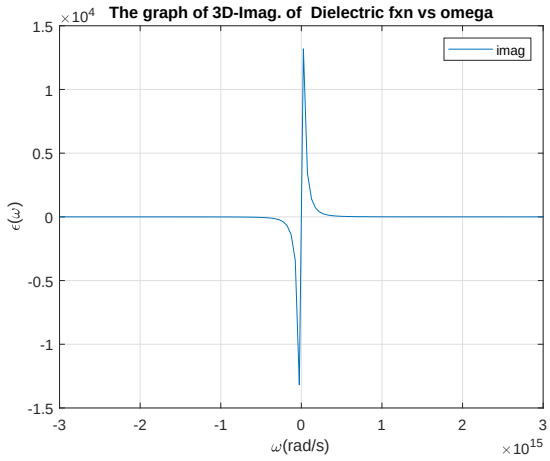

(b) The graph of imaginary part of the dielectric function vs ω

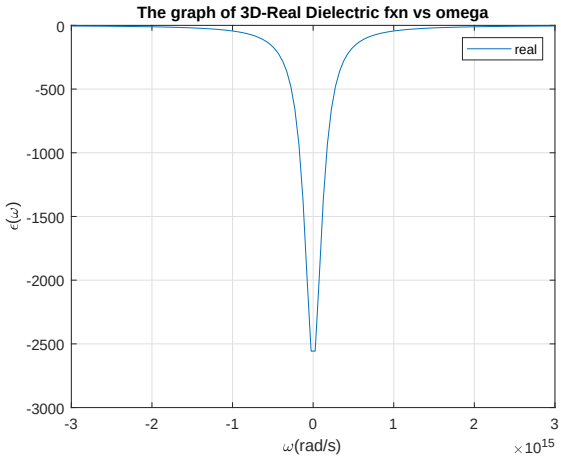

(c) The graph of real-part of Diel.fxn vs ω

Figure 7.4: Plots of the real and the imaginary parts for the dielectric function DFT-KS vs ω

$v_f = 1.39 \times 10^6 ms^{-1}$ for Fermi velocity, $\omega_p = 1.36 \times 10^{16} rads^{-1}$ for plasma frequency, $\gamma_{bulk} = 0.016$ for the damping constant in eV.

The numerical KS equations were solved on an ACER computer system with core i7, 20G RAM, 1 Terabyte of Hard drives, 250 GB Solid-state drive (SSD). The computation

was nearly the same for a 1-D system in terms of the populating the matrix. However, there are few disparities with respect to populating the matrix and computation of coefficients using both methods.

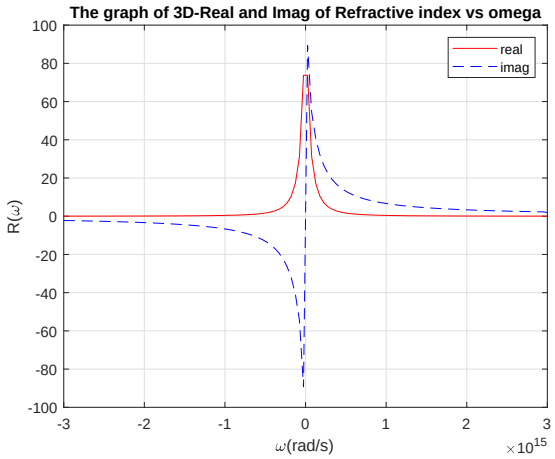

(a) The graph of real and imaginary parts of the refractive index vs ω

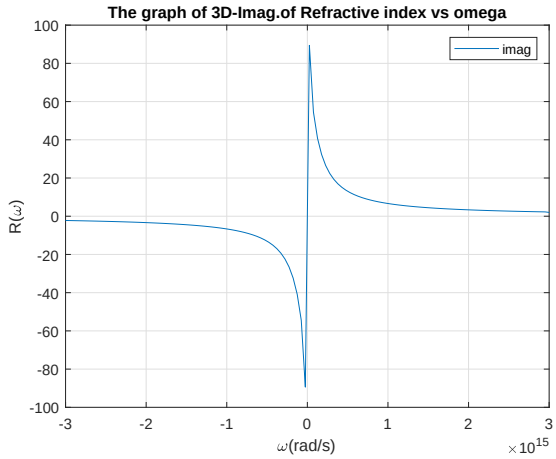

(b) The graph of real-part of the refractive index vs ω

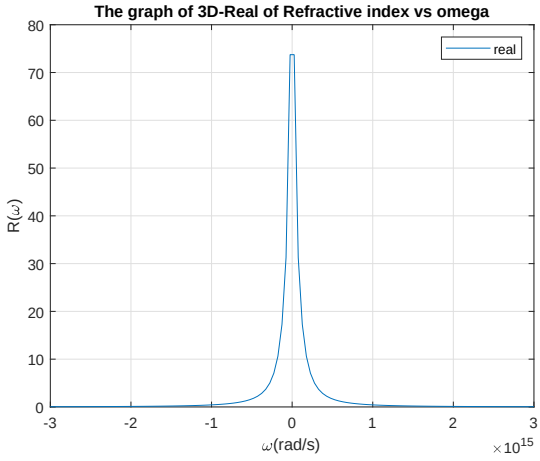

(c) The graph of imaginary part of the refractive index vs ω

Figure 7.5: Plots of the real-and imaginary parts for the refractive index using DFT-KS vs ω

The results for a case of 3D is presented. in Figs. 7.4 (a)-(c). The higher the number of grid points, the smoother the computed curve.

We choose silver (Ag) as the metallic material due to the availability of a range of data for the material. The real-part of the dielectric function is an even function while the imaginary counterpart of the frequency-dependent dielectric function is odd as shown in Figs. 7.4. The imaginary-part of the dielectric function exhibits a negative and positive slopes at some regions . The dielectric function decays to zero as the frequency tends to infinity as shown in Fig. 7.4*b* . Additionally, the corresponding results obtained for the frequency-dependent refractive index are displayed in Fig. 7.5.

Presumably, at a point close to operating frequency, the operating frequency ω is greater than the frequency difference $\omega_{i,f}$ giving rise to dips or side lobes for the real-part of the frequency-dependent dielectric function of metallic nano-wire. This suggests that different behaviour at different frequency windows (low, middle, and high frequency regions) in the dielectric function of metallic function as shown in the Fig. 7.4 exists. The plot of the real- and imaginary parts of the dielectric function of the geometry in consideration (3D) metallic system is shown in Fig. 7.4.

Owing to a change of sign in operating frequency ω and the frequency difference $\omega_{i,f}$, there is a negative shape of the real-part giving rise to dips. Furthermore , due to comparison of frequency at various regions, the real-and imaginary parts intersect. At $\omega_{i,f} > \omega$, the real-part of $\epsilon(\omega)$ is positive and $\omega_{i,f} < \omega$, $\epsilon(\omega)$ is negative and assumes dips or side lobes as shown in Fig. 7.4. In summary, the results obtained via the DFT by solving Kohn-Sham equation agrees appreciably with the previous results obtained using SFDM and CFDM as

reported in the previous chapter concerning the computation of optical properties such as frequency-dependent dielectric function.

7.6 Summary of the Chapter

The electronic structure computations play a vital role to play in forecasting crucial physical features such as optical frequency-dependent dielectric function of condensed-matter physics. Predicated on Density Functional Theory (DFT), the equation put forward by Kohn-Sham stands in for the interacting many-body systems as a challenge to solve by a corresponding set of self-consistently unique particle equations. It is, however, distinguishable from well-approved basis set scheme. In this study, a Standard Finite Difference Method (SFDM) is employed to discretize the Kohn-Sham (KS) equation in which the Laplacian operator (Δ) is discretized in the Finite Difference Scheme. Following the spatial discretization, the resulting eigenvalue problem is determined using a self-consistent iteration scheme with the updated information of electron density $n(r)$ and potential energies. Notwithstanding, the simplicity and flexibility of the SFDM, one has to carry out extensive computation of both eigenvalue and eigenvector alongside the potentials at every iteration stage. Additionally, for the eigenvalue problem, the conjugate-gradient method (CGM) is employed to solve for the potentials. The CGSM and SFDM have been employed to determine the eigenpairs of largely sparse system matrix. Furthermore, a Dirichlet boundary condition is utilized for the geometry in question. The starting point is the KS which comprises kinetic energy, external potential, Hartree potential, and exchange potential for which the complete set of eigenfunctions is easily obtainable using Kronecker products in compact form. Hence,

the eigepairs alongside wavefunctions and electron density are calculated. These eigepairs are employed to compute the physical properties of metallic nano-particles of interest such as frequency-dependent dielectric function. This study is crucial to quantum-mechanical modelling and simulation of nano-structures with arbitrary geometrical shapes and subject to boundary conditions dictated by real-life device constraints. This study promises to have set the foundation for a promising rigorous analysis of the electronic and photonic properties of small-scale devices. The results obtained produce reliable agreement with ones in this study and literature beside having fast convergence rate.

Chapter 8

Conclusion and Future Works

In this dissertation, quantum mechanical modelling and simulation of materials used in small-scale plasmonic devices have been investigated. Furthermore, different device problems have been studied using closed-form solutions and numerical approaches including SFDM, CFDM, and other closed-form, approximate, and semi-numerical schemes. Some of the assumptions adopted in this thesis aim to simplify the problems considered. In this dissertation, the focus has been to create models and to develop suitable methods for obtaining solutions of the developed models, for efficient calculation of the frequency-dependent dielectric function of nano-scale devices in low and high-frequency regions. The schemes presented in this thesis model device performance in terms of optical properties of metallic materials such as dielectric function, susceptibility, refractive index, and absorption coefficient. This doctoral thesis goes further to establish and employ different approaches for examining the frequency-dependent dielectric function of metallic material. The methods presented in this thesis are assessed by carrying out extensive systemic level simulations. Results of the simulations

enabled us to make observations and draw conclusions about the examined optical properties. In Sections 8.1-8.3, summary of the key contributions of the thesis, areas for future research, and some final remarks are outlined.

8.1 Explanatory Summary of Contributions in this Work

The need to develop robust and computationally-efficient models addressing changes in device responses as their size tends toward the nano-scale region constitute the fundamental goal of device characterization for next generation electronics and other areas of nanotechnology. With the ever-growing demand for new technologies based on nano-scale devices, the conventional and classical models need to be modified, amended, or fundamentally reconsidered to address and satisfy the many users' requirements on the basis of extreme miniaturization of signal processing and storage devices without compromising their operational functionalities. Therefore, the focal point of this study is to examine and offer efficacious model schemes that possess possibilities to reduce some of the technical challenges such as breaking down of device at certain range of frequencies, improper modelling and use of incorrect models and so on. This is necessary to ensure the designed devices perform optimally and efficiently for a specified range of frequencies.

In this study, vital factors including damping constant, size of the nano-particle, frequency, and material type have been examined in the modelling of the small-scale plasmonic device. In the instances considered, performance evaluation of the performance,

assessments of the existing models, along with the suggested schemes have been implemented, and painstakingly analysed. A comprehensive overview of this study follows next.

- A far-reaching review of latest developments in optical communications, plasmonics for the future of device modelling of small-scale device applications has been brought forward in **Chapter 2** regarding models used in macro- and bulk metallic devices. Notably, a comprehensive explanation of the types of models for the bulky materials has been presented. Furthermore, the technical problems which may occur as a consequence of incorrect use of material types and models for a particular case have been outlined. Additionally, existing classical models for the device modelling and their applications have been thoroughly scrutinized to offer deeper understanding into the modelling of the schemes as espoused in this dissertation. Furthermore, a concise explanation of some of the existing models concerning the modelling of plasmonic devices alongside their formulation has been put forward.

- In **Chapter 3**, the concept of plasmonics and its applications have been discussed. The applications include the MIM and IMI system . The implementation of these cases has been assessed based on the propagation length, H-field, E-field, and the dispersion relation of the materials used. The findings show that the wavevector can be used to compute relevant parameters as depicted in the chapter. The implemented algorithm requires a careful and well-structured scheme for the calculation of the wavevector, by using the cursor of the mouse as a way of customizing the software program. Subsequently, the dispersion relation, propagation length, and other metrics such as fields are computed with the convergence rate depending on the initial guesses.

- A quantum model for metallic nano-particles has been put forward for device modelling in **Chapter 4**. The application of theoretical band models for 1-D via rigorous theory is presented alongside its approximation using *Arctangent function approximation*. The performance measure in terms of optical properties such as susceptibility, dielectric function, and refractive index for both the theory and approximation schemes are presented, and the computed results thoroughly interpreted. Of particular interest is the comparison of the refractive index and the dielectric function for the theory and approximation with encouraging agreement. The observed disparities can be adduced to the uncertainty in the true value of material type volume fraction. It may also be a consequence of aggregation and backscattering effects which are not included in the model.

- **In Chapter 5**, application of quantum model to nano-particles has been established and presented for cubical, cuboid, and spherical particles. The optical characteristics and other relevant features such as absorption coefficient, dielectric function have been investigated and assessed with striking results obtained for each of the particles considered.

- **In Chapter 6**, the Standard- and Conservative Finite Difference Methods are presented to solve boundary value problems modelling metallic nano-particles. A customized and flexible software package for implementing SFDM and CFDM has been developed for 1- and 2-D models with and without punctured geometries. Due to paucity of time, 3-D geometries have not been considered. The package enables

the numerical solution of the desired homogeneous Dirichlet boundary value problems. The developed program is applied to solve time-independent Schrödinger equation for the modelling and simulation of physical properties of metallic nano-particles. The results obtained from SFDM and CFDM are compared. To the best of author's knowledge, it is the first time that the CFDM has been developed and applied to this class of boundary value problems to investigate the optical properties such as frequency-dependent dielectric function.

- **In Chapter 7**, DFT alongside KS equation has been employed as a powerful numerical investigation tool of optical properties of metallic nano-particles. In advantageous instances, the computed optical properties such as frequency-dependent dielectric function are adequately correct analytically and numerically. The DFT seems most reliable for geometrical structures, total energies and oscillating frequencies having over eigenfunction-based schemes in which the merit of fast convergence is key in this regard. The method can be employed to predict optical, molecular and electronic properties likewise. Being a numerical technique, there are limitations and inherent accuracies associated with DFT In spite of significant advancements in the DFT and achievable accuracy in simulations, it is observed that there is neither a procedural, systematic approach of improving the theory, accelerating its convergence rate nor in further increasing the accuracy of the method in terms of results to the precision. Here, the concept of density functional theory hybridized with the KS equation has been demonstrated to be a worthwhile candidate in solving and computing optical properties of interest. Therefore, the results obtained via DFT by jointly solving

Kohn-Sham equation agrees well with the previous results obtained using SFDM and CFDM as reported in the preceding chapter. The computational results concerning of optical properties including frequency-dependent dielectric function were compared.

8.2 Future Work

There are several lacunae in our knowledge around modelling small-scale plasmonic devices research that can be deduced from our findings; and would benefit from further investigation, and advancement of the theory presented in this work. The obtained results in this dissertation have also established the basis for a quantum mechanical understanding of the optical properties of metallic materials and their applications for future work in this field of research.

- One aspect for future work is in the combination of the knowledge gained regarding small-scale plasmonic devices with knowledge about the functionalities and behaviour of metallic materials in a certain band of operating frequencies.

- Another aspect is in applying the results obtained here to the many real-world situations using machine learning in which quantum-based metallic devices and materials have important challenges. More specifically, we mean that the data regarding material properties can be learnt over time and as such can be used to predict the behaviour and characteristic of any material at desired operating frequencies.

- A customized and flexible program for the implementation of SFDM and CFDM for punctured and irregular geometries can be developed for 2-D and 3-D structures

involving two interacting particles with spin effects. Additionally, the use of multi-physics simulation should be used to implement this while incorporating this CFDM into the simulation package.

- Adding a graphical user interface (GUI) to the developed program will enable the user to see how things go on in real-life cases.

- The DFT can be applied to boundary value problems involving punctured and unpunctured structures as this was out of the scope of this thesis. Additionally, the applications of these schemes can be extended to include multi-physics simulations. The comparison of DFT scheme can be carried out against SFDM and CFDM.

8.3 Final Remarks

This doctoral thesis investigated the quantum-based modelling and simulation of materials used in small-scale plasmonic devices. The work suggests recommendations for the future work. Consequently, this study has made contributions to the existing findings in the literature and proves useful to the design, modelling, and simulation of future exceedingly miniaturized devices and their applications at ultra-high frequencies. The hybridization of DFT and CFDM promises the creation of a computational platform for multi-physics modelling and simulation at nano-scale.

References

[1] R.Waser, *Nanoelectronics and Information Technology*. John Wiley & Sons, New York, 2005. 1, 3

[2] R. P. Feynman, R. B. Leighton, and M. Sands, "The feynman lectures on physics; vol. i," *American Journal of Physics*, vol. 33, no. 9, pp. 750–752, 1965. 2

[3] T. K. Sarkar and M. Salazar-Palma, "Maxwell, jc maxwell's original presentation of electromagnetic theory and its evolution," in *Handbook of Antenna Technologies*. Springer Singapore, 2016, pp. 3–30. 3

[4] O. Auciello and R. Waser, *Science and technology of electroceramic thin films*. Springer Science & Business Media, 1995, vol. 284. 3

[5] M. Dragoman and D. Dragoman, "Nanoelectronics. principles and devices, artech house," *Inc., Norwood, MA*, 2006.

[6] K. Goser, P. Glösekötter, P. Glosekotter, and J. Dienstuhl, *Nanoelectronics and nanosystems: from transistors to molecular and quantum devices*. Springer Science & Business Media, 2004.

[7] S. Oda and D. Ferry, *Silicon nanoelectronics.* CRC press, 2005.

[8] W. Fahrner, *Nanotechnology and nanoelectronics.* Springer, 2005. 3

[9] A. Pais, "Einstein and the quantum theory," *Reviews of Modern Physics*, vol. 51, no. 4, p. 863, 1979. 3

[10] D. R. Murdoch, *Niels Bohr's philosophy of physics.* Cambridge University Press, 1989. 3

[11] E. Merzbacher, "Quantum mechanics, john wiley & sons, new york, 1970." 3, 4

[12] A. T. Fromhold, *Quantum mechanics for applied physics and engineering.* Courier Corporation, 2012. 4

[13] J. T. Devreese, "The light came in 1905," *arXiv preprint physics/0602083*, 2006. 6

[14] J. Z. Buchwald, "From maxwell to microphysics: Aspects of electromagnetic theory in the last quarter of the nineteenth century," 1987. 6

[15] J. P. Dahl, *Introduction to the quantum world of atoms and molecules.* World Scientific Publishing Company, 2001. 6, 7

[16] S. Wieder, *The foundations of quantum theory.* New York, NY: Academic Press, 1973. [Online]. Available: http://cds.cern.ch/record/105182 7

[17] K. Gottfried, *Quantum mechanics: fundamentals.* CRC Press, 2018. 7

[18] S. Ivanov, *Theoretical and quantum mechanics: fundamentals for chemists.* Springer Science & Business Media, 2006. 8

[19] A. F. J. Levi, *Applied quantum mechanics*. Cambridge University Press, 2006. 8

[20] D. Porath, A. Bezryadin, S. De Vries, and C. Dekker, "Direct measurement of electrical transport through dna molecules," *Nature*, vol. 403, no. 6770, p. 635, 2000.

[21] Y. Xue, S. Datta, S. Hong, R. Reifenberger, J. I. Henderson, and C. P. Kubiak, "Negative differential resistance in the scanning-tunneling spectroscopy of organic molecules," *Physical Review B*, vol. 59, no. 12, p. R7852, 1999.

[22] C. Joachim and J. K. Gimzewski, "A nanoscale single-molecule amplifier and its consequences," *Proceedings of the IEEE*, vol. 86, no. 1, pp. 184–190, 1998.

[23] I. Lyo, "Science 245 1369 avouris ph, lyo iw, bozso f and kaxiras e 1990," *J. Vac. Sci. Technol. A*, vol. 8, p. 3405, 1989.

[24] R. M. Metzger, B. Chen, U. Höpfner, M. Lakshmikantham, D. Vuillaume, T. Kawai, X. Wu, H. Tachibana, T. V. Hughes, H. Sakurai *et al.*, "Unimolecular electrical rectification in hexadecylquinolinium tricyanoquinodimethanide," *Journal of the American Chemical Society*, vol. 119, no. 43, pp. 10 455–10 466, 1997.

[25] J. K. Gimzewski and C. Joachim, "Nanoscale science of single molecules using local probes," *science*, vol. 283, no. 5408, pp. 1683–1688, 1999.

[26] S. Datta, W. Tian, S. Hong, R. Reifenberger, J. I. Henderson, and C. P. Kubiak, "Current-voltage characteristics of self-assembled monolayers by scanning tunneling microscopy," *Physical Review Letters*, vol. 79, no. 13, p. 2530, 1997.

[27] J. Chen, M. Reed, A. Rawlett, and J. Tour, "Large on-off ratios and negative differential resistance in a molecular electronic device," *science*, vol. 286, no. 5444, pp. 1550–1552, 1999.

[28] S. J. Tans, M. H. Devoret, H. Dai, A. Thess, R. E. Smalley, L. Geerligs, and C. Dekker, "Individual single-wall carbon nanotubes as quantum wires," *Nature*, vol. 386, no. 6624, p. 474, 1997.

[29] C. Collier, E. Wong, M. Belohradskỳ, F. Raymo, J. Stoddart, P. Kuekes, R. Williams, and J. Heath, "Electronically configurable molecular-based logic gates," *Science*, vol. 285, no. 5426, pp. 391–394, 1999. 8

[30] D. L. Aronstein and C. Stroud, "Fractional wave-function revivals in the infinite square well," *Physical Review A*, vol. 55, no. 6, p. 4526, 1997. 9

[31] B. Hu, B. Li, J. Liu, and Y. Gu, "Quantum chaos of a kicked particle in an infinite potential well," *Physical review letters*, vol. 82, no. 21, p. 4224, 1999.

[32] R. W. Robinett, "Visualizing the collapse and revival of wave packets in the infinite square well using expectation values," *American Journal of Physics*, vol. 68, no. 5, pp. 410–420, 2000.

[33] D. Wójcik, I. Białynicki-Birula, and K. Życzkowski, "Time evolution of quantum fractals," *Physical Review Letters*, vol. 85, no. 24, p. 5022, 2000.

[34] G. Bonneau, J. Faraut, and G. Valent, "Self-adjoint extensions of operators and the teaching of quantum mechanics," *American Journal of physics*, vol. 69, no. 3, pp. 322–331, 2001.

[35] F. Gori, D. Ambrosini, R. Borghi, V. Mussi, and M. Santarsiero, "The propagator for a particle in a well," *European Journal of Physics*, vol. 22, no. 1, p. 53, 2001.

[36] J.-P. Antoine, J.-P. Gazeau, P. Monceau, J. Klauder, and K. Penson, "Temporally stable coherent states for infinite well and pöschl–teller potentials," *Journal of Mathematical Physics*, vol. 42, no. 6, pp. 2349–2387, 2001. 9

[37] Wikipedia contributors, "Heterojunction — Wikipedia, the free encyclopedia," 2006, [Online; accessed 30-November-2019]. [Online]. Available: https://en.wikipedia.org/w/index.php?title=Heterojunction&oldid=90134440 9

[38] ——, "Quantum well — Wikipedia, the free encyclopedia," 2006, [Online; accessed 30-November-2019]. [Online]. Available: https://en.wikipedia.org/w/index.php?title=Quantum_well&oldid=85773851 10

[39] S. A. Maier, *Plasmonics: fundamentals and applications*. Springer Science & Business Media, 2007. xxiv, 20, 40, 41, 42, 46, 47, 54

[40] A. Alu and N. Engheta, "Multifrequency optical invisibility cloak with layered plasmonic shells," *Physical review letters*, vol. 100, no. 11, p. 113901, 2008. 21

[41] D. K. Mynbaev and V. Sukharenko, "Plasmonic-based devices for optical communications," in *Frontiers in Electronics*. World Scientific, 2013, pp. 201–220. 21

[42] C. Hägglund and B. Kasemo, "Nanoparticle plasmonics for 2d-photovoltaics: mechanisms, optimization, and limits," *Optics Express*, vol. 17, no. 14, pp. 11 944–11 957, 2009. 21

[43] Wikipedia contributors, "Lycurgus cup — Wikipedia, the free encyclopedia," 2019, [Online; accessed 30-November-2019]. [Online]. Available: https://en.wikipedia.org/w/index.php?title=Lycurgus_Cup&oldid=911323885 21

[44] C. F. Bohren and D. R. Huffman, *Absorption and scattering of light by small particles*. John Wiley & Sons, 2008. 22

[45] M. Beckers, B. Weise, S. Kalapis, T. Gries, G. Seide, and C.-A. Bunge, "Basics of light guidance," in *Polymer Optical Fibres*. Elsevier, 2017, pp. 9–46. 23

[46] J. A. Dionne, K. Diest, L. A. Sweatlock, and H. A. Atwater, "Plasmostor: a metal-oxide- si field effect plasmonic modulator," *Nano letters*, vol. 9, no. 2, pp. 897–902, 2009. 23

[47] P. Jahanshahi, M. Ghomeishi, and F. R. M. Adikan, "Study on dielectric function models for surface plasmon resonance structure," *The Scientific World Journal*, vol. 2014, 2014. 24, 27, 29, 30, 31

[48] H. Li, S. Zhou, J. Li, Y. Chen, S. Wang, Z. Shen, L. Chen, H. Liu, and X. Zhang, "Analysis of the drude model in metallic films," *Applied optics*, vol. 40, no. 34, pp. 6307–6311, 2001. 24, 27, 28

[49] H. Ehrenreich, "The optical properties of metals," *IEEE spectrum*, vol. 2, no. 3, pp. 162–170, 1965. 24, 29, 30

[50] M. I. Markovic and A. D. Rakic, "Determination of the reflection coefficients of laser light of wavelengths from the surface of aluminum using the lorentz-drude model," *Applied optics*, vol. 29, no. 24, pp. 3479–3483, 1990. 24, 27, 29, 30, 31

[51] Y. Mirzaei, G. Rostami, M. Dolatyari, and A. Rostami, "Investigation of efficient mathematical permittivity modeling for modal analysis of plasmonics layered structures," *Optik*, vol. 126, no. 3, pp. 323–327, 2015. xxiii, 24, 27, 28, 29, 30, 31, 32

[52] R. Brendel and D. Bormann, "An infrared dielectric function model for amorphous solids," *Journal of applied physics*, vol. 71, no. 1, pp. 1–6, 1992. 31

[53] S. Wetzel, M. Klevenz, H.-P. Gail, A. Pucci, and M. Trieloff, "Laboratory measurement of optical constants of solid sio and application to circumstellar dust," *Astronomy & Astrophysics*, vol. 553, p. A92, 2013. 31

[54] J. A. C. Weideman, "Computation of the complex error function," *SIAM Journal on Numerical Analysis*, vol. 31, no. 5, pp. 1497–1518, 1994. 24, 31

[55] V. E. Ferry, L. A. Sweatlock, D. Pacifici, and H. A. Atwater, "Plasmonic nanostructure design for efficient light coupling into solar cells," *Nano letters*, vol. 8, no. 12, pp. 4391–4397, 2008. 27

[56] J. Dionne, L. Sweatlock, H. Atwater, and A. Polman, "Planar metal plasmon waveguides: frequency-dependent dispersion, propagation, localization, and loss beyond the free electron model," *Physical Review B*, vol. 72, no. 7, p. 075405, 2005. 27

[57] S. Huang, Z. Wang, J. Xu, D. Lu, and T. Yuan, "Determination of optical constants of functional layer of online low-e glass based on the drude theory," *Thin solid films*, vol. 516, no. 10, pp. 3179–3183, 2008. 27

[58] Y. Kanamori, R. Hokari, and K. Hane, "Mems for plasmon control of optical metamaterials," *IEEE Journal of Selected Topics in Quantum Electronics*, vol. 21, no. 4, pp. 137–146, 2015. 27, 29

[59] Ş. E. Kocabaş, "Nano-metallic optics for waveguides and photodetectors," Ph.D. dissertation, Citeseer, 2009. 29

[60] A. D. Rakić, A. B. Djurišić, J. M. Elazar, and M. L. Majewski, "Optical properties of metallic films for vertical-cavity optoelectronic devices," *Applied optics*, vol. 37, no. 22, pp. 5271–5283, 1998. 30

[61] M. J. Mageto, C. Maghanga, and M. Mwamburi, "The lorentz oscillator model simulation illustrating a broad maximum in the bulk reflectance for frequencies just above the resonance frequency," 2012. 30

[62] H. Hobert and H. Dunken, "Modelling of dielectric functions of glasses by convolution," *Journal of non-crystalline solids*, vol. 195, no. 1-2, pp. 64–71, 1996. 31

[63] S. Wolfram, *Mathematica® 3.0 Standard Add-on Packages*. Cambridge University Press, 1996. 31

[64] A. Rakic, M. Majewski, and M. Cohen, "The effect of broadening on the optical dielectric function of gaas and alas," in *1996 Conference on Optoelectronic and Microelectronic Materials and Devices. Proceedings*. IEEE, 1996, pp. 317–320. 31

[65] M. L. Brongersma and P. G. Kik, *Surface plasmon nanophotonics*. Springer, 2007, vol. 131. 39

[66] M. L. Brongersma and V. M. Shalaev, "The case for plasmonics," *science*, vol. 328, no. 5977, pp. 440–441, 2010. 39

[67] D. Sarid and W. A. Challener, *Modern introduction to surface plasmons: theory, Mathematica modeling, and applications*. Cambridge University Press, 2010. 40

[68] J. A. Schuller, E. S. Barnard, W. Cai, Y. C. Jun, J. S. White, and M. L. Brongersma, "Plasmonics for extreme light concentration and manipulation," *Nature materials*, vol. 9, no. 3, pp. 193–204, 2010. 40

[69] W. Cai, W. Shin, S. Fan, and M. L. Brongersma, "Elements for plasmonic nanocircuits with three-dimensional slot waveguides," *Advanced materials*, vol. 22, no. 45, pp. 5120–5124, 2010. 40

[70] S. J. Orfanidis, "Electromagnetic waves and antennas," 2002. 41

[71] D. K. Cheng *et al.*, *Field and wave electromagnetics*. Pearson Education India, 1989. 41

[72] M. N. Sadiku, *Elements of electromagnetics*. Oxford university press, 2014. 41

[73] S. A. Maier, M. L. Brongersma, P. G. Kik, S. Meltzer, A. A. Requicha, and H. A. Atwater, "Plasmonics—a route to nanoscale optical devices," *Advanced materials*, vol. 13, no. 19, pp. 1501–1505, 2001. 50

[74] E. Merzbacher, "Quantum mechanics john wiley & sons," *Inc., New York*, 1998. 50

[75] P. B. Johnson and R.-W. Christy, "Optical constants of the noble metals," *Physical review B*, vol. 6, no. 12, p. 4370, 1972. 63, 130

[76] J. M. J. Santillán, F. A. Videla, M. F. van Raap, D. Muraca, L. B. Scaffardi, and D. C. Schinca, "Influence of size-corrected bound-electron contribution on nanometric silver dielectric function. sizing through optical extinction spectroscopy," *Journal of Physics D: Applied Physics*, vol. 46, no. 43, p. 435301, 2013. 74

[77] C. Kumarasinghe, M. Premaratne, and G. P. Agrawal, "Dielectric function of spherical dome shells with quantum size effects," *Optics express*, vol. 22, no. 10, pp. 11 966–11 984, 2014. 75, 96, 109

[78] R. Esteban, A. G. Borisov, P. Nordlander, and J. Aizpurua, "Bridging quantum and classical plasmonics with a quantum-corrected model," *Nature communications*, vol. 3, p. 825, 2012. 75

[79] J. A. Scholl, A. L. Koh, and J. A. Dionne, "Quantum plasmon resonances of individual metallic nanoparticles," *Nature*, vol. 483, no. 7390, p. 421, 2012. 76, 131, 133

[80] M. Zhang, H. Xiang, X. Zhang, and G. Lu, "Quantum electrodynamics and plasmonic resonance of metallic nanostructures," *Journal of Physics: Condensed Matter*, vol. 28, no. 15, p. 155302, 2016. 76

[81] M. Cini and P. Ascarelli, "Quantum size effects in metal particles and thin films by an extended rpa," *Journal of Physics F: Metal Physics*, vol. 4, no. 11, p. 1998, 1974. 76, 108, 110, 112

[82] D. Wood and N. Ashcroft, "Quantum size effects in the optical properties of small metallic particles," *Physical review B*, vol. 25, no. 10, p. 6255, 1982. 76

[83] S. L. Adler, "Quantum theory of the dielectric constant in real solids," *Physical Review*, vol. 126, no. 2, p. 413, 1962. 77

[84] S. Pakdel and M. Miri, "Faraday rotation and circular dichroism spectra of gold and silver nanoparticle aggregates," *Physical Review B*, vol. 86, no. 23, p. 235445, 2012. 77

[85] V. Gasparian and Z. S. Gevorkian, "Faraday rotation in a disordered medium," *Physical Review A*, vol. 87, no. 5, p. 053807, 2013. 77

[86] Y. Liu, S. Begin-Colin, B. P. Pichon, C. Leuvrey, D. Ihiawakrim, M. Rastei, G. Schmerber, M. Vomir, and J. Y. Bigot, "Two dimensional dipolar coupling in monolayers of silver and gold nanoparticles on a dielectric substrate," *Nanoscale*, vol. 6, no. 20, pp. 12 080–12 088, 2014. 77

[87] G. M. Wysin, V. Chikan, N. Young, and R. K. Dani, "Effects of interband transitions on faraday rotation in metallic nanoparticles," *Journal of Physics: Condensed Matter*, vol. 25, no. 32, p. 325302, 2013. xxv, 78, 79, 84, 85, 153

[88] S. Datta, *Quantum phenomena*. Addison-Wesley Longman, 1989, vol. 8. 83

[89] C. Kittel *et al.*, *Introduction to solid state physics*. Wiley New York, 1976, vol. 8. 83

[90] L. A. Akinyemi and A. Baghai-Wadji, "Quantum physics-based modelling of frequency-dependent dielectric function for small-scale devices in optical communications," in *2017 Global Wireless Summit (GWS)*. IEEE, 2017, pp. 78–82. xxv, 92, 93, 94, 112

[91] I. Ahmed, "Canonical and perturbed quantum potential-well problems: a universal function approach," 2007. 93

[92] F. Wooten, *Optical properties of solids*. Academic press, 2013. 96

[93] M. Dresselhaus, "Solid state physics part ii optical properties of solids," *Lecture Notes (Massachusetts Institute of Technology, Cambridge, MA)*, vol. 17, 2001. 96

[94] F. Rana, "Lecture note for ece 407," *spring*, 2009. 101

[95] M. Rice, W. Schneider, and S. Strässler, "Electronic polarizabilities of very small metallic particles and thin films," *Physical Review B*, vol. 8, no. 2, p. 474, 1973. 108

[96] L. Genzel, T. Martin, and U. Kreibig, "Dielectric function and plasma resonances of small metal particles," *Zeitschrift für Physik B Condensed Matter*, vol. 21, no. 4, pp. 339–346, 1975. 108, 118, 120, 131

[97] J. Ferreyra and C. Proetto, "Excitons in inhomogeneous quantum dots," *Physical Review B*, vol. 57, no. 15, p. 9061, 1998. 108

[98] S. Westcott, J. Jackson, C. Radloff, and N. Halas, "Relative contributions to the plasmon line shape of metal nanoshells," *Physical Review B*, vol. 66, no. 15, p. 155431, 2002. 108

[99] S. Smaili and Y. Massoud, "A system-based model for the scattering by two spherical nanoparticles," in *2011 11th IEEE International Conference on Nanotechnology*. IEEE, 2011, pp. 1220–1225.

[100] M. Zapata-Herrera and A. S. Camacho, "Size change effect on the optical behavior of ultra small metal particles," *arXiv preprint arXiv:1404.6827*, 2014. 108, 109

[101] S.-S. Kim, S.-K. Hong, and K.-H. Yeon, "Linear optical properties of the semiconductor quantum shell," *Physical Review B*, vol. 76, no. 11, p. 115322, 2007. 109

[102] K. Guo, G. Liu, L. Huang, and X. Zheng, "Linear and nonlinear optical absorption coefficients of spherical dome shells," *Optical materials*, vol. 46, pp. 361–365, 2015.

[103] G. Liu, K. Guo, and Z. Zhang, "Nonlinear optical rectification in spherical dome semiconductor nanoshells," *Physica B: Condensed Matter*, vol. 503, pp. 81–85, 2016. 109

[104] D. Nasri and N. Bettahar, "Magneto-optical properties in inhomogeneous quantum dot: The aharonov-bohm oscillations effect," *Physica B: Condensed Matter*, vol. 501, pp. 68–73, 2016. 109

[105] G. Barmparis, G. Kopidakis, and I. Remediakis, "Shape-dependent single-electron levels for au nanoparticles," *Materials*, vol. 9, no. 4, p. 301, 2016. 109

[106] H. Fröhlich, "Theory of electrical breakdown in ionic crystals," *Proceedings of the Royal Society of London. Series A-Mathematical and Physical Sciences*, vol. 160, no. 901, pp. 230–241, 1937. 110

[107] R. Kubo, "Electronic properties of metallic fine particles. i." *Journal of the Physical Society of Japan*, vol. 17, no. 6, pp. 975–986, 1962. 110

[108] R. Jaklevic, J. Lambe, M. Mikkor, and W. Vassell, "Observation of electron standing waves in a crystalline box," *Physical Review Letters*, vol. 26, no. 2, p. 88, 1971. 110

[109] D. Tanner, A. Sievers, and R. Buhrman, "Far-infrared absorption in small metallic particles," *Physical Review B*, vol. 11, no. 4, p. 1330, 1975. 110

[110] R. Doremus, "Optical properties of small silver particles," *The Journal of Chemical Physics*, vol. 42, no. 1, pp. 414–417, 1965. 110

[111] J.-D. Ganiere, R. Rechsteiner, and M.-A. Smithard, "On the size dependence of the optical absorption due to small metal particles," *Solid State Communications*, vol. 16, no. 1, pp. 113–115, 1975.

[112] M. Smithard and R. Dupree, "The preparation and optical properties of small silver particles in glass," *physica status solidi (a)*, vol. 11, no. 2, pp. 695–703, 1972.

[113] U. Kreibig and C. v. Fragstein, "The limitation of electron mean free path in small silver particles," *Zeitschrift für Physik*, vol. 224, no. 4, pp. 307–323, 1969.

[114] U. Kreibig and P. Zacharias, "Surface plasma resonances in small spherical silver and gold particles," *Zeitschrift für Physik A Hadrons and nuclei*, vol. 231, no. 2, pp. 128–143, 1970.

[115] M. Smithard, "Size effect on the optical and paramagnetic absorption of silver particles in a glass matrix," *Solid State Communications*, vol. 13, no. 2, pp. 153–156, 1973.

[116] U. Kreibig, "Electronic properties of small silver particles: the optical constants and their temperature dependence," *Journal of Physics F: Metal Physics*, vol. 4, no. 7, p. 999, 1974.

[117] C. Duthler, S. Johnson, and H. Broida, "Plasma-resonance scattering from small sodium particles formed in a flowing gas stream," *Physical Review Letters*, vol. 26, no. 20, p. 1236, 1971. 110

[118] A. Lushnikov and A. Simonov, "Surface plasmons in small metal particles," *Zeitschrift für Physik*, vol. 270, no. 1, pp. 17–24, 1974. 110

[119] A. Kawabata and R. Kubo, "Electronic properties of fine metallic particles. ii. plasma resonance absorption," *Journal of the physical society of Japan*, vol. 21, no. 9, pp. 1765–1772, 1966. 110

[120] L. Sander, "Quantum theory of perpendicular electrical conductivity in a thin metallic film," *Journal of Physics and Chemistry of Solids*, vol. 29, no. 2, pp. 291–294, 1968. 113

[121] L. Genzel and T. Martin, "Infrared absorption by surface phonons and surface plasmons in small crystals," *Surface Science*, vol. 34, no. 1, pp. 33–49, 1973. 118

[122] ——, "Infrared absorption in small ionic crystals," *physica status solidi (b)*, vol. 51, no. 1, pp. 91–99, 1972.

[123] J. C. MAXWELL-GARNETT, "Colours in metal glasses and in metallic films," *Phil. Trans. R. Soc. Lond, A*, vol. 203, pp. 385–420, 1904. 118

[124] C. Sönnichsen, "Plasmons in metal nanostructures, ludwig-maximilians-university munich ph. d," Ph.D. dissertation, thesis, 2001. 130

[125] G. Mie, "Beiträge zur optik trüber medien, speziell kolloidaler metallösungen," *Annalen der physik*, vol. 330, no. 3, pp. 377–445, 1908. 130

[126] G. B. Arfken and H. Weber, "Mathematical methods for physicists, burlington, ma," 2001. 132, 134

[127] G. B. Arfken, H. J. Weber, and F. Harris, "Mathematical methods for physicists, 1182 pp," 2005. 134, 147

[128] A. Lindner and D. Strauch, "A complete course on theoretical physics," *A Complete Course on Theoretical Physics, Undergraduate Lecture Notes in Physics, ISBN 978-3-030-04359-9. Springer Nature Switzerland AG, 2018, p.*, 2018.

[129] P. L. DeVries and J. E. Hasbun, *A first course in computational physics*. Jones & Bartlett Publishers, 2011. 132

[130] W.-C. Huang and J.-T. Lue, "Optical properties of quantum confined small metallic particles with diffuse surface," *Journal of Physics and Chemistry of Solids*, vol. 58, no. 10, pp. 1529–1538, 1997. 134

[131] W. Ames, "Numerical methods for partial differential equations academic press," *New York*, 1977. 143

[132] L. Bers, F. John, and M. Schechter, "Partial differential equations (lectures in appl. math. vol. 3)," 1964. 143

[133] J. W. Thomas, *Numerical partial differential equations: finite difference methods*. Springer Science & Business Media, 2013, vol. 22. 144

[134] S. Chakraverty, N. Mahato, P. Karunakar, and T. D. Rao, *Advanced Numerical and Semi-Analytical Methods for Differential Equations*. John Wiley & Sons, 2019. 144

[135] A. Samarskii, V. Tishkin, A. Favorskii, and M. Y. Shashkov, "Operational finite-difference schemes," *Differential Equations*, vol. 17, no. 7, pp. 854–862, 1981. 145, 160

[136] N. Zettili, "Quantum mechanics: concepts and applications," 2003. 152, 153

[137] H. A. Bethe and E. E. Salpeter, *Quantum mechanics of one-and two-electron atoms*. Springer Science & Business Media, 2012.

[138] H. Friedrich and H. Friedrich, *Theoretical atomic physics*. Springer, 1991, vol. 2.

[139] L. M. Ugray and R. C. Shiell, "Elucidating fermi's golden rule via bound-to-bound transitions in a confined hydrogen atom," *American Journal of Physics*, vol. 81, no. 3, pp. 206–210, 2013.

[140] S. Olszewski, "Thomas-reiche-kuhn sum rule for electron transitions in solids," *Acta Physica Polonica Series A*, vol. 94, pp. 49–70, 1998. 152, 156

[141] R. Jackiw, *Intermediate quantum mechanics*. CRC Press, 2018. 154

[142] A. Favorskii, A. Samarskii, V. Tishkin, and M. Shashkov, "On constructing fully conservative difference schemes for gas dynamic equations in eulerian form by the method of basic operators," *Preprint Keldysh Inst. of Appl. Math. the USSR Ac. of Sc*, vol. 63, pp. 13–21, 1981. 160

[143] M. Shashkov, *Conservative finite-difference methods on general grids*. CRC press, 2018. 161

[144] C. A. Fletcher, "Computational techniques for fluid dynamics. volume 1-fundamental and general techniques. volume 2-specific techniques for different flow categories," in *Berlin and New York, Springer-Verlag, 1988, p. Vol. 1, 418 p.; vol. 2, 493 p.*, vol. 1, 1988.

[145] E. Copson, "Bernard epstein, partial differential equations—an introduction (mcgraw-hill, new york, 1962), x+ 273 pp., 74s." *Proceedings of the Edinburgh Mathematical Society*, vol. 13, no. 2, pp. 193–193, 1962.

[146] J. M. Hyman and M. Shashkov, "Approximation of boundary conditions for mimetic finite-difference methods," *Computers & Mathematics with Applications*, vol. 36, no. 5, pp. 79–99, 1998.

[147] M. Shashkov and S. Steinberg, "Support-operator finite-difference algorithms for general elliptic problems," *Journal of Computational Physics*, vol. 118, no. 1, pp. 131–151, 1995.

[148] R. Liska, M. Y. Shashkov, and A. V. Solovjov, "Support-operators method for pde discretization: symbolic algorithms and realization," *Mathematics and Computers in Simulation*, vol. 35, no. 2, pp. 173–183, 1993.

[149] S. Datta, *Quantum transport: atom to transistor*. Cambridge university press, 2005. 160

[150] A. Szabo and N. Ostlund, "Modern quantum chemistry, revised 1st edition," 1989. 181

[151] W. Koch and M. Holthausen, "A chemist's guide to density functional theory. wileyvch, verlag gmbh," 2000. 181

[152] R. G. Parr, "W. yang density functional theory of atoms and molecules," *O xford University Press*, vol. 1, p. 989, 1989. 181

[153] P. Hohenberg and W. Kohn, "Inhomogeneous electron gas," *Physical review*, vol. 136, no. 3B, p. B864, 1964. 182, 186

[154] T. L. Beck, "Real-space mesh techniques in density-functional theory," *Reviews of Modern Physics*, vol. 72, no. 4, p. 1041, 2000. 182

[155] W. Kohn and L. Sham, "Quantum density oscillations in an inhomogeneous electron gas," *Physical Review*, vol. 137, no. 6A, p. A1697, 1965. 183, 188

[156] W. Kohn and L. J. Sham, "Self-consistent equations including exchange and correlation effects," *Physical review*, vol. 140, no. 4A, p. A1133, 1965. 183, 186, 188, 193

[157] E. Baerends, D. Ellis, and P. Ros, "Self-consistent molecular hartree—fock—slater calculations i. the computational procedure," *Chemical Physics*, vol. 2, no. 1, pp. 41–51, 1973. 193

[158] C. D. Pun, *Recent Advances In Density Functional Methods, Part I.* World Scientific, 1995, vol. 1.

[159] R. Bauernschmitt and R. Ahlrichs, "Treatment of electronic excitations within the adiabatic approximation of time dependent density functional theory," *Chemical Physics Letters*, vol. 256, no. 4-5, pp. 454–464, 1996. 185

[160] A. D. Becke, "Density-functional exchange-energy approximation with correct asymptotic behavior," *Physical review A*, vol. 38, no. 6, p. 3098, 1988. 183, 190

[161] ——, "A new mixing of hartree–fock and local density-functional theories," *The Journal of chemical physics*, vol. 98, no. 2, pp. 1372–1377, 1993. 193

[162] M. C. Payne, M. P. Teter, D. C. Allan, T. Arias, and a. J. Joannopoulos, "Iterative minimization techniques for ab initio total-energy calculations: molecular dynamics and conjugate gradients," *Reviews of modern physics*, vol. 64, no. 4, p. 1045, 1992.

[163] T. Sarkar, "The conjugate gradient method as applied to electromagnetic field problems," *IEEE Antennas and Propagation Society Newsletter*, vol. 28, no. 4, pp. 4–14, 1986.

[164] T. K. Sarkar, "From" reaction concept" to" conjugate gradient": Have we made any progress," *IEEE Antennas and Propagation Society Newsletter*, vol. 31, no. 4, pp. 5–12, 1989. 193

Appendices

A Plasmon-polariton Dispersion Relation and Numerical Scheme for its Solution

In this appendix, the dispersion relations and the field profiles in multi-layered media are described. In particular, the three-layered systems and five-layered wave-guide structures with arbitrary materials, focusing on metallic ones and emphasizing scale considerations are explained. Details of the employed numerical techniques are also presented.

A.1 Derivation of Dispersion Relations for Three-layer Symmetric Structures

In this section, the derivation of dispersion relations and the electromagnetic fields for the geometrical structure as depicted in Fig. (6.1) are presented. The geometrical structure is infinite along the y-axis, with propagation of wave taken to be parallel to the x-axis and metal-dielectric boundaries are taken to be perpendicular to the z-axis. The cladding and core consist of material "2" and "1", respectively. Assume $\partial y \equiv 0$. Then,

$$\mathbf{E}(x, z; t) = \mathbf{E}(z)e^{i(k_x x - \omega t)} \tag{1}$$

$$\mathbf{B}(x, z; t) = \mathbf{B}(z)e^{i(k_x x - \omega t)} \tag{2}$$

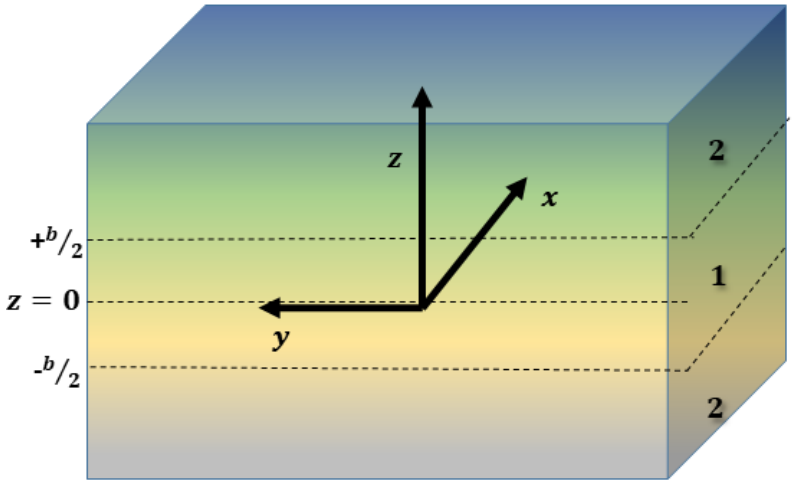

Figure 1: The geometry used for the formulation of three-layer system assuming prorogation along the x-axis

Assuming that there are no free charges and currents present in the material, the Maxwell's equations can be expressed as:

$$\left.\begin{aligned} \nabla \cdot \mathbf{D} &= 0 \\ \nabla \cdot \mathbf{B} &= 0 \\ \nabla \times \mathbf{D} &= -\frac{1}{c}\frac{\partial \mathbf{B}}{\partial t} \\ \nabla \times \mathbf{B} &= \frac{1}{c}\varepsilon_m \frac{\partial \mathbf{E}}{\partial t} \end{aligned}\right\} \tag{3}$$

Expanding the curl operator,

$$\nabla \times \mathbf{W} = \left(\frac{\partial W_z}{\partial y} - \frac{\partial W_y}{\partial z}\right)\hat{x} + \left(\frac{\partial W_x}{\partial z} - \frac{\partial W_z}{\partial x}\right)\hat{y} + \left(\frac{\partial W_y}{\partial x} - \frac{\partial W_x}{\partial y}\right)\hat{z}. \tag{4}$$

Substituting the solution ansatzes (1) and (2), for the curls of **E** and **B**, respectively, we obtain

$$\left.\begin{aligned} \hat{x} : -\frac{\partial E_y}{\partial z} &= \frac{i\omega}{c} B_x \\ \hat{y} : \frac{\partial E_x}{\partial z} - ik_x E_z &= \frac{i\omega}{c} B_x \\ \hat{z} : ik_x E_y &= \frac{i\omega}{c} B_z \end{aligned}\right\} \tag{5}$$

and,

$$\left.\begin{aligned} \hat{x} : -\frac{\partial B_y}{\partial z} &= -\frac{i\omega}{c} \epsilon_m E_x \\ \hat{y} : \frac{\partial B_x}{\partial z} = -ik_x B_z &= -\frac{i\omega}{c} \epsilon_m E_y \\ \hat{z} : -ik_x B_y &= -\frac{i\omega}{c} \epsilon_m E_z \end{aligned}\right\} \tag{6}$$

The equations comprise transverse electric components (0, E_y, 0) or (E_y, B_x, B_z) and transverse magnetic components (E_x, 0, E_z) or (E_x, E_z, B_y). Hence, there is also the possibility that the solution is obtained from (5) via (6) with no assumption of the field component being equal to zero (i.e $E_y \neq 0$, $B_x \neq 0$, $E_y \neq 0$). This presents a general solution for the problem. By substituting the y-axis ($\hat{y}$) component of (5) into the z-component $\hat{z}$ and also the x-component ($\hat{x}$) of (6) into the z-component ($\hat{z}$) in (6), we obtain:

$$\left.\begin{aligned} \frac{\partial E_x}{\partial z} - ik_x E_z &= \frac{i\omega}{c} - \frac{\omega}{ck_x} \varepsilon_m E_z \\ -\frac{\partial}{\partial z}\left(-\frac{\omega}{ck_x} \varepsilon_m E_z\right) &= -\frac{\omega}{c} \varepsilon_m E_x \\ B_y &= \frac{-\omega}{k_x c} \varepsilon_m E_z \\ E_x &= \frac{i}{k_x} \frac{\partial E_z}{\partial z} \\ \frac{\partial^2 E_z}{\partial z^2} - \left[k_x^2 - \left(\frac{\omega}{c} \varepsilon_m\right)\right] E_z &= 0 \end{aligned}\right\} \tag{7}$$

By letting $k_{z,m}^2 = k_x^2 - \left(\frac{\omega}{c}\right)^2 \epsilon_m$, the last equation becomes:

$$\frac{\partial^2 E_z}{\partial z^2} - k_{z,m}^2 E_z = 0. \tag{8}$$

Assuming field variation according to $e^{\lambda z}$, $\lambda^2 - k_{z,m}^2 = 0 \rightarrow \lambda = \pm k_{z,m}$. Then, the general solution for E_z can be cast as:

$$E_z = A_1 e^{k_{z,m} z} \pm A_2 e^{-k_{z,m} z} \tag{9}$$

Correspondingly, the E_x can be solved in the like manner:

$$\frac{\partial E_z}{\partial z} = -ik_x E_x = A_1 k_{z,m} e^{k_{z,m} z} \mp A_2 k_{z,m} e^{-k_{z,m} z} \tag{10}$$

$$E_x = -\frac{k_{z,m}}{ik_x}\left(A_1 e^{k_{z,m} z} \pm A_2 e^{-k_{z,m} z}\right) \tag{11}$$

More so, the E_y can be solved likewise as:

$$\left.\begin{aligned} B_x &= -\frac{c}{i\omega}\frac{\partial E_y}{\partial z} \\ \frac{\partial B_x}{\partial z} - ik_z B_z &= -\frac{i\omega}{c}\varepsilon_m E_y \\ \frac{\partial}{\partial z}\left(-\frac{c}{i\omega}\frac{\partial E_y}{\partial z}\right) - ik_x\left(\frac{ck_x}{\omega}\right)E_y - \frac{i\omega}{c}\varepsilon_m E_y &\\ -\frac{c}{i\omega}\frac{\partial^2 E_y}{\partial z^2} + \frac{c}{i\omega}k_x^2 E_y + \frac{\omega}{c}\epsilon_m E_y & \end{aligned}\right\} \tag{12}$$

This gives rise to a second-order equation in terms of E_y expressed as:

$$\frac{\partial^2 E_y}{\partial z^2} + \left[-k_x^2 + \left(\frac{i\omega}{c} \right)^2 \epsilon_m \right] E_y = 0 \tag{13}$$

By defining that $\beta_m^2 = -k_x^2 + \left(\frac{i\omega}{c}\right)^2 \epsilon_m \rightarrow \beta_m = ik_{z,m}$, then it simplifies to:

$$\frac{\partial^2 E_y}{\partial z^2} + \beta_m^2 E_y = 0 \tag{14}$$

Then, the solutions are :

$$\left.\begin{aligned} E_y &= A_3 e^{i\beta_m z} \pm A_4 e^{-i\beta_m z} \\ E_y &= A_3 e^{-k_{z,m} z} \pm A_4 e^{k_{z,m} z} \end{aligned}\right\} \tag{15}$$

Furthermore, due to the relationship, $ik_x E_y = \frac{i\omega}{c} B_z$,

$$B_z = \frac{ck_x}{\omega} \left(A_3 e^{i\beta_m z} \pm A_4 e^{-i\beta_m z} \right). \tag{16}$$

B_x and B_y can be obtained similarly:

$$\left.\begin{aligned} -\frac{\partial E_y}{\partial z} &= -A_3 \beta_m e^{i\beta_m z} \pm A_4 \beta_m e^{-i\beta_m z} = \frac{i\omega}{c} B_x \\ B_x = \frac{c}{\omega} \beta_m \left(-A_3 e^{i\beta_m z} \pm A_4 e^{-i\beta_m z} \right) & \; ik_x B_y = -\frac{i\omega}{c} \varepsilon_m E_z \\ B_y &= -\frac{\omega}{ck_x} \varepsilon_m \left(A_1 e^{k_{z,m} z} \mp A_2 e^{-k_{z,m} z} \right) \end{aligned}\right\} \tag{17}$$

Outside the waveguide, we require the field approach zero for z tending to infinity. With no loss of generality, it is assumed that the waves inside the waveguide consist of both right- and left propagating waves by the same proportion by setting the normalization factors to be equal to unity. Summarizing the results, the components of the fields outside and inside in the waveguide are expressed as:

$$\left.\begin{aligned} E_x &= -\frac{k_{z,2}}{ik_x}\left(\mp A_2 e^{-k_{z,2}z}\right) \\ E_y &= A_3 e^{-k_{z,2}z} \\ E_z &= \pm A_2 e^{-k_{z,2}z} \\ B_x &= -\frac{ic}{\omega}k_{z,2}A_3 e^{-k_{z,2}z} \\ B_y &= -\frac{\omega}{k_x c}\varepsilon_m\left(\mp A_2 e^{-k_{z,2}z}\right) \\ B_z &= \frac{ck_x}{\omega}A_3 e^{-k_{z,2}z} \end{aligned}\right\} \quad \text{Outside the Waveguide} \tag{18}$$

Note that these formulas are valid for both $z > \frac{b}{2}$ and $z < -\frac{b}{2}$. Assume $k_{z,2}z > 0$, then $e^{-k_{z,2}z} \to 0$ for $z \to \infty$. However, $e^{-k_{z,2}z} \to \infty$ for $z \to -\infty$. Similar considerations can be made for $e^{k_{z,2}z}$. As $e^{k_{z,2}z} \to 0$ for $z \to -\infty$ but $e^{k_{z,2}z} \to \infty$ for $z \to \infty$. Compactly, the

solutions are rather of this form: $e^{-k_{z,2}|z-\frac{b}{2}|}$ for $z > \frac{b}{2}$ and $e^{-k_{z,2}|z+\frac{b}{2}|}$ for $z < -\frac{b}{2}$

$$\left.\begin{aligned} E_x &= -\frac{k_{z,1}}{ik_x}\left(e^{k_{z,1}z} \mp e^{-k_{z,1}z}\right) \\ E_y &= e^{-k_{z,1}z} \pm e^{k_{z,1}z} \\ E_z &= e^{k_{z,1}z} \pm e^{-k_{z,1}z} \\ B_x &= -\frac{ic}{\omega}k_{z,1}\left(-e^{-k_{z,1}z} \pm e^{k_{z,1}z}\right) \\ B_y &= -\frac{\omega}{ck_x}\varepsilon_m\left(e^{k_{z,1}z} \mp e^{-k_{z,1}z}\right) \\ B_z &= \frac{ck_x}{\omega}\left(e^{-k_{z,1}z} \pm e^{k_{z,1}z}\right) \end{aligned}\right\} \quad \text{Inside the Wave-guide} \tag{19}$$

In order to compute the coefficients A_2 and A_3 , the boundary conditions must be enforced: E_x, D_z are continuous at z=$\pm b/2$; E_y is continuous at z=$\pm b/2$; B_x is continuous at z=$\pm b/2$; and $H_{x,y} = \frac{B_{x,y}}{\mu}$ continuous z=$\pm b/2$.

First boundary constraint: E_x and D_z are continuous at the interface:

$$\left.\begin{aligned} E_x \to \frac{ik_{z,1}}{k_x}\left(e^{k_{z,1}z} \mp e^{-k_{z,1}z}\right) &= \pm\frac{k_{z,2}}{ik_x}A_2e^{-k_{z,2}z} \\ D_z \to \epsilon_1\left(e^{k_{z,1}z} \pm e^{-k_{z,1}z}\right) &= \pm\epsilon_2 A_2 e^{-k_{z,2}z} \end{aligned}\right\} \tag{20}$$

This results in:

$$\left.\begin{aligned} ik_{z,1}\left(e^{k_{z,1}z} \mp e^{-k_{z,1}z}\right) &= \frac{k_{z,2}}{i}\frac{\epsilon_1}{\epsilon_2}\left(e^{k_{z,1}z} \pm e^{-k_{z,1}z}\right). \\ -\epsilon_2 k_{z,1}\left(e^{k_{z,1}z} \mp e^{-k_{z,1}z}\right) &= \epsilon_1 k_{z,2}\left(e^{k_{z,1}z} \pm e^{-k_{z,1}z}\right). \end{aligned}\right\} \tag{21}$$

By putting it in compact form, it can be expressed as:

$$-\epsilon_2 k_{z,1} = \epsilon_1 k_{z,2} \left\{ \begin{array}{l} \coth\left(\frac{k_{z,1}b}{2}\right) \\ \tanh\left(\frac{k_{z,1}b}{2}\right) \end{array} \right\}. \tag{22}$$

Or, alternatively,

$$\epsilon_1 k_{z,2} + \epsilon_2 k_{z,1} \left\{ \begin{array}{l} \coth\left(\frac{k_{z,1}b}{2}\right) \\ \tanh\left(\frac{k_{z,1}b}{2}\right) \end{array} \right\}. \tag{23}$$

Second boundary constraint: E_y is continuous at the interface:

$$e^{-k_{z,1}z} \pm e^{k_{z,1}z} = A_3 e^{-k_{2,1}z} \tag{24}$$

and leads to this when $z = \frac{b}{2}$ is substituted:

$$A_3 = e^{k_{z,2}\frac{b}{2}} \left(e^{-k_{z,1}\frac{b}{2}} \pm e^{k_{z,1}\frac{b}{2}}\right) \tag{25}$$

However, **Third boundary constraint**: H_x, H_y and B_z are continuous at the interface:

$$\left. \begin{array}{r} H_y \to -\frac{\omega}{c}\left(\frac{\epsilon_1}{k_x \mu_1}\right)\left(e^{k_{z,1}\frac{b}{2}} \mp e^{-k_{z,1}\frac{b}{2}}\right) = -\frac{\omega}{c}\left(\frac{\epsilon_1}{k_x \mu_1}\right)\left(\mp A_2 e^{-k_{z,1}\frac{b}{2}}\right) \\ \epsilon_1 \mu_2 \left(e^{k_{z,1}\frac{b}{2}} \mp e^{-k_{z,1}\frac{b}{2}}\right) = \epsilon_2 \mu_1 \left(\mp A_2 e^{-k_{z,1}\frac{b}{2}}\right) \end{array} \right\} \tag{26}$$

Hence, on further simplification, it leads to:

$$\left.\begin{aligned} A_2 &= \frac{\epsilon_1\mu_2}{\epsilon_2\mu_1}e^{k_{z,2}\frac{b}{2}}\left(e^{k_{z,1}\frac{b}{2}} \mp e^{-k_{z,1}\frac{b}{2}}\right) \\ B_z \rightarrow \frac{ck_x}{\omega}\left(e^{-k_{z,1}\frac{b}{2}} \pm e^{k_{z,1}\frac{b}{2}}\right) &= \frac{ck_x}{\omega}A_3e^{-k_{z,2}\frac{b}{2}} \\ A_3 &= e^{k_{z,2}\frac{b}{2}}\left(e^{-k_{z,1}\frac{b}{2}} \pm e^{k_{z,1}\frac{b}{2}}\right) \end{aligned}\right\} \tag{27}$$

$$\left.\begin{aligned} H_x \rightarrow \frac{ick_{z,1}}{\mu_1\omega}\left(-e^{-k_{z,1}\frac{b}{2}} \pm e^{k_{z,1}\frac{b}{2}}\right) &= -\frac{ick_{z,2}}{\mu_2\omega}A_3e^{-k_{z,2}z} \\ A_3 &= -\frac{\mu_2k_{z,1}}{\mu_1k_{z,2}}e^{k_{z,2}\frac{b}{2}}\left(-e^{-k_{z,1}\frac{b}{2}} \pm e^{k_{z,1}\frac{b}{2}}\right) \end{aligned}\right\} \tag{28}$$

This implies that:

$$\left.\begin{aligned} -\frac{k_{z,1}}{k_{z,2}}\left(-e^{-k_{z,1}\frac{b}{2}} \pm e^{k_{z,1}\frac{b}{2}}\right) &= \left(e^{-k_{z,1}\frac{b}{2}} \pm e^{k_{z,1}\frac{b}{2}}\right) \\ \frac{\mu_2k_{z,1}}{\mu_1k_{z,2}}\left(e^{-k_{z,1}\frac{b}{2}} \mp e^{k_{z,1}\frac{b}{2}}\right) &= \left(e^{-k_{z,1}\frac{b}{2}} \pm e^{k_{z,1}\frac{b}{2}}\right) \\ \mp\mu_2k_{z,1}\left(e^{k_{z,1}\frac{b}{2}} \mp e^{-k_{z,1}\frac{b}{2}}\right) &= \pm\mu_1k_{z,2}\left(e^{k_{z,1}\frac{b}{2}} \pm e^{-k_{z,1}\frac{b}{2}}\right) \end{aligned}\right\} \tag{29}$$

Compactly, the pair of the transcendental equations can be expressed as:

$$\mp\,\mu_2k_{z,1} = \pm\mu_1k_{z,2}\left\{\begin{array}{c} \coth\left(\frac{k_{z,1}b}{2}\right) \\ \tanh\left(\frac{k_{z,1}b}{2}\right) \end{array}\right\} \tag{30}$$

Upon further simplification, it gives:

$$\pm\,\mu_1k_{z,2} \pm \mu_2k_{z,1}\left\{\begin{array}{c} \tanh\left(\frac{k_{z,1}b}{2}\right) \\ \coth\left(\frac{k_{z,1}b}{2}\right) \end{array}\right\} \tag{31}$$

The dispersion relation here is not the same as the to the one obtained through the condition of continuity when E_x and D_z as stated in (22) and (23). Hence, it can either meet the condition of continuity at the interface for E_x, ϵE_z, H_y or for the case of E_y, H_z and H_x equivalent to the presence of transverse electric (TE) or transverse magnetic (TM) waves in the optical waveguide device.

A.2 Derivation of the Dispersion Relations for Five-layer Waveguides

In this section, the derivation of the dispersion relation for five-layered structure for metal-dielectric interface is presented. The dispersion relation presented here is general and can be expanded to N-layers. The structure considered is depicted in Fig. (2). It is assumed

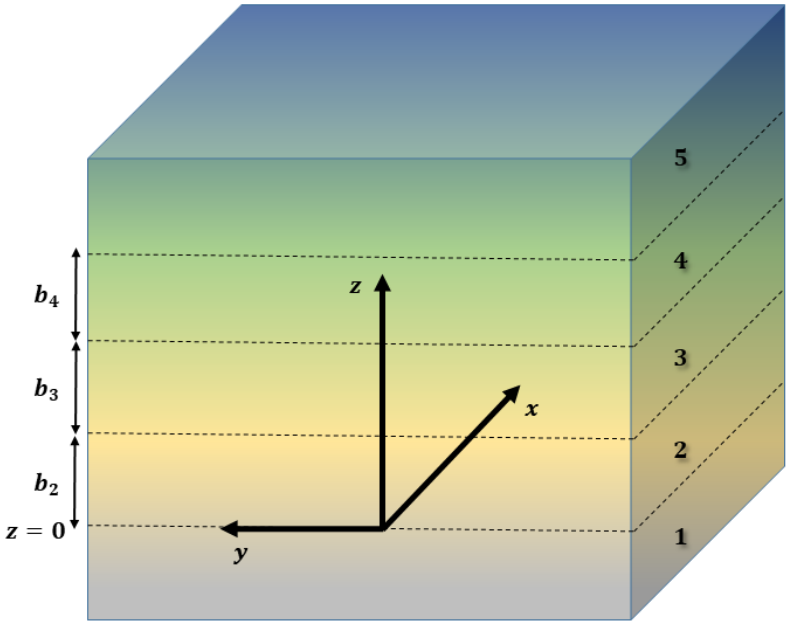

Figure 2: The geometry used for the formulation of the five-layer system assuming prorogation is along the x-axis

that the propagation of wave is along the x-axis. Referring to the preceding section, the components of electric fields can be expressed as:

$$\left.\begin{aligned} E_{x,m} &= e^{ik_x x}\left(g_m e^{k_{z,m}z} + h_m e^{-k_{z,m}z}\right) \\ E_{y,m} &= 0 \\ E_{z,m} &= \left(\frac{ik_x}{k_{z,m}}\right) e^{ik_x x}\left(-g_m e^{k_{z,m}z} + h_m e^{-k_{z,m}z}\right) \end{aligned}\right\} \tag{32}$$

where $m = 1, ..., 5$. By imposing the boundary conditions for the field components D_z and E_x which are continuous at the interface between 1 and 2 (i.e **1-2 interface**) from the Fig. 2, it gives upon substitution:

$$\left.\begin{aligned} g_1 + h_1 &= g_2 + h_2 \\ \frac{\epsilon_1}{k_{z,1}}(-g_1 + h_1) &= \frac{\epsilon_2}{k_{z,2}}(-g_2 + h_2) \end{aligned}\right\} \tag{33}$$

At the interface between **2 and 3**, the expression is given as:

$$\left.\begin{aligned} g_2 e^{k_{z,2}b_2} + h_2 e^{-k_{z,2}b_2} &= g_3 e^{k_{z,3}b_2} + h_2 e^{-k_{z,3}b_2} \\ \frac{\epsilon_2}{k_{z,2}}\left(-g_2 e^{k_{z,2}b_2} + h_2 e^{-k_{z,2}b_2}\right) &= \frac{\epsilon_3}{k_{z,3}}\left(-g_3 e^{k_{z,3}b_2} + h_3 e^{-k_{z,3}b_2}\right) \end{aligned}\right\} \tag{34}$$

At the interface between **3 and 4**, the expression can be cast as:

$$\left.\begin{aligned} g_3 e^{k_{z,3}(b_2+b_3)} + h_3 e^{-k_{z,3}(b_2+b_3)} &= g_4 e^{k_{z,4}(b_2+b_3)} + h_4 e^{-k_{z,4}(b_2+b_3)} \\ \frac{\epsilon_3}{k_{z,3}}\left(-g_3 e^{k_{z,3}(b_2+b_3)} + h_3 e^{-k_{z,3}(b_2+b_3)}\right) &= \frac{\epsilon_4}{k_{z,4}}\left(-g_4 e^{k_{z,4}(b_2+b_3)} + h_4 e^{-k_{z,4}(b_2+b_3)}\right) \end{aligned}\right\} \tag{35}$$

Finally, at the interface between **4 and 5**, the expression can be cast as:

$$\left.\begin{aligned} g_4 e^{k_{z,4}(b_2+b_3+b_4)} + h_4 e^{-k_{z,4}(b_2+b_3+b_4)} &= g_5 e^{k_{z,5}(b_2+b_3+b_4)} + h_5 e^{-k_{z,5}(b_2+b_3+b_5)} \\ \frac{\epsilon_4}{k_{z,4}}\left(-g_4 e^{k_{z,4}(b_2+b_3+b_4)} + h_4 e^{-k_{z,4}(b_2+b_3+b_4)}\right) &= \frac{\epsilon_5}{k_{z,5}}\left(-g_5 e^{k_{z,5}(b_2+b_3+b_4)} + h_5 e^{-k_{z,5}(b_2+b_3+b_4)}\right) \end{aligned}\right\} \tag{36}$$

Hence, as E_z goes to zero, when the $z \to \pm\infty$, the values of coefficients h_1 and g_5 have to be set equal to zero. Based on the equations Eqs. $(32-36)$, a system of equations; i.e, ten in number has been produced with ten unknown coefficients: g_i and h_j with i, j=1,2,...,5. The solvability condition for the coefficient requires that the determinant of the resulting matrix B is set equal to zero: $\det\{B\}$=0. This requirement determines the dispersion relation linking k_x and ω.

$$
\begin{bmatrix}
0 & 1 & 0 & 0 & 0 & 0 & 0 & 0 & 0 & 0 \\
1 & 1 & -1 & -1 & 0 & 0 & 0 & 0 & 0 & 0 \\
-\frac{\epsilon_1}{k_{z,1}} & \frac{\epsilon_1}{k_{z,1}} & \frac{\epsilon_2}{k_{z,2}} & -\frac{\epsilon_2}{k_{z,2}} & 0 & 0 & 0 & 0 & 0 & 0 \\
0 & 0 & e^{k_{z,2},b_2} & e^{-k_{z,2},b_2} & -e^{k_{z,3},b_2} & -e^{-k_{z,3},b_2} & 0 & 0 & 0 & 0 \\
0 & 0 & -\frac{\epsilon_2}{k_{z,2}} e^{k_{z,2}b_2} & \frac{\epsilon_2}{k_{z,2}} e^{-k_{z,2}b_2} & \frac{\epsilon_3}{k_{z,3}} e^{k_{z,3}b_2} & -\frac{\epsilon_3}{k_{z,3}} e^{-k_{z,3}b_2} & 0 & 0 & 0 & 0 \\
0 & 0 & 0 & 0 & e^{k_{z,3}b23} & e^{-k_{z,3}b23} & -e^{k_{z,4}b23} & -e^{k_{z,4}b23} & 0 & 0 \\
0 & 0 & 0 & 0 & -\frac{\epsilon_3}{k_{z,3}} e^{k_{z,3}b_{23}} & \frac{\epsilon_3}{k_{z,3}} e^{-k_{z,3}b_{23}} & \frac{\epsilon_4}{k_{z,4}} e^{k_{z,4}b_{23}} & -\frac{\epsilon_4}{k_{z,4}} e^{-k_{z,4}b_{23}} & 0 & 0 \\
0 & 0 & 0 & 0 & 0 & 0 & e^{k_{z,4},b_{234}} & e^{-k_{z,4},b_{234}} & -e^{k_{z,5},b_{234}} & -e^{k_{z,5},b_{234}} \\
0 & 0 & 0 & 0 & 0 & 0 & -\frac{\epsilon_4}{k_{z,4}} e^{k_{z,4},b_{234}} & \frac{\epsilon_4}{k_{z,4}} e^{-k_{z,4},b_{234}} & \frac{\epsilon_5}{k_{z,5}} e^{k_{z,5},b_{234}} & -\frac{\epsilon_4}{k_{z,5}} e^{-k_{z,5},b_{234}} \\
0 & 0 & 0 & 0 & 0 & 0 & 0 & 0 & 1 & 0
\end{bmatrix}
\tag{37}
$$

Here, $b_{23} = b_2 + b_3$ and $b_{234} = b_2 + b_3 + b_4$. The matrix in Eq. (37) is general and uniformly incorporates matrices associated with layered structures having 2, 3, 4, and 5 layers. For instance, the structure for two layers gives rise to a 4×4 matrix formation (from which the determinant can be computed:

$$\mathbf{B} = \begin{bmatrix} B_{1,1} & B_{1,2} & B_{1,3} & B_{1,4} \\ B_{2,1} & B_{2,2} & B_{2,3} & H_{2,4} \\ B_{3,1} & B_{3,2} & B_{3,3} & B_{3,4} \\ B_{4,1} & B_{4,2} & B_{4,3} & B_{4,4} \end{bmatrix} \tag{38}$$

which simplifies to the following matrix based on the above general formulation:

$$\mathbf{B} = \begin{bmatrix} 0 & 1 & 0 & 0 \\ 1 & 1 & -1 & -1 \\ -\frac{\epsilon_1}{k_{z,1}} & \frac{\epsilon_1}{k_{z,1}} & \frac{\epsilon_2}{k_{z,2}} & -\frac{\epsilon_2}{k_{z,2}} \\ 0 & 0 & 1 & 0 \end{bmatrix} \tag{39}$$

Additionally, for a three- and four-layered structure, the matrix formation size is 6×6 and 8×8, respectively, and expressed as:

$$\mathbf{B} = \begin{bmatrix} 0 & 1 & 0 & 0 & 0 & 0 \\ 1 & 1 & -1 & -1 & 0 & 0 \\ -\frac{\epsilon_1}{k_{z,1}} & \frac{\epsilon_1}{k_{z,1}} & \frac{\epsilon_2}{k_{z,2}} & -\frac{\epsilon_2}{k_{z,2}} & 0 & 0 \\ 0 & 0 & e^{k_{z,2}b_2} & e^{-k_{z,2}b_2} & -e^{k_{z,3}b_2} & -e^{-k_{z,3}b_2} \\ 0 & 0 & -\frac{\epsilon_2}{k_{z,2}}e^{k_{z,2}b_2} & \frac{\epsilon_2}{k_{z,2}}e^{-k_{z,2}b_2} & \frac{\epsilon_3}{k_{z,3}}e^{k_{z,3}b_2} & -\frac{\epsilon_3}{k_{z,3}}e^{-k_{z,3}b_2} \\ 0 & 0 & 0 & 0 & 1 & 0 \end{bmatrix} \tag{40}$$

$$\mathbf{B} = \begin{bmatrix} B_{1,1} & B_{1,2} & B_{1,3} & B_{1,4} & B_{1,5} & B_{1,6} & B_{1,7} & B_{1,8} \\ B_{2,1} & B_{2,2} & B_{2,3} & B_{2,4} & B_{2,5} & B_{2,6} & B_{2,7} & B_{2,8} \\ B_{3,1} & B_{3,2} & B_{3,3} & B_{3,4} & B_{3,5} & B_{3,6} & B_{3,7} & B_{3,8} \\ B_{4,1} & B_{4,2} & B_{4,3} & B_{4,4} & B_{4,5} & B_{4,6} & B_{4,7} & B_{4,8} \\ B_{5,1} & B_{5,2} & B_{5,3} & B_{5,4} & B_{5,5} & B_{5,6} & B_{5,7} & B_{5,8} \\ B_{6,1} & B_{6,2} & B_{6,3} & B_{6,4} & B_{6,5} & B_{6,6} & B_{6,7} & B_{6,8} \\ B_{7,1} & B_{7,2} & B_{7,3} & B_{7,4} & B_{7,5} & B_{7,6} & B_{7,7} & B_{7,8} \\ B_{8,1} & B_{8,2} & B_{8,3} & B_{8,4} & B_{8,5} & B_{8,6} & B_{8,7} & B_{8,8} \end{bmatrix} \tag{41}$$

$$\mathbf{B} = \begin{bmatrix} 0 & 1 & 0 & 0 & 0 & 0 & 0 & 0 \\ 1 & 1 & -1 & -1 & 0 & 0 & 0 & 0 \\ -\frac{\epsilon_1}{k_{z,1}} & \frac{\epsilon_1}{k_{z,1}} & \frac{\epsilon_2}{k_{z,2}} & -\frac{\epsilon_2}{k_{z,2}} & 0 & 0 & 0 & 0 \\ 0 & 0 & e^{k_{z,2}b_2} & e^{-k_{z,2}b_2} & -e^{k_{z,3}b_2} & -e^{-k_{z,3}b_2} & 0 & 0 \\ 0 & 0 & -\frac{\epsilon_2}{k_{z,2}}e^{k_{z,2}b_2} & \frac{\epsilon_2}{k_{z,2}}e^{-k_{z,2}b_2} & \frac{\epsilon_3}{k_{z,3}}e^{k_{z,3}b_2} & -\frac{\epsilon_3}{k_{z,3}}e^{-k_{z,3}b_2} & 0 & 0 \\ 0 & 0 & 0 & 0 & e^{k_{z,3}b_{2,3}} & e^{-k_{z,3}b_{2,3}} & -e^{k_{z,4}b_{2,3}} & -e^{-k_{z,4}b_2} \\ 0 & 0 & 0 & 0 & -\frac{\epsilon_3}{k_{z,3}}e^{k_{z,3}b_{2,3}} & \frac{\epsilon_3}{k_{z,3}}e^{-k_{z,3}b_{2,3}} & \frac{\epsilon_4}{k_{z,4}}e^{k_{z,4}b_{2,3}} & -\frac{\epsilon_4}{k_{z,4}}e^{-k_{z,4}b_{2,3}} \\ 0 & 0 & 0 & 0 & 0 & 0 & 1 & 0 \end{bmatrix} \tag{42}$$

In general, when the number of the layers is N, the size of the matrix formation will be $2N$ with a pattern being followed. Similarly, the above scheme can be applied to cylindrical and spherical structural, even though the algebraic manipulations are comparatively more tedious.

A.3 Numerical Solution of Dispersion Relations

This section outlines briefly the numerical approaches employed for finding solutions to the dispersion relations. In principle, the dispersion relations comprises transcendental equations in which the wavenumber k and the operating frequency ω are complex-valued. In the furtherance of homo-chromatic excitation of modes of waveguides, it makes sense to enforce the frequency being real. Regrettably, $\det(\mathbf{B}) = 0$ does not in any way have definite solutions in the region of real frequency, hence, the scheme adopted in Chapter three suffices to solve

this transcendental equations. Furthermore, other schemes such as minimization methods can be employed. Depending on the geometry of the waveguide, one or more solutions exist for every wavelength in the complex region as demonstrated in Chapter three of this thesis. Furthermore, in this thesis, numerical solutions in terms of algorithm proposed have been employed to solve the complex wavevectors in a given frequency, repeating it in the frequency-region to obtain a continuous dispersion diagram.

B Higher-Order Terms in Perturbed density Formulation

This section describes the concept of higher-order terms based in perturbed density calculations, discussed in Chapter four of this thesis, using equation of motion called Liouville's equation of motion:

$$i\hbar\frac{\partial\hat{\rho}}{\partial t} = [\hat{H},\hat{\rho}] = [\hat{H}_0,\hat{\rho}_0] + [\hat{H}_0,\hat{\rho}_1] + [\hat{H}_1,\hat{\rho}_0] + [\hat{H}_1,\hat{\rho}_1] \tag{43}$$

Assuming $[\hat{H}_0,\hat{\rho}_0] = 0$, and writing out the remaining commutators:

$$i\hbar\frac{\partial\hat{\rho}}{\partial t} = \hat{H}_0\hat{\rho}_1 - \hat{\rho}_1\hat{H}_0 + \hat{H}_1\hat{\rho}_0 - \hat{\rho}_0\hat{H}_1 + \hat{H}_1\hat{\rho}_1 - \hat{\rho}_1\hat{H}_1 \tag{44}$$

Let $\hat{\rho}_1 = \hat{\rho}^{(1)}$, $\hat{H}_1 = \hat{H}^{(1)}$, $\hat{\rho}^{(1)} = \sum_i\sum_f C_{f,i}|f\rangle\langle i| = \sum_i\sum_f \hat{\rho}^{(1)}_{f,i}|f\rangle\langle i|$. In this section, we have defined $\hat{\rho}^{(1)}_{f,i} = \left\langle f|\hat{\rho}^{(1)}|i\right\rangle$, $\hat{H}^{(1)} = \sum_i\sum_f |f><f|\hat{H}^{(1)}|i><i|$. Furthermore, assuming

a harmonic time variation according to $e^{-i\omega t}$

$$i\hbar\left(-i\omega\hat{\rho}_1\right) = \hat{H}_0\hat{\rho}_1 - \hat{\rho}_1\hat{H}_0 + \hat{H}_1\hat{\rho}_0 - \hat{\rho}_0\hat{H}_1 + \hat{H}_1\hat{\rho}_1 - \hat{\rho}_1\hat{H}_1 \tag{45}$$

Let $[\hat{H}_1, \hat{\rho}_1] = \left(\sum_{f,i} |f><i|\hat{H}_{if}^{(1)}\right)\left(\sum_{f,i} |f><i|\hat{\rho}_{if}^{(1)}\right) - \left(\sum_{f,i} |f><i|\hat{\rho}_{if}^{(1)}\right)\left(\sum_{f,i} |f><i|\hat{H}_{if}^{(1)}\right)$.

Also, let $\hat{H}_{if}^{(1)} =< f|\hat{H}_1|i >$ and $\hat{\rho}_{if}^{(1)} =< f|\hat{\rho}_1|i >$. Upon substitution and further simplification, Eq. (44) leads to

$$\hbar\omega P_{1if} + \left(E_i - E_f\right)P_{1if} = \left(w_1 - w_f\right)H_{if} + \Gamma_{if} - \Theta_{if} \tag{46}$$

where $P_{1if} = \sum_{i,f} \hat{\rho}_{if}^{(1)} |f><i|$, $H_{if} = \sum_{if} \hat{H}_{if}^{(1)} |f><i|$. Additionally, we let also $\Gamma_{if} = \left(\sum_{f,i} |f><i|\hat{H}_{if}^{(1)}\right)\left(\sum_{f,i} |f><i|\hat{\rho}_{if}^{(1)}\right)$, and $\Theta_{if} = \left(\sum_{f,i} |f><i|\hat{\rho}_{if}^{(1)}\right)\left(\sum_{f,i} |f><i|\hat{H}_{if}^{(1)}\right)$. Assuming a damping, $\hbar\gamma$ is present in the system. Therefore, Eq. (46) further simplifies to

$$P_{1if} = \frac{\left(w_i - w_f\right)H_{if}}{\hbar\left(\omega + i\gamma\right) + \left(E_i - E_f\right)} + \frac{\Gamma_{if}}{\hbar\left(\omega + i\gamma\right) + \left(E_i - E_f\right)} - \frac{\Theta_{if}}{\hbar\left(\omega + i\gamma\right) + \left(E_i - E_f\right)} \tag{47}$$

For further simplification, Eq.(47) can be written compactly as

$$\tilde{P}_{if} = \alpha_{ij}\tilde{H}_{if} + \tilde{\Gamma}_{if} + \tilde{\Theta}_{if} \tag{48}$$

where we have made the following variable transformations in a set of equations as

$$\left.\begin{aligned} P_{1if} &= \tilde{P}_{if} \\ \frac{H_{if}}{\hbar\left(\omega + i\gamma\right) + \left(E_i - E_f\right)} &= \tilde{H}_{if} \\ \left(w_i - w_f\right) &= \alpha_{ij} \\ \frac{\Gamma_{if}}{\hbar\left(\omega + i\gamma\right) + \left(E_i - E_f\right)} &= \tilde{\Gamma}_{if} \\ \frac{-\Theta_{if}}{\hbar\left(\omega + i\gamma\right) + \left(E_i - E_f\right)} &= \tilde{\Theta}_{if} \end{aligned}\right\} \tag{49}$$

Hence, the Eq. (48) can be solved numerically to obtain the optical properties of material of interest.

C Summary of Fundamental Equations in CFDM

In this appendix, the details concerning the computation of CFDM coefficients are presented for enabling a better understanding of the method. The underlying idea of CFDM follows this pattern: Dicretization method that preserves the main properties of the originating operator ensures more accurate numerical results than the discretization schemes that lack the property. The Standard Finite Difference Method (FDM) is a case in point. The ability of preserving crucial operator properties is achieved to a sophisticated usage of cell- and grid points, following the discretization of the simulation domain and its boundary. To this end Green's formula, or other allied theorems in mathematical physics are employed when applying CFDM. This section demonstrates relevant differential operators in CFDM,

assuming 2-D boundary value problems. Following the analysis outlined in this appendix, extensions to 3-D or other boundary conditions is immediate.

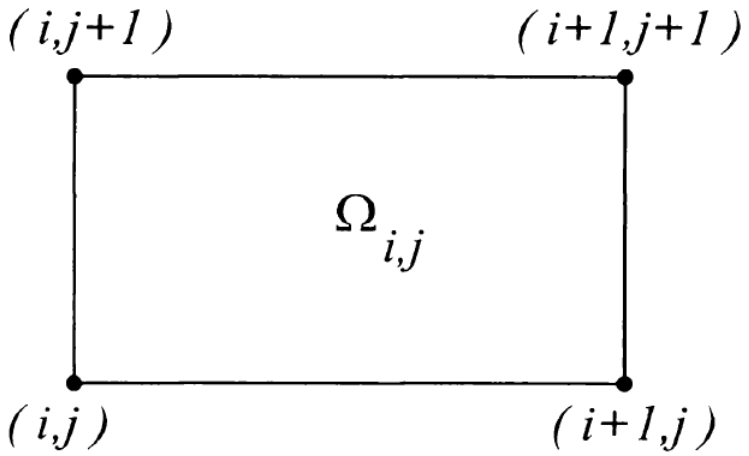

Figure 3: The geometry used for the formulation of CFDM on a rectangular stencil

C.1 Different Ways to Carry-out Discretization in CFDM

There are two ways to discretize the simulation domain: i) discretizing Scalar Functions on the Nodes and Vector Functions in the Cell-Centre, and discretizing Scalar Functions in the Cell-Centre and ii) discretizing Vector Functions on the Nodes. The Green's Theorem is employed to construct the Difference operators corresponding to originating Differential counterpart. To demonstrate this, the starting point is the Green's theorem formulated on the domain D with the oriented boundary curve C, is depicted in Fig. (5),

$$\int_C (L\partial x + M\partial y) = \iint_D \left(\frac{\partial M}{\partial x} - \frac{\partial L}{\partial y}\right) dx\, dy. \tag{50}$$

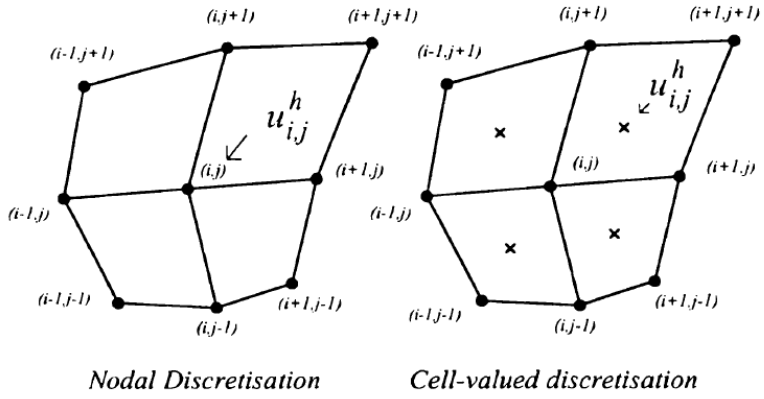

Figure 4: The geometry used for the formulation of CFDM using nodal- and cell-valued discretization

The following special cases and approximations thereof can be deduced:

$$\left.\begin{aligned} \int_C M\partial y = \iint_D \left(\frac{\partial M}{\partial x}\right) dA \\ \int_C L\partial x = \iint_D \left(\frac{-\partial L}{\partial y}\right) dA \\ \int_C M\partial y = A\left(\frac{\partial M}{\partial x}\right) \\ \frac{\int_C M\partial y}{A} = \frac{\partial M}{\partial x} \end{aligned}\right\} \tag{51}$$

By relating this to the eigenstate (wavefunction) of the particle denoted by ψ,

$$\frac{\partial \psi}{\partial x} = \lim_{S\to 0} \frac{\int_\ell \psi \partial y}{S} \tag{52}$$

This relationship is outstanding: the differential (derivative) operator is expressed in terms of a lower-dimensional contour integral. The Eq.(52) can be applied to general logically rectangular stencils. However, the presentation here is restricted to geometrically rectangular

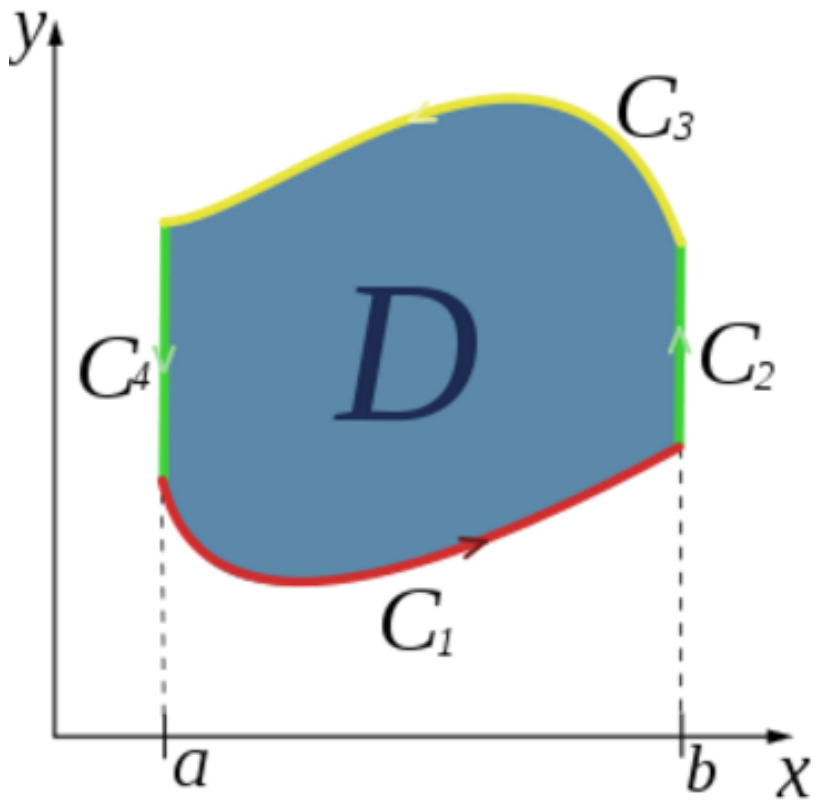

Figure 5: The demonstration of Green's theorem application for discretizing differential operators

stencils. The ability of emplying logically rectangular stencils is another hallmark of CFDM, beside the preservation of the operator properties. With reference to Fig. (3):

$$\begin{aligned}\left(D_x\psi^h\right)_{ij} = \\ \frac{1}{\Omega_{i,j}}\Bigg\{&\left(\frac{\psi_{i+1,j}+\psi_{i,j}}{2}\right)\left(y_{i+1,j}-y_{i,j}\right)+\left(\frac{\psi_{i+1,j+1}+\psi_{i+1,j}}{2}\right)\left(y_{i+1,j+1}-y_{i,j+1}\right)\\ &+\left(\frac{\psi_{i,j+1}+\psi_{i+1,j+1}}{2}\right)\left(y_{i,j+1}-y_{i+1,j+1}\right)+\left(\frac{\psi_{i,j}+\psi_{i,j+1}}{2}\right)\left(y_{i,j}-y_{i,j+1}\right)\Bigg\}\end{aligned} \quad (53)$$

C.2 Formulae for the Determination of CFDM Coefficients

Let a_1, a_2, b_1, b_2, c_1, c_2, d_1, d_2, f_1, f_2, g_1, g_2, h_1, h_2, k_1, and, k_2 are real values and α_i are the coefficients of each of the contributing nodes. The following are the definitions of each of the parameters as defined in Eqs.(6.46) and (6.47):

$$a_1 = \left(\frac{y_{i,j+1} - y_{i+1,j}}{2}\right)\left(\frac{y_{i,j+1} - y_{i+1,j}}{2Vc_{i,j}}\right) \tag{54}$$

$$a_2 = -\left(\frac{y_{i,j+1} - y_{i+1,j}}{2}\right)\left(\frac{y_{i+1,j+1} - y_{i,j}}{2Vc_{i,j}}\right) \tag{55}$$

$$b_1 = \left(\frac{y_{i-1,j} - y_{i,j+1}}{2}\right)\left(\frac{y_{i-1,j+1} - y_{i,j}}{2Vc_{i-1,j}}\right) \tag{56}$$

$$b_2 = -\left(\frac{y_{i-1,j} - y_{i,j+1}}{2}\right)\left(\frac{y_{i,j+1} - y_{i-1,j}}{2Vc_{i-1,j}}\right) \tag{57}$$

$$c_1 = \left(\frac{y_{i,j-1} - y_{i-1,j}}{2}\right)\left(\frac{y_{i-1,j} - y_{i,j-1}}{2Vc_{i-1,j-1}}\right) \tag{58}$$

$$c_2 = -\left(\frac{y_{i,j-1} - y_{i-1,j}}{2}\right)\left(\frac{y_{i,j} - y_{i-1,j-1}}{2Vc_{i-1,j-1}}\right) \tag{59}$$

$$d_1 = \left(\frac{y_{i+1,j} - y_{i,j-1}}{2}\right)\left(\frac{y_{i+1,j} - y_{i,j-1}}{2Vc_{i,j-1}}\right) \tag{60}$$

$$d_2 = -\left(\frac{y_{i+1,j} - y_{i,j-1}}{2}\right)\left(\frac{y_{i,j} - y_{i+1,j-1}}{2Vc_{i,j-1}}\right) \tag{61}$$

$$f_1 = \left(\frac{x_{i,j+1} - x_{i+1,j}}{2}\right)\left(\frac{x_{i,j+1} - x_{i+1,j}}{2Vc_{i,j}}\right) \tag{62}$$

$$f_2 = -\left(\frac{x_{i,j+1} - x_{i+1,j}}{2}\right)\left(\frac{x_{i+1,j+1} - x_{i,j}}{2Vc_{i,j}}\right) \tag{63}$$

$$g_1 = \left(\frac{x_{i-1,j} - x_{i,j+1}}{2}\right)\left(\frac{x_{i-1,j+1} - x_{i,j}}{2Vc_{i-1,j}}\right) \tag{64}$$

$$g_2 = -\left(\frac{x_{i-1,j} - x_{i,j+1}}{2}\right)\left(\frac{x_{i,j+1} - x_{i-1,j}}{2Vc_{i-1,j}}\right) \tag{65}$$

$$h_1 = \left(\frac{x_{i,j-1} - x_{i-1,j}}{2}\right)\left(\frac{x_{i-1,j} - x_{i,j-1}}{2Vc_{i-1,j-1}}\right) \tag{66}$$

$$h_2 = -\left(\frac{x_{i,j-1} - x_{i-1,j}}{2}\right)\left(\frac{x_{i,j} - x_{i-1,j-1}}{2Vc_{i-1,j-1}}\right) \tag{67}$$

$$k_1 = \left(\frac{x_{i+1,j} - x_{i,j-1}}{2}\right)\left(\frac{x_{i,j} - x_{i+1,j-1}}{2Vc_{i,j-1}}\right) \tag{68}$$

$$k_2 = -\left(\frac{x_{i+1,j} - x_{i,j-1}}{2}\right)\left(\frac{x_{i+1,j} - x_{i,j-1}}{2Vc_{i,j-1}}\right) \tag{69}$$

The α_i are expressed in terms of the above parameters as follows:

$$\left.\begin{aligned}
\alpha_1 &= a_1 + f_1 \\
\alpha_2 &= a_1 + f_1 + d_2 + k_2 + b_2 + g_2 + c_2 + h_1 \\
\alpha_3 &= a_2 + b_1 + f_2 + g_1 \\
\alpha_4 &= a_2 + f_2 + d_1 + k_2 \\
\alpha_5 &= b_1 + c_2 + h_2 + g_1 \\
\alpha_6 &= b_2 + g_2 \\
\alpha_7 &= c_1 + h_1 \\
\alpha_8 &= d_2 + k_2 \\
\alpha_1 &= c_2 + d_1 + h_2 + k_1
\end{aligned}\right\} \tag{70}$$